UNIVERSITY OF SOUTHAMPTON

A Long Timescale High-Resolution Fault Activity History of the Whakatane Graben, Bay of Plenty, New Zealand.

Susanna K. Taylor

This thesis is submitted for

Doctor of Philosophy

Faculty of Science

School of Ocean and Earth Science

May, 2003

Graduate School of the
Southampton Oceanography Centre

This PhD dissertation by

Susanna K. Taylor

has been produced under the supervision of the following persons

Supervisors

Dr. Jonathan Bull

Dr. Patience Cowie
Prof. David Sanderson

Dr. Geoffroy Lamarche

Members of Advisory Panel

Dr. Andrew Barker

Dr. Andrew Roberts

Acknowledgements

I would like to thank all the people who have made completing this work both successful and enjoyable. I would particularly like to thank my main supervisor Jon Bull for his support and advice throughout the three years I was in Southampton. I would also like to thank my other supervisors Geoffroy Lamarche, Dave Sanderson and Patience Cowie for support and helpful comments.

Phil Barnes provided invaluable expertise in determining the stratigraphy of the field area. I am grateful to the officers and crew of R/V Tangaroa and R/V Kaharoa for their dedication during TAN99-14 and KAH01-02, and to Justin Dix and the technical team at NIWA for their expertise in geophysical data acquisition. Steve Wilcox and Andy Hill are thanked for their help in preparation for the Kaharoa Cruise.

This work was funded by the Natural Environment Research Council (GR3/11862) with an associated tied studentship, United Kingdom and the New Zealand Foundation for Research Science and Technology (FRST-CO1X0038).

Sheila, Nat, Babbette, Al and Mike have been good friends and great company, and helped me keep the last shreds of my sanity together towards the end.

UNIVERSITY OF SOUTHAMPTON

ABSTRACT

FACULTY OF SCIENCE

SCHOOL OF OCEAN AND EARTH SCIENCE

Doctor of Philosophy

A LONG-TIMESCALE HIGH-RESOLUTION FAULT ACTIVITY HISTORY FOR THE WHAKATANE GRABEN, BAY OF PLENTY, NEW ZEALAND

by Susanna Katharine Taylor

The Whakatane Graben is a back-arc basin situated in the Bay of Plenty, North Island, New Zealand, associated with the oblique westward subduction of the Pacific Plate beneath the Australian Plate. The data presented in this thesis reveal both long-term and short-term normal fault behaviour in a fault population surrounding and including one of the most active faults in the offshore graben.

Closely spaced (100 - 200 m separation) multichannel seismic and high resolution (chirp sonar, 3.5 kHz and boomer) profiles were collected during cruises in December 1999 and January 2001. These data were processed and interpreted and fault displacement data were extracted.

The Rangitaiki Fault lies in the centre of the Whakatane Graben, and is now recognised as a 20 km long, linked, segmented normal fault. The displacement profile of the fully linked Rangitaiki Fault resembles that of a single fault, with a maximum close to the centre and displacements decreasing towards the tips. The fault was found to have initiated as 5 isolated segments, which grew together over 1 Ma. Fault tip propagation was the dominant faulting process initially, followed by the development of relay zones and their subsequent breaching. The system became fully linked between 300 ka and 17 ka, and increased in displacement rate from 0.52 ± 0.18 mm yr^{-1} prior to linkage, to 1.41 ± 0.31 mm yr^{-1} afterward. Accurate observations of fault growth rates are hampered by the limited age control of the seismic horizons.

The fault propagated northwards and the fault system present today is interpreted as a highly evolved damage zone, where optimally oriented and located faults have linked to form the major Rangitaiki Fault structure and have increased in displacement rate. Displacement is transferred southward from the Rangitaiki Fault onto the newly identified Thornton Fault. The Thornton Fault is along-strike from the onshore surface ruptures caused by the 1987 Edgecumbe earthquake (magnitude 6.3). A repeat time of 320 – 600 years is inferred for Edgecumbe size events on the Rangitaiki Fault, close to the maximum magnitude for that size of fault. The combined extension rate for all observed faults across the pseudo-3D survey area for the last 17 ± 1 ka is 2.4 – 3.4 $mmyr^{-1}$, increased from 0.7 – 0.9 $mmyr^{-1}$ for the time interval between 300 – 17 ka. The increase in extension rate observed in the Whakatane Graben is interpreted as resulting from the eastward migration of the locus of deformation within the Bay of Plenty towards the Hikurangi subduction zone.

Contents

List of Figures

List of Tables

Chapter 1

Introduction

Understanding the growth of faults is important as they control fluid flow, create hydrocarbon traps and cause earthquakes. Fault systems are imaged in a variety of settings around the world, in many different stages of development. The observed faults are the end results of the fault development history, and often retain little or no information about the processes that led to their formation. Sediment deposits in areas of syn-sedimentary faulting (where faults are active at or near the surface at the time of sedimentary deposition) can retain information about the location and timing of fault movements throughout the fault activity history. The data presented in this thesis are from an area of syn-sedimentary faulting that has recorded fault activity over the last c. 1.3 Ma. The data are from two pseudo-3D seismic surveys that image an area around the Rangitaiki Fault, an actively growing, syn-sedimentary, segmented normal fault in the Whakatane Graben, New Zealand. The Whakatane Graben is ideal for this study because it is a young (< 2 Ma) and highly active structure situated on the New Zealand continental shelf where it has been well supplied with sediment. The sediment supply is sufficient to infill any accommodation space created by the rapidly active faults, thus providing a record of past fault motions. Furthermore, the shallow water depths (up to 200 m) of the graben on the continental shelf mean it is well placed for acquisition of high-resolution seismic data and core samples.

The temporal resolution of fault growth provided by this study area means that fault development processes could be well defined over both long-timescales (100s of thousands of years) and short-timescales (thousands of years). The spatial and temporal constraints on fault growth are used here to demonstrate which fault propagation processes occur, and the rates and timescales over which they operate. In addition, the results are used to improve the level of understanding of the tectonics of the Whakatane Graben and Taupo Volcanic Zone.

This thesis focuses on recent fault activity within the Whakatane Graben, which is situated on the continental shelf north of New Zealand in the Bay of Plenty. The graben is the offshore extension of the Taupo Fault Belt, which is the youngest and current active rift system within the Taupo Volcanic Zone (TVZ). In this chapter the geology and tectonics of the region is outlined, before a review of normal faults and fault growth models is made, and finally the thesis structure is summarised.

1.1 Regional Geology

1.1.1 Regional Tectonic Setting

The Whakatane Graben is situated in shallow water depths in the Bay of Plenty. The graben is part of the Taupo Fault Belt, which is the youngest and current active rift system within the Taupo Volcanic Zone (TVZ). The TVZ marks the zone of Quaternary back-arc rifting and calc-alkaline volcanism associated with the oblique westward subduction of the Pacific plate beneath the Australian plate at the Hikurangi plate-boundary margin (Figure 1.1)(Wright, 1992). North of New Zealand, the oceanic Pacific Plate is subducted beneath the continental Australian Plate forming the Lau-Havre back-arc system, passing southward into the Taupo-Hikurangi subduction system on land (Cole and Lewis, 1981). The subduction becomes progressively more oblique southwards as the Hikurangi Trough merges with the Alpine Fault system. South of New Zealand the subduction is eastward; with the Pacific plate overriding the Australian plate at the Puysegur Trench. The transition between westward and eastward subduction occurs along the reverse dextral Alpine fault and the associated compression and uplift has caused the development of the Southern Alps. The pole of Pacific-Australian rotation lies close to New Zealand, at 62°S 174°E (Chase, 1978), and has moved steadily southwards through time making different plate configurations progressively stable and unstable (Ballance, 1999).

The 030° trending TVZ extends northwards from the Tongariro volcanic centre south of Lake Taupo to up to 150 km offshore (Wright, 1992). Onshore, the TVZ contains the Taupo fault belt and the Taupo-Rotorua depression to the northwest, and at the coast, the Whakatane Graben. The Taupo fault belt is a zone of late Quaternary, dominantly normal, mostly NNE-trending faults extending from Mt Ruapehu to the Bay of Plenty coast (Grindley, 1960). The fault belt is about 20 km wide with an overall strike of 40°, rotating to 055° in the northeast (Healy et al., 1964). Some fault movement in the fault belt post-dates the 1.85 ka Taupo eruption (Nairn and Hull, 1985) and historical surface ruptures have been noted from 1922 (Grindley and Hull, 1986), 1983 (Otway, 1986) and

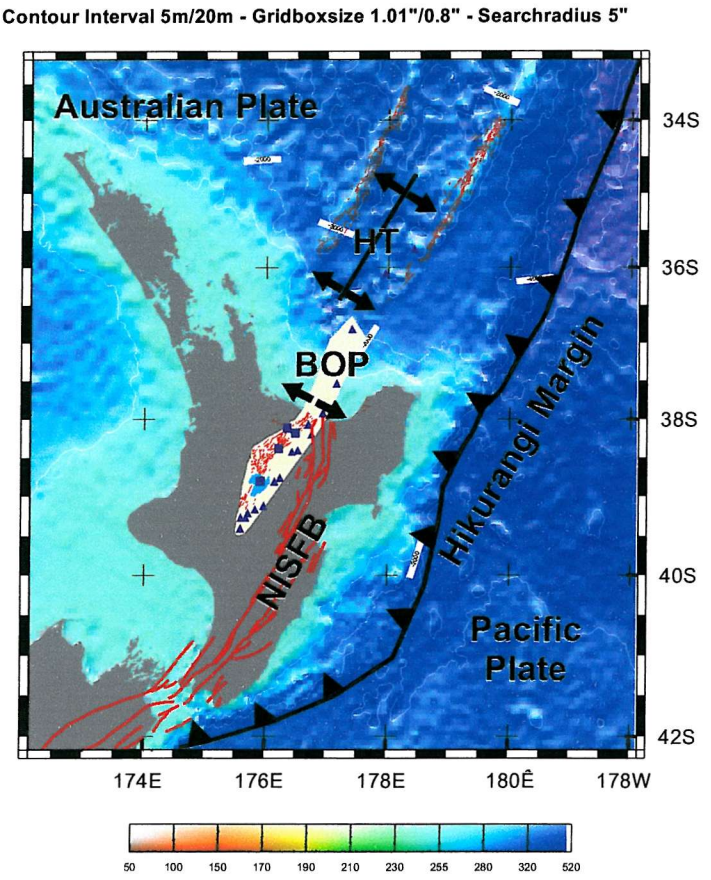

FIgure 1.1: Map showing the Plate Boundary in Northern New Zealand. The Australian Plate is subducted beneath the Pacific Plate at the Hikurangi Margin, resulting in back-arc extension at the Havre Trough (HT) and Bay of Plenty (BOP) and volcanism in the Taupo Volcanic Zone (TVZ) (yellow area, volcanic centres shown by purple triangles. Active faults are shown by red lines, the faults are extensional within the TVZ and dextral strike-slip in the North Island Shear Fault Belt (NISFB). Bathymetry from Global Seafloor Topography from satelite altimetry and ship depth soundings (Smith and Sandwell, 1997).

the Edgecumbe earthquake of 1987 (Beanland et al., 1990).The Taupo-Rotorua depression is a back-arc graben containing rhyolitic volcanic centres infilled with 2 – 4 km of rhyolitic pyroclastics and lavas erupted from at least four late Quaternary volcanic centres (Cole, 1990).

Offshore, the TVZ is bounded to the west and east by the Tauranga and White Island fault zones respectively and comprises three parallel, tectono-morphological units (Wright, 1992). These units are (from southeast to northwest) the frontal, non-volcanic Whakatane Graben, the volcanic Rurima Ridge and the volcanic back-arc Motiti Graben. Active faulting in the offshore TVZ is largely restricted to the 15 – 20 km wide Whakatane Graben where many laterally discontinuous northeast trending normal faults are observed (Wright

1990) (Figures 1.2 – 1.4). The seismic profile interpreted by Davey et al. (1995) shows the deep structure of the offshore TVZ; the faults are dominantly NW dipping and listric, and sole out at c. 3 seconds TWT. The major listric faults (including the Rangitaiki Fault) have resulted in several rotated blocks of greywacke basement. The faults in the overlying sediment cover are generally steeper than the basement faults, and have less vertical continuity.

The deep structure of the White Island Fault is poorly imaged on seismic data, possibly as a result of a large velocity contrast across the structure. Davey et al. (1995) identify the White Island Fault as the easternmost listric fault in the Whakatane Graben, but subsequent analysis has shown that this is not the case (J. Bull, pers. comm. 2003). The feature now identified as the White Island Fault is poorly resolved at depth, but has a notable surface scarp.

The western boundary of the TVZ, the Tauranga Fault Zone, is clearly different to the eastern boundary in that it is formed of several, relatively low displacement faults dipping toward the southeast. Davey et al. (1995) suggest that the western margin of the offshore TVZ is a caldera structure formed at the initiation of TVZ extension approximately 2 Ma ago, with subsequent faulting propagating eastwards forming a crustal decollement. Figure 1.4 shows the top 2 seconds TWT through the TVZ and demonstrates the respective ages of the western Motiti Graben and the younger Whakatane Graben to the east. Faulting in the Motiti Graben affects deeper (older) sediments than in the Whakatane Graben, and few of the faults in the Motiti Graben displace the surface sediments whereas the majority of faults in the Whakatane Graben break the surface. These faults show that the Motiti Graben is older and now less active than the Whakatane Graben.

East of the onshore TVZ (east of the Whakatane Fault; Figure 1.3) is the presently active North Island Shear Belt (NISB), a zone of dextral strike slip faults that shows a total Holocene shear displacement rate of 14 – 18 $mmyr^{-1}$ (Lensen, 1975). The NISB extends through the North Island of New Zealand to the Bay of Plenty coast. The faults within the NISB dominantly trend north-south where they approach and intersect the Whakatane Graben (Nairn and Beanland, 1989). Despite the intersection of the Whakatane Graben and the NISB, no shear faults are observed within the Whakatane Graben itself, either on land or offshore. East of the Whakatane Graben, however, the NISB is clearly active, with faulting observed onshore at Ohiwa (Sanderson and Bull, pers. com.)

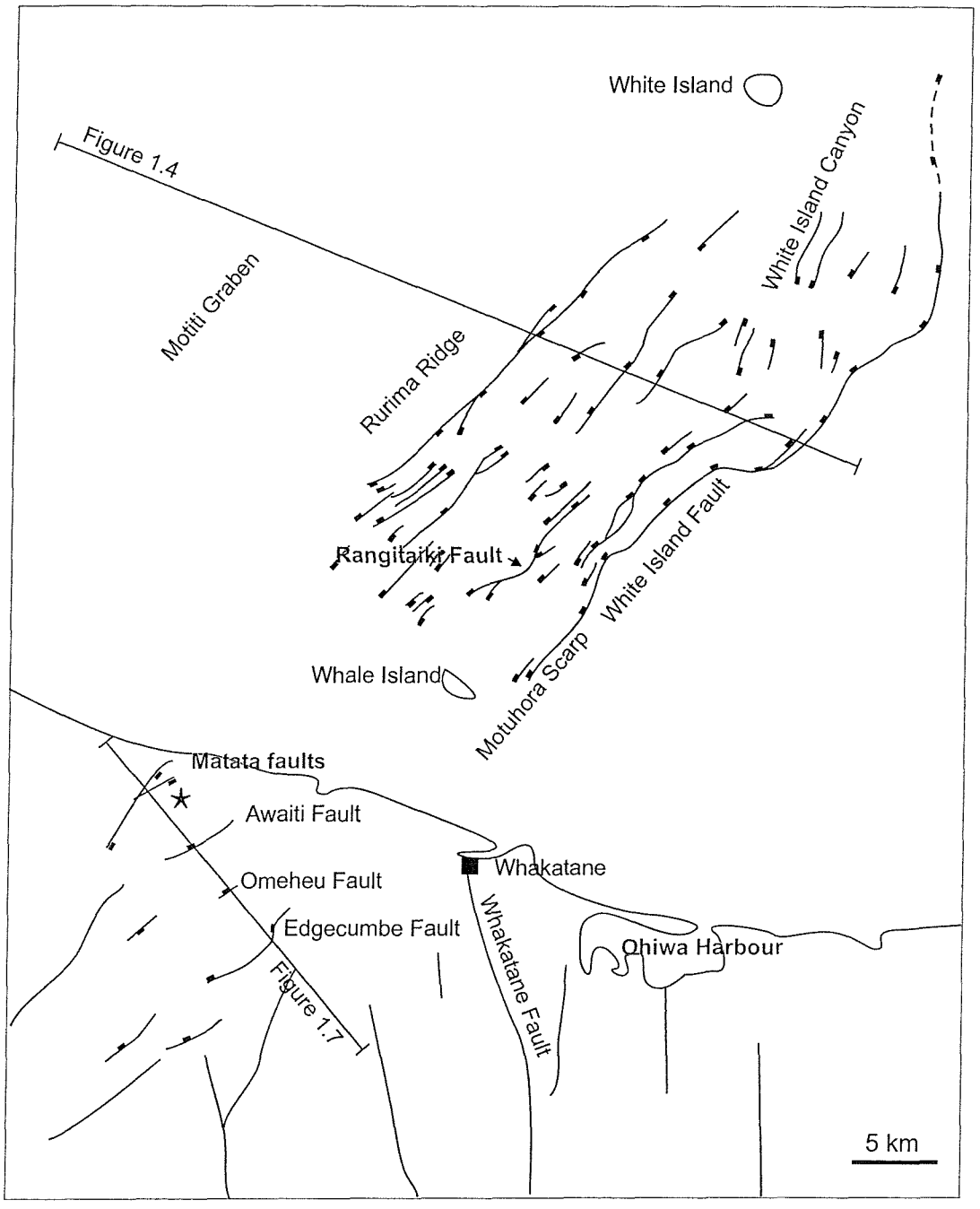

Figure 1.2: Active faulting in the Whakatane Graben, mapped prior to cruises TAN99-14 and KAH01-02. Offshore faults mapped by Wright (1990), onshore faults mapped by Nairn and Beanland (1989) (see figure 1.6 for complete map). The location of the Edgecumbe earthquake main-shock epicentre is shown by a star. Locations of the profiles shown in figures 1.4 and 1.7 are marked on the map.

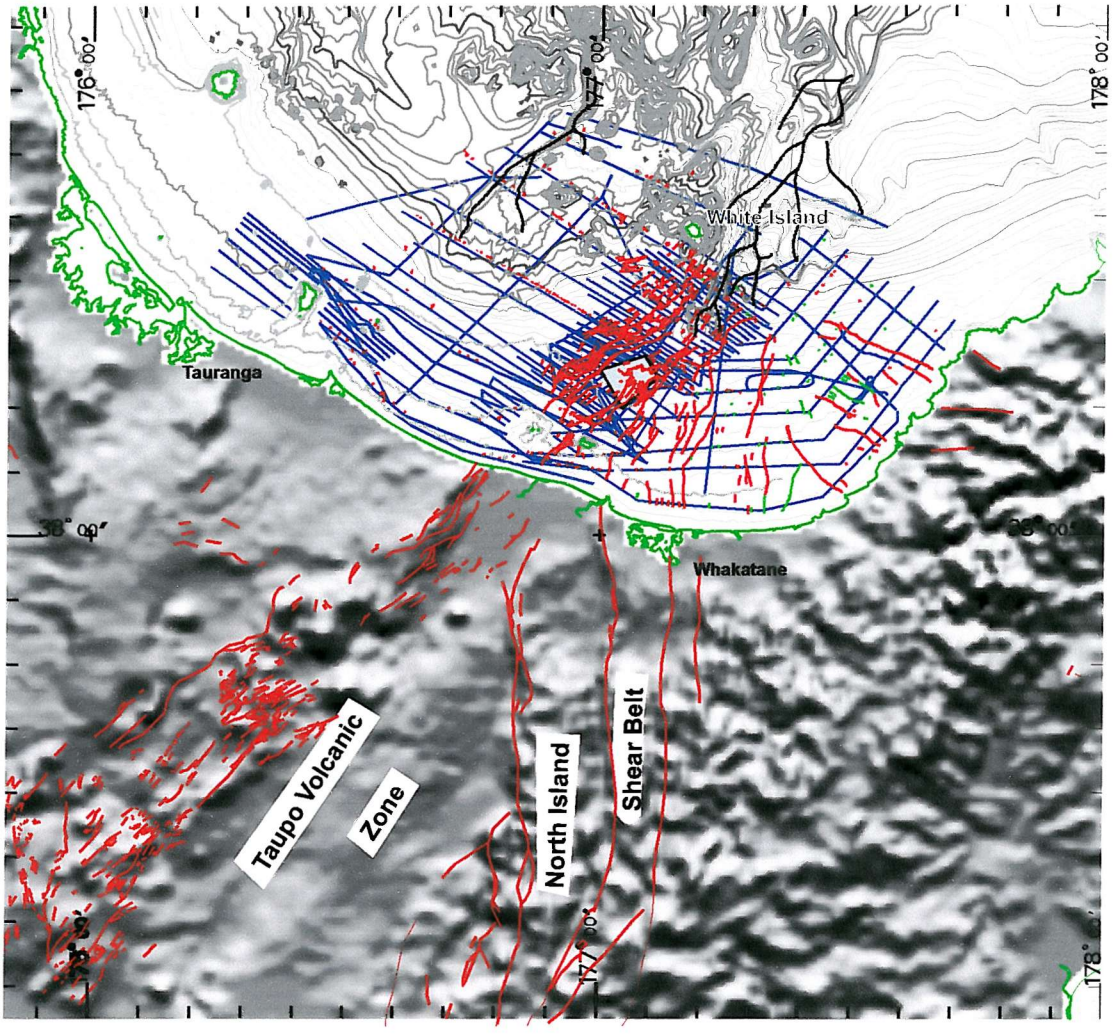

Figure 1.3: Active Faulting, Topography and Bathymetry of the Bay of Plenty Region, North Island, New Zealand. Onshore and offshore active faults are shown in red. Locations of seismic profiles collected during cruise TAN99-14 are shown in blue, the location of the psuedo-3D survey area is highlighted in grey. Black lines show locations of submarine channels.

1.1.2 TVZ Seismicity

The Taupo Volcanic Zone is one of the most seismically active parts of New Zealand. The depth profile of earthquake foci (Figure 1.5) shows deep earthquakes defining the location of the subducting Pacific plate. In addition to these deep earthquakes there are numerous shallow earthquakes, largely restricted to the TVZ (Figure 1.5) related to back-arc extension. The base of the seismogenic zone, defined as the depth above which 80% of the earthquakes occur (Smith and Bruhn, 1984), is identified at 6 km depth within the TVZ (Bryan et al., 1999). Normal faulting focal mechanism of earthquakes within the TVZ are generally absent, despite the dominance of normal fault traces. Instead, transcurrent mechanisms

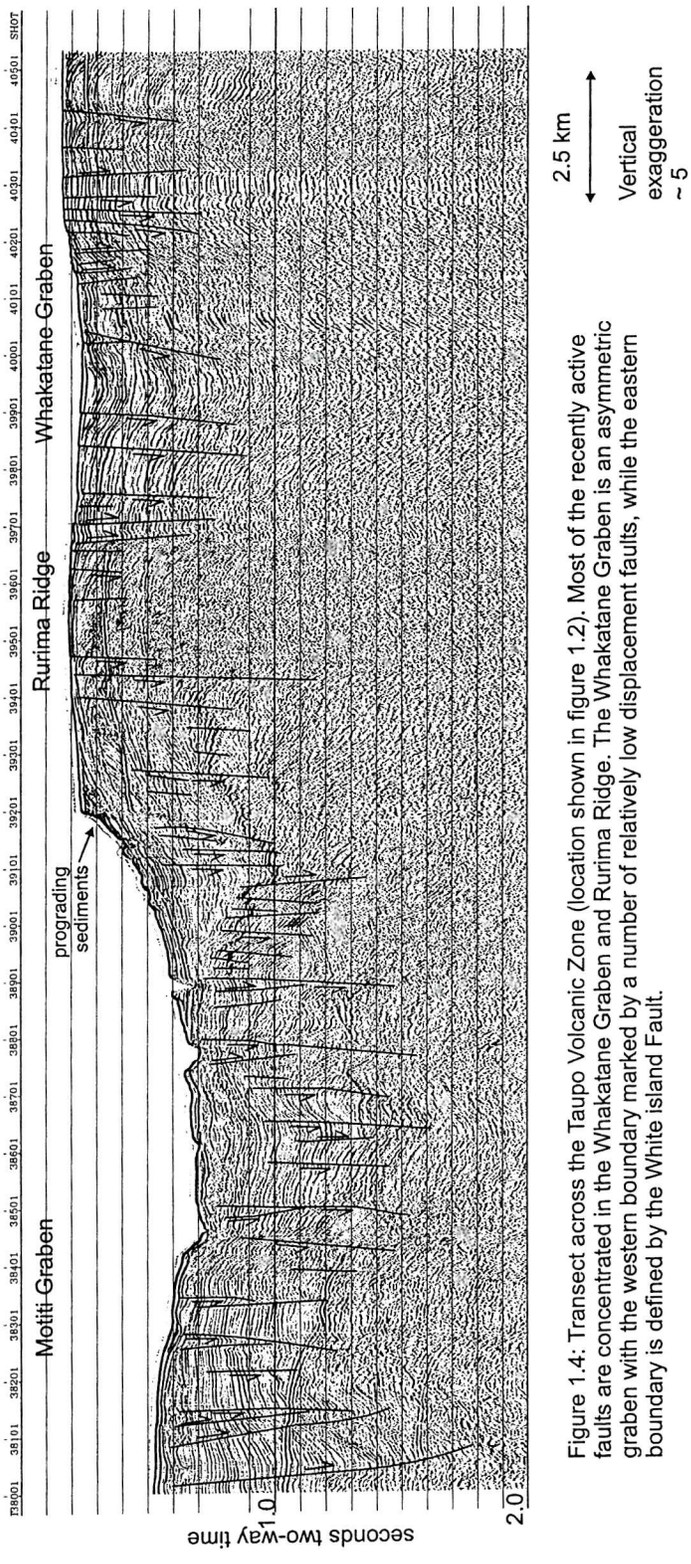

Figure 1.4: Transect across the Taupo Volcanic Zone (location shown in figure 1.2). Most of the recently active faults are concentrated in the Whakatane Graben and Rurima Ridge. The Whakatane Graben is an asymmetric graben with the western boundary marked by a number of relatively low displacement faults, while the eastern boundary is defined by the White island Fault.

are more commonly observed, with both sinistral and dextral strike slip components (e.g. Smith et al., 1984; Webb et al., 1986; Richardson, 1989).

A strong correlation is observed between seismicity and active faulting, where non-faulted areas are regions of lower seismicity (Bryan et al., 1999). Despite this, there are

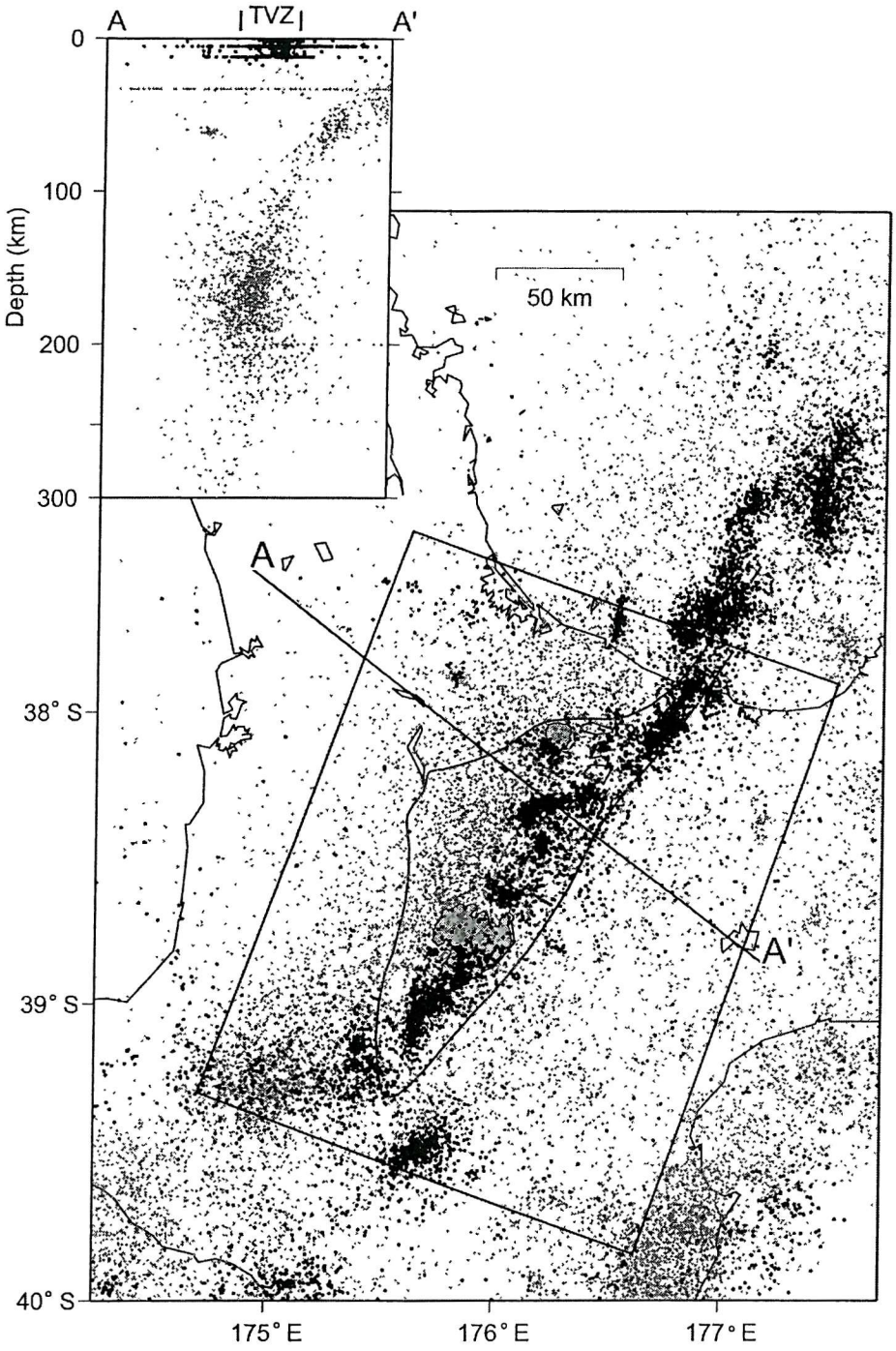

Figure 1.5: Epicentres of earthquakes occurring in the central North Island between 1987 and 1994 (after Bryan et al., 1999). Black symbols represent earthquakes shallower than 20 km; grey symbols show those deeper than 20 km. Inset: Cross section of all events within 25 km of the projection line A-A'.

few examples of earthquakes associated with movement on an individual mapped fault (e.g. Morgan, 1923; Grindley and Hull 1986). The most recent of these earthquakes is the March 2 1987 Magnitude 6.3 Edgecumbe earthquake (Anderson et al., 1990). Surface ruptures associated with the Edgecumbe earthquake were studied shortly after the event.

The earthquake occurred at 8 km depth and caused surface ruptures on several faults and causing new surface breaks on three, the largest fault movement, 2.5 m vertical and 1.8 m extensional, was recorded in the centre of the Edgecumbe fault (Beanland et al., 1989). The largest surface ruptures trend NE-SW, range in length from 0.5 to 7 km and are mostly downfaulted to the northwest (Figures 1.6 and 1.7).

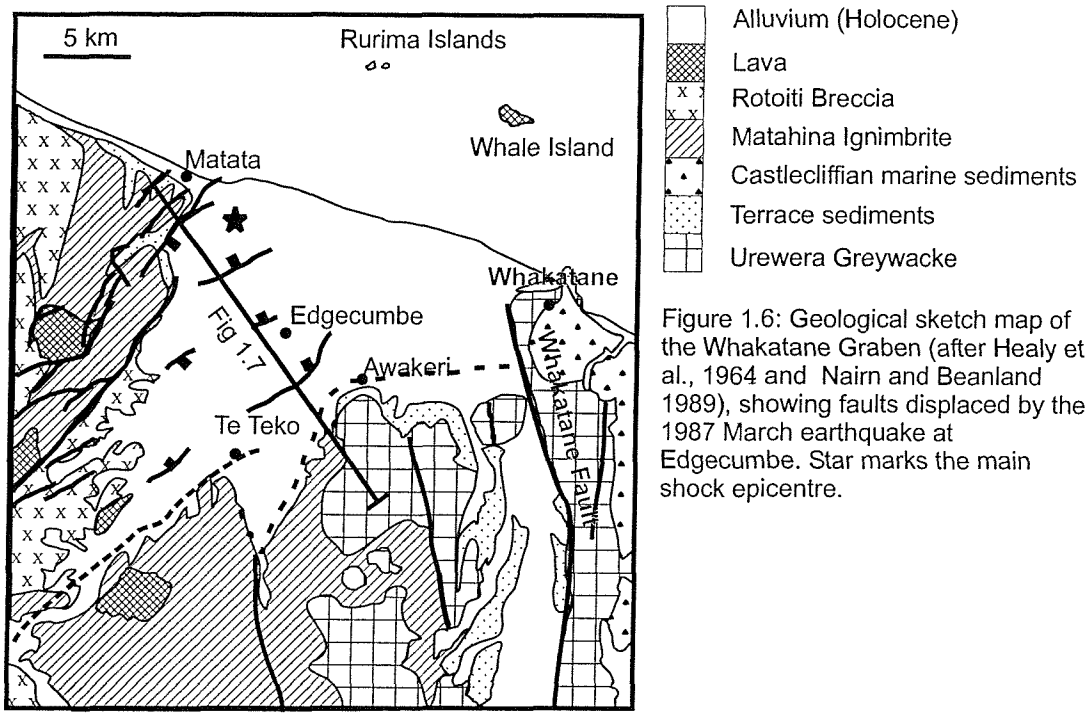

Figure 1.6: Geological sketch map of the Whakatane Graben (after Healy et al., 1964 and Nairn and Beanland 1989), showing faults displaced by the 1987 March earthquake at Edgecumbe. Star marks the main shock epicentre.

The Edgecumbe earthquake is significant to this study as its focus lies within the Whakatane Graben, and unlike many of the earthquakes recorded in the TVZ, had a focal mechanism that showed normal fault slip. The focal mechanism determined by Beanland et al., (1989, 1990) was consistent with an average slip vector trending 330°, plunging 55° on a fault striking at 55°. A fault model was proposed with the fault dipping at 55° curving upwards to become almost vertical near the surface (Figure 1.7). The Edgecumbe earthquake model of Anderson et al., (1990) was of a fault with strike 225° ± 20°, dip 45° ± 10° and rake -110° ± 20°, consistent with the strike and slip vector of surface faulting described by Beanland et al., (1989).

1.1.3 The Whakatane Graben

The most recent plate reorganisation took place at around 5 Ma, caused by an increase in convergence rate and a south-westerly shift in the pole of rotation. The Lau-Havre-Taupo back-arc complex began to form in the north, propagating southwards through the ocean

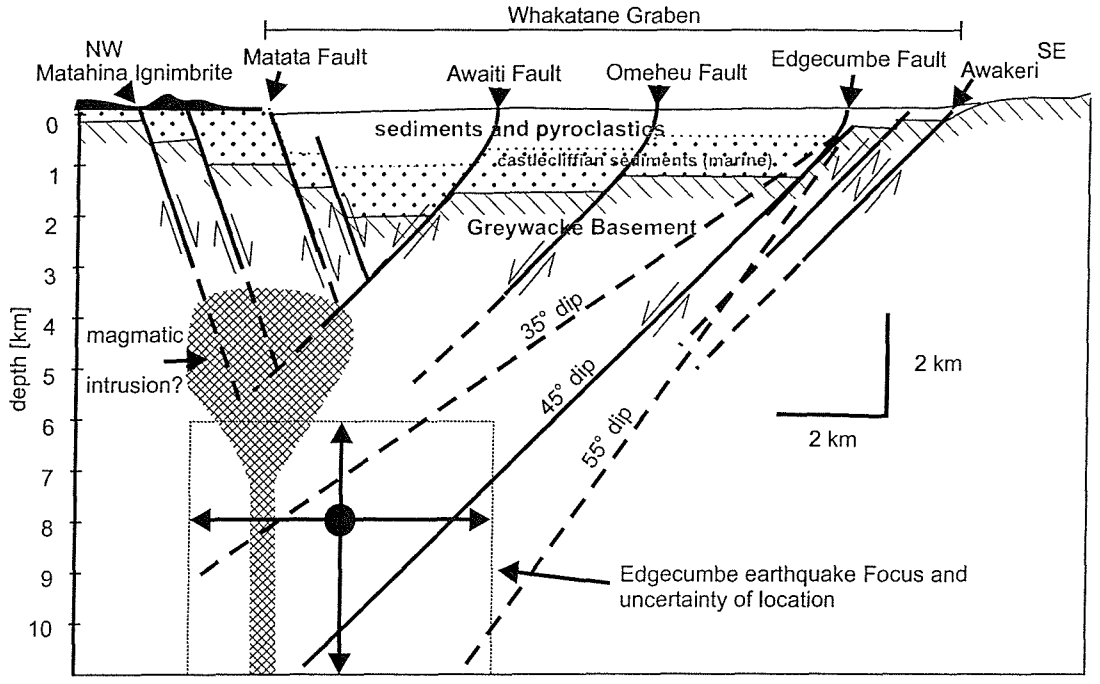

Figure 1.7: Schematic cross section through the onshore Whakatane Graben (after Nairn and Beanland, 1989). Castlecliffian sediments within the graben were deposited c. 1.07 - 0.35 Ma.

towards New Zealand.

Back-arc extension in the TVZ, the southern extension of the Lau-Havre-Taupo back-arc, has been active for the last 2 Ma, while large caldera-forming ignimbrite eruptions have occurred for the last 1.6 Ma (Houghton et al., 1995). The Whakatane Graben began to subside between 0.6 and 1 Ma (Nairn and Beanland; 1989; Walcott, 1984; Wright, 1990; 1992; Davey et al., 1995). Near the Bay of Plenty coast, extension has been estimated to be 12 mm yr^{-1} in a NNW-SSE direction across the full 120 km of the bay (Walcott, 1987), although Nairn and Beanland (1989) note that the strain will be concentrated within the Whakatane Graben. The most recent reanalysis of geodetic data within the Taupo Volcanic Zone shows that strain is not homogeneous, and suggests an extension for the period 1949-1997 of 8 $\pm$ 2 mm yr^{-1} (1 SE) oriented 300 - 320° (Darby et al., 2000).

The Quaternary normal faulting of the Whakatane Graben is observed both onshore (e.g. Nairn and Beanland, 1989) and offshore (e.g. Wright, 1990). In both the onshore and offshore data sets, the faults dominantly dip towards the NW, with the few SE dipping faults predominantly located at the northwestern margin of the Whakatane Graben. The onshore and offshore faults are similar in style (see below), but the absence of near-shore

seismic data means there is a large break in data coverage between the onshore geological maps and the offshore seismic data (Figure 1.2).The fault map of Wright (1990) shown in Figure 1.2 is complied from data collected prior to this project, the updated fault map (joint work of Bull, Barnes, Lamarche and Taylor) is shown in Figure 6.1.

The onshore Whakatane Graben is described in detail by Nairn and Beanland (1989) and a summary is given here. On land, the Whakatane Graben is the expression of the TVZ at the coast between Matata and Whakatane (Figure 1.6). On the eastern margin of the Whakatane Graben the basement greywacke is overlain by Matahina Ignimbrite and Mid-Quaternary (Castlecliffian) marine and younger non-marine sediments (Figure 1.7). West of the Whakatane Graben, Matahina Ignimbrite overlies Castlecliffian sediments and is displaced by more than 200 m by northeast trending faults. Several geothermal drill-holes and water supply wells as well as gravity data have been used to study the stratigraphy within the Whakatane Graben. These data indicate that the greywacke basement dips northeast from Kawerau into the Whakatane Graben where it reaches depths of up to 2 km and show that it was once sub-aerially exposed. Seismic surveying on land (Woodward, 1988) identified the upper surface of the Matahina Ignibrite dipping gently into the graben and displaced by many normal faults. Nairn and Beanland (1989) infer vertical faulting rates of more than 1.9 $mmyr^{-1}$ from the offset of the 0.28 Ma Matahina ignimbrite. Beanland et al., (1990) estimate horizontal extension within the Whakatane Graben at a minimum of 4 – 6 $mmyr^{-1}$ across its width.

The Whakatane Graben extends some 50 km offshore beneath the continental shelf of the Bay of Plenty from the coastline to White Island volcano (Wright, 1990). The graben lies in less than 200 m water depth except for deeply incised canyons in the north. Prior to cruises TAN99-14 and KAH01-02, seismic data showing the structure of the offshore Whakatane Graben was limited to a single deep seismic profile (Davey et al. 1995) and a series of shallow 3.5 kHz profiles (Wright 1990). These data show that the Whakatane Graben is characterised by a 15 – 20 km-wide zone of active normal faulting with shallow sub-surface displacements on many faults (Wright 1990), actively widening and subsiding at average rates of at least 3.5 $mmyr^{-1}$ and 2 – 2.5 $mmyr^{-1}$ respectively (Wright 1992). The graben is filled with approximately 3 km of sediments overlying an irregular basement interpreted as Mesozoic greywackes with volcanic intrusions (Davey et al. 1995). The offshore graben is then blanketed by up to 60 m of a transgressive sequence of marine sediments associated with the postglacial rise in sea level.

Multichannel seismic data within the graben suggest an average fault dip of 60° in the top kilometre, soling out at about 3 km depth (Davey et al., 1995), while the shallow 3.5kHz

sediment profiles show the faults in the near-surface are close to vertical (Wright, 1990). The offshore graben is limited to the east by the west dipping White Island Fault and to the west by a diffuse zone of intense faulting on the crest of Rurima Ridge (Figure 1.4). The White Island Fault has a conspicuous seabed expression along the Motuhora scarp, which reaches 80 m in height, and along the White Island Canyon. Using the 3.5 kHz profiles, Wright (1990) identified 50 normal faults that displace the post-18 ka transgressive sediments (Figure 1.2). The faults strike NE-SW, generally dip to the northwest, and are laterally discontinuous over distances of < 10 km. These faults show repeated movements within the last 18 ka. With the exception of the White Island Fault, which bounds the graben, the faults are well supplied with sediments and have low scarps (less than 16 m) despite their high displacement rates (up to 2.4 mmyr^{-1}).

1.1.4 Rangitaiki Fault

The Rangitaiki Fault is one of the most active faults within the Whakatane Graben; previous work by Wright (1990) identified the Rangitaiki Fault as a 9 km long NW dipping fault with up to 4 m displacement at the seabed and a post-glacial displacement rate of 2.3 ± 0.05 mmyr^{-1}, although Wright (1990) considers this to be a low estimate. The Rangitaiki Fault was chosen for further study from preliminary shipboard analysis during cruise TAN99-14 that indicated a well-developed stratigraphy with good potential for recording fault evolution (Lamarche et al., 1999). Furthermore, the fault was recognised as comprising several linked segments, which combined with the well developed stratigraphy, presented an opportunity to observe the growth of a linked fault array. Excellent quality multichannel seismic profiles imaged down to c. 1.5 km, showing three laterally continuous horizons displaced by up to 826 m. High resolution 3.5 kHz, chirp and boomer profiles imaged the top c. 60 m of sediments giving excellent images of fault displacement within the post-glacial sediments.

Using the combination of multichannel seismic data and high-resolution sediment profiles allows the growth of the Rangitaiki Fault to be studied at two timescales; both the long-term development since the onset of fault activity (c. 2 million years ago), and the short-term activity of the linked fault over the last 18 thousand years. These data areegi integrated with present day observations of fault movements from seismic studies and geodetic measurements of extension.

1.2 Normal Faults and Fault Growth

The combination of fault growth information on different timescales can be used to study fault growth processes and rates. The multichannel seismic data presented here shows a record of faulting in the Whakatane Graben from its initiation nearly 2 million years ago through to the present day and records the development of the Rangitaiki Fault into a mature and fully-linked segmented fault. The temporal controls provided by the stratigraphic framework of New Zealand can be used to ascribe timescales and rates to the processes of fault growth that have been observed elsewhere in the world. In the following, commonly observed features of faults and fault systems are described, and the processes that led to their formation are outlined. Proposed models of fault growth are described.

1.2.1 Fault Populations

Field studies have shown that strains in the Earths crust are accommodated by fault populations that range in size (length and displacement) over several orders of magnitude (e.g. Schliche et al., 1996). There is a systematic distribution of fault sizes and positions; each fault population has many more small faults than large faults and the faults tend to cluster so that the resulting strain distribution is heterogeneous, producing zones of heavily faulted rock surrounding relatively undeformed blocks. The distribution of displacement along faults and the scaling relationship between displacement and length are often similar for faults within a particular setting (Cowie and Scholz 1992).

The maximum displacement of a normal fault commonly occurs near the centre, tapering to the tips where displacement is zero (e.g. Dawers et al., 1993). Faults often show linear displacement gradients over all or part of their profile (Muraoka and Kamata, 1983; Walsh and Watterson, 1987; Manighetti et al., 2001). Field observations of faults show them to be simple structures only to first order; faults are often segmented forming physically linked compound faults or en echelon fault arrays. Secondary structures associated with faults include branches, splays and bends in fault traces - both horizontal and vertical (figure 1.8). Higher displacement gradients are often observed where offset faults interact (Peacock and Sanderson, 1991), and displacement profiles are modified by changing rock types and interactions with neighbouring faults (Burgmann et al., 1994).

Faults grow by accumulation of both displacement and length, implying a relationship between displacement and length. This relationship between the length and displacement of a fault is often described by the ratio of displacement to length (d-L ratio), and has been difficult to define with confidence over many scales. Accurate recording of the relationship is

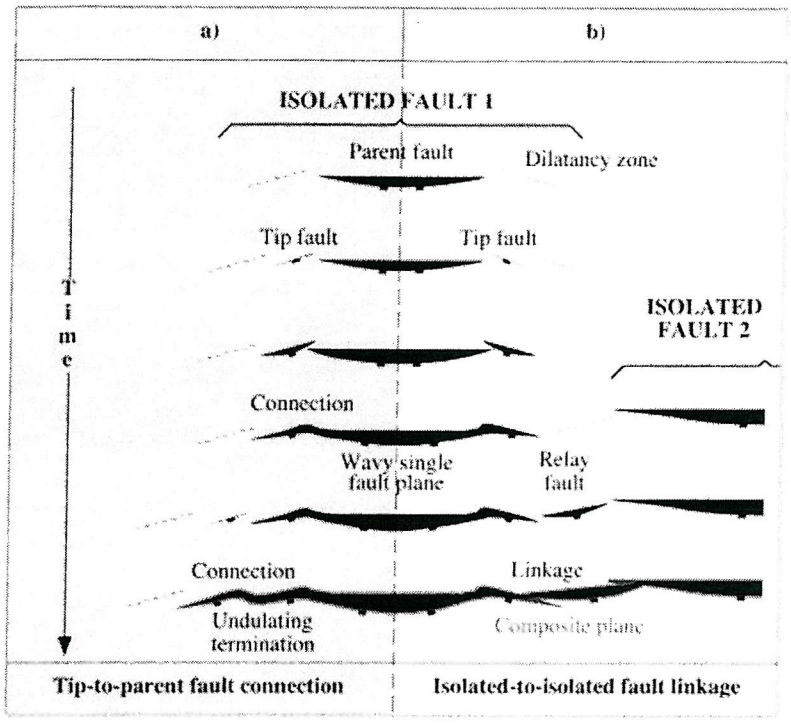

Figure 1.8: Illustration of isolated normal fault propagation processes (Marchal et al., 2003, figure 2).

hindered by the variation of displacement with lithology, measurement errors and truncation and problems with, not measuring the maximum fault length and displacement (Gillespie et al., 1992). While isolated faults and hard-linked faults that kinematically behave like isolated faults can be used to define the d-L ratio, the length and maximum displacement of faults in various stages of linkage produce widely scattered data (Cartwright et al., 1995). Schlische et al. (1996) observe a linear relationship with an average displacement-length ratio of 0.01 over more than eight orders of magnitude on several fault systems. Using a combination of field examples and post yeild fracture mechanics models, Cowie and Scholz (1992) show that the displacement/length ratio is linear, but that the constant of proportionality is dependent on the rock properties and will vary for different tectonic regions and rock types. Faults that form part of an interacting network (fault segments) tend to have higher displacement length ratios as there is more displacement for length (Peacock and Sanderson, 1991).

Other workers have described non-linear relationships between fault displacement and

length in field examples, with the form d = $PL^{1.5}$ (Gillespie et al., 1992; Marrett and Allmendinger, 1991) and d = PL^2 (Watterson, 1986; Walsh and Watterson, 1987, 1988) where d and L are the maximum displacement and length respectively, and P is a function of rock properties. These non-linear relationships describe large faults well, but predict displacements on metre scale faults that are much smaller than those observed (Schliche et al., 1996).

The size distribution of a fault population is best described by a power law relationship of the form $N_{\geq S} = cS^{-D}$, where S is the size of a fault (either length or displacement), $N_{\geq S}$ is the number of faults having size greater than or equal to S, c is a measure of the size of the sample and D is the fractal dimension of the population. Larger values of D imply a greater number of small faults for each large fault in the population.

The scaling relationship may be extrapolated to estimate numbers and relative strain contributions of faults below the survey resolution (Scholz and Cowie, 1990; Walsh et al., 1991; Marrett and Allmendinger, 1992; Pickering et al., 1995), however, the range of the size frequency distribution must be limited because the total fault strain in a deforming region must be finite (Scholz and Cowie, 1990).

Walsh et al. (2003) observe that many of the small faults formed in early phases of faulting in the Inner Moray Firth are no longer present in the younger sediments, and the fault population is instead dominated by a relatively small number of large faults. The larger faults are more vertically (and by inference, temporally) continuous and are present on horizons of all ages, whereas smaller faults decrease in number on the younger horizons. This observation implies a decrease in the value of D and ultimately a breakdown of the power-law relationship as the population becomes dominated by a small number of small faults. Localisation of strain onto major linked fault systems has been observed in association with an increase in displacement rate on the linked fault (e.g. McLeod et al. 2000) with the corresponding decrease in displacement rate on surrounding faults meaning that no overall change in strain rate is required (Gupta et al., 1998). Strain localisation is manifest in smaller faults having higher mortality rates than larger faults (Nicol et al., 1997; Walsh et al., 2003).

1.2.2 Fault Propagation Processes and Resulting Structures

Faults grow by accumulating both length and displacement. The two main processes by which this occurs are fault tip propagation into previously unfaulted rock and linkage between pre-existing faults. Cartwright et al., (1996) show that faults in the Canyonlands Grabens of south-eastern Utah grow by a combined process of radial propagation and link-

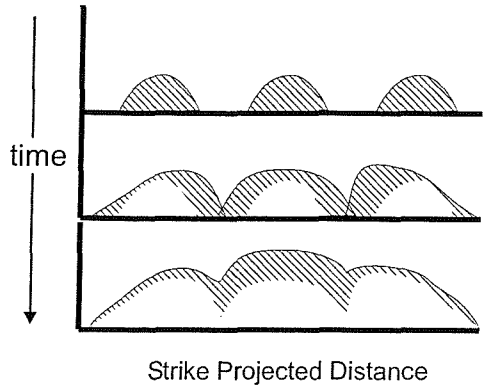

Figure 1.9: Cartoon model of fault growth by tip propagation and linkage (after Cartwright et al., (1996). The hatched areas represent new fault displacement at each fault development stage.

age (figure 1.9). In this model, individual segments grow by tip propagation following the ideal displacement-length ratio for the rock, until two of the propagating segments overlap. The stress fields of the overlapping faults interfere, inhibiting further tip propagation. Relay structures develop between the interacting faults that eventually breach to form a linked fault. The linked fault increases in length compared with the fault segments forming it, but without an increase in maximum displacement. The newly linked fault is then under-displaced with respect to the ideal displacement-length ratio. Further tip propagation of the linked fault is inhibited until the linked fault reaches the displacement-length ratio for an isolated fault. After fault linkage, central segments often show enhanced slip rates (Conteras et al., 2000; Cowie, 1998; Cowie and Roberts 2001).

The profiles (throw or displacement) of overlapping segments are complementary and usually form an aggregate profile that is similar to that of an equivalent continuous single fault trace, often without the under-displaced stage interpreted by Cartwright et al. (1995) (e.g. Dawers and Anders, 1995). In the stages of linkage when the stress fields of the faults are interfering but the faults are not yet physically connected (soft linked stage, e.g. Walsh and Watterson, 1991; Roberts and Yielding, 1994), the displacement profiles of the interacting faults are already distorting to make the displacement profile of the soft-linked fault resemble a single fault (Willemse, 1997).

Sediments where two isolated faults overlap and begin to interact become distorted into a relay ramp. The development of a relay ramp is separated into four stages by Peacock and Sanderson (1994). These stages are (1) no interaction between faults, (2) reorientation of bedding between two interacting faults to produce a relay ramp, (3) connecting fractures begin to break up the relay ramp and (4) the relay ramp is destroyed producing a single fault with an along strike bend. The evolutionary stages may occur through time, as faults propagate towards each other, but can also occur spatially, down the dip of a fault zone (figure 1.10). Marchal et al. (1998) describe fault propagation through development of

secondary structures at the fault tip (tip faults) that are progressively linked to the primary fault plane (figure 1.8).

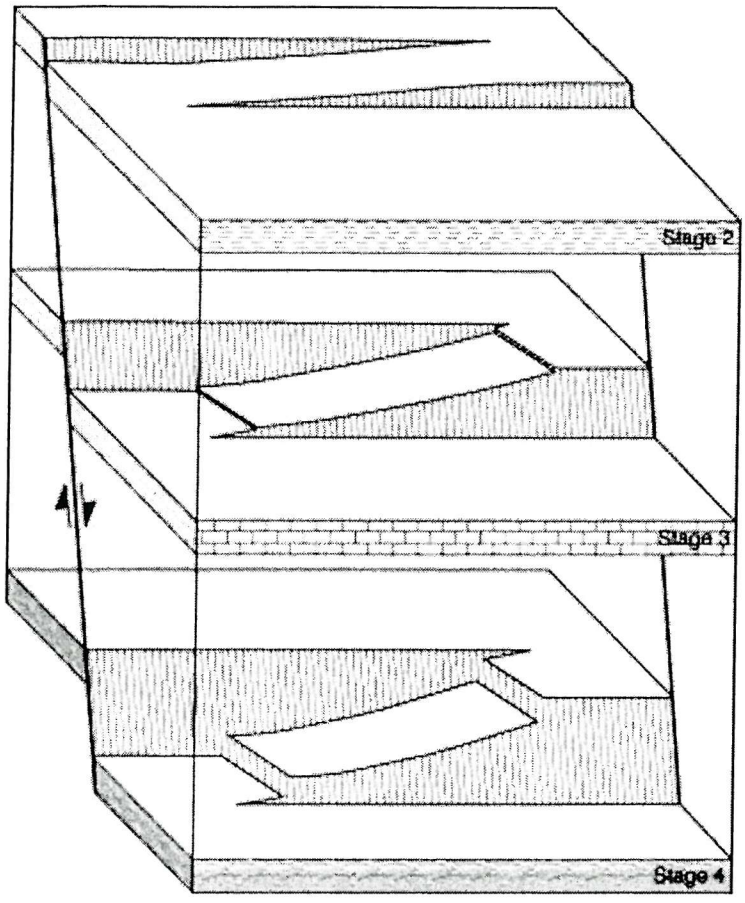

Figure 1.10: Block diagram of possible 3D geometry of a relay ramp (Peacock 2003 figure 6)

Over long-term displacement accumulation, linked segmented faults exhibit systematic growth and coherent displacement profiles. Over shorter time scales, analogue models show the linked segments often demonstrate considerable independent activity that persists for long periods after the faults have linked (Mansfield and Cartwright, 2001). The persistence of segmented behaviour in linked fault networks leads to preservation of displacement minima at fault boundaries (e.g. McLeod et al., 2000). Peacock and Sanderson (1994) attribute the minimum at fault oversteps and linkage points to rotation of bedding and folding in the hangingwall and footwall.

1.2.3 Fault Growth Models

Fault growth models have developed from models of single slip events in elastic media to models incorporating inelastic behaviour at fault tips, multiple slip events and interaction

with surrounding structures. The simplest models of a single slip event in an ideal elastic material result in a semi-circular displacement profile with maximum displacement in the centre and infinite displacement gradient at the tips (Pollard and Segall, 1987). These fault models break down at the fault tips, where infinitely high stresses are predicted. This problem is resolved in the post-yield fracture mechanics model of Cowie and Scholz (1992). In this model, if the yield strength of the rock is exceeded at the fault tip (where stress is highest) then inelastic deformation will occur, and continue until the stress at the fault tip equals the yield strength. This model produces bell-shaped displacement profiles, in which the central portion of the fault is elliptical, but the displacement gradient tapers to zero at the tips. In addition to inelastic deformation at fault tips, the d-x profile of a single slip event can be modified by changes in frictional strength along faults, spatial variations in the stress field and variations in the elastic modulus of wall rocks (Burgmann et al., 1994).

Walsh and Watterson (1987) and Peacock and Sanderson (1996) model displacement on faults as the superposition of many single slip events, producing a cumulative displacement profile with displacement gradients closer to those of real faults. These models of fault growth are for a single fault that ruptures across its whole surface, and all produce symmetrical profiles. Movement on a fault alters the local stress field, increasing the shear stress along strike of the fault, but decreasing the shear stress across strike. The perturbation of the stress field can increase or decrease the rupture likelihood of a neighbouring fault, depending on their relative positions. Models that include fault interactions produce asymmetric profiles, for example models of overlapping faults that form relays show increased displacement gradient and positioning of the maximum slip towards the relay zone (e.g. Peacock and Sanderson, 1991, 1994). Fault linkage produces faults that are 'underdisplaced' for their length, and will accumulate displacement without length increase to re-establish a critical fault profile for the whole fault (Cartwright et al., 1996) while increasing the displacement-length ratio of the individual segments (Peacock and Sanderson, 1991). Cowie (1998) presents a model of fault growth in which the fault recovers its strength after each rupture event. Healing and reloading of ruptured faults allows a positive stress feedback between nearby ruptures that are aligned approximately along strike, and negative feedback on faults across strike. The feedback mechanism promotes rapid localisation of strain and formation of major through-going faults. Fault displacement profiles resulting from this feedback model are controlled by the balance between accumulation of displacement on previously ruptured elements, new ruptures forming at the tips, and linkage with other nearby faults.

Further complexity is added to the description of faulting when faults are considered

to rupture only on part of their surface. Cowie and Shipton (1998) present a model for fault growth in which only patches of the fault slips in any single rupture event. This model predicts linear displacement gradients towards the fault tip when the size of the slipping patch is much smaller than the dimensions of the fault plane and fault healing is instantaneous.

1.3 Thesis Summary

The data presented in this thesis (see chapter 2) consist of several regional multichannel seismic profiles, and a pseudo-3D seismic experiment comprising both conventional multichannel seismic data and high-resolution chirp and boomer profiles. Using these data, with core samples, XBT profiles and a refraction sonobuoy record (detailed in chapter 3), seven horizons are identified, interpreted and dated at 1340 ± 420 ka, 770 ± 240 ka, 300 ± 87 ka, 17 ± 1 ka, 13 ± 1 ka, 11 ± 1 ka and 9 ± 1 ka. The stratigraphic information and methods used in determining these ages are given in chapter 4 (for MCS data) and chapter 5 (for high-resolution data).

In chapter 4, the geometry of faulting within the pseudo-3D survey area is described, fault lengths, dips and orientations are used to characterise the fault population and extensional setting. The history of faulting in the pseudo-3D survey area is explored using back-stripping of syn-sedimentary growth faults from 1340 ka to present, considering the post-glacial sediments as a single unit. Fault displacement rates are calculated for the survey area, and are used to estimate strain and extension rates in the Whakatane Graben, both at the present day and back to 300 ka in the past. Displacement rates are further used to estimate earthquake repeat times on the Rangitaiki Fault.

The high-resolution data are considered in more detail in chapter 5, where fault growth and interaction are studied over short-timescales. Smaller details of the fault structure are resolved that compliment the lower resolution deep multichannel seismic data. Rapid changes in fault displacement rate are observed on segments of the Rangitaiki Fault related to former segment boundaries and fault intersections. The White Island Fault, poorly defined in multichannel seismic data, is clearly imaged in the high-resolution data and its structure is described and used to infer the development history of the fault.

The evolution of the Rangitaiki Fault is studied in detail in chapter 6, the temporal controls on fault growth provided by this data set allow fault displacement rates to be measured throughout the growth history of the fault. The data shows the progression from its beginnings as isolated and laterally propagating faults to the fully linked and segmented

fault seen today and the timing and rates of fault propagation processes can be defined.

In chapter 7, the results presented in the previous chapters are integrated and used to describe the development of the fault population in the Whakatane Graben, Taupo Volcanic Zone and the onshore Bay of Plenty. The detailed measurements of displacement rates and style of faulting described for the Rangitaiki Fault offshore are considered in terms of seismic risk for the onshore Bay of Plenty. A summary of results and conclusions presented in this thesis is provided in chapter 8.

Chapter 2

Data Sources

In this chapter the seismic data used in this thesis are introduced, and the processing steps are outlined and explained in detail where appropriate. Data used to derive the variation of seismic velocity with depth are also described. These data are XBT profiles, sediment cores and a refraction sonobuoy. The modelling of these data and resulting velocity profile is also included in this chapter.

The data were collected during two cruises in the Bay of Plenty, New Zealand. Multichannel seismic data, 3.5 kHz sediment profiles, sediment cores, XBT profiles and sonobuoy refraction profiles were collected throughout the offshore Taupo Volcanic Zone (TVZ) during cruise TAN99-14 aboard the *R/V Tangaroa*. High-resolution chirp and boomer profiles were collected the following year during cruise KAH01-02 aboard the *R/V Kaharoa*. These data were collected with the aim of quantifying the recent (post-glacial) fault activity of the Rangitaiki Fault, one of the dominant structures of the currently active Whakatane Graben. In addition, chirp profiles were collected to tie two core profiles collected during the previous cruise (TAN99-14/14 and /15) and chirp profiles were collected close to the shore to enable correlation of onshore and offshore fault structures.

2.1 Cruise TAN99-14

Between 10th November and 4th December 1999 a geophysical cruise was carried out aboard R/V Tangaroa, providing extensive coverage of the offshore Taupo Volcanic Zone. The data acquired include approximately 2200km of multichannel seismic reflection (MCS) profiles, nine refraction profiles and 18 core samples. As well as regional seismic profiles covering the Whakatane Graben, the cruise also included a pseudo-3D seismic experiment over part of the active fault zone. The locations of the seismic profiles collected during this cruise are shown in figure 2.1.

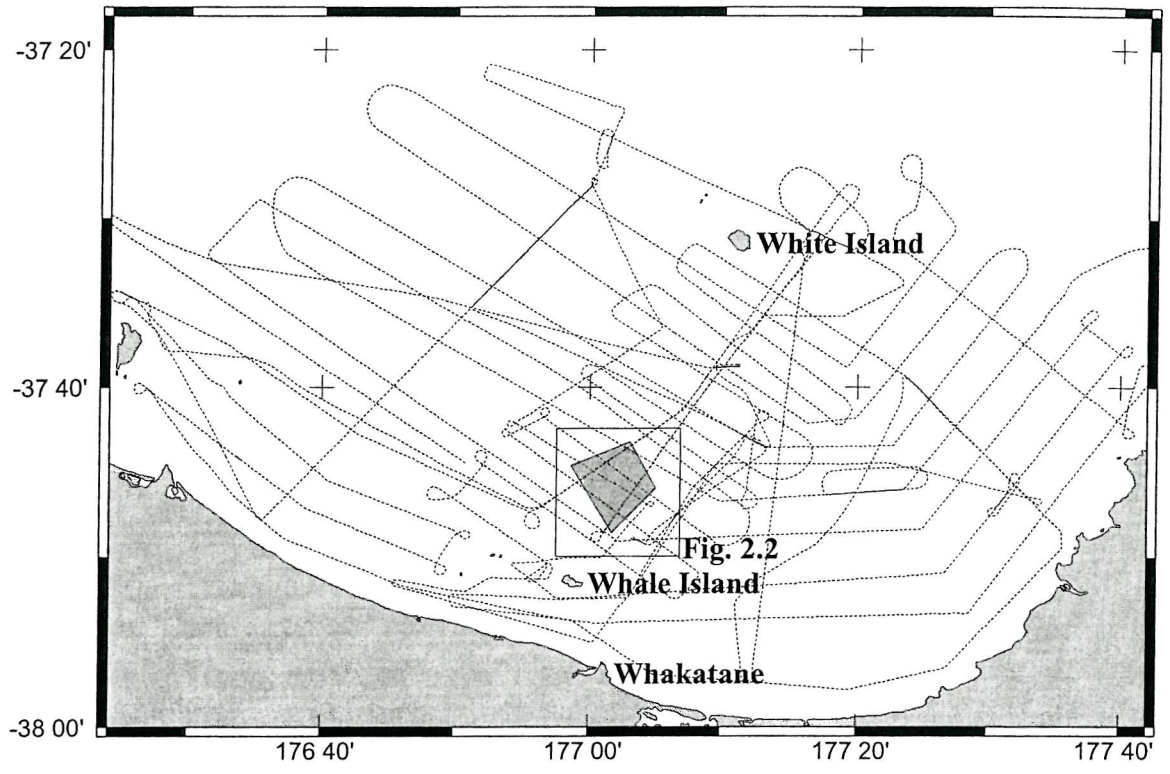

Figure 2.1: Location of Regional Seismic Lines and Pseudo-3D survey box (shaded grey) collected on cruise TAN99-14 (Lamarche et al. 1999).

The cruise objectives were to determine the contemporaneous processes of extensional faulting, subsidence and sedimentation in the Bay of Plenty and to study the mechanisms of extension and potential seismicity of offshore faults (Lamarche et al., 1999, 2000). The pseudo-3D seismic experiment was conducted to image a developing fault network with the aim of making quantitative measurements of fault growth rates and changes in fault geometry over time. This survey area is centred on the Rangitaiki Fault, an actively growing and segmented normal fault (figure 2.2).

2.1.1 The Pseudo-3D Seismic Survey

The pseudo-3D seismic survey covers an area approximately 7.5x5km, over a section of the Rangitaiki Fault system. The area was chosen from preliminary shipboard analysis, which indicated a well-developed stratigraphy that had good potential for recording fault evolution. In addition, the subsurface gas that obscures much of the faulting to the south, is not observed in this area.

The survey consists of 50 parallel MCS profiles (lines BOP101 - BOP150, figure 3.2) and two tie lines (BOP151 and BOP152). Three lines from the regional survey were also

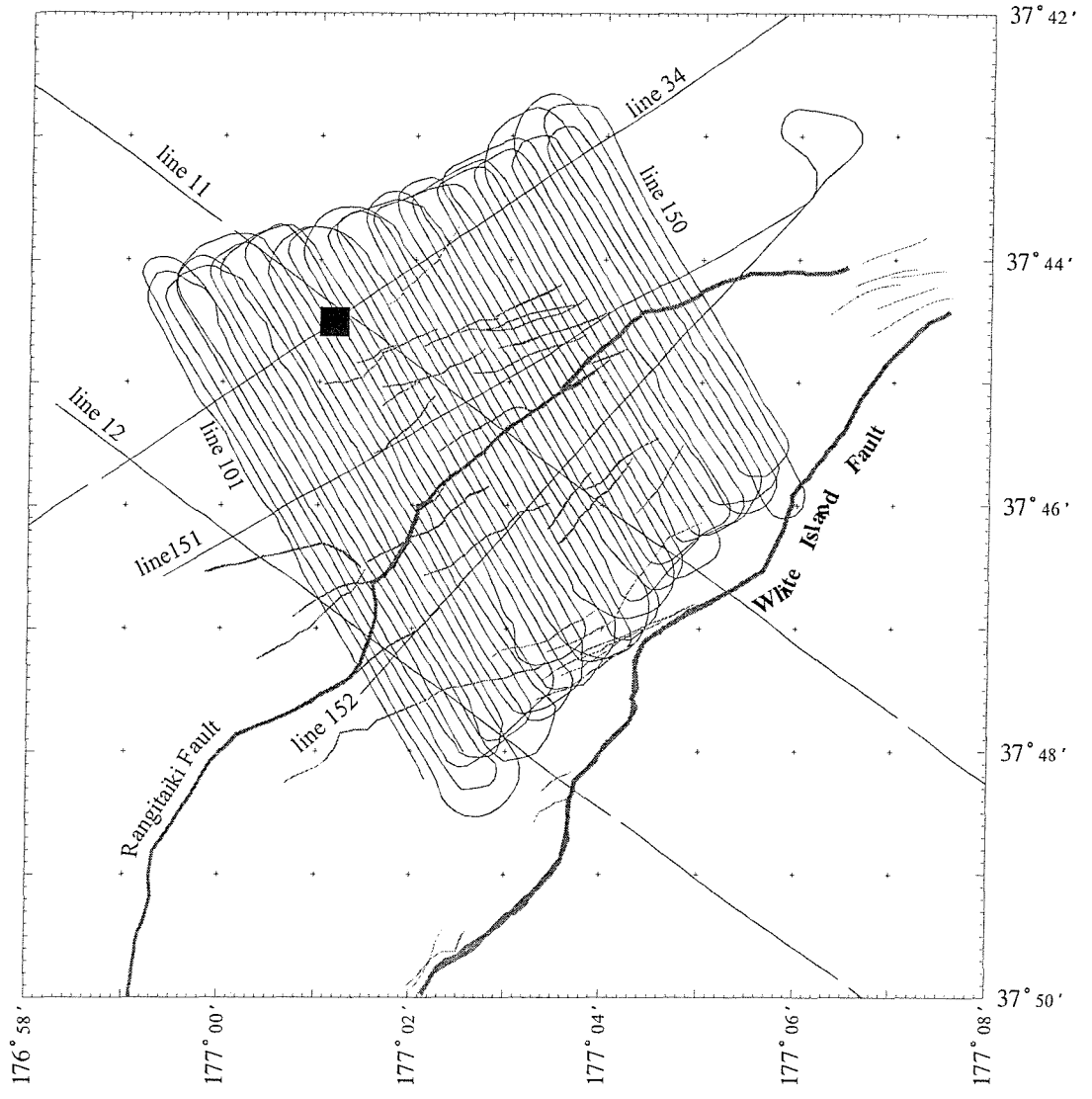

Figure 2.2: Multichannel seismic profiles in the pseudo-3D survey area. Location of figure shown in figure 3.1. The location of core TAN99-14/14 is shown with a back square, interpreted faults are shown in grey.

included to aid interpretation (lines BOP11, BOP12 and BOP34). The 50 parallel seismic profiles are 150m apart and oriented at 147^o perpendicular to the mean strike direction of the Rangitaiki Fault within the survey area.

Lines BOP101 - BOP150 and BOP152 were collected with the airgun in Harmonic mode. This gives the shortest duration, highest frequency source (dominant frequency 50Hz). Primary reflections were observed down to a maximum of 2 seconds two-way time.

Refraction sonobuoys were recorded along lines BOP151 and BOP34, and during the

recording of these lines the airgun was operated in true airgun mode, giving the best depth penetration and long-offset recording. Lines BOP11 and BOP12 are part of the regional survey and were collected using the true GI source. No mis-tie was found between lines collected with differing sources, although the appearance of the reflectors was slightly altered. The refraction sonobuoy deployed along line BOP151 gave a clear record through the pseudo-3D survey area. Refracted and reflected arrivals were found from three subsurface layers, and refracted arrivals were observed up to 4.5km offset, 2.5seconds two-way time.

Several gravity and piston cores were collected during the cruise, one of these - Core TAN99/14-14 - lies within the pseudo-3D survey area (figure 2.1). The sedimentation rate derived from this core is used in dating the seismic horizons.

2.1.2 MCS Data Acquisition

The seismic data were recorded using a 300m long, 48-channel streamer with a group spacing of 6.25m. The streamer is attached to a 25m long elastic section deployed 170m astern of the vessel. The streamer had four mechanical depth controllers, and was deployed between 5 and 10m depth, depending on sea state and seismic target (figure 2.3.

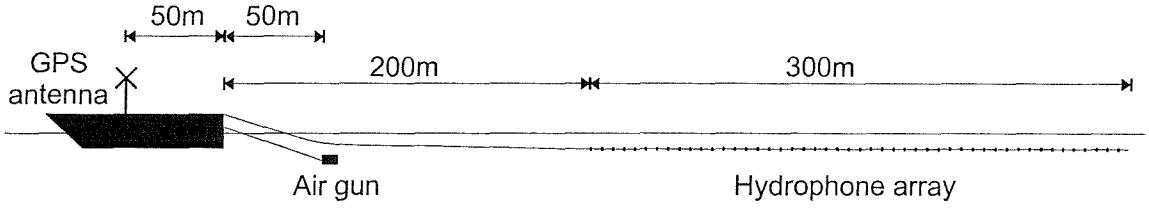

Figure 2.3: Multichannel seismic data acquisition geometry

The seismic source used is a SODERA GI gun towed at 10m depth, 50m astern of the vessel. The generator-injector airgun has two chambers that fire in rapid succession, giving some control of the bubble oscillation. By altering the air volume in each chamber the gun can be made to operate in three different modes, each producing a seismic source of different frequency content suitable for a variety of seismic targets. For the regional seismic lines, the gun was used in true GI mode (generator/injector chamber capacities 45/105in^3). The harmonic mode source (75/75in^3) gives the highest frequency content and shortest primary impulse, and was used for the high-resolution pseudo-3D seismic experiment. Along lines where refraction sonobuoys were deployed, the gun was operated using true-airgun mode with a single firing chamber of 210in^3 capacity.

R/V Tangaroa is equipped with differential GPS (DGPS) navigation and a Digital Acquisition System (DAS). The DGPS positioning showed unexplained fluctuation in the form of spikes from the satellite. These positioning spikes are removed in the navigation processing (appendix A).

During recording of the pseudo-3D survey, care was taken that the streamer was lying directly behind the vessel at all times. Long lead-in and lead-out distances of the profiles ensured that the streamer was directly behind the vessel at the beginning of lines and that the streamer had reached the end of the profile before recording stopped and beginning the turn at the end of lines.

A shot spacing of 25m was achieved with a vessel speed of 5 knots and a firing rate of 9.7 s. Reduced air capacity later in the cruise meant that the firing rate had to be reduced to 11 seconds, so the vessel speed was reduced to 4.8 knots to maintain the 25m shot spacing.

Average noise levels on the streamer channels generally remained between 5 and 7 μbar although values of up to 20 μbar were not uncommon as sea conditions deteriorated. Channels close to the depth controllers often recorded poor data, and were not included in final stacked data. Good weather during the three days of acquisition of the pseudo-3D survey meant that these data were of excellent quality throughout.

2.1.3 MCS Data Processing

The seismic processing involves navigation processing and seismic trace processing. The navigation data are processed using a series of FORTRAN programs and GMT and UNIX commands. The seismic records are merged with the navigation data and processed using ProMAX. The processing work-flow is summarised in figure 2.4 and a full account is provided in Appendix A.

2.2 Cruise KAH01-02

Approximately 160km of chirp sonar data, 460km of boomer data and 30km of sidescan data were acquired in the southern Whakatane Graben during an eight day cruise aboard the R/V Kaharoa between January 17th and 26th 2001 [Bull et al., 2001].

Chirp profiles were collected to tie two core sites from cruise TAN99-14 (cores TAN99-14/14 and /15). The pseudo-3D survey area of cruise TAN99-14 was revisited, with the aim of quantifying the recent (post-glacial) fault activity of the Rangitaiki Fault. Chirp profiles were also collected south of the pseudo-3D box, including a coastal transect aimed at tying the onshore and offshore fault interpretations.

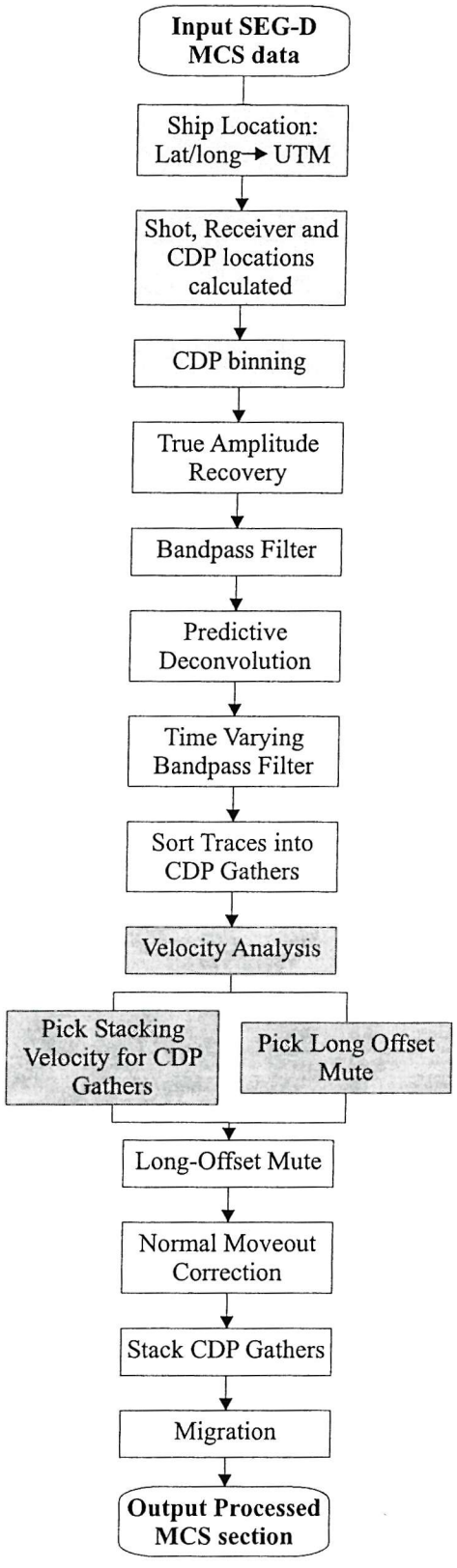

Figure 2.4: Multichannel seismic data processing work flow

Forty-six strike-perpendicular boomer profiles were collected across the Rangitaiki Fault, covering a similar area to the pseudo-3D box of cruise TAN99-14 and extended farther to the south and east to include the hanging-wall sediments of the White Island Fault (figure 2.5). Profiling at a 200 m line spacing had been completed, and in-filling at a line separation

of 100 m had begun when equipment failure prevented any further seismic profiling.

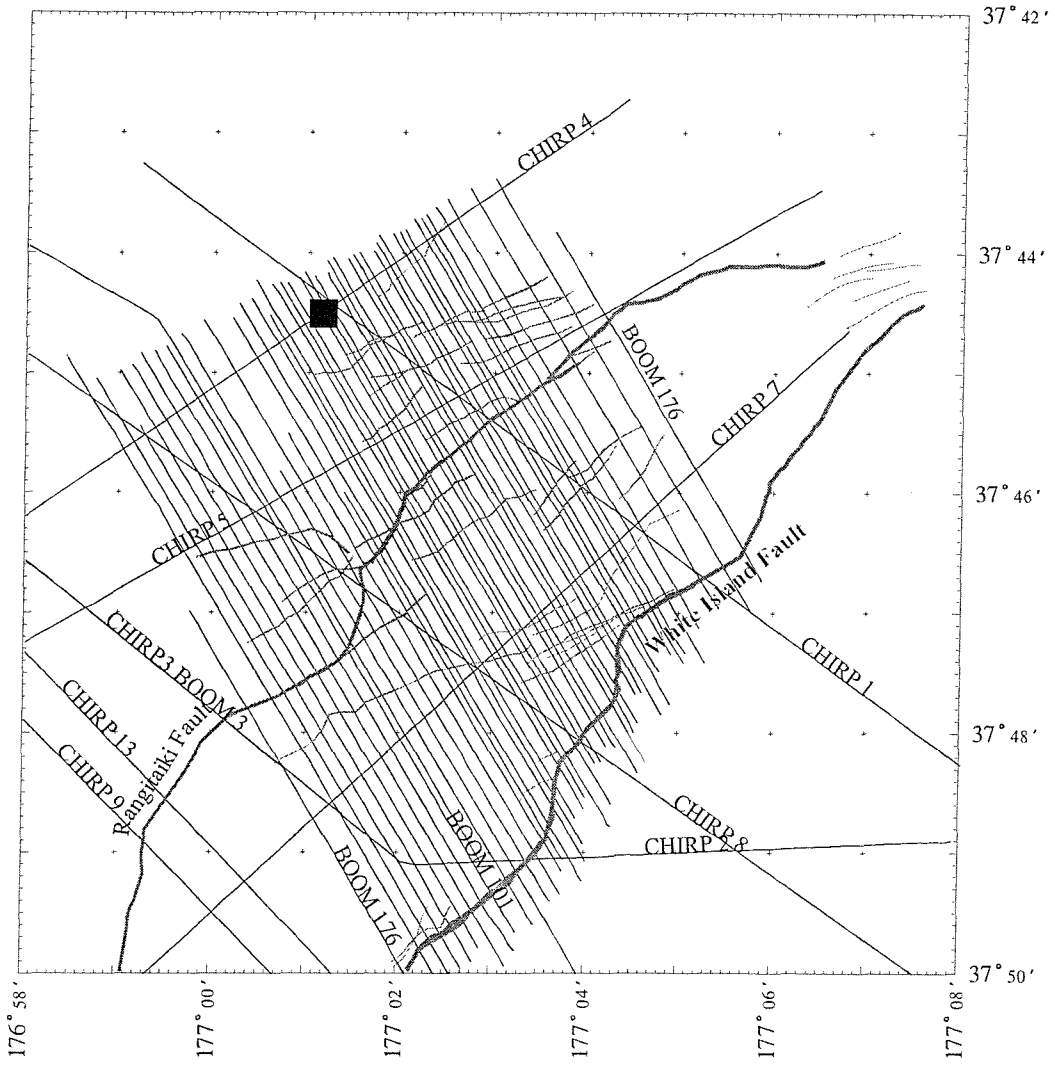

Figure 2.5: High resolution seismic profiles in the pseudo-3D survey area. Location of figure shown in figure 3.1. The location of core TAN99-14/14 is shown by the black square, interpreted faults are shown in grey.

The parallel profiles within the pseudo-3D survey area are recorded using the boomer system. The firing rate is less frequent than on the chirp profiles and is lower frequency. Boomer data has the advantage over chirp of deeper penetration into the subsurface. The penetration of the boomer profiler was always sufficient to record the base of the post-glacial sedimentary package, and in some cases underlying structures were resolved.

Six chirp tie lines were collected through the pseudo-3D survey area, one of which passes through core sites TAN99-14/14 and TAN99-14/15. Owing to equipment failure, no tie lines were collected using the boomer source, although several tie lines were collected using

the chirp source. Fortunately the clarity and lateral continuity of the observed subsurface horizons mean that no problems were encountered as a result of this limitation in tie points. Sea state was fault to strongly influence the quality of data, both in terms of swell noise affecting reflector continuity and in signal-to-noise ratio.

2.2.1 Data Acquisition

Chirp Sonar

A GeoAcoustics GeoChirp system was used with logging on a Sonar Enhancement System (SES). A 32 ms chirp sweep between 2-8kHz was used at 3 chirps/second. 120 ms of correlated data were recorded for each chirp, sampled at 0.04 ms. The start time of the recording interval can be delayed by 0, 50 or 100 ms within the chirp profiling unit, and was altered to accommodate a range of water depths.

The chirp system was deployed at 4 m beneath the water surface, 20m astern of the GPS antenna. Static delays are introduced by the depth of the tow-fish and the processing time required to correlate data.

The chirp system failed after 28 hours of data collection due to an unfortunate deployment problem, and no more chirp profiles could be collected.

Boomer

An Applied Acoustics boomer catamaran, bang-box and hydrophone were used with logging on a GeoAcoustics SES system. The trigger for the boomer was provided by either the GeoChirp profiling unit or the Octopus 360 system. The boomer was deployed on the starboard side at the rear, with the hydrophone on the port side. The effective reflection point was 30.5 m astern of the GPS antenna

Navigation

Navigation data were collected using DGPS and recorded from the Omnistar GPS system using HydroPRO software on a PC. Location fixes were taken every 0.1 s and recorded in UTM co-ordinates against time in milliseconds. The navigation and seismic recording systems were not linked, so the clocks were regularly compared and synchronised if necessary.

2.2.2 High Resolution Data Processing

The high resolution seismic processing involves navigation processing, seismic trace processing and static corrections. The separately recorded navigation and seismic trace data are

merged, and the separation between the GPS antenna and the source/receiver location (lay-back) is accounted for (see appendix B). The seismic records are merged with the navigation data and processed using ProMAX. The processing workflows for chirp and boomer data are summarised in figure 2.6 and a full account is provided in Appendix B. Interpretability of the chirp data was improved using F-X deconvolution and Dynamic signal/noise filtering, both of which enhance the lateral coherency of the data. These processing steps were found to produce no appreciable improvement in the boomer data.

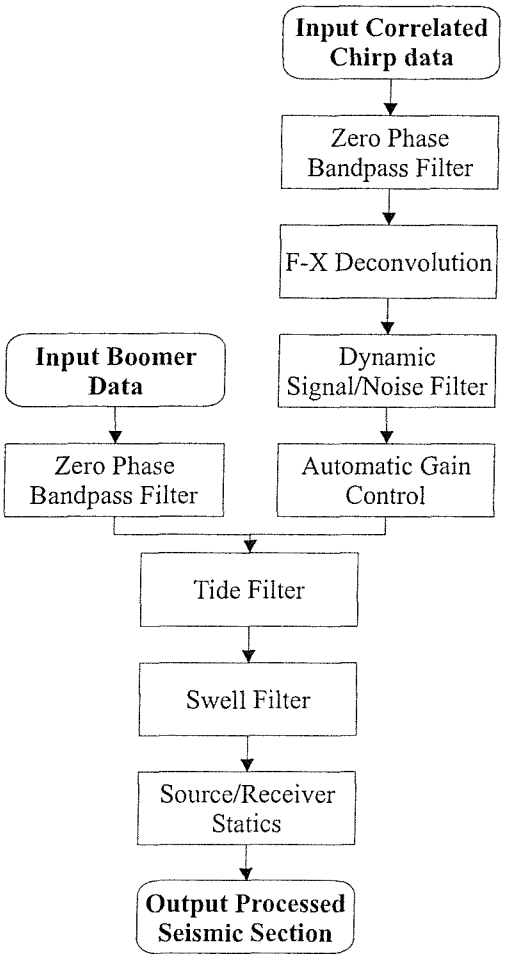

Figure 2.6: High Resolution (Chirp and Boomer) seismic data processing work flow

Both the chirp and boomer data were affected by swell noise and the tidal range. Removal of swell noise dramatically improved the interpretability of both the chirp and boomer profiles, resulting in previously un-resolved reflection arrivals becoming clearly interpretable (for example, structures below the post-glacial sequence were observed in the boomer data). Removal of tidal effects had no effect on the data quality, but decreased mis-ties between

profiles.

The different tow depths of the chirp and boomer led to static shifts being introduced between the two data types. In addition, the chirp traces had a delay resulting from the computing time required to correlate the data before recording. Through necessity, two different triggering devices were used during the cruise, resulting in an unexplained static shift. The methods of quantification of and correction for these static shifts are explained below.

Static Corrections

Static shifts have been introduced into the data by swell noise, tides, towfish depth and electronic delays in triggering, correlation and recording.

Swell noise is readily identifiable in the Fourier Transform of the seabed arrivals of the chirp data and is removed using a low-pass filter. After swell noise is removed, mis-ties in the seabed are measured on all of the tie points in the survey (188 tie-points in total). These mis-tie values are then used to identify and calculate corrections for the other static shifts that have been introduced into the data.

Swell Filtering

The method employed for swell filtering makes use of the generally smooth structure of the sea floor in the survey area. Figure 2.7a shows a section of profile CHIRP3 before swell filtering. The seabed is gently curved across the length of this profile, with a slight step at CDP9000, where it crosses a fault. This is in stark contrast to the apparent change in water depth caused by swell during acquisition, which is seen as up to 1.5 ms amplitude short-wavelength zigzag chatter in the seabed. The effect of the swell noise continues downward in the section and is reproduced in all of the sub-surface horizons.

In recording seismic data, the sea surface is assumed to be completely flat, which for low frequency sources (such as the MCS airgun) is an appropriate approximation. High frequency records such as the chirp and boomer are able to record the changes in sea level produced by the swell, but with an artificially flat sea surface, swell is recorded as seabed bathymetry. The chirp data has recorded a combination of signal and noise. The signal part comes from the true bathymetry of the seabed, while the noise is produced by the swell. The structure of the seabed can be described as a curve composed of a superposition of waves of different wave-numbers and amplitudes. The spatial Fourier Transform of the seabed structure shows the amplitude of each wave-number component (figure 2.8). In these data, the high sedimentation rate ensures that the seabed is smooth (no large changes in depth over short distances). This is represented in the Fourier Transform as a low wavenumber

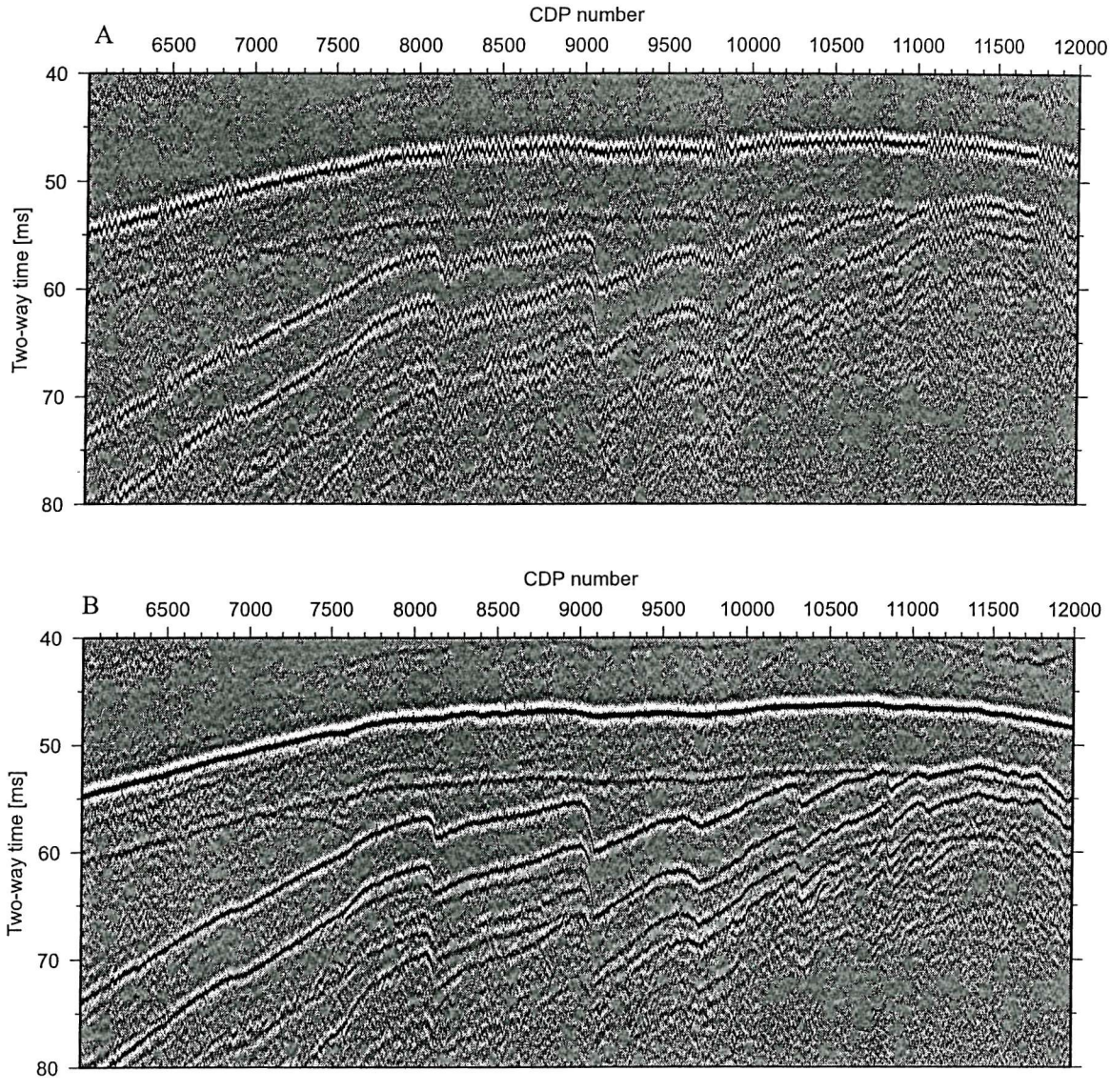

Figure 2.7:Profile CHIRP3 after processing (a) without swell filter and (b) with swell filter applied.

peak (between 0.00 and 0.001 cycles-per-trace). In contrast, the swell noise produces changes over short distances, represented in the Fourier transform as a high amplitude peak centred on 0.02 cycles-per-trace.

This clear separation of signal and noise in the wavenumber domain allows the use of a low-pass filter to attenuate the high-wavenumber swell noise whilst retaining the quality of the bathymetry signal. Figure 2.8 shows the Fourier transformed seabed arrivals after application of a zero-phase low-pass filter. Between 0.00 and 0.01 cycles-per-trace there is very little change in the wavenumber content of the seabed after low-pass filtering, but the peak in amplitude at 0.02 cycles-per-trace caused by swell noise is removed.

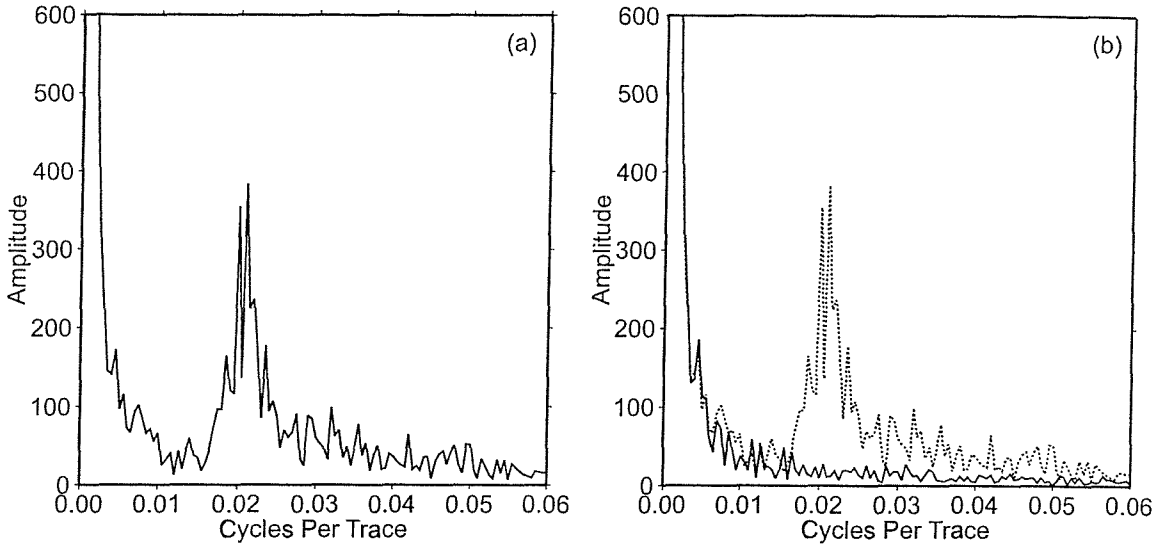

Figure 2.8: Fourier transforms of seabed bathymetry. (a) FT of seabed arrival picks as recorded. The wavenumber spectrum is separated into bathymetry signal (< 0.01 cycles-per-trace) and swell noise (~0.02 cycles-per-trace). (b) FT of seabed after low pass filtering, FT of unfiltered seabed shown as a dotted line for comparison. The low pass filter removes the peak at 0.02 cycles-per-trace but has little effect on the amplitude of wavenumbers below 0.01 cycles-per-trace.

To apply the swell filter, the uncorrected seabed arrivals are picked in ProMAX. The seabed arrivals can be exported as a two-column text file (trace number, two-way time) and the swell-filtered seabed arrivals calculated by applying a low pass filter using the filter1d command in UNIX. The filtering may be done within ProMAX using the smoothing operation within the Trace Display function. This operation applies a running-mean filter to the data. The running mean acts as a low pass filter that removes signal content with higher wavenumber than the reciprocal of the width of the filter window. To remove noise at 0.02 cycles-per-trace, the running mean is applied over a window of 51 traces (the closest odd number to 1/0.02). The filter is applied to the data in ProMAX using the Horizon Flattening function. This function applies static corrections to each trace to force the recorded seabed picks to lie in a horizontal line. The profiles are then unflattened, this time using the smoothed seabed values.

Figure 2.7b shows the effect on the data of applying this low-pass filter to the seabed. The continuity and interpretability of the horizons is significantly improved. The large-scale structure of the seabed remains unchanged, and smaller structures, such as the fault-related fold at CDP9700, are more clearly defined.

The swell noise in sea-surface multiples has twice the amplitude of swell noise in the

primary reflections. As a result, swell filtering halves the amplitude of swell in the sea-surface multiples so they become easily distinguishable from primary reflections.

Source Receiver Residual Static Shift

Figure 2.9 shows the range of mis-tie values observed after the swell filter has been applied. Of the 188 mis-tie values, 10 come from chirp lines tied with other chirp lines, 97 come from chirp lines tied with boomer lines triggered by the SES, and the final 81 come from chirp lines tied with boomer triggered by the OCTOPUS360.

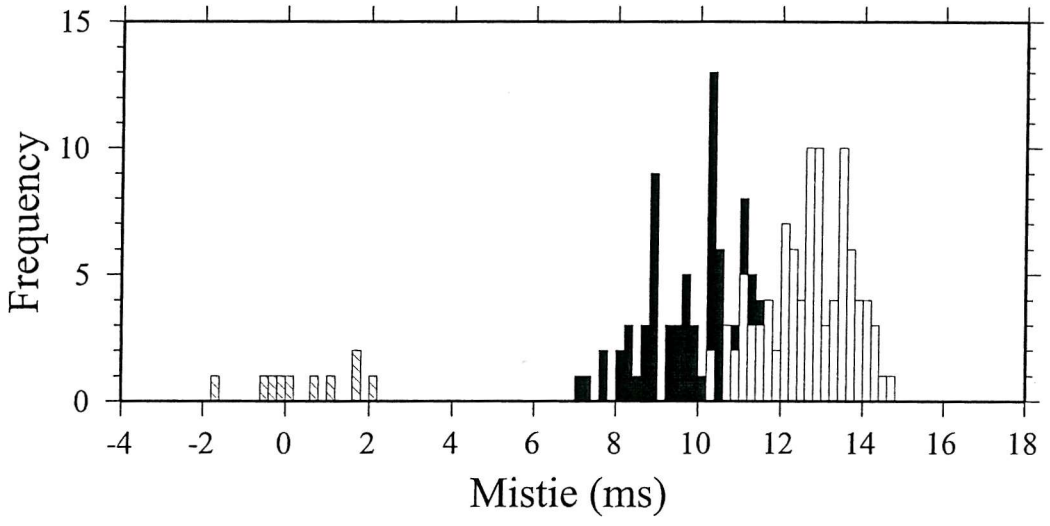

Figure 3.9: The range of miss tie values observed in the High Resolution data. Chirp to chirp ties (hatching), chirp to boomer triggered with SES (solid) and chirp to boomer triggered with OCTOPUS360 (no fill).

Table 2.1 shows the mean values and standard deviations of these mis-ties. The three source-trigger combinations have similar standard deviations, but very different mean values. The range of values for each source-trigger combination is a result of the tidal range (see below), but the different mean values are caused by changes of source and triggering device.

Change of Source

The chirp towfish is towed at 4 m below the surface, whereas the boomer catamaran is towed at the surface. A further delay is introduced by the time taken to produce correlated data. A static shift of 10 ms is applied to all of the chirp profiles to correct for these delays.

	Standard Deviation [ms]	Mean Value [ms]
Chirp/chirp	1.18	0.43
Chirp/boomer(SES)	1.20	10.00
Chirp/boomer(OCTOPUS360)	1.03	12.64

Table 2.1: Standard deviations and mean values of mis-ties for different combinations of source and receiver

Change of Trigger

Profiles recorded using the OCTOPUS360 have a mean mis-tie value 2.6 seconds larger than those recorded using the SES. The reason for this shift is unknown, the traces recorded using the OCTOPUS360 trigger have a static correction applied to bring them into agreement with those recorded using the SES.

Tidal Correction

Land Information New Zealand (LINZ) provide tide tables for the port of Tauranga with time corrections for White Island and Whale Island. The high tide and low tide times and heights are shown in figure 2.10, along with a simple best-fit sinusoid calculated for the tide data. The best-fit sinusoid is used to calculate the tide height at the time each trace was recorded, and by changing the mean value and amplitude of the best fit sinusoid, it can be used directly as the tide correction value. The sinusoidal tidal correction that gave the smallest mis-tie over the whole survey was:

tide =0.9 x sin(s x 2 x pi / 44810)

Where tide is the tidal correction in milliseconds TWT and s is the time in seconds from midnight on 18th January (see section appendix B). This correction is applied in ProMAX using Trace Header Math to calculate the correction value for each trace and Header Statics to extend the beginning of the trace by this value. The effect of applying the tidal correction on the mis-tie values can be seen in figure 2.11. The standard deviation of the mis-tie values is decreased from 1.03 ms to 0.48 ms.

2.3 Velocity Profiles

The variation of velocity with depth in the sediments imaged by the seismic data must be known in order to convert two-way travel time picks in to depths. Velocity profiles from the sea surface to the depth of the lowest reflection surface are calculated using information

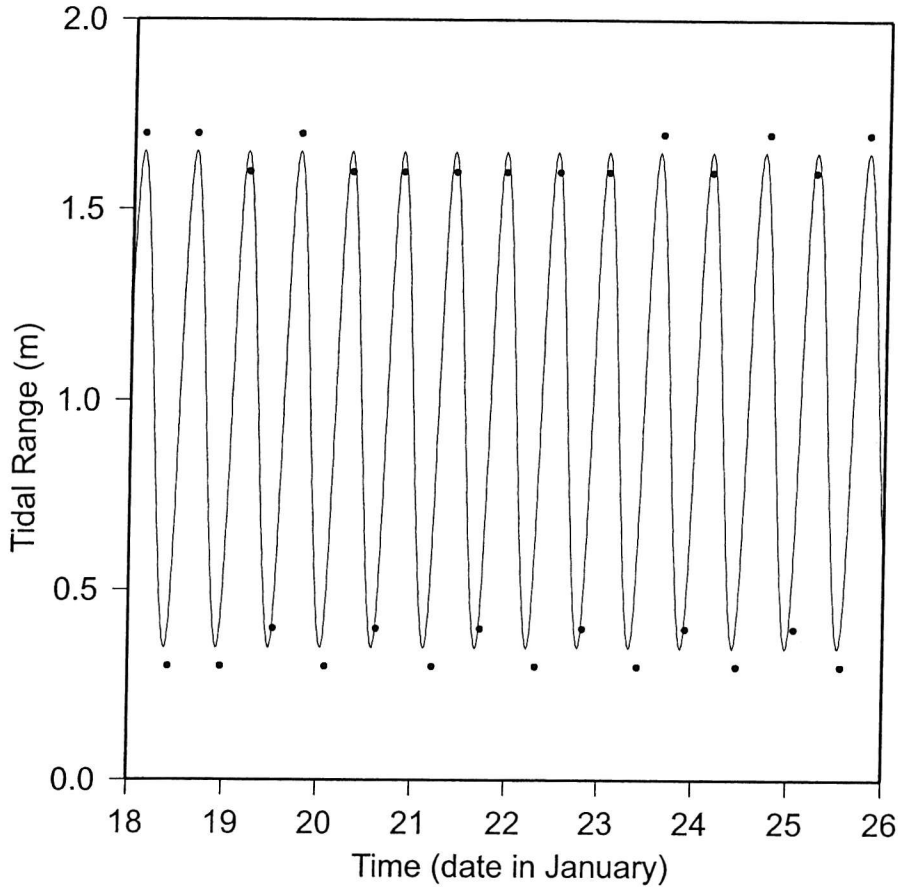

Figure 2.10: Tide heights and times for the pseudo-3D survey. Tide observations from Land Information New Zealand (black circles).The best fit sinusoid is also shown.

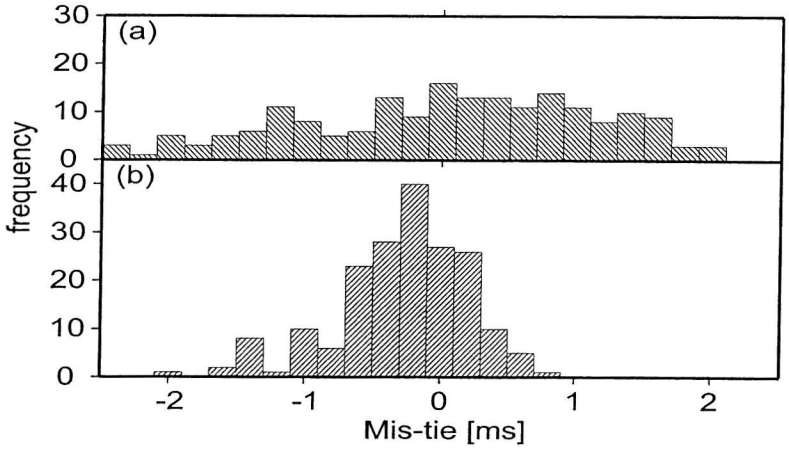

Figure 2.11: Range of mis-tie values (a) before and (b) after tide filtering

from expendable bathy-thermographs, cores and refraction sonobuoy records.

2.3.1 Speed of Sound in Water - XBT Experiment

Six expendable bathy-thermographs (XBTs) were used during the cruise, recording the changing temperature with depth in the water column. The speed of sound in water is related to its temperature, salinity and depth by the equation

$$\mathbf{V=1449.2+4.6T-0.55T^2+0.00029T^3+(1.34-0.01T)(S-35)+0.016D}$$

Where T is the temperature in degrees centigrade, S is the salinity in parts per thousand and D is the depth in metres (Jensen et al., 1994). The salinity of the water on the Bay of Plenty continental shelf is 35.5ppt (J. Sharples, pers comm.). The calculated velocity profile of the water column in the Whakatane Graben is shown in figure 2.12. In this figure the black lines are the individual XBT records, the bold line is the mean value - the step-like profile between 100 and 150 m is an artefact caused by the XBT records being different lengths. The grey line on figure 2.12 is not a true velocity profile, but gives an apparent interval velocity for the water column. At each depth the mean value of the velocity measurements above is calculated, so for example, in 50 m water depth an interval velocity of 1514 ms^{-1} can be used.

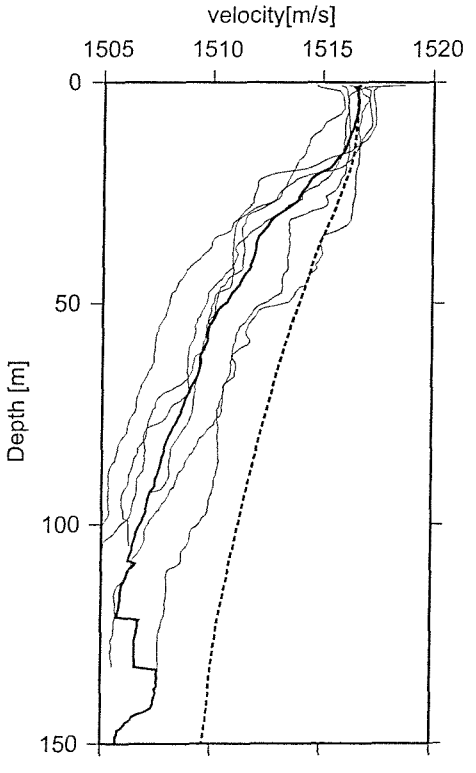

Figure 2.12 Water column velocity profile calculated from XBT data. Black lines: individual XBT profiles. Bold line: Averaged profile, steps in the profile below 100 m depth are caused by the different lengths of the profiles. Dashed line: variation of apparent interval velocity for entire water column with depth.

2.3.2 Physical Property Measurements from Cores

Locations of sediment cores and dredge samples collected during cruise TAN99-14 are shown in figure 2.13. Sediment cores collected during cruise TAN99-14 were logged using the multi-sensor core logger at the Southampton Oceanography Centre (Gunn and Best, 1998). Compressional (P) wave velocity, bulk density (using gamma-ray attenuation) and magnetic susceptibility were measured at a 1 cm sample interval down the length of each core (Cooil, 2000). Cores were collected from a variety of locations within and around the Whakatane Graben.These cores are described in detail in Cooil (2000). Here, the focus is core 14, which lies within the pseudo-3D survey. Sedimentary logs and the results from the physical property measurements are shown in figure 2.14.

These cores are dominantly composed of green coarse - fine silty-clay with mean P-wave velocities of 1570 ms^{-1} and 1550 ms^{-1} for cores 14 and 15 respectively. Many thin ash layers are present within the cores that could be used for tephrachronology studies. Several samples of organic matter have been used for C14 dating. See chapter 5 for a discussion of sedimentation rates and horizon ages. The shallowest reflector used to measure fault displacement offsets, inferred to be the still-stand terrace at c. 9 ka (Gibbs, 1986), is just beneath the base of the core (c. 4.2 m), and is consistent with the presence of the primary Mamaku Tephra (7.35 ka) at a depth of 3.40 – 3.43 m down the core. The lower sedimentation rate for the post- 6.5 ka sediments can be ascribed to the sea-level maximum, and the landward movement of the locus of sedimentation.

2.3.3 Sediment Velocities - Refraction Sonobuoy Record

The purpose of the refraction experiment is to construct a velocity profile for use in the depth-conversion of the seismic data. Refracted and reflected arrivals are modelled using the ray tracing package Rayinvr (Loss et al., 1998). Nine sonobuoys were deployed during cruise TAN99-14, the deployment locations and recorded transects are shown in figure 2.13. Generally the seismic source was too weak or too high-frequency to image deep reflectors in the crust, and the stratification of the shallow sediments was not well enough defined to produce useful results. Within the central Whakatane Graben, however, the sedimentary boundaries are well enough defined to provide a clear sonobuoy record with refractions and reflections from at least three subsurface layers.

The interpretation of seismic refraction data depends on modelling the variation of travel time with offset. The source position is recorded for each shot, and from this the straight line distance from the initial shot is calculated for each subsequent shot (the GPS-offset). The

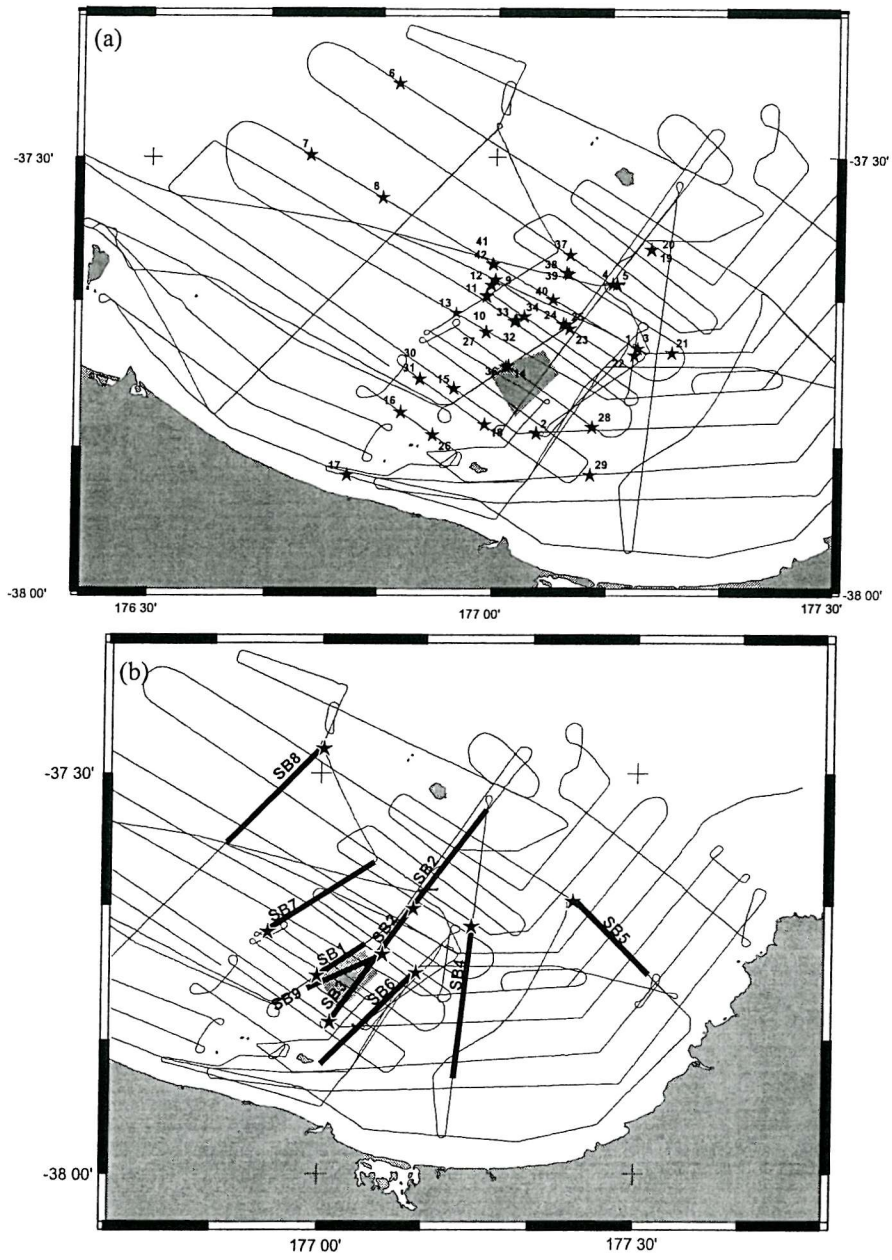

Figure 2.12.(a) Sampling stations - gravity and piston cores and dredge samples collected during cruise TAN99-14. Core 14 lies within the survey area and physical property measurements from this core have been used in depth conversion of the seismic data.(b) Refraction Sonobuoy transects. Star symbols denote sonobuoy deployment location, bold lines show recorded transect. The transect of sonobuoy 9 lies in the survey area. In both figures multichannel seismic data profiles are shown, and the pseudo-3D survey area is highlighted in grey.

position of the sonobuoy in relation to the initial shot location is more difficult to obtain. Firstly, the launching of the sonobuoy and beginning of recording are not synchronised, so the distance between the first recorded shot and the sonobuoy (initial-offset) is not well constrained. In addition, the sonobuoy is free to drift once it has been launched, so it does not necessarily retain its initial position.

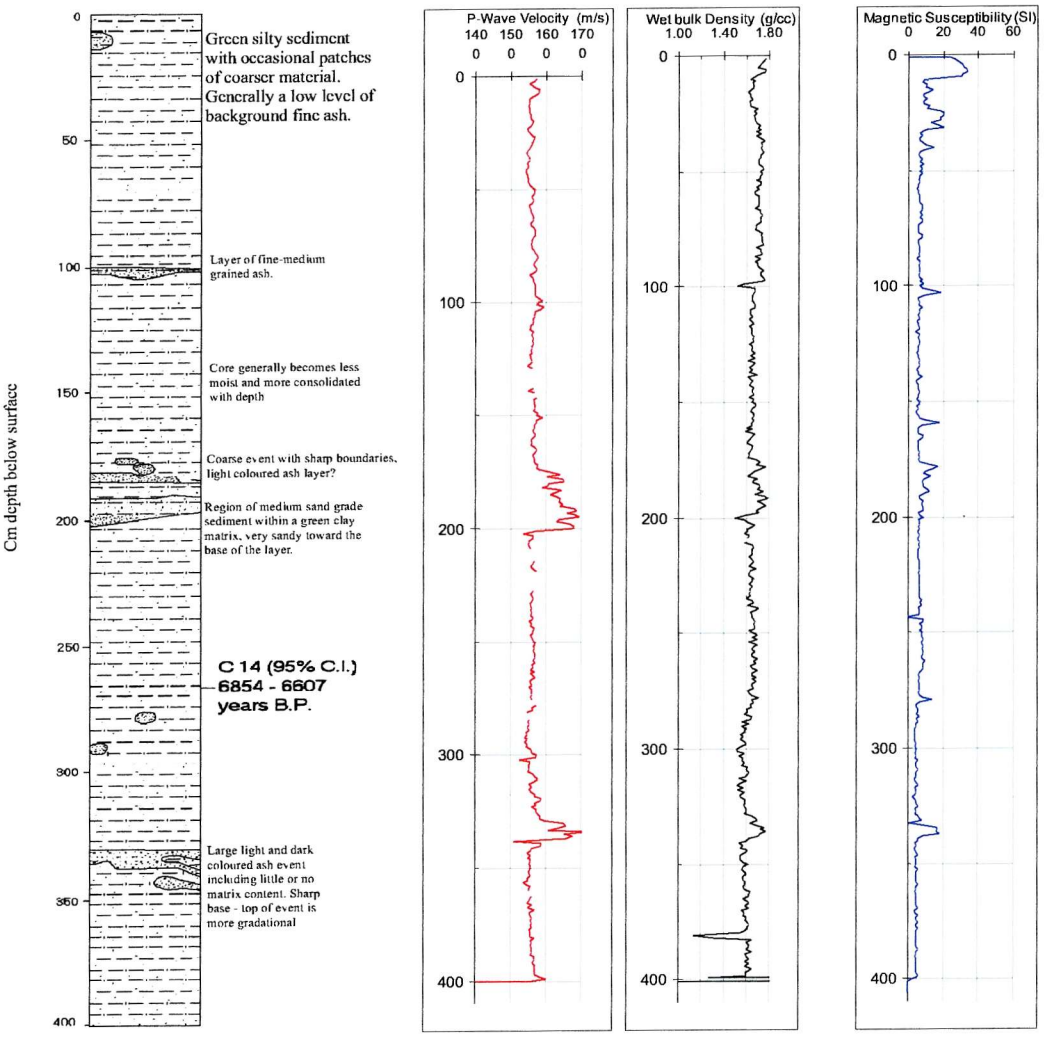

Figure 2.14. Sedimentary log and physical property results for core **TAN99/14-14**, located within the central Whakatane Graben. From Cooil (2000).

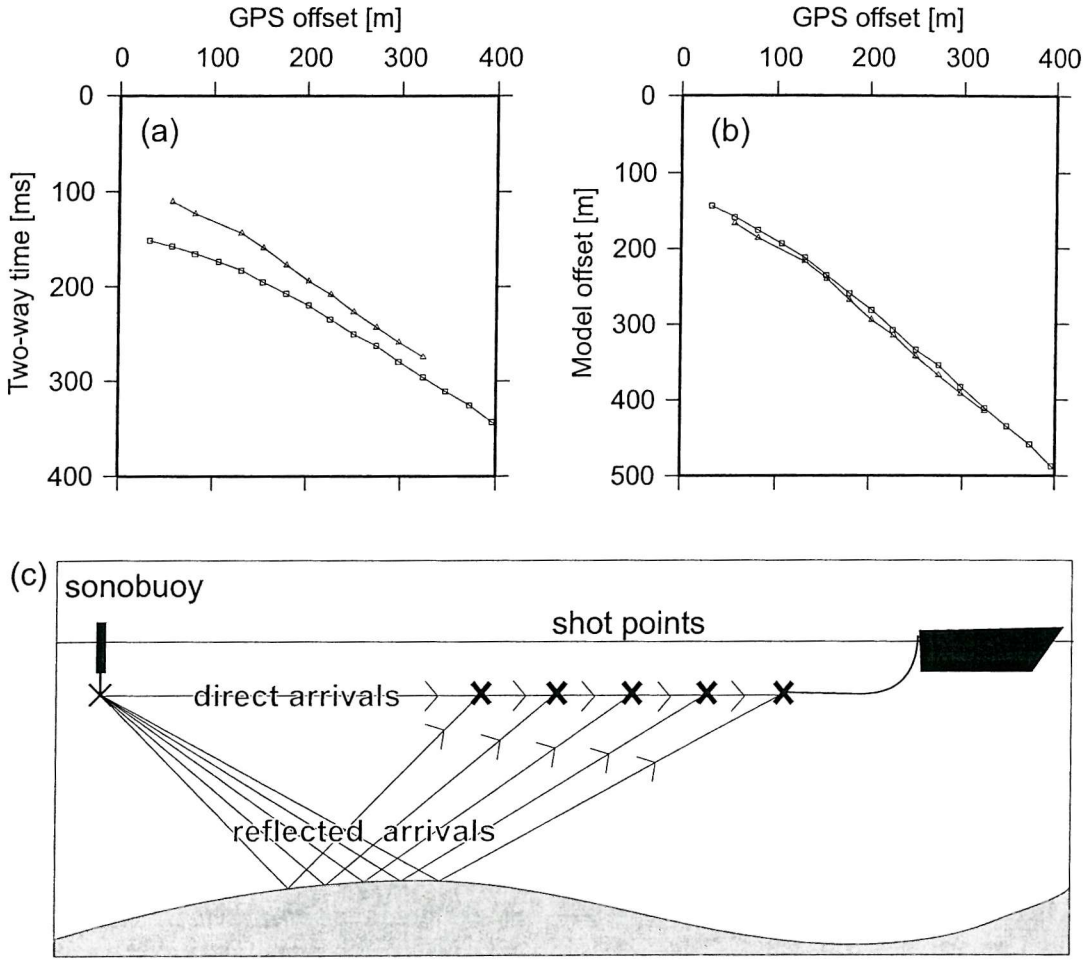

Figure 2.15 (a) seabed arrival picks for sonobuoy 9. Direct arrivals (triangles) and reflected arrivals (squares) plotted in two-way time against GPS (recorded) offsets. (b) modelled offsets for each pick of direct (triangles) and reflected (squares) arrivals plotted against GPS (recorded) offset. (c) schematic geometry of sonobuoy recording of direct and reflected rays.

Direct water wave arrivals are commonly used to calculate source-receiver offsets for sonobuoy records as these do not interact with the seabed and the velocity of sound in the water column is easily found from XBTs. The velocity of sound in the top 10m of water in the Whakatane Graben was found to be 1516ms^{-1} (see section 2.1 above). The shallow water of the survey area meant that the direct arrival was lost into the reflected and refracted arrivals after only a few traces; for sonobuoy 9 direct arrivals are only observed on nine traces close to the start of recording (figure 2.15a).

Although offsets can only be directly calculated for nine traces, the few observations available can be used to model the initial offset and drift of the sonobuoy (Bruguier and Minshull, 1996). Figure 2.15b shows the offset modelled from the direct arrival plotted against the recorded shot-offset (the location of the first trace is defined as the origin, and

the offset of all following traces is measured from this point). If the location of the sonobuoy was at the origin (initial offset = 0) and did not drift, the graph would show a straight line of gradient 1.0 passing through the origin. Figure 2.14b shows the data lie on a straight line with intercept 83 m and a gradient of 1.03. The intercept gives the model offset when the shot-offset is equal to zero, i.e. the initial offset of the sonobuoy and shot point. A gradient greater than 1.0 means the model offset is increasing faster than the shot-offset, implying that the sonobuoy is drifting in the opposite direction to the direction of recording.

A simple model for the reflected seabed arrivals was also attempted, using the bathymetry data and the calculated interval velocity for the full water column (see section 2.1). For each recorded reflection arrival time, 2-D ray tracing through the water column was used to find the source-receiver separation that gave the smallest absolute error was calculated. The sonobuoy position was considered fixed and the source position was varied. At each location the depth to the mid point of the source-receiver offset was found from the bathymetry data and the travel time calculated assuming the surface was horizontal. The results of the reflection modelling were similar to the results for the direct arrival modelling (figure 2.15b).

Since the model for the direct arrivals uses the same amount of data but involves less assumptions than the reflection model (no influence from bathymetry, and the sonobuoy is assumed to be drifting), the sonobuoy positions are calculated using these results. The true offset of the source and receiver for each trace is given by:-

offset=1.03 x shot-offset + 83m

This equation is applied to the each trace before picks are made for ray tracing. The drift-corrected sonobuoy record is shown in figure 2.15.

Modelling using rayinvr

Rayinvr is a 2D ray tracing package, allowing forward modelling and inversion of direct, reflected and refracted arrivals in a layered velocity model. The velocity model consists of a series of layers with velocities defined at the top and bottom of each layer. Velocity discontinuities at layer boundaries are allowed but not required.

Sonobuoy 9 was modelled successfully using a simple 1D velocity model as the subsurface layers are gently dipping. The model was constructed iteratively downwards from the well-constrained velocity profile of the water column and upper sediments (from physical property measurements in the sediment cores). A further constraint placed on the model was that velocity discontinuities at layer boundaries were kept as small as possible. This constraint is applied because the subsurface layers encountered in the seismic data are

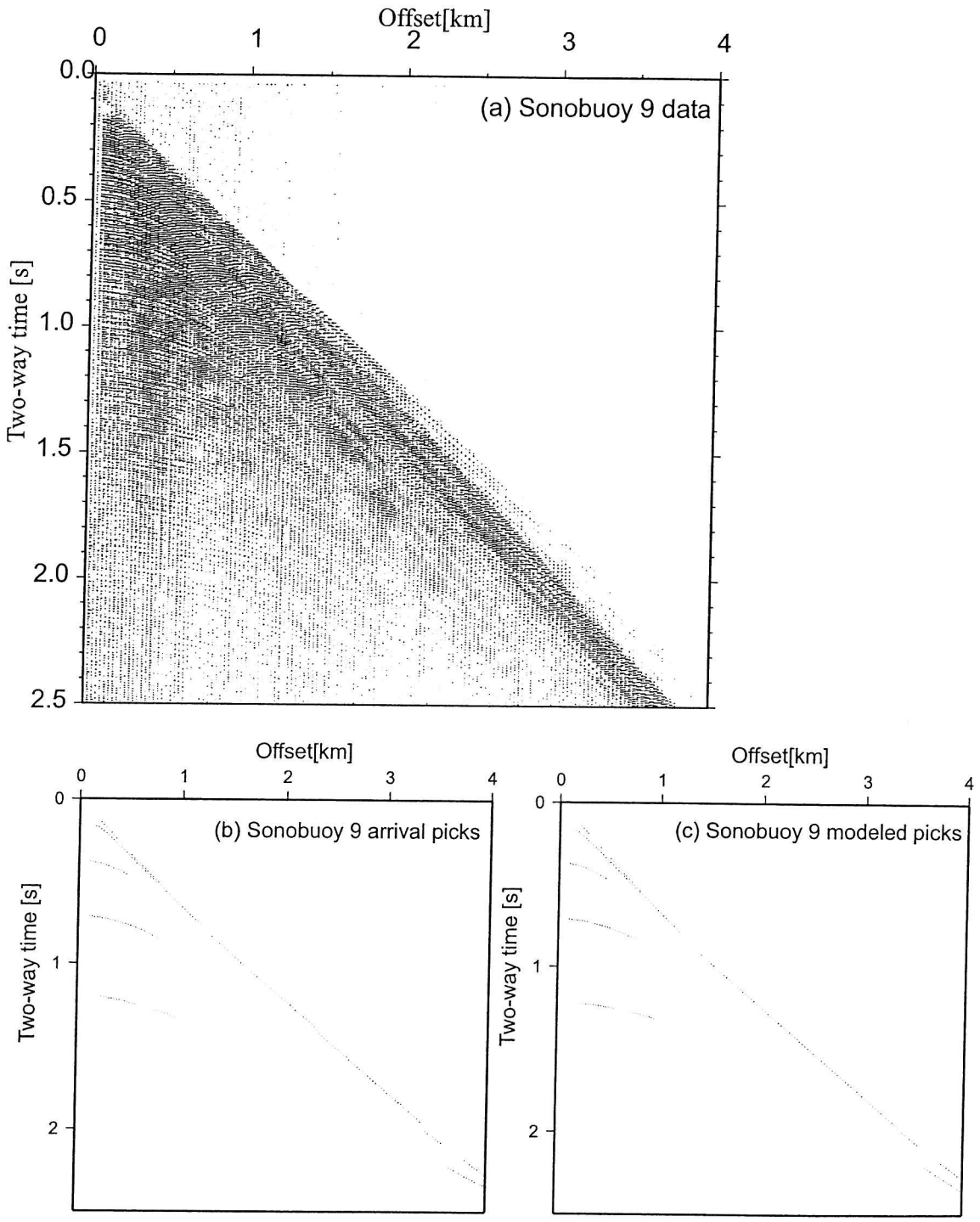

Figure 2.16 (a) drift corrected sonobuoy record, (b) travel time picks from record and (c) travel time picks derived from rayinvr model.

not thought to represent significant changes in rock type. Once constructed, the model is inverted to minimise the least-squares error between modelled and observed travel time picks.

Model Results

The drift-corrected sonobuoy record is shown in figure 2.16a, and the travel time picks used in the model are shown in figure 2.16b. Three subsurface horizons were identified in the reflected and refracted arrivals. The velocity model arrived at for sonobuoy 9 is summarised in table 2.2 and the modelled travel time picks are shown in figure 2.15c. The interval and layer boundary velocities obtained from the sonobuoy analysis agree well with those from velocity analysis of the MCS reflection data. The velocity model suggests a compacting sedimentary succession overlying a horizon, C, that is significantly more compacted (higher velocity). Horizons A and C map to prominent unconformities on the MCS reflection data (MCS1 and MCS3). Horizon C, at a mean depth within the detailed study area of c. 1.2 km, is inferred to reflect sediments present prior to full rift development. The interval velocities 1715,1925 and 2160 ms^{-1} are used in the depth conversion of the fault data and the uncertainty limits constrained by the model are carried forward in mesurements of fault displacements.

Refractor	Layer depth in model [m]	Interval Velocity [ms^{-1}]	Boundary upper	Velocity [ms^{-1}] lower	Calculated TWT to Horizon [ms]
Sea Surface	0			1490	0
		1500 ± 10			
Seabed	100±10		1510	1610	133±10
		1715±20			
A	300±30		1820	1850	366±40
		1925±50			
B	630±60		2000	2050	709±82
		2160±50			
C	1180±100		2270	2400	1218±137
		2700±100			

Table 2.2: Model Velocity Profile derived from refraction sonobuoy data

Chapter 3

Structural Analysis - Methodology

In this chapter the methods required to obtain fault displacement data from interpreted seismic profiles are described. The seismic profiles were interpreted using Geoframe^{TM}, a seismic interpretation package that allows horizon and fault interpretations on 2D seismic lines to be compiled into surface in 3D. In addition, fault-horizon contacts can be exported and used in fault analysis. Fault-horizon contact points exported from the Geoframe^{TM} software were projected onto the vertical plane parallel to the mean fault strike (strike projection). Two-way travel times were converted to depths using a velocity profile, leaving the fault-horizon contact points with x- y- and z-coordinates in metres. The straight-line distance between upthrown and downthrown contact pairs gives the fault displacement. A correction was applied to the displacement to account for the progressive compaction of the sediments as the displacement was accumulating.

3.1 Strike Projection

The fault-horizon contact points were projected onto a vertical plane parallel to the mean fault strike in the survey area. This projection is used throughout the fault analysis (chapters 4 – 6), as it is useful for making comparisons between faults and horizons, and between the two sets of survey data. The geometry of the projection is shown in Figure 3.1 and the method is outlined below.

The best-fit strike line in Figure 3.1 is at θ^{o} to North and passes through the local origin (line OB). For point **a** with co-ordinates (X_A, Y_A), the projected distance along strike is equal to the distance between points **a** and **d**. The equation of the line passing through point (X_A, Y_A) and parallel to line OB is

$$Y_A = X_A cot\theta + Y_C \tag{3.1}$$

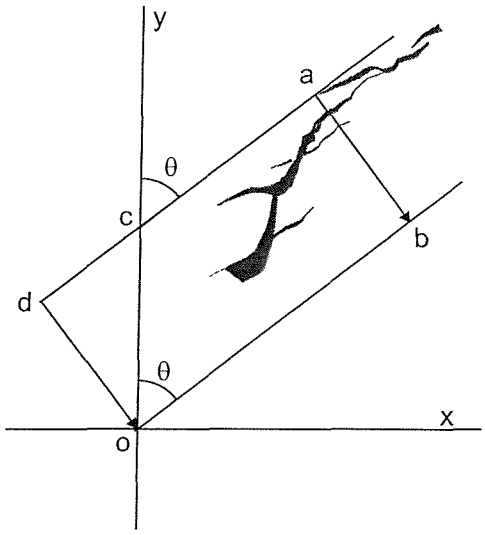

Figure3.1: Sketch map showing strike projection geometry.

where $\cot\theta$ is the gradient of the line, and Y_C is the intercept on the y axis. Y_C can be found by rearranging equation 3.1, and using this the distances AC and CD may be found.

$$AC = \sqrt{X_A^2 + (Y_A - Y_C)^2} \tag{3.2}$$

$$CD = Y_C cos\theta \tag{3.3}$$

The distance along strike AD is given by

$$AD = AC + CD = \sqrt{X_A^2 + (Y_A - Y_C)^2} + Y_C cos\theta \tag{3.4}$$

For the pseudo-3D survey area, the mean strike angle was 57°, perpendicular to the seismic profiles. The local origin was chosen as 500000,5816000 UTM metres.

The strike angle of faults within the survey deviate from the average strike by no more than 15° in all cases, resulting in a maximum of 5% error in displacement measurements (see figure 3.2)

3.2 Depth Conversion

To depth convert the seismic data the velocity profile through the sediments must be known. The velocities used in the depth conversion of the seismic data are shown in table 3.1.

3.2.1 MCS Data

The multichannel seismic profiles are depth converted using the results of the refraction sonobuoy model (table 3.1, this chapter; section 2.1 chapter 2). The upthrown and downthrown side of each fault interpretation are depth converted separately, i.e. the upthrown

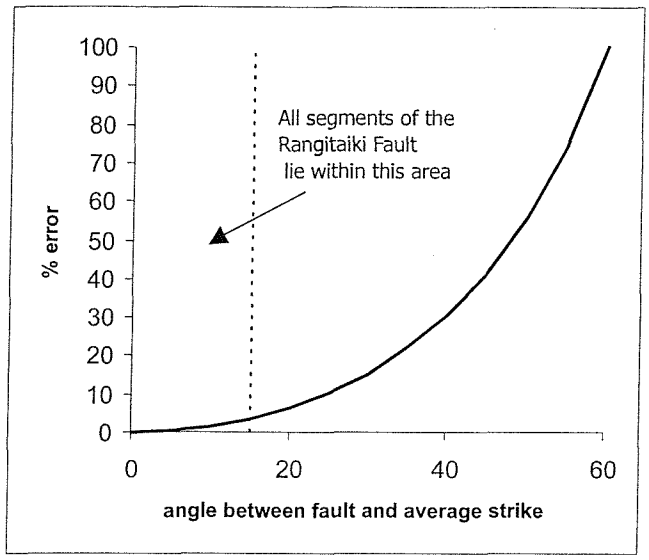

Figure 3.2: Impact of strike angle variation on displacement measurements. All the faults in the survey lie to the left of the dashed line, and have less than 5% error introduced due to strike variations.

Data Source	Depth Range	Velocity [ms^{-1}]
XBT	Water Column, 50-100 m	1511-1514
Sediment Cores	0-4 m	1550±20
Sonobuoy Model	0-300 m	1715±20
	300-600 m	1925±50
	600-1200 m	2160±50

Table 3.1: Summary Velocity Profile through the pseudo-3D survey area

contact points for a fault on the seabed and horizons MCS1, MCS2 and MCS3 are treated as one profile, and the downthrown points as another. In this way both sides of the fault are depth converted iteratively from the seabed downward. Errors in depth conversion are additive, and included in the final estimation of uncertainty in displacement measurements.

3.2.2 HRS Data

The high-resolution seismic data are depth converted using a single sediment velocity obtained from the physical property measurements of cores 14 and 15. The p-wave velocity profiles through cores 14 and 15 are shown in Figure 2.14 (chapter 2). The average velocity 1550 ± 20 ms^{-1} was used throughout in depth conversion of HRS data. No velocity variation with depth was considered, large variations are unlikely as the post-glacial sedi-

ments imaged are young and shallow and are not thought to have undergone any significant diagenesis.

3.3 Age Control of Seismic Horizons

Determination of horizon ages, and estimation of associated errors, has been a troublesome issue, and has been given much thought during the project. The horizons have not been sampled directly, but self-consistent evidence is presented which can be used to form a temporal framework. Stratigraphic evidence is used to define the age of horizon MCS1, but no such evidence is available for the deeper horizons, so an estimate is used based on sediment volumes. Using sediment volumes in a faulted area is open to large uncertainties as the active faulting leads to variable sediment deposition. An area within the pseudo-3D survey was found that had no faults and close to horizontal sedimentation - thus limiting the effects of faulting related sedimentation. A sedimentation rate of 1.05 $mmyr^{-1}$ is used, with an estimated error bound of 30 %. The results of this calculation give an age for the deepest horizon (MCS3) of 1340 $\pm$ 420 ka. This is younger than the onset of faulting (1600 ka), and MCS3 lies above the basement horizon associated with this time. The horizons formed over short periods of time in relation to the time between them, so even though the absolute age of the horizon is not well defined, the relative displacement rates calculated for the faults gives strong evidence of fault growth processes.

3.4 Decompaction

Mechanical compaction of sediments is the result of progressively increasing overburden load as the sediment becomes buried. The main effects of compaction are partial collapse of grain framework, plastic deformation of soft fragments, fracturing and pressure solution or grain boundary dissolution, which usually lead to a reduction in porosity (Gallagher, 1989). Sorting, grain size, composition and mineralogy are important parameters in compaction (Scherer, 1987); a well sorted, coarse-grained sandstone would be expected to have a higher porosity than a poorly sorted, generally finer grained one.

The thickness and total mass of the unit will decrease as pore fluid is progressively expelled (Perrier and Quiblier, 1974; Sclater and Christie, 1980), implying that the mass is conserved at all times and the matrix material is incompressible. Conservation of mass occurs if dissolution and precipitation occurs on a local scale only. The low compressibility of sedimentary grains justifies the assumption that matrix material is incompressible

(Gallagher, 1989).

Porosity reduction with depth is generally modeled empirically (e.g. Magara, 1980; Baldwin and Butler, 1987; Scherer, 1987; Stam et al., 1987; Schmoker and Gautier, 1989) and is often described as an exponential function of depth of the form

$$\Phi(z) = \Phi_0 e^{-cz} \tag{3.5}$$

where z is the depth, Φ_0 is the surface porosity and c is a constant (e.g. Sclater and Christie, 1980; Korvin, 1984). Linear relationships between porosity and depth have been suggested (e.g. Magara, 1980; Shelley, 1978), however such relationships are only apropriate for deeply buried sandstones as most of the porosity loss in sediment occurs near the surface.

3.4.1 Mathematical Approach to Decompaction

Decompaction is commonly used to reconstruct subsidence histories of basins (e.g. Sclater and Christie, 1980) by calculating the thickness of buried sediment packages once the top of the package has been brought to the surface, with the sediment still compacted under its own weight. Compaction of sediments affects measurements of depth, and consequently also affects measurements of displacement. For example, a measurement of displacement on a horizon that was faulted when it was at the surface and was subsequently buried will be too small, as the distance between footwall and hanging-wall has decreased since the rocks have compacted. In contrast, displacement measured on a horizon that was buried and faulted after burial does not need decompaction, as the distance between footwall and hanging-wall has not been changed.

The growth history of a syn-sedimentary fault is more complex in terms of decompaction, as the displacement is accumulated whilst the rock is being buried. The amount of decompaction required is dependent on (i) the rock porosity when the slip event occurred, and (ii) the rock porosity when the slip event was measured.

The decompaction of a syn-sedimentary fault may be approached by assuming that the accumulation of throw is constant with depth. The average throw rate (with respect to depth) is given by the distance between the upthrown and downthrown fault contacts divided by the depth to the midpoint between them;

$$\theta_{av} = \frac{z_2 - z_1}{m} \tag{3.6}$$

where z_1, z_2 and m are the upthrown and downthrown fault contacts and fault midpoint, respectively (see figure 3.3). The total throw at each depth θ_z, is related to the depth of

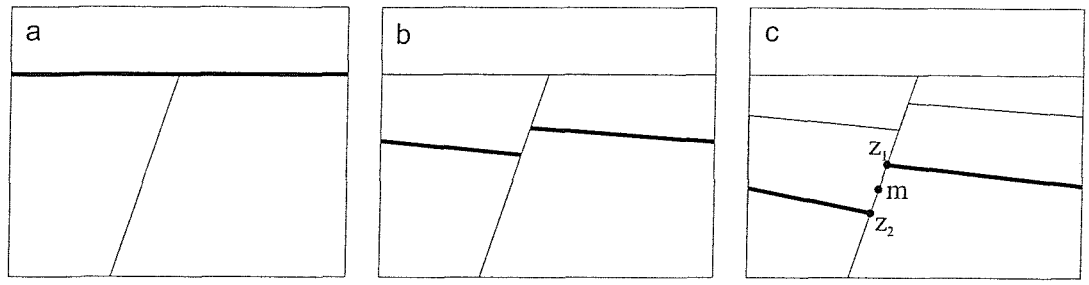

Figure 3.3: Development of a syn-sedimentary growth fault. The position and displacement of the fault is defined by fault midpoint m and upthrown and downthrown cut-off points z_1 and z_2.

the horizon, z, by:

$$\theta_z = \theta_{av} \times z \tag{3.7}$$

If sediment compaction is not considered, then for each incremental increase in depth, dz, the incremental increase in throw dθ is equal to:

$$d\theta = \theta_{av} dz \tag{3.8}$$

and the total throw can be considered as the integral over the depth range 0 to m of these throw increments:

$$\theta_m = \int_0^m \frac{z_2 - z_1}{m} dz \tag{3.9}$$

If the sediment is compacting then each measured throw contribution will have been compressed by an amount depending on the porosities of the rock when it was faulted and when it was measured. To correct for the compaction, each throw increment dθ must be multiplied by the compaction factor (equation 3.18, box 1 below)

$$\frac{(1 - \Phi(z_2))}{(1 - \Phi(z_1))} \tag{3.10}$$

where z_2 is replaced by the final fault midpoint depth (m) and z_1 the original depth the throw increment came from, which will range from 0 to m. This means that an uncompressed throw increment (dθ_{uc}) that was accumulated on a fault at depth z now lying at depth m is;

$$d\theta_{uc} = \theta_{av} \frac{(1 - \Phi(m))}{(1 - \Phi(z))} dz \tag{3.11}$$

and the total uncompressed throw is given by the integral

$$\theta_{uc} = \theta_{av} \int_0^m \frac{(1 - \Phi(m))}{(1 - \Phi(z))} dz \tag{3.12}$$

by substituting equations 3.5 and 3.6 and rearranging,

$$\theta_{uc} = (1 - \Phi_0 e^{-cm}) \left(\frac{z_2 - z_1}{m} \right) \int_0^m \frac{1}{(1 - \Phi_0 e^{-cz})} dz \tag{3.13}$$

solving the integral using the standard form (Beyer, 1987) gives

$$\theta_{uc} = (1 - \Phi_0 e^{-cm}) \left(\frac{z_2 - z_1}{m} \right) \left[z + \frac{ln(1 - \Phi_0 e^{-cz})}{c} \right]_0^m \tag{3.14}$$

$$\theta_{uc} = (1 - \Phi_0 e^{-cm}) \left(\frac{z_2 - z_1}{m} \right) \left(m + \frac{ln(1 - \Phi_0 e^{-cm})}{c} - \frac{ln(1 - \Phi_0}{c} \right) \tag{3.15}$$

3.4.2 Decompaction of Sediments observed in MCS data

The total compaction-corrected throw is given in equation 3.15, and requires z1, z2, m, Φ_0 and c to be known. The values of z1 and z2 are measured from the seismic profiles, and from these the fault midpoint, m, can be calculated. The value of c was determined empirically by Sclater and Christie (1980) to lie between 0.39 x 10^{-5} cm^{-1} and 0.51 x 10^{-5} cm^{-1} for shaley-sand to shale lithologies (table 3.2). Surface porosity, Φ_0, can be determined using the P-wave velocity of the cores and the regressions of Bachman (1985). A velocity of 1550 ms^{-1} (see chapter 2) yields a surface porosity of 0.70. This value of surface porosity is very high, leading to a large compaction effect. Since the depth dependence of porosity is not constrained a lower value of 0.60 was used in preference. This value is the median value between the surface porosities observed by Sclater and Christie (1980) for Shale and shaley-sand. The values of c and Φ_0 from Sclater and Christie (1980) result in a compaction correction that is always within the estimated error range of displacement measurements.

Sediment Type	C [cm x 10^{-5}]	Surface porosity
Shale	0.51	0.63
Shaley sand	0.39	0.56
Sand	0.27	0.49

Table 3.2: Parameters for exponential relation between porosity and depth for various normal pressured lithologies (Sclater and Christie, 1980)

3.4.3 HRS Data

Since the high-resolution seismic data are limited to the top c. 60 m (compared with up to 1500 m in the MCS data), the effect of compaction on the displacement measurements is expected to be negligible. The decompaction algorithm was not applied to any high-resolution data.

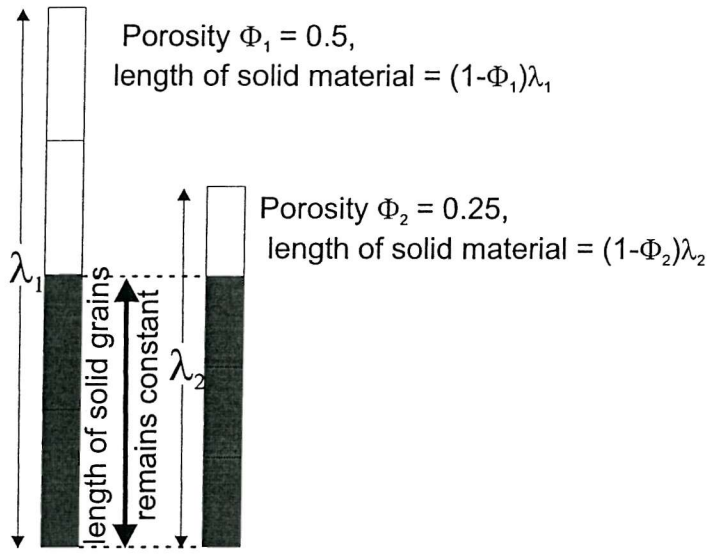

Figure 3.a: Variations in porosity with sediment compaction.

BOX 1 – The effect of compaction on sediment lengths

A column of sediment of length l_1 at depth z_1 has porosity $\Phi(z_1)$. Porosity is the fraction of the sediment that is made up of pore space, so the length of the solid fraction of this sediment column is given by $(1 - \Phi(z_1)) \times l_1$.

If the column of sediment is buried deeper, to depth z_2, the porosity will decrease to $\Phi(z_2)$ and the sediment will decrease in length to l_2, but the length of solid fraction will remain the same (figure 3.a),

$$(1 - \Phi(z_1)) \times l_1 = (1 - \Phi(z_2)) \times l_2 \tag{3.16}$$

The original length l_1, can be found by re-arranging this equation if the current and original depths (z_2 and z_1), the current length (l_2) and the porosity dependence with depth ($\Phi(z)$) are known.

$$l_1 = \frac{(1 - \Phi(z_2))}{(1 - \Phi(z_1))} \times l_2 \tag{3.17}$$

the change in length between the original length, l_1, and the compacted length l_2, is described by the 'compaction factor'

$$\frac{(1 - \Phi(z_2))}{(1 - \Phi(z_1))} \tag{3.18}$$

3.4.4 Effect of Compaction on Displacement Results

Decompacting sediments results in increases in displacement measurements, as the footwall and hanging-wall vertical separation is increased. The effect of any decompaction algorithm increases with depth - meaning that however the decompaction is approached, the difference in displacement between successive horizons will increase, thereby systematically increasing measured displacement rates calculated from older sediments. The effect of this is that if sediment compaction is *under*-corrected, a constant displacement rate will apparently increase with time – but *over*-corrected, a constant displacement rate will appear to decrease. Since the variation of porosity with depth is poorly constrained it is impossible to know if the compaction is over- or under-corrected. However, since the effect of decompaction is found always to be within the estimated uncertainty for each horizon, no large effect on displacement rate is expected.

3.5 Calculation of Fault Displacement Rates

The fault planes exhibit variable dip laterally and vertically, so both the heave and throw components of fault movement are measured, and combined to give the displacement. The difference in displacement on a fault between successive horizons represents the displacement increment in the period between deposition of the two horizons (Childs et al., 1993). Fault displacement rates for each time period were calculated using the displacement difference between horizons and age estimates of those horizons.

3.5.1 Aggregate Displacement Profiles and Average Displacement Rate Values

Strike projected displacement measurements are summed across strike to produce aggregate displacement profiles for the Rangitaiki Fault on each horizon. The aggregate displacement rates are averaged along strike to give a mean value of displacement rate for the survey area. Mean displacement rates are used to describe relative changes in activity on the Rangitaiki Fault as they include more of the data and are more reliable than single observations of maximum displacement (Dawers et al., 1993).

3.5.2 Sources of Error

Errors in the measurement of fault displacements and sediment thickness come from uncertainties in horizon picks, the interval velocities used in depth conversion and corrections

for sediment compaction. Other sources of uncertainty - for example acquisition and time migration - are considered negligible (see Thore, 2002 for a review on error in MCS interpretation). Uncertainties in horizon picks are estimated to be one wavelength. The nominal frequency of the data at horizon MCS1 is 70Hz, reducing to 40Hz at MCS3. This equates to $\pm$ 15 ms at MCS1 and $\pm$ 25 ms at MCS3. For the high-resolution boomer profiles, an estimated uncertainty of $\pm$0.5 ms is included in each horizon pick. Seismic profiles where the interpretation of the horizons was ambiguous were not included in calculating the fault displacements. The velocity used for depth migration of high-resolution profiles was determined from in situ physical property measurements made on cores collected within the Whakatane Graben, a value of 1550 $\pm$ 25 ms^{-1}. Velocities used for depth migration of the MCS horizons were determined from the sonobuoy model using wide angle reflected and refracted arrivals. The errors derived from inverting the model are shown in table 3.1.

The effect of sedimentary compaction is greatest where the sediments are thickest - the difference between decompacted and compacted fault displacement measurements remains within the estimated uncertainty range for the displacement, see section 3.3.4 above.

In many cases there is some fault drag adjacent to the fault planes observed in both the footwall and the hanging-wall. This local perturbation to the displacement fields was corrected for using the technique employed by Chapman and Menielly (1991) and Mansfield and Cartwright (1996) whereby the horizons are projected towards the fault plane.

Chapter 4

Development of the Extensional Fault Population in the Whakatane Graben

In this chapter the history of faulting in the pseudo-3D survey area from 1340 ± 420 ka (the deepest horizon in the multichannel data) to c. 17 ± 1 ka (the deepest horizon in the high-resolution survey) is explored using back-stripping of syn-sedimentary growth faults. Measurements of fault dip, strike, displacement and length on four horizons aged 1340 ± 420 ka, 770 ± 240 ka, 300 ± 100 ka and 17 ± 1 ka are used to make estimates of rates of displacement, extension and strain in the survey area. These values are discussed in the context of the geology of the Taupo Volcanic Zone and the attendant seismic risk.

4.1 Multichannel Seismic Stratigraphy

Three example multichannel seismic (MCS) profiles from the pseudo-3D survey area are shown in Figure 4.1, and line drawings of interpretations of ten of the profiles are shown in Figure 4.2. The locations of these profiles are shown in Figure 4.3. The profiles shown in the figure are evenly spaced at 600 m apart and are a sample of the 50 MCS profiles (at 150 m spacing) that comprise the pseudo-3D data set.

The profiles show a layered sedimentary package above a faulted higher velocity layer (Section 3.3 Chapter 2). The sediments are displaced by active extensional faults producing rotated fault blocks and thickening of sediments into the hanging-wall of the faults (e.g. profile 7, Figure 4.2). Many of the faults cross the full vertical extent of the seismic section. These faults dominantly dip towards the northwest at an average angle of 60° in the top

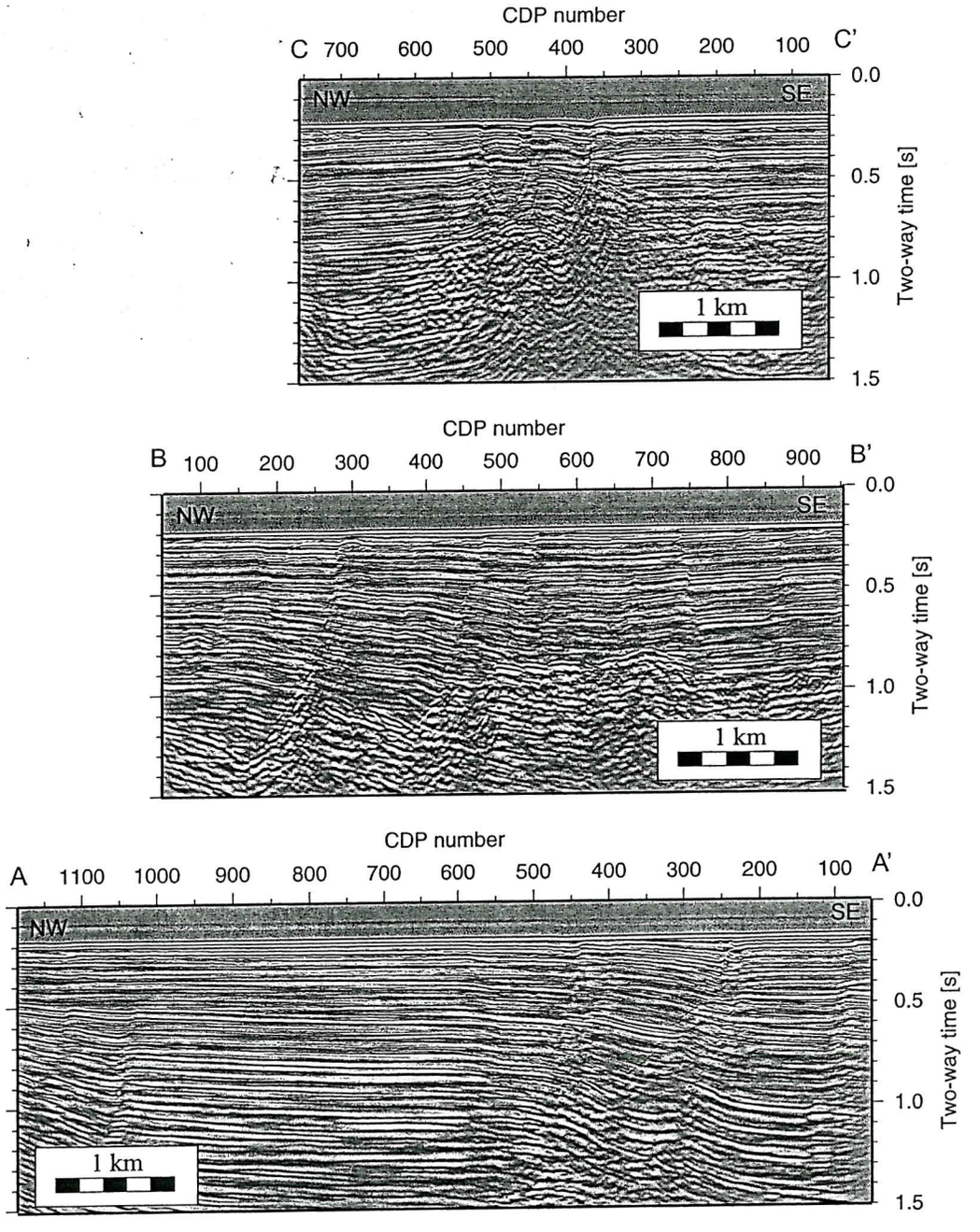

Figure 4.1a: Example multichannel seismic profiles as a time section with approximately 1:1 vertical scaling. Location of the profiles shown in figure 4.3.

1.5 kilometres, but are almost vertical in the near surface and sole out at around 3 seconds TWT (approximately 5km depth) (Davey et al., 1995). In addition, the dip of the faults is highly variable along strike (e.g. change in dip of R3 from profile 3 to profile 7). In addition to these large vertically extensive faults, there are several smaller faults that are limited in

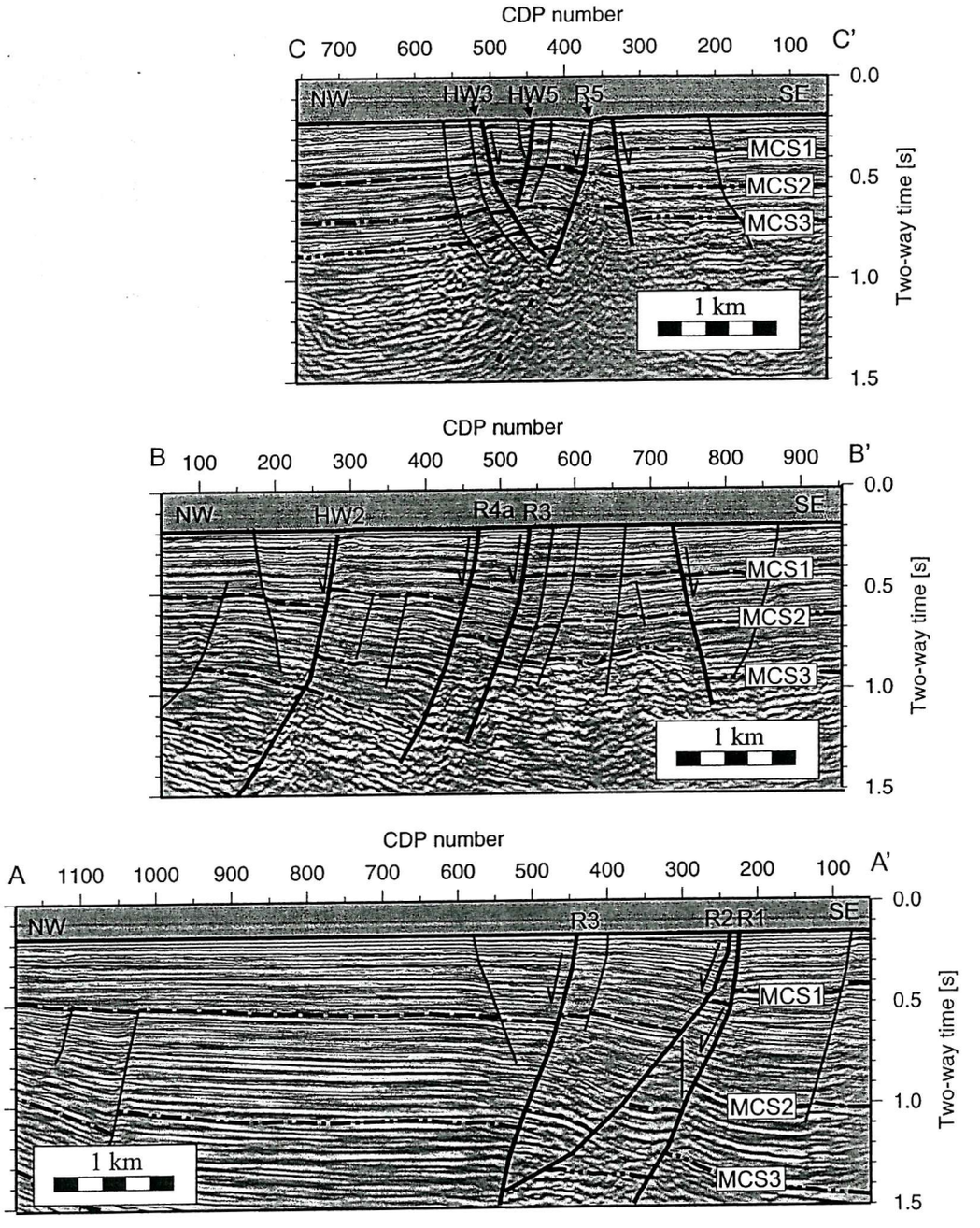

Figure 4.1b: Example multichannel seismic profiles with interpretation as a time section with approximately 1:1 vertical scaling. Major faults labelled R1, R2, Hw1, Hw2 etc. Sense of movement is indicated with arrows. Location of the profiles shown in figure 4.3.

vertical extent.

The data presented here are from the top 2 seconds TWT of MCS profiles collected during cruise TAN99-14 (Chapter 2). Beneath 2 seconds TWT there is very little primary reflection energy and no interpretations could be made. The seismic section presented in

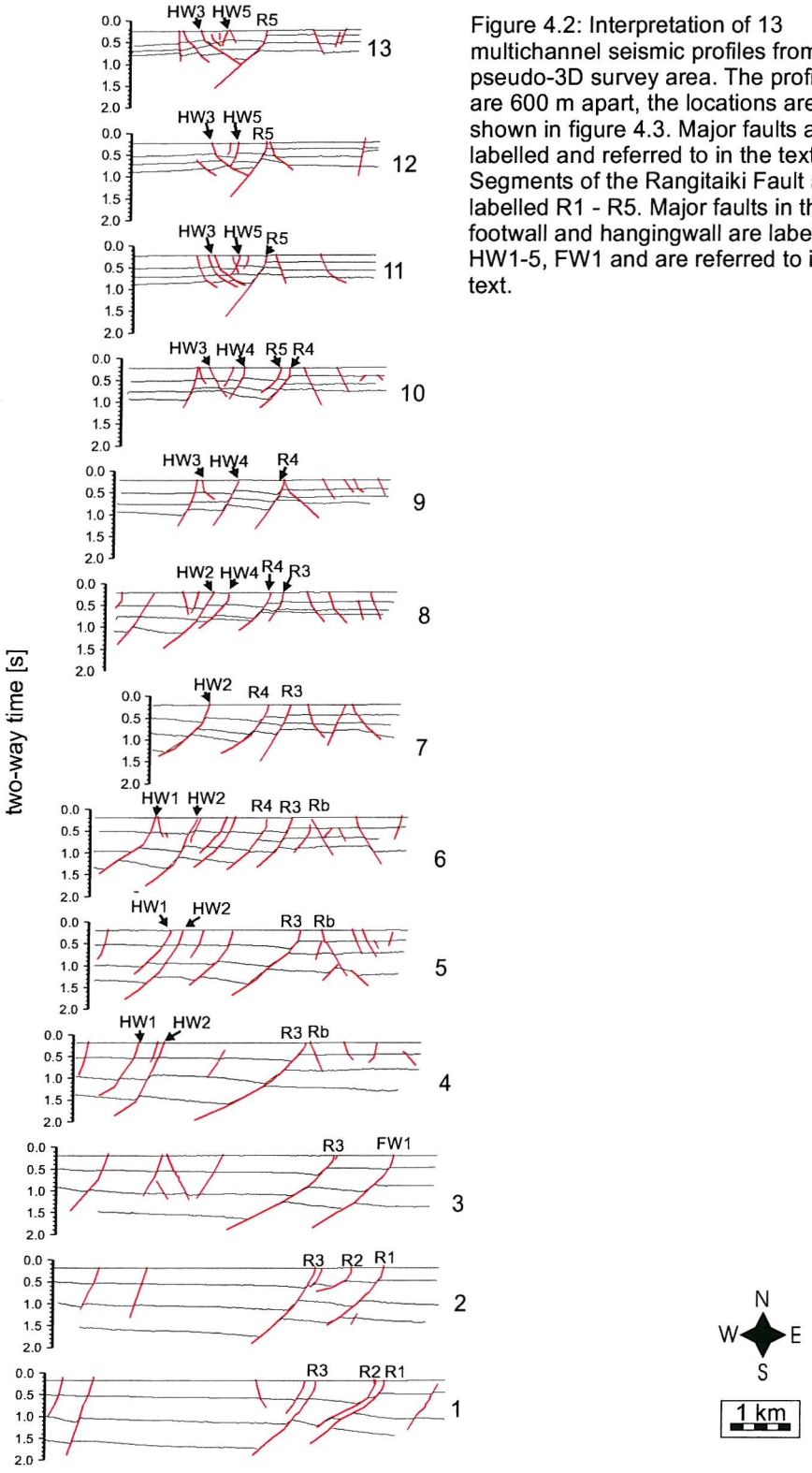

Figure 4.2: Interpretation of 13 multichannel seismic profiles from the pseudo-3D survey area. The profiles are 600 m apart, the locations are shown in figure 4.3. Major faults are labelled and referred to in the text. Segments of the Rangitaiki Fault are labelled R1 - R5. Major faults in the footwall and hangingwall are labelled HW1-5, FW1 and are referred to in the text.

Chapter 1 (Figure 1.5) lies to the north of the pseudo-3D survey area and is interpreted to 2 seconds TWT.

Three subsurface horizons are identified and mapped in the MCS data. These horizons were chosen for interpretation because of their clarity and lateral continuity and because

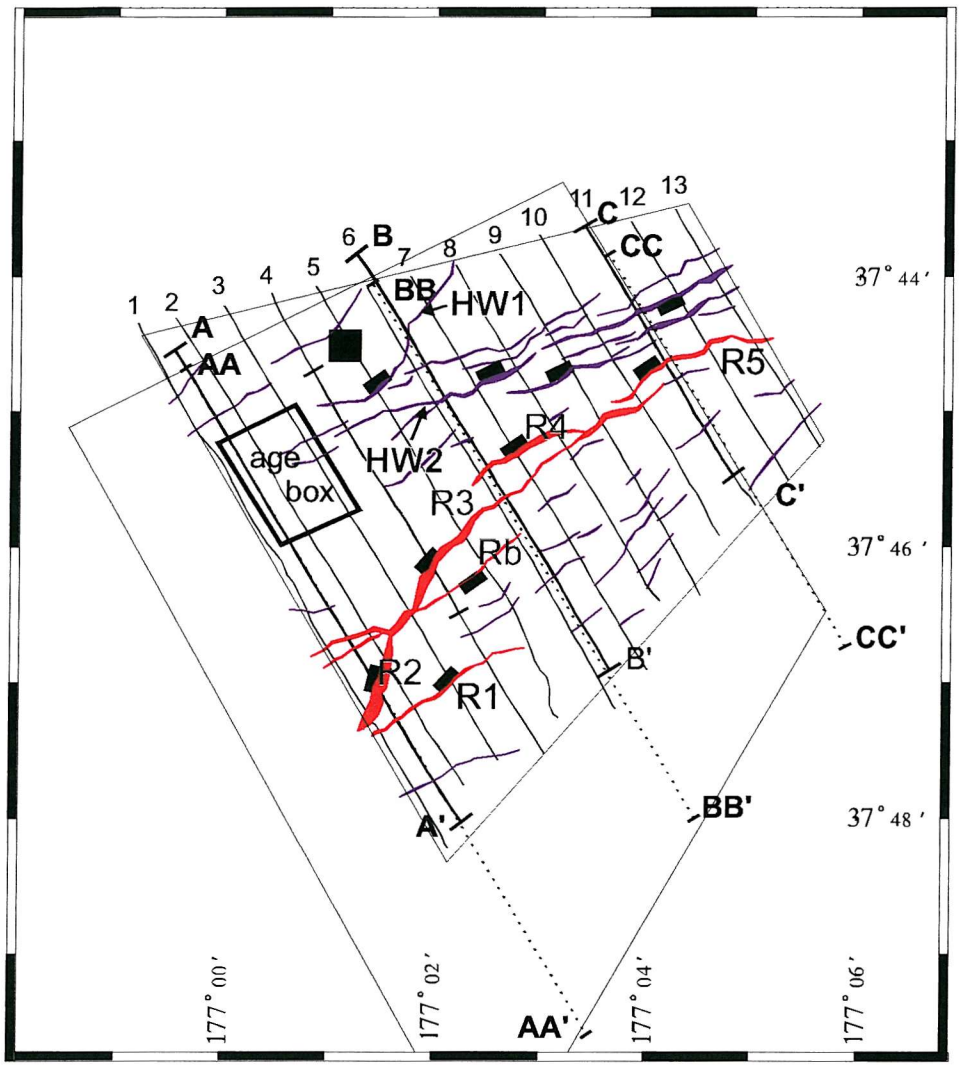

Figure 4.3: Map showing positions of interpreted multichannel seismic profiles from the pseudo-3D survey area shown in figures 4.1 and 4.2. High-resolution and multichannel seismic survey areas shown in thin lines, lines A, B and C from figure 4.1 in bold. The location of core TAN99-14/14 is shown with a black square. Rangitaiki fault segments are shown in red and labelled R1-R5, other faults are shown in purple, black rectangles indicate downthrown side of major faults. The area used to calculate representative sediment thicknesses for estimating horizon ages is shown by the black rectangle and labelled 'age box'.

they are evenly spread through the sedimentary package (Figure 4.1). The sediments between the horizons are thickest in the south of the pseudo-3D survey area and thin progressively northwards, with the result that all of the subsurface horizons dip towards the coast increasingly steeply with depth. The increase in sediment thickness and dip of the horizons coincides with an increase in fault displacement, and is likely to be a localised

feature caused by subsidence associated with growth on the Rangitaiki and White Island Faults.

Horizon MCS1 is identified as a strong positive and laterally continuous layer overlying a unit of variable thickness characterised by up to three strong negative peaks. Above horizon MCS1 the overlying sediments onlap, although this angular relationship is often not well developed on dip sections. The onlap is likely to have been caused by the development of depocentres in the hanging-walls of active faults.

Horizon MCS2 is similar to MCS1 in that it is a positive reflection with onlapping sediments above. MCS2 is less well defined than MCS1 as it does not have as strong a reflection and the negative peaks beneath are not present. Horizon MCS3 is defined mainly as a change in seismic character, the seismic attribute becoming noticeably lower frequency beneath, but also on the basis of a sharp increase in velocity observed both in velocity analysis and the sonobuoy model, giving rise to a strong reflector. There are often diffractions from the tops of the fault blocks on horizon MCS3, although these have been reduced considerably by migration.

The large velocity contrast across horizon MCS3 (section 3.3, Chapter 2) and diffractions from its topography suggest that it is older and more compacted than the sediments above. Horizon MCS3 has a similar seismic character to the basement described by Davey et al. (1995). Their basement lies at up to 2.5 seconds TWT in the Whakatane Graben interpreted on a profile lying south of the pseudo-3D survey area, and is interpreted as the pre-rift greywacke that underlies the graben. If MCS3 is the pre-rift greywacke basement, then the seismic data is imaging the entire history of rifting and fault development. Within the pseudo-3D survey area, MCS3 is observed as deep as c. 2 seconds TWT, but not as deep as the 2.5 seconds two way time to basement interpreted by Davey et al. (1995). If the slope of the sub-surface horizons continues beyond the extent of the pseudo-3D survey area, then MCS3 could be expected at around 2.5 seconds and may be the basement, however, if the slope is more localised then MCS3 lies above the horizon interpreted as basement by Davey et al. (1995).

4.1.1 Age Control

Rock dredge samples from seafloor exposures were used to constrain the age of the MCS stratigraphic sequence. Dredge samples 5, 19 and 40 lie in sediments stratigraphically above MCS1, or within 200 ms TWT of this horizon. These samples have been dated biostratigraphically using nannoflora, foraminifera and palynology to be of New Zealand Haweran (Wq) stage (< 0.34 Ma). Considering the stratigraphic positions of these samples,

an inferred age range of 300 ± 100 ka is estimated (Table 1). To calculate a representative sedimentation rate to MCS1, the depth to the horizons is calculated in the pseudo-3D as far from major faulting as possible. An area of approximately 2 km^2 was chosen where the sediments are flat lying, away from active faulting and close to core TAN99-14 (Figure 4.3). The average thickness of sediment between each horizon in this area is calculated from two-way arrival times and the interval velocity derived from the refraction experiment (section 3.3, Chapter 3). The depth to horizon MCS1 is 315±18 m, leading to an accumulation rate of 1.05 ± 0.30 $mmyr^{-1}$. Below horizon MCS1, there are no biostratigraphically defined ages, and ages for horizons MCS2 and MCS3 have been inferred by extrapolating the sediment accumulation rate above MCS1 to the depth converted positions of these horizons (Table 1). The ages for MCS2 and MCS3 of 770 ± 240 and 1340 ± 420 ka seem reasonable considering their position in the stratigraphic sequence in relation to the age of the onset of rifting (c. 1.6 Ma). Using this same sediment accumulation rate, a tectonic basement formed at 1.5 – 2.0 Ma should lie at 1575 – 2100 m depth, and would be expected in a seismic section at between 1600 and 2100 ms TWT.

Layer	Thickness [ms TWT]	Interval Velocity [m/s]	Thickness [m]	Age of Horizon [ka]
Seabed- MCS1	367±21	1715±20	315±18	300±100
MCS1-MCS2	513±25	1925±50	493±27	770±240
MCS2-MCS3	556±32	2160±50	601±37	1340±420

Table 4.1: Estimated ages of horizons. Sedimentation rate assumed to be 1 ± 0.2 $mmyr^{-1}$. Error bounds quoted on travel times are one standard deviation.

The estimated age of MCS1 is in broad agreement with the age of the Matahina Ignimbrite (230 ± 30 ka, Nairn and Beanland, 1989), a widespread and thick (>30 m) volcanic deposit observed on both sides of the Whakatane Graben and in seismic profiles under much of the western side of the Rangitaiki Plains (Woodward, 1988). The ignimbrite is overlain by a sequence of unconsolidated pumice and ash layers that have a large acoustic impedance contrast with the welded ignimbrite and would be expected to provide a strong seismic reflection. On the profiles interpreted by Woodward (1988), the Matahina ignimbrite was observed as a strong positive reflection forming a flat sheet dipping gently towards the basin. These observations are consistent with the interpretation that MCS1 is at least associated with the formation of the Matahina Ignimbrite, and in conjunction with the rock dredge information described earlier, leads to a consistent estimation of an age of

300 ± 100 ka.

4.2 Summary of High-Resolution Seismic Stratigraphy

The high-resolution data and stratigraphic framework are described in more detail in Chapter 5. The chirp and boomer profiles record the post-glacial transgressive sequence overlying an eroded ravinement surface (Figure 4.4). In this chapter, the post-glacial sequence is considered in its entirety (subdivided in Chapter 5); fault maps and displacement are calculated for the low-stand erosion surface (HRS4, Figure 4.4) only. Within the pseudo-3D survey area, this horizon is inferred to have formed between 16 ka and 18 ka (17 ± 1ka).

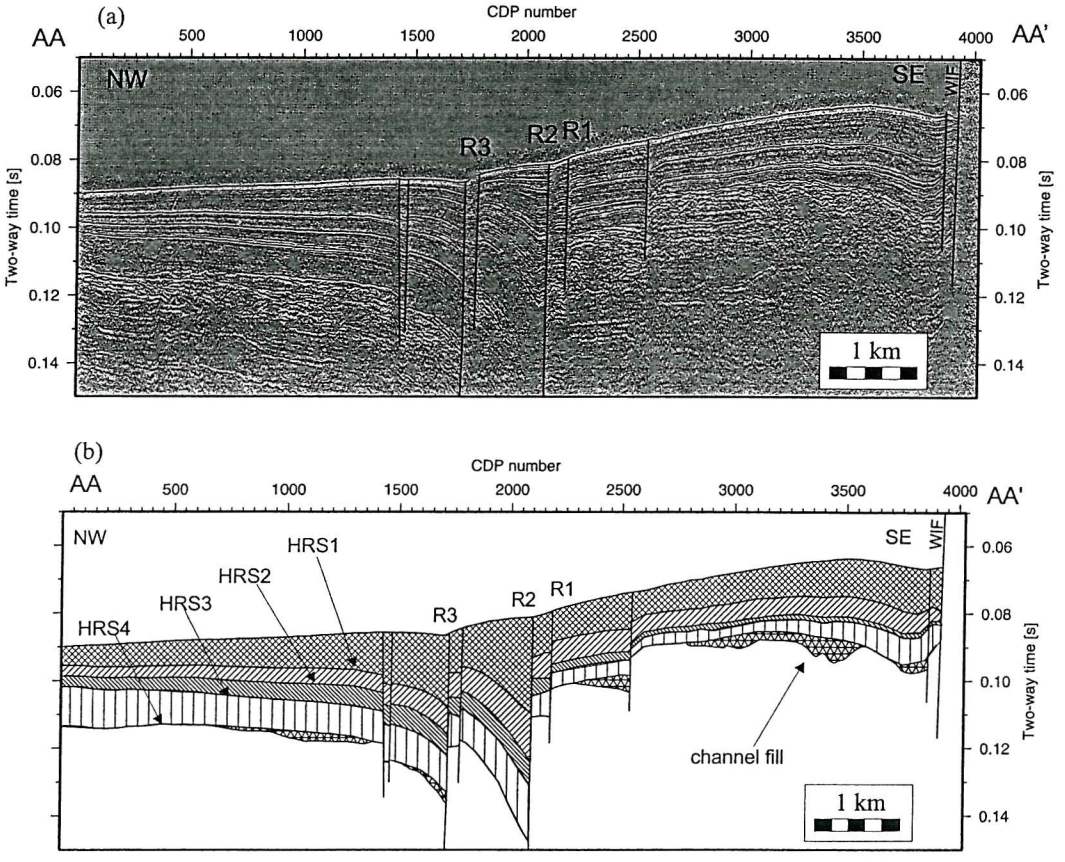

Figure 4.4: Example boomer profile (a) data and (b) interpretation showing segments of the Rangitaiki Fault (R1, R2, R3), the White Island Fault (WIF) and interpreted horizons (HRS1 - HRS). Location of profile AA-AA' shown on figure 4.3. Vertical exaggeration approximately X 40.

4.3 Descriptions of horizons

Figures 4.5 to 4.8 show structure contours for the interpreted horizons HRS4, MCS1, MCS2 and MCS3 respectively, depth is measured in milliseconds two-way time. The faults are shown as red and purple polygons marking the contacts between the faults and the upthrown and downthrown sides of the horizon, and thus show the horizontal component of displacement (fault heave). The Rangitaiki Fault is shown in red, its major segments are labelled R1-R5; major faults in the hanging-wall and footwall are labelled in a similar manner (HW1, FW1 etc.). The overall trends of the horizons have been calculated using the gridding function of the Geoframe software. Both HRS4 and MCS1 have a negligible dip when the effect of faulting is not taken into account. Horizons MCS2 and MCS3 have dips of 4° and 7° respectively, with dip directions of 79° and 83°. If the hanging-wall and footwall of the Rangitaiki Fault are considered separately, the horizons are seen dipping towards the south west (towards the coast). Measured along strike, the angle of dip is again negligible for horizons MCS1 and HRS4, and angles of 4° and 5° were found for horizons MCS2 and MCS3 respectively. The direction and development of the onlapping relationships in the seismic profiles suggests that this horizon rotation is caused by the large-scale development of the Rangitaiki and White Island Faults, although the limited spatial extent of the pseudo-3D survey area means that this assumption cannot be tested. In addition to this survey-wide trend, the segmented nature of faulting causes localised depressions in the horizons in the hanging-walls of active faults. This is seen where the structure contours close against a fault trace, and is most clearly seen on the major faults in the higher horizons (HRS4, MCS1) where the broader scale survey-wide rotation is less pronounced.

Variations in fault dip result in relative variations of the heave and throw components of fault separation, even when the total separation does not change. A low dip section of R3 between 4000 and 5000 m (dip decreases to 35 -40° at MCS3) along strike causes the heave to be larger than the throw, whereas to the north the heave is much lower as the faults increase to around 60° dip (e.g. profiles 4 and 7, Figure 4.2).

4.4 Fault Geometry

The faults imaged by the multichannel seismic in the pseudo-3D survey are divided into three groups - the Rangitaiki Fault system, faults in its hangingwall (hangingwall faults) and faults in its footwall (footwall faults). These divisions are made based on lateral coherence of fault displacement and physical connectivity of segments of the Rangitaiki Fault. Figure 4.9 shows a displacement map (the thickness of the fault trace denotes the displacement at

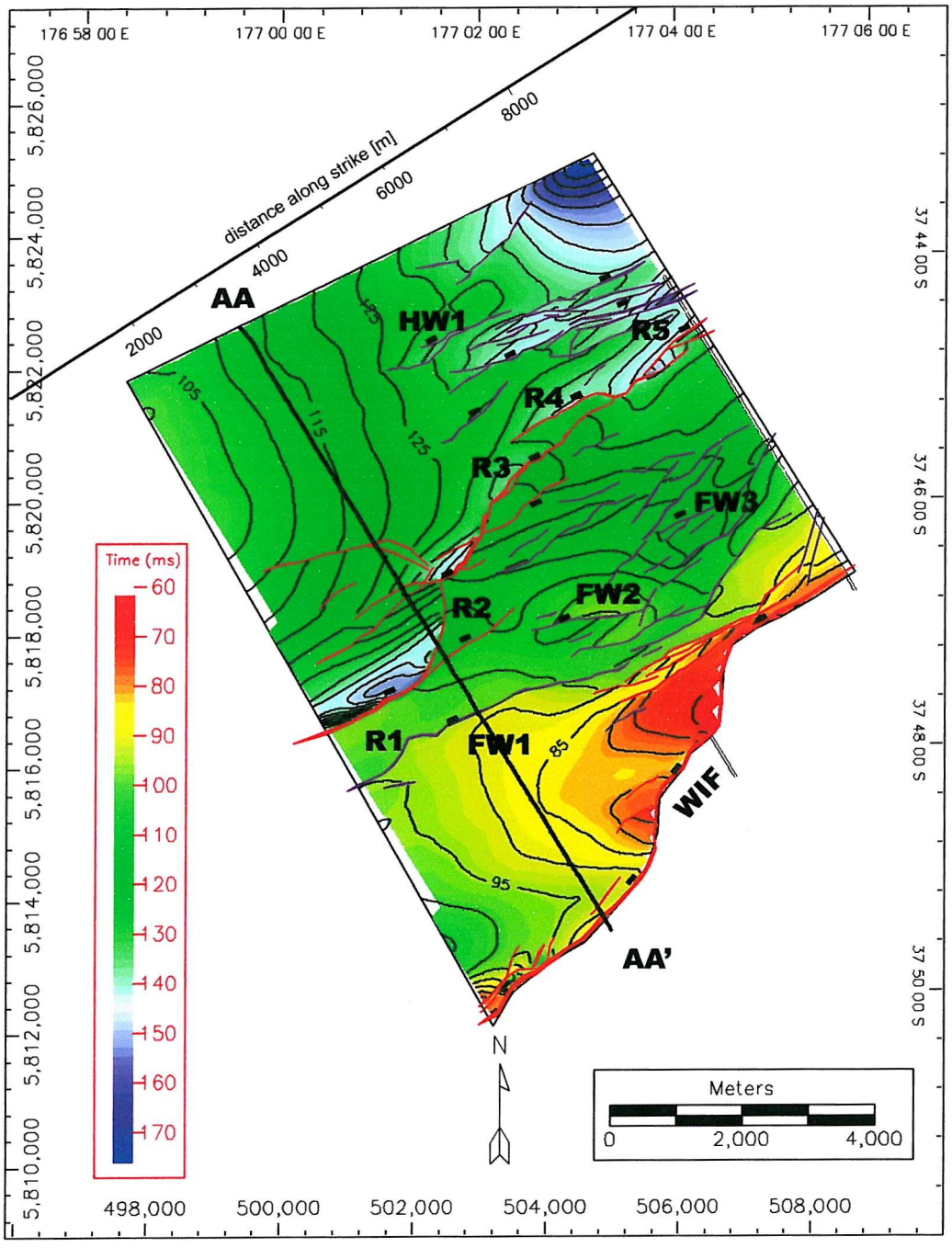

Figure 4.5: Structure map of horizon HRS4. Rangitaiki Fault segments shown in red and labelled R1-R5, other faults shown in purple and labelled Fw1, Hw1 etc., Black rectangles mark downthrown side of major faults. Profile AA-AA' shown in figure 4.4.

the horizon) for horizon HRS4, with the faults separated into the three groups discussed in this chapter (the White Island Fault is described in Chapter 5). The data have been strike projected (Chapter 3), so the Rangitaiki Fault lies across the page. The vertical continuation

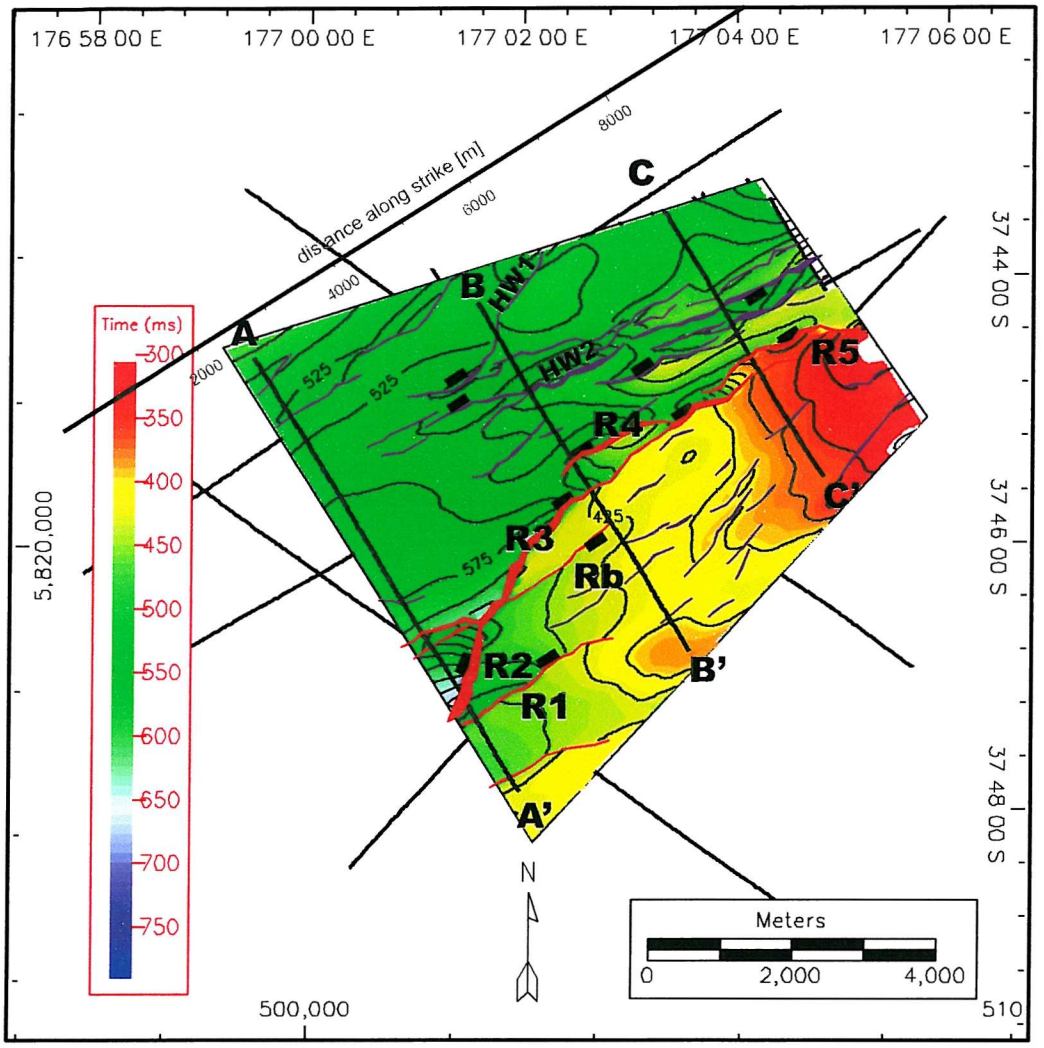

Figure 4.6: Structure map of horizon MCS1. Rangitaiki Fault segments shown in red and labelled R1 - R5 and Rb. Other faults are shown in purple. Profiles A-A', B-B' and C-C' refer to figure 4.1.

of most of the faults observed in the multi-channel seismic data can be identified in the high-resolution profiles. The large faults in the area are readily identified, but direct correlation of the smaller faults is more difficult in some places. The change in resolution highlights the fact that displacement in the hangingwall faults is likely to be under-sampled as closely spaced faults may not be properly resolved in the deeper horizons of the multichannel seismic data. In the south of the survey area, faulting is concentrated on a few high-displacement faults leaving much of the profiles undisturbed (profiles 1 – 3, Figure 4.2). Faulting is more evenly distributed in the centre of the survey area (profiles 5 – 8, Figure

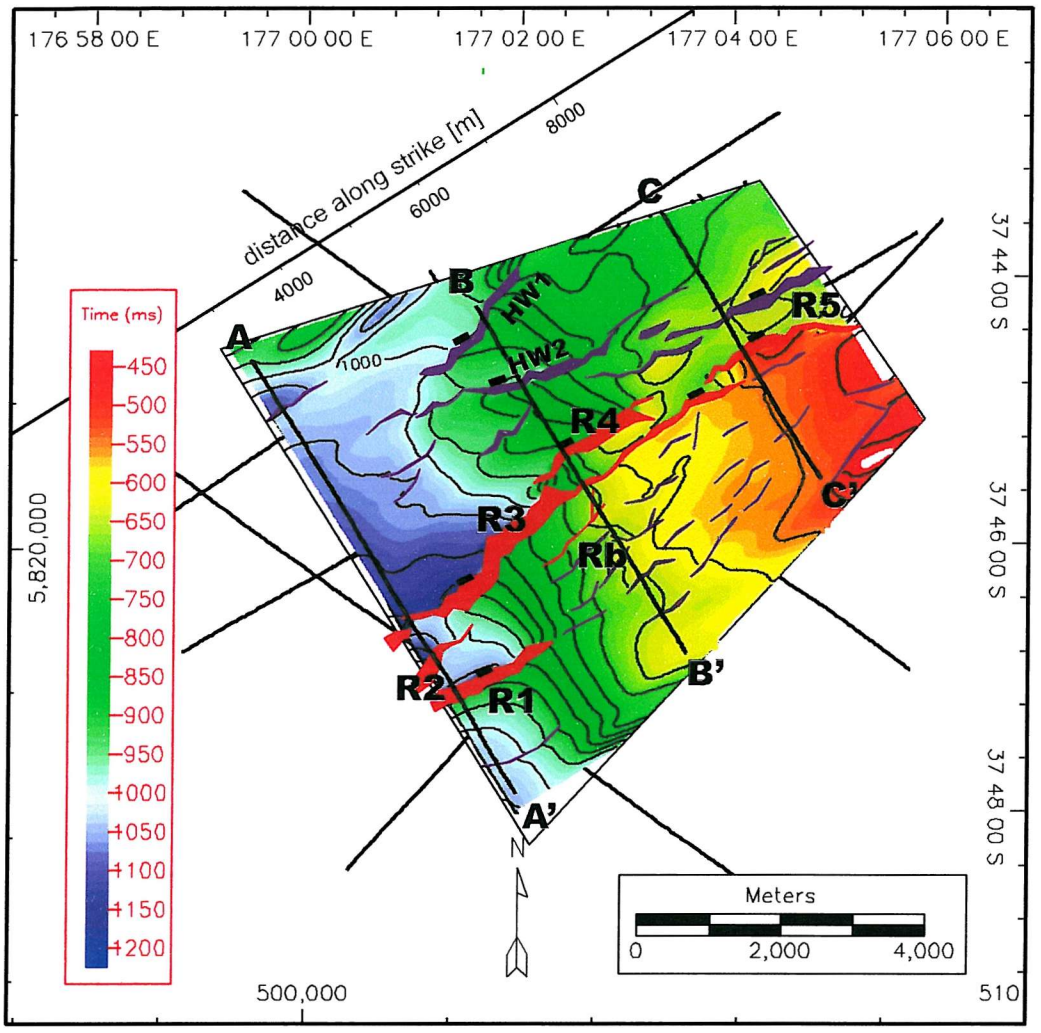

Figure 4.7: Structure map of horizon MCS2. Rangitaiki Fault segments shown in red and labelLed R1-R5 and Rb. Other faults shown in purple. Profiles A-A', B-B' and C-C' refer to figure 4.1.

4.2), as there are larger and more active faults in the Rangitaiki Fault hangingwall leading to the development of a series of rotated fault blocks (e.g. profile 7, Figure 4.2). The even distribution of faults gives way northwards to a graben in the hanging-wall of the Rangitaiki Fault. The hanging-wall graben is observed to be physically linked to the Rangitaiki Fault in profiles 11 – 13 (figure 4.2), but may be linked at depth further south (e.g. profile 10). The complexity of faulting in this area reduces the quality of the seismic data beneath the heavily faulted hanging-wall graben. The closely spaced faulting of the hanging-wall graben is better resolved in the high-resolution data because of the more closely spaced CDPs (2.5 m in the boomer data, 12 m in the MCS). However, because the number of faults increases

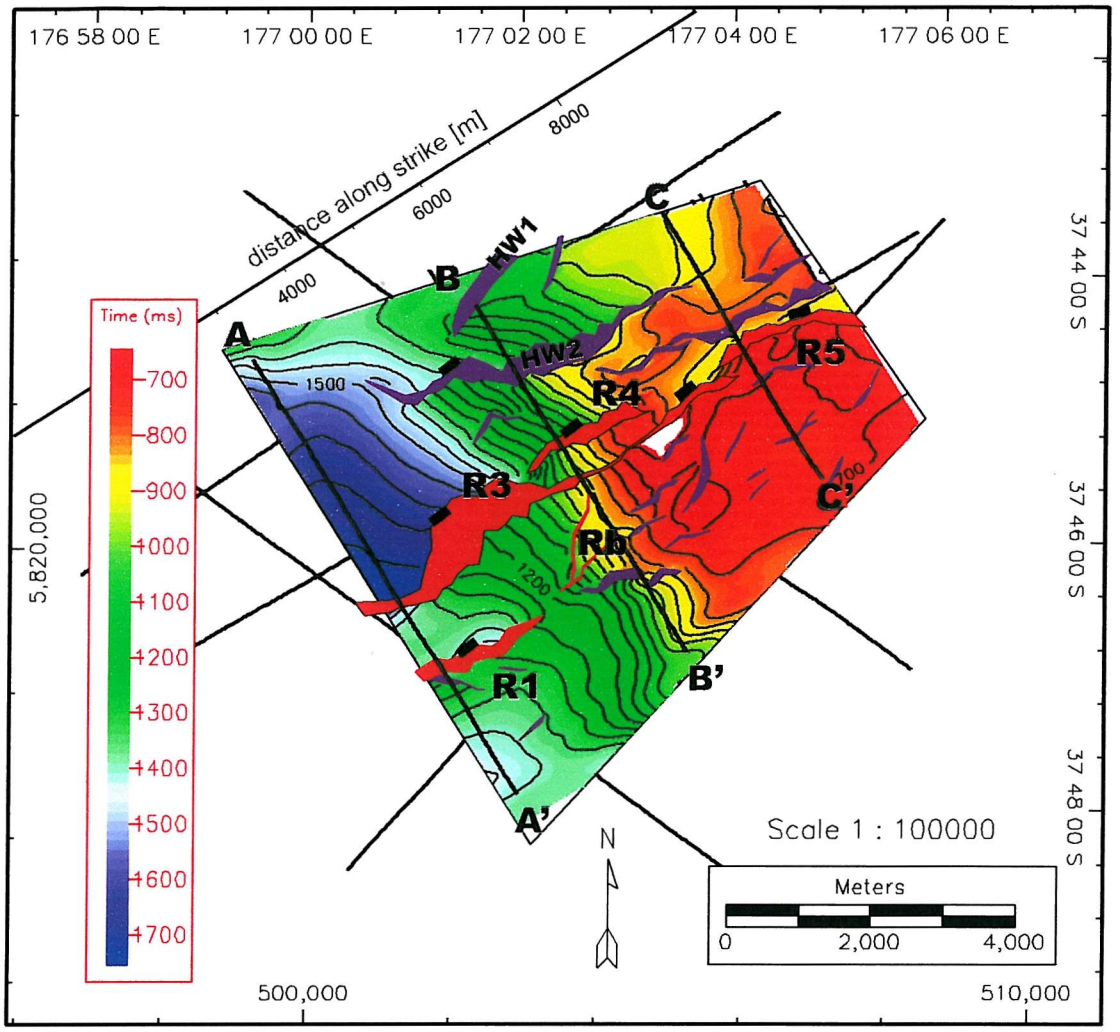

Figure 4.8: Structure map of horizon MCS3. Rangitiaki Fault segments shown in red and labelled R1- R5 and Rb. Other faults shown in purple. Profiles A-A', B-B' and C-C' refer to figure 4.1.

upwards, correlation of the small faults forming this feature is difficult.

The Rangitaiki Fault is a fully linked, segmented structure crossing the full length of the survey area on all of the horizons. The sediments lying between overlapping fault segments are rotated, this is especially evident between R4 and R5. The present day structure of the Rangitaiki Fault and the sediment architecture in its hanging-wall and footwall show its evolution from its initially isolated fault segments. The evidence for this and the fault history is described in detail in Chapter 6.

Faults in the footwall of the Rangitaiki Fault remain relatively short in length and low

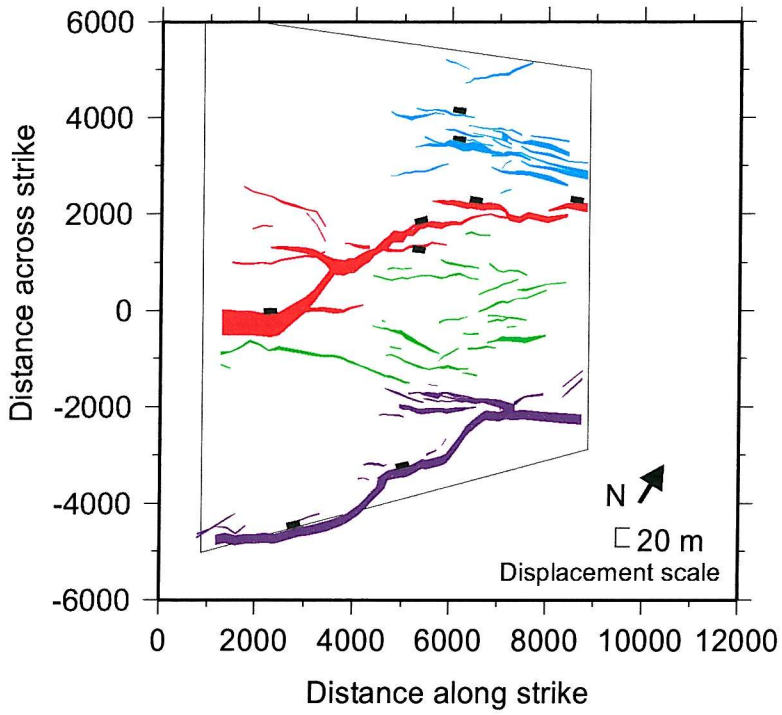

Figure 4.9: Fault displacement map for horizon HRS4 showing faults divided into: Rangitaiki Fault (red), hangingwall faults (blue), footwall faults (green) and White Island Fault (purple, see chapter 5). Thickness of fault trace shows fault displacement instead of heave.

in displacement on all of the horizons. The map of horizon HRS4 (Figure 4.5) shows that this remains the case up to the White Island fault, at least in the near surface. An exception is FW1, which at 5 km length is much longer than other faults in the footwall. Faulting is evenly distributed in the footwall area, although the extended area shown in the high-resolution survey (Figure 4.5) shows an unfaulted area between the southern limit of the pseudo-3D box and 4000 m along strike.

Faulting in the hanging-wall of the Rangitaiki Fault becomes progressively more intense northwards. Where the faults form a graben the zone of faulting is c. 1 km wide. In the south of the survey area faulting in the Rangitaiki Fault, hanging-wall is more evenly distributed across strike and has lower displacement than in the north. Progressing to the deeper horizons (MCS2 and MCS3, Figures 4.7 and 4.8) the hanging-wall graben is represented by fewer and fewer faults (Figure 4.2), with faults HW1 and HW2 become increasingly prominent.

4.5 Displacement Profiles and Descriptions of faults

4.5.1 Rangitaiki Fault Network

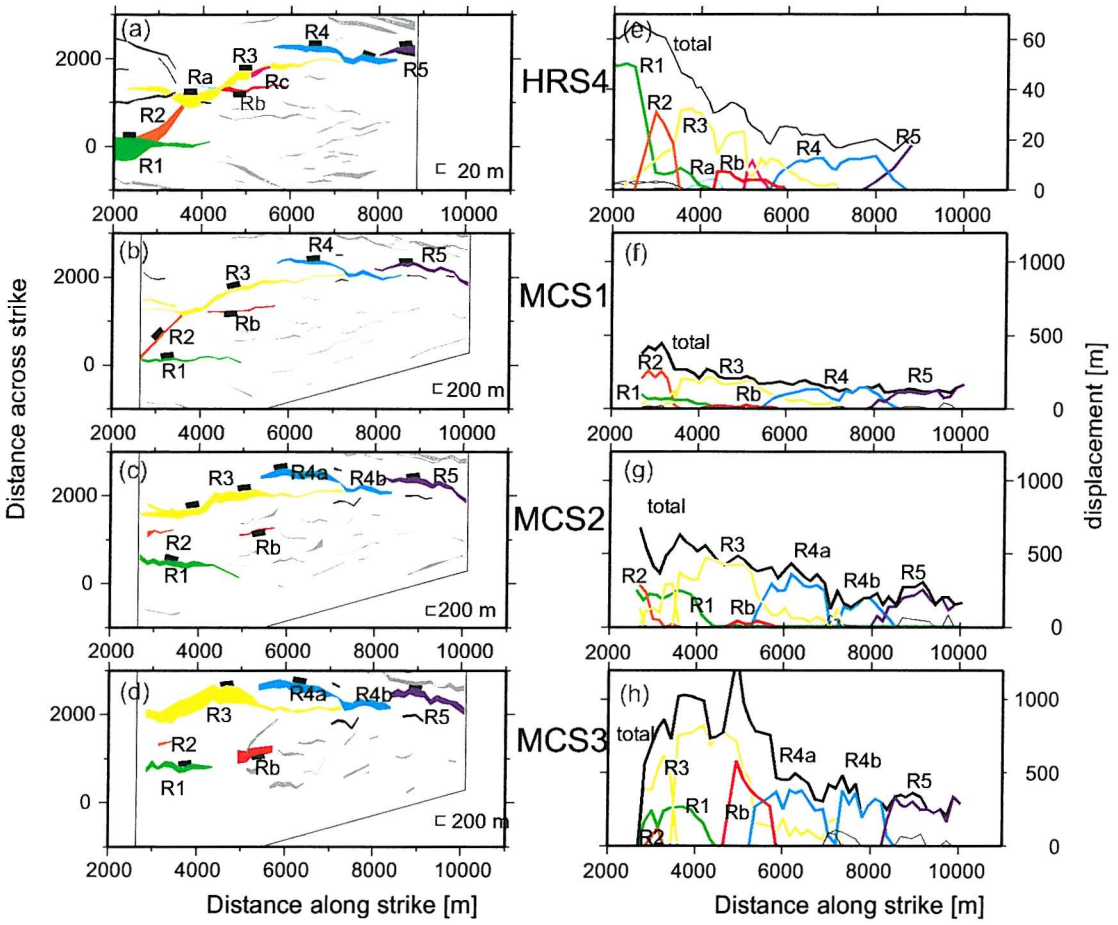

Figure 4.10: Displacement maps and profiles for the Rangitaiki Fault on all horizons (HRS4 - MCS3). Faults referred to in the text are labelled (R1-R5,Ra-Rc), minor segments of the Rangitaiki Fault are in black, faults belonging to other groups are shown in grey on the map figures. Total displacement profiles for the Rangitaiki Fault system are shown by thick black lines, the grey shadow shows the estimated uncertainty of the data. Error bars are not shown on the individual fault segments. Estimated errors are: MCS3, 44m; MCS2, 28m; MCS1, 20m; HRS4,1m.

Fault interpretations for the Rangitaiki Fault segments are shown in Figure 4.10. This figure shows the displacement in map view and as displacement profiles for horizons HRS4 – MCS3. Much of the irregularity seen in the heave of the faults is removed when looking at displacement maps (note the more regular appearance of R3 at horizon MCS3 compared with the heave map in Figure 4.8).

The Rangitaiki Fault comprises five major segments in the pseudo-3D box (labelled R1 – R5) and several other smaller faults that are physically linked to these major segments.

The development of the Rangitaiki Fault over time is discussed in more detail in chapter 6, and a summary is given here.

The maximum displacement on horizon MCS3 is c. 1000 m at 4000 m along strike (excluding the spike at 5000 m along strike). On the other horizons, the maximum displacement is found at the southern limit of the survey area, with displacement decreasing to the north. The maximum displacement lies at or close to the centre of the 21 km long, linked Rangitaiki Fault, the displacements on the composite segments are complimentary and sum to produce a profile that resembles a single, isolated fault.

The displacement gradients on individual fault segments decrease upwards: displacement on R3 reduces from 826 m to c. 150 m between 4000 to 6000 m along strike a displacement gradient of 0.3, whereas at horizon HRS4, the displacement gradient has decreased to 0.01 as the displacement reduces from 31 m at 4000 m to 12 m at 6000 m along strike.

The decrease in displacement gradient of individual fault segments is interpreted to have been caused by the development of surface ruptures of the Rangitaiki Fault through time. When horizon MCS3 formed the seabed, the Rangitaiki Fault segments were unlinked. Continued faulting on this horizon has resulted in the current displacement map where the fault segments are linked but individual segments have high displacement gradients. In contrast, when HRS4 formed the seabed the Rangitaiki Fault was already a linked structure, and the development of the fault segments with low displacement gradients reflects this.

4.5.2 Hanging-wall Faults

In horizon MCS3 the displacement profiles of faults in the hangingwall of the Rangitaiki Fault are dominated by HW2, which is the large rotational block-bounding fault seen in profile B (Figure 4.1). HW2 has a maximum displacement of 646 $\pm$ 44 m at 6300 m along strike on horizon MCS3. The dominance of this fault decreases up section, although it remains one of the larger faults right up to horizon HRS4 where it has a maximum displacement of 17 m at 6200 m along strike. Faulting in the hangingwall propagates southwards between MCS3 and MCS2, and crosses the whole survey area at horizons MCS2 and MCS1 (Figure 4.11). In the postglacial sediments (horizon HRS4) faulting ceases south of 5000 m along strike and it is only the hanging-wall graben that is active across strike of faults R4 and R5.

The low displacement between 8000 m and 9000 m along strike in MCS2 and MCS3 may be caused by under-sampling of the fault displacement, as this is the horizon where the hanging-wall graben appears and a series of antithetic faults connecting with R4 and R5. Where these faults connect there is very poor seismic quality and in places, the horizons

MCS3 and MCS2 have been faulted out of the section entirely. At MCS1 and above, the hanging-wall graben is well developed and the faults are well imaged.

4.5.3 Footwall Faults

Displacement maps and profiles for the faults in the footwall of the Rangitaiki Fault system are shown in Figure 4.12. These faults are low displacement relative to the other fault groups in the survey area (maximum displacement on MCS3 of 400 m compared with 1000 m and 600 m in the Rangitaiki Fault system and hanging-wall faults respectively).

The aggregate displacement profiles for these faults are uneven and do not look like a coherent fault. Because this fault group comprises many low displacement faults, it is

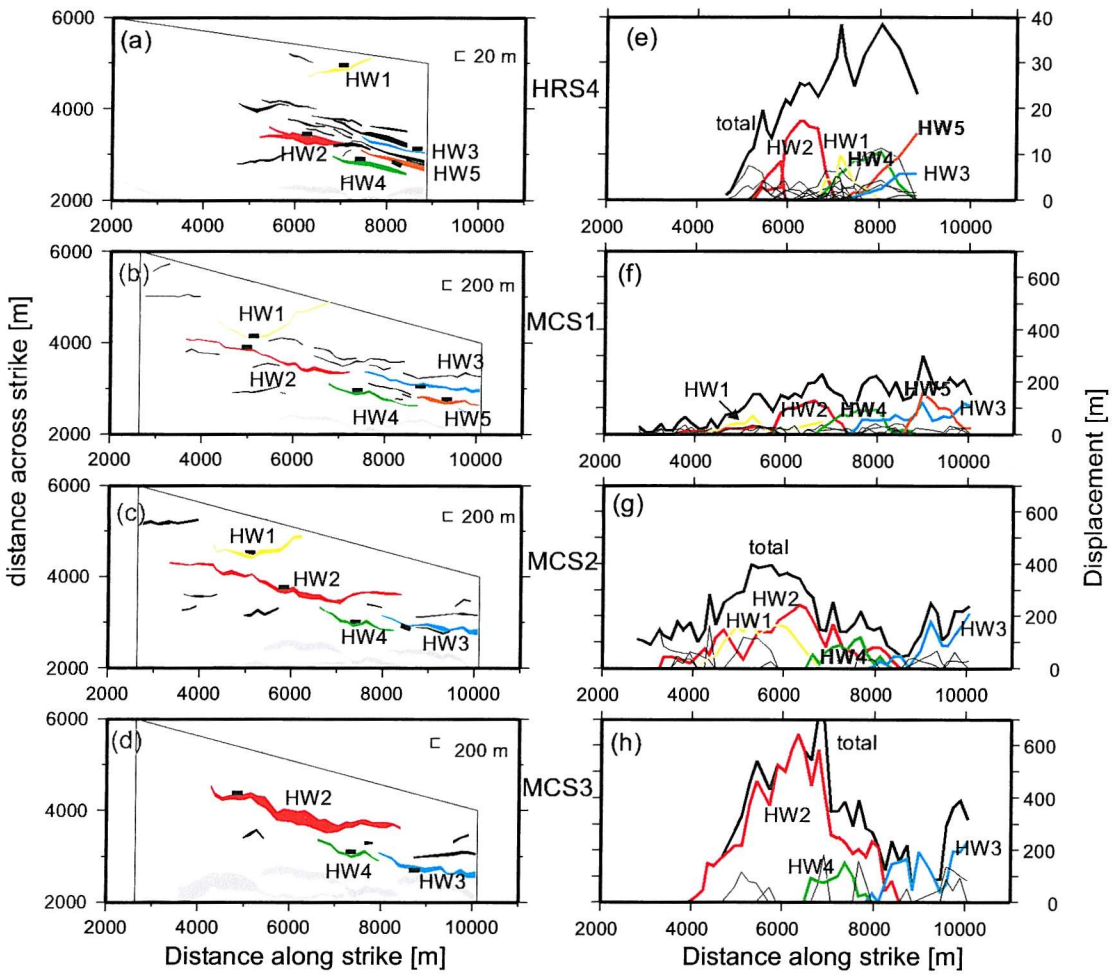

Figure 4.11: Displacement maps and profiles for the hanging-wall faults on all horizons (HRS4 - MCS3). Faults referred to in the text are labelled (HW1-HW5), minor hanging-wall faults in black, faults belonging to other fault groups in grey. Total displacement profiles are shown by thick black lines, the grey shadows show the estimated uncertainty of the data. Error bars are not shown on the individual fault segments. Estimated errors are: MCS3, 44m; MCS2, 28m; MCS1, 20m; HRS4, 1m.

likely that a greater proportion of the displacement is below seismic resolution, leading to under-sampling, particularly in the deeper horizons.

In the displacement profiles for the HRS horizons there are two larger faults (FW2 and FW3), creating two displacement maxima of c. 20 m displacement at 5000 m and at 7000 m along strike. These displacement maxima flank the splay of faults formed south of a bend in the White Island Fault (Figure 4.9). The longest of the footwall faults (FW1) is at least 3 km long at HRS4 and runs between the Rangitaiki Fault and White Island Fault systems.

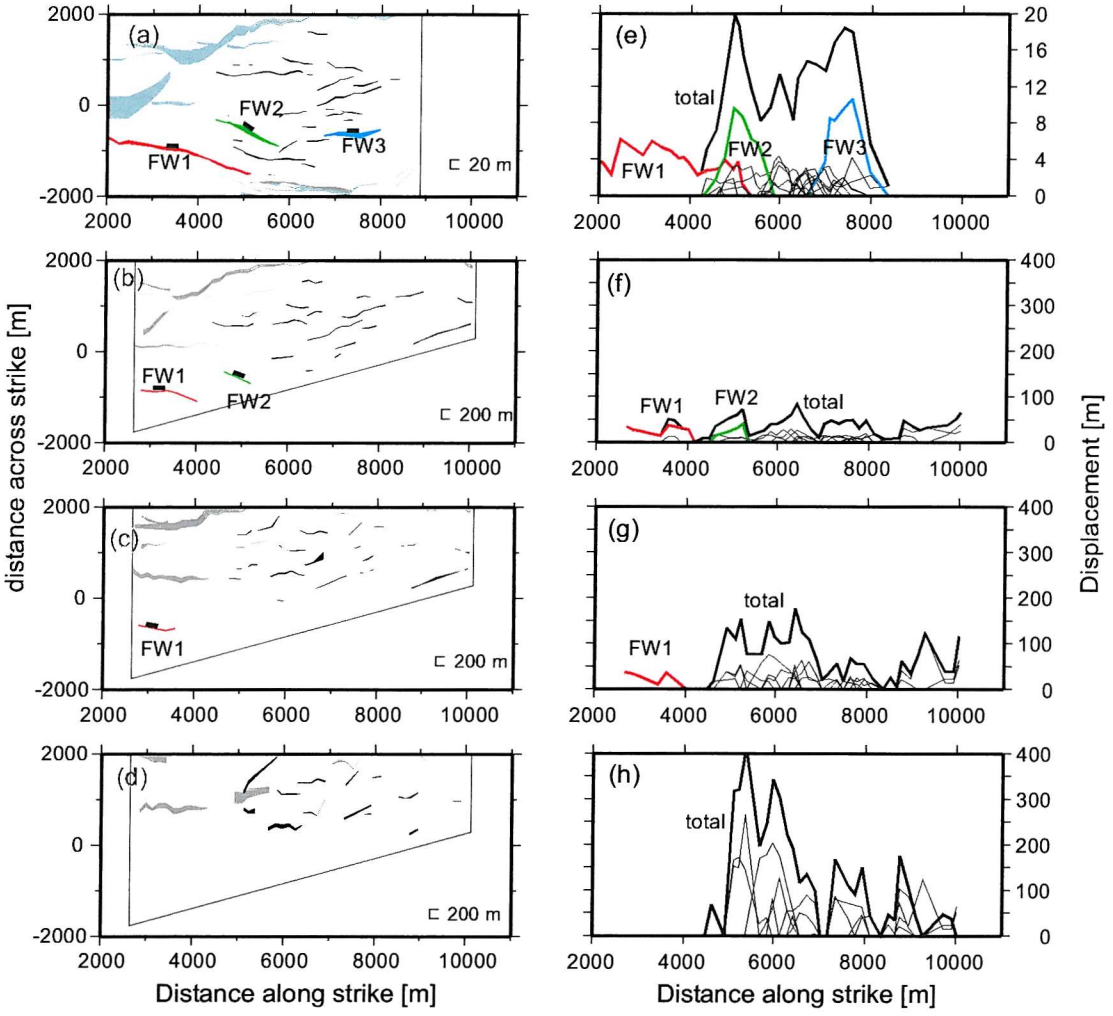

Figure 4.12: Displacement maps and profiles for the footwall faults on all horizons (HRS4 - MCS3). Faults referred to in the text are labelled (FW1-FW3), minor footwall faults in black, faults belonging to other fault groups in grey. Total displacement profiles are shown by thick black lines, the grey shadows show the estimated uncertainty of the data. Error bars are not shown on the individual fault segments. Estimated errors are: MCS3, 44m; MCS2, 28m; MCS1, 20m; HRS4, 1m.

4.5.4 Aggregate Displacement Profiles for Faults in the Pseudo-3D Survey Area

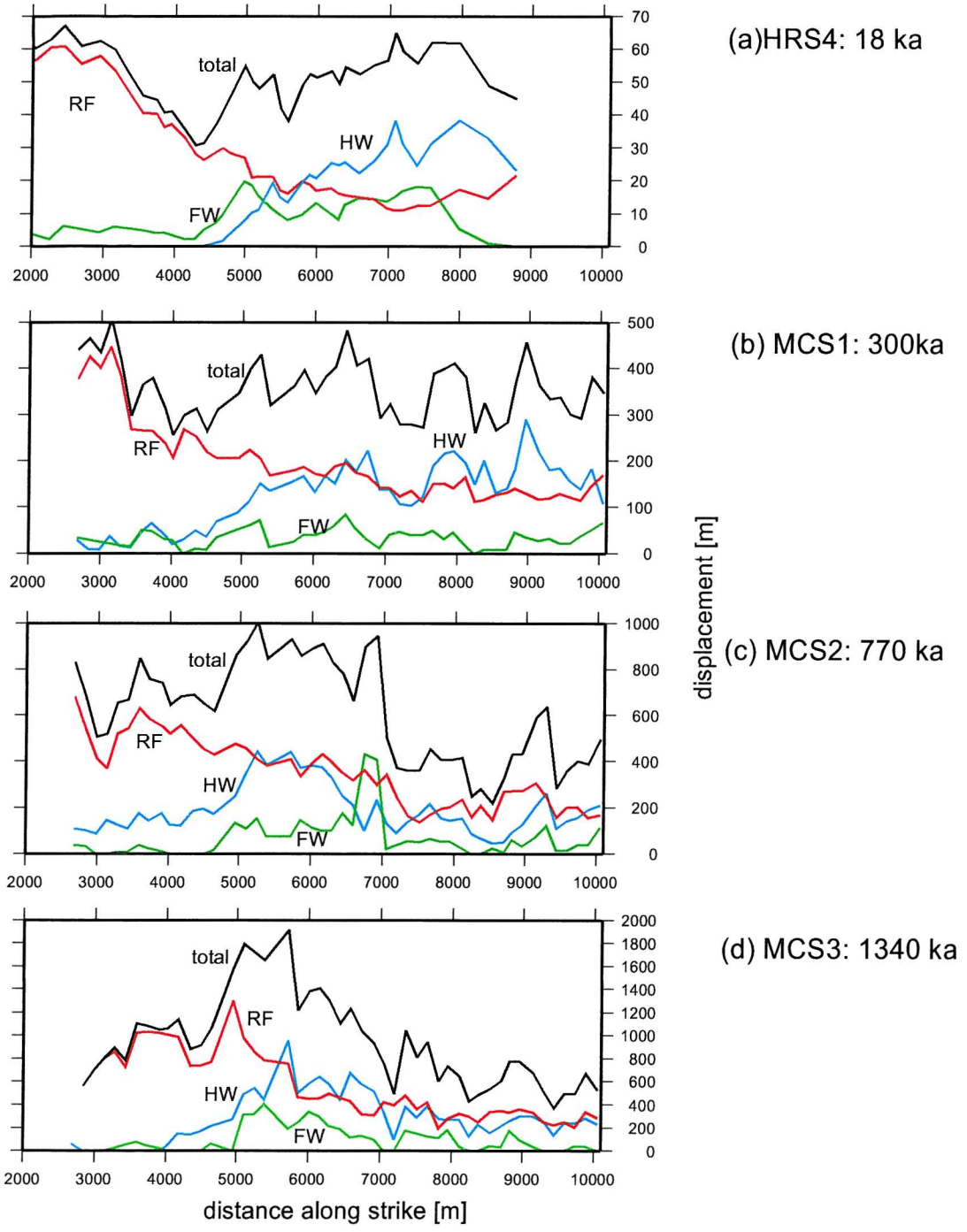

Figure 4.13: Aggregate displacement profiles for horizons HRS4 (a) to MCS3 (d). Total displacement summed across strike (black line) with estimated uncertainty range (hatching), Rangitaiki Fault system (RF) red; hanging-wall faults (HW) blue; and footwall faults (FW) green.

Figure 4.13 shows the aggregate displacement profiles for the three fault groups as well as the aggregate profile for all of the faults in the area. Across all of the horizons, the displacement on the Rangitaiki Fault decreases to the north. On horizons MCS1 and HRS4 the displacement on the hangingwall faults increases northwards, and the sum of displacements across the Rangitaiki Fault and hanging-wall faults produces a roughly even displacement profile across the survey area. In horizons MCS2 and MCS3 however, the observed displacement does not increase northwards on the hanging-wall faults, with the effect that the total displacement decreases northwards on these horizons.

The high proportion of displacement taken up on low displacement, poorly imaged faults results in the total displacement on the hanging-wall faults being under-sampled on MCS2 and MCS3 (note the c. 500 m drop in total displacement at 7000 m along strike in Figure 4.13c). Where the structure remains simple and there are fewer, larger faults (e.g. the Rangitaiki Fault and hanging-wall faults north of 7000 m along strike) the under-sampling of displacement does not occur. Results reliant on displacement measurements on hanging-wall faults north of 7000 m along strike are therefore not reliable. Because of this, mean displacement rates (see section 6 below and figure 4.14) are calculated over the strike range 3000 – 7000 m where the displacements are more accurately known.

4.6 Displacement Rates

Displacement rates are calculated for the intervals between the interpreted horizons by taking the difference in displacement and dividing by the length of time between the horizons. Rates are calculated for each of the aggregate displacement profiles for the fault groups and the total displacement profile (Figure 4.14). The displacement rate of the Rangitaiki Fault from 18 ka to the present decreases northwards from maximum value of 3.4 ± 0.2 mm yr^{-1} at 2447 m to a minimum of 0.6 ± 0.1 $mmyr^{-1}$ at 7000 m along strike. The displacement rate profile for the hanging-wall faults is broadly complimentary to this trend, as here the rate increases northwards from zero at 4500 m along strike up to a maximum of 2.1 ± 0.1 $mmyr^{-1}$. The displacement rates of the footwall faults remains below 0.4 $mmyr^{-1}$ south of 4500 m along strike, northwards the rate increases to a maximum value of 1.1 ± 0.1 $mmyr^{-1}$ at 5000 m along strike. The displacement rates of the three fault groups are broadly complimentary, resulting in displacement rates being similar across the survey area, with the exception of a 1 – 2 km wide displacement rate low centred on 4400 m along strike. This feature is discussed in more detail in chapter 5.

The displacement rates for the preceding time period (300 – 18 ka, Figure 4.14b) shows

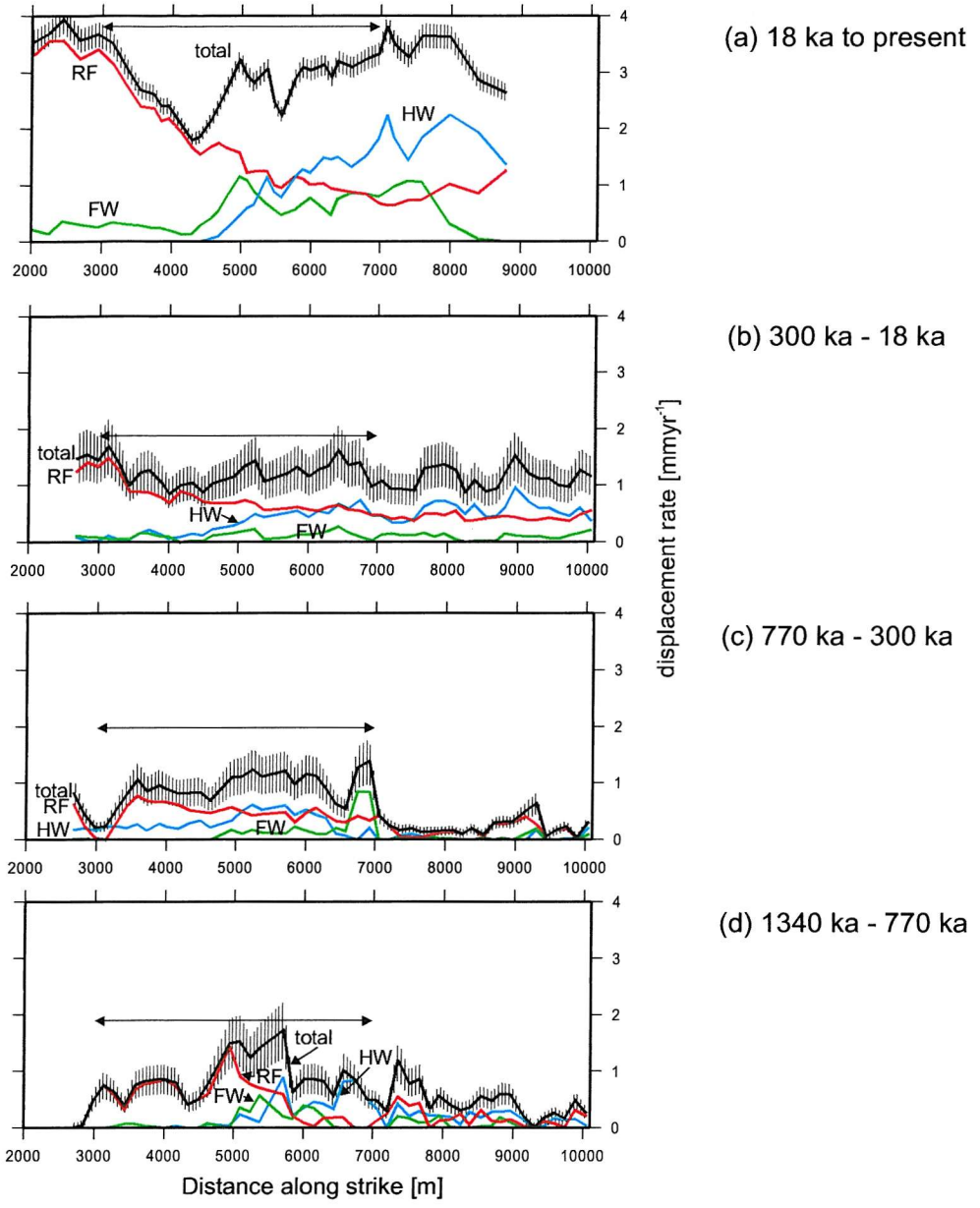

Figure 4.14: Displacement rate profiles for time intervals 18 ka to present (a), 300 ka to 18 ka (b), 770 ka to 300 ka (c) and 770 ka to 1340 ka (d). Total displacement rate summed across strike (black line) with estimated uncertainty range (hatching), Rangitaiki Fault system (RF), red; hanging-wall faults (HW), blue; and footwall faults (FW), green. Double headed arrow shows where faults are well sampled in horizons MCS2 and MCS3.

similar features, although the displacement rates are lower. The displacement rate for the Rangitaiki Fault decreases northwards from 1.5 ± 0.4 mmyr^{-1} at 3131 m to a minimum of 0.4 ± 0.1 mmyr^{-1}. Displacement rates of the hanging-wall faults increase northwards from negligibly small values in the south (where the calculated result is smaller than the calculated uncertainty) to a maximum of 1.0 ± 0.3 mmyr^{-1} at 9000 m along strike. The

total displacement rate for this time period is variable along strike, but does not show the large decrease in displacement rate at 4400 m along strike seen between 18 ka and the present.

The displacement rate profiles for 1340 – 770 ka and 770 – 300 ka are less regular for two reasons. Firstly, the under-sampling of the hanging-wall faults described above section 5.2) means the displacement rates for these faults are not resolved accurately north of 7000 m along strike. Secondly, during this time the segments of the Rangitaiki Fault were unlinked and propagating laterally, and did not cover the full length of the survey area (see chapter 6).

The average displacement rates for the entire fault system were determined by summing the aggregate strike projected displacement rates and dividing by the number of observations (line crossings) (chapter 3). Using average is useful because of the variability in displacement rates, particularly in the earlier time periods when the Rangitaiki Fault was unlinked. As noted above, the displacement of the hangingwall faults is under-sampled north of 7000 m along strike in horizons HRS2 and HRS3, so mean displacement rates calculated between 3000 and 7000 m along strike are likely to be more representative of the rates than across the whole survey area. Table 2 shows the mean displacement rates calculated for each time interval across the whole survey area and for the strike distance between 3000 and 7000 m.

The displacement rates calculated in the limited range (between 3000 m and 7000 m along strike) are generally larger than rates calculated using the full survey for the time intervals that rely on data from horizons MCS2 and MCS3 (1340 – 770 ka and 770 – 300 ka). At MCS1 the same average displacement rate of 1.2 $\pm$ 0.4 mmyr^{-1} is recorded over both lengths. At HRS4 the displacement rate found between 3000 and 7000 m along strike is lower than the average rate for the whole survey area.

The displacement rates for all the faults in the survey area show a three-fold increase from 0.9 $\pm$ 0.3 mmyr^{-1} in the time interval 1340 – 300 ka, to 2.6 $\pm$ 0.2 mmyr^{-1} in the time interval 17 ka to present. This displacement rate increase is similar to the increase seen on the Rangitaiki Fault alone, showing that the Rangitaiki Fault has not increased its activity through localisation of strain reducing the activity of neighbouring faults.

4.7 Fault Populations

Fault populations are often described as having a power law size-frequency distribution (e.g. Scholz and Cowie, 1990; Yielding et al., 1992; Pickering et al., 1996; Hunsdale and Sanderson, 1998), where the number N of faults having size greater than or equal to S

	Mean – whole survey distance [mmyr^{-1}]	Mean – 3000 - 7000 m strike distance [mmyr^{-1}]	Mean – Rangitaiki Fault only [mmyr^{-1}]
1340 – 770 ka MCS3 – MCS2	0.7 ± 0.2	0.9 ± 0.3	0.5 ± 0.2
770 – 300 ka MCS2 – MCS1	0.6 ± 0.2	0.9 ± 0.3	0.5 ± 0.2
300 – 17 ka MCS1 – HRS4	1.2 ± 0.4	1.2 ± 0.4	0.8 ± 0.2
17ka – present HRS4 – seabed	3.1 ± 0.2	2.6 ± 0.2	1.4 ± 0.3

Table 4.2: Mean displacement rates in the pseudo-3D survey area from 1340 ka to present.

(either length or maximum displacement) is given by

$$N = cS^{-D} \tag{4.1}$$

Here c is a constant related to the size of the sample, and higher magnitudes of the power law exponent D imply a greater proportion of smaller faults. A power-law distribution theoretically extends over an infinite scale range, so a scale-limited sample may be used to predict the number and magnitude of similar features at other scales, which can be used to estimate total strain (e.g. Scholz and Cowie 1990, Walsh et al. 1991, Jackson and Sanderson 1992, Marrett and Allmendinger, 1992) or predict the impact of sub-seismic faults on hydrocarbon production (e.g. Heffer and Bevan 1990, Yielding et al. 1992, Gauthier and Lake 1993). However, in sampling only a limited range of the distribution, the power-law relationship may not be properly defined (Pickering et al, 1995) or a change in scaling properties may be missed (Hunsdale and Sanderson 1998).

The scale invariance is limited at the small scale because of tensile fractures (Pickering et al., 1996) and the particulate nature of rock (Walsh and Watterson, 1992) and at the large scale by the distinction between intra-crust and crust-spanning faults (Marrett and Allmendinger, 1991, Pacheo et al. 1992, Westaway, 1994). Hunsdale and Sanderson (1998) identify a change in the scaling relationship of faults. Small faults are controlled to some extent by the lithological character of the fracturing rock, whereas larger faults become independent of lithological controls and conform to a different scaling relationship. They found larger faults (>2 m displacement) have a higher D value than smaller faults. Such changes in scale will lead to inaccurate estimates of strain when extrapolating power-law relationships. Extrapolations may be tested using core data to identify numbers of millimetre scale faults within a fault population (e.g. Yielding et al., 1992).

4.7.1 Censoring and Truncation

If the scale range of the sample is less than that of the population as a whole then the sample is truncated. A sample is censored when some or all of the values within it are systematically under-estimated. Any fault that lies only partially within the survey area will be censored, as the measured length will be below the actual length.

Left hand truncation (LHT) is caused by a lower limit to the resolution, often due to the sampling method, for example the limit of resolution on a seismic section due to the band-width of the seismic signal (Pickering et al. 1996), or as in this case, the spatial sampling of the pseudo-3D grid. There is often a loss of data as this limit is approached, as the seismic resolution will depend in practice on the noise level, and the spatial sampling resolution will depend on how close to the sample points the truncated faults reach (any fault could cross a line, but the smaller they are the more likely they are to tip out between lines).

The LHT fall-off appears as a decrease in gradient at the left-hand end of a cumulative frequency graph and results in an under-estimate of D. If these data are excluded from the analysis the D value will not require any correction (Pickering et al., 1996).

Right hand truncation (RHT) is caused by exclusion of large faults from the sample. This may be because the fault is too large to be recorded properly and so partially lies outside the survey area, or because the large faults are few in number and have a low probability of being sampled.

Deviation from the power-law distribution can occur at the large scale because of the finite range effect. If the largest faults are omitted from a sample the right-hand end of a cumulative frequency plot becomes distorted and increases in gradient, leading to an over-estimate of D. A correction for this effect can be applied where the number of missing large faults is estimated, providing the sample size is large enough for the number of missing large faults to be a small proportion of the true number of faults. Pickering et al. (1995) have outlined the full methodology and derivation of this process. The sample size of faults within the pseudo-3D survey area was too small for the approximation to hold, and the correction could not be applied to the data presented here.

4.7.2 Methods of analysis

Power law distributions may be defined by the cumulative frequency function (e.g. Childs et al., 1990, Walsh et al.,1991 and Jackson and Sanderson, 1992), the discrete frequency distribution (e.g. Kakimi, 1980, Heffer and Bevan, 1990) or the discrete frequency of log S (e.g. Gutenberg and Richter, 1954, Pickering et al, 1995).

Cumulative Frequency Method

Taking logs of equation 4.1 gives $log\mathbf{N} = log\mathbf{c}$ - D $log\mathbf{S}$, which defines a linear relationship between log **N** and log**S** with gradient -D. Displayed graphically, the effects of censoring and truncation on the linear relationship are easily detected as a deviation from the straight line. Figures 4.15 and 4.16 respectively show cumulative frequency plots for fault lengths and displacements on the MCS horizons within the pseudo-3D survey area. Least-squares best-fit straight lines are shown for the central sections of the distributions avoiding the edges of the distribution affected by LHT fall-off and RHT finite range effect. The limit of seismic resolution causes smaller faults to be under-sampled resulting in LHT fall-off on both the length and displacement distributions. This effect is more pronounced on the deeper horizons where the seismic signal has lower frequency. At the larger scale, the spatial limits of the survey area mean that long faults are missed or only partially included in the survey area. Rather than omitting partial faults or including the full length of partial faults, the population is best represented by including the section of the partial fault that lies in the survey area (Yielding et al, 1996). The length distributions on the four horizons are shown in Figure 4.15. The lengths of faults are poorly represented on deep horizons because low displacements near fault tips fall below the seismic resolution at higher values, leading to an under-estimate of the fault length. Measurement of fault length is limited by the 150 m profile separation in the pseudo-3D survey area and by the detection limit of small displacements near fault tips. The distribution shown is for minimum length of the faults, which for each fault excludes a possible extra 300 m if the observed tips are close to, but not crossing the adjacent lines. Faults of up to 300 m in length may only cross one profile; these faults are excluded from the distribution because they have no measurable length. The shorter the fault, the truncation due to the lateral sampling distance is proportionally greater, leading to curvature of the left hand end of the distribution. The power-law exponents (-D) for each distribution are shown in table 3, and range between -0.97 and -1.12. The displacement distributions (Figure 4.16) show that displacement progressively decreases from MCS3 to MCS1 (the corresponding lines on the graphs progress to the left). The minimum measured displacement on each horizon decreases upwards from 35 m at MCS3 to 1 m at HRS4 as the detection limit improves. D values for the displacement distributions ranging between 0.71 to 0.95 are observed on the four horizons. The displacement distributions observed on the two upper horizons (MCS1 and HRS4) show two sections to the curve separated by a cusp (point B at 45 m displacement, Figure 4.16b: point C at 4.5 m displacement, Figure 4.16a).

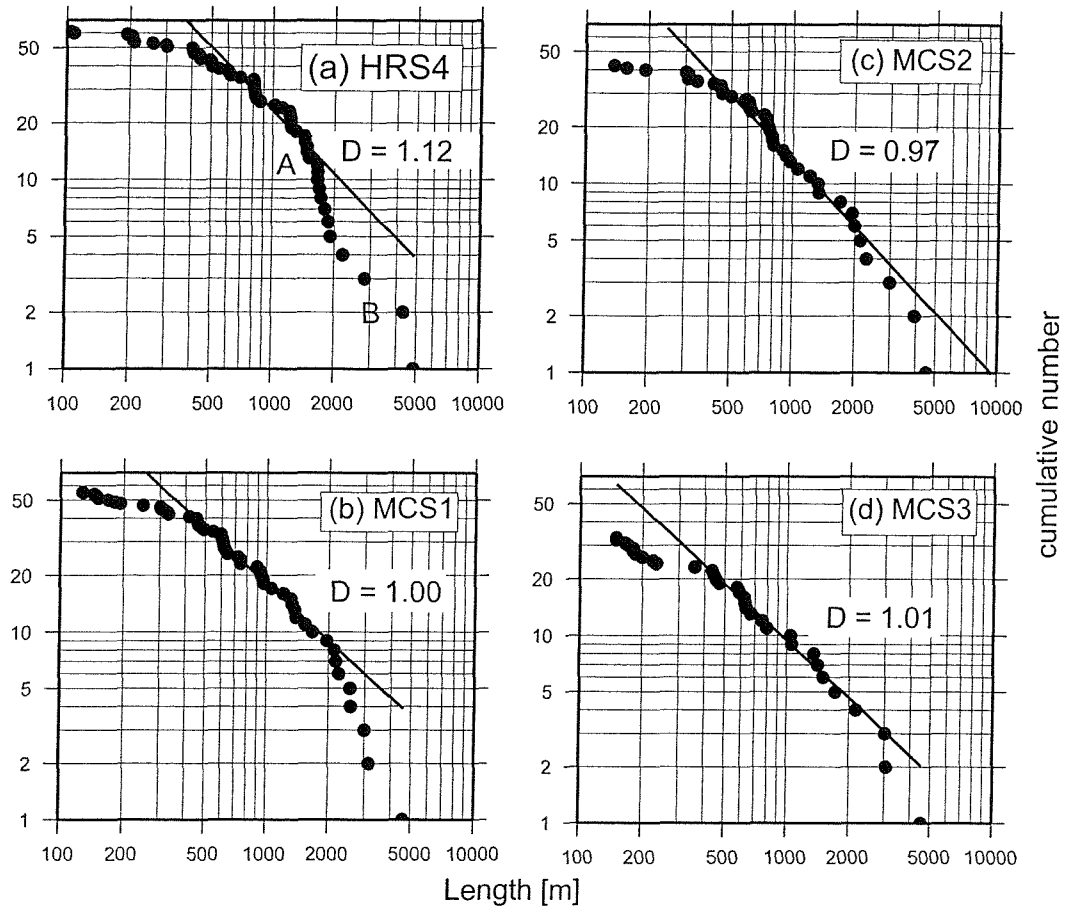

Figure 4.15: Length cumulative frequency distribution for horizons HRS4 (a) to MCS3 (d). 'Best fit' straight lines and corresponding D values are shown on each graph.

The faults that lie in the right-hand section of the distribution are the main segments of the Rangitaiki Fault (R1 -R5) and faults HW1-HW5 (see displacement-length distribution section below); these faults are the major basement faults that have propagated up to the surface. The cusp in the displacement distribution may be related to the evolution of the fault network. The Rangitaiki Fault became a linked structure between 300 and 18 ka with an increased displacement rate relative to the isolated fault segments (Chapter 6). The fault displacements measured on MCS1 have largely been since the fault linked, but for MCS2 and MCS3 proportionally more of the displacements were accumulated on unlinked fault segments.

The break in slope seen in the displacement distribution is not present in the length

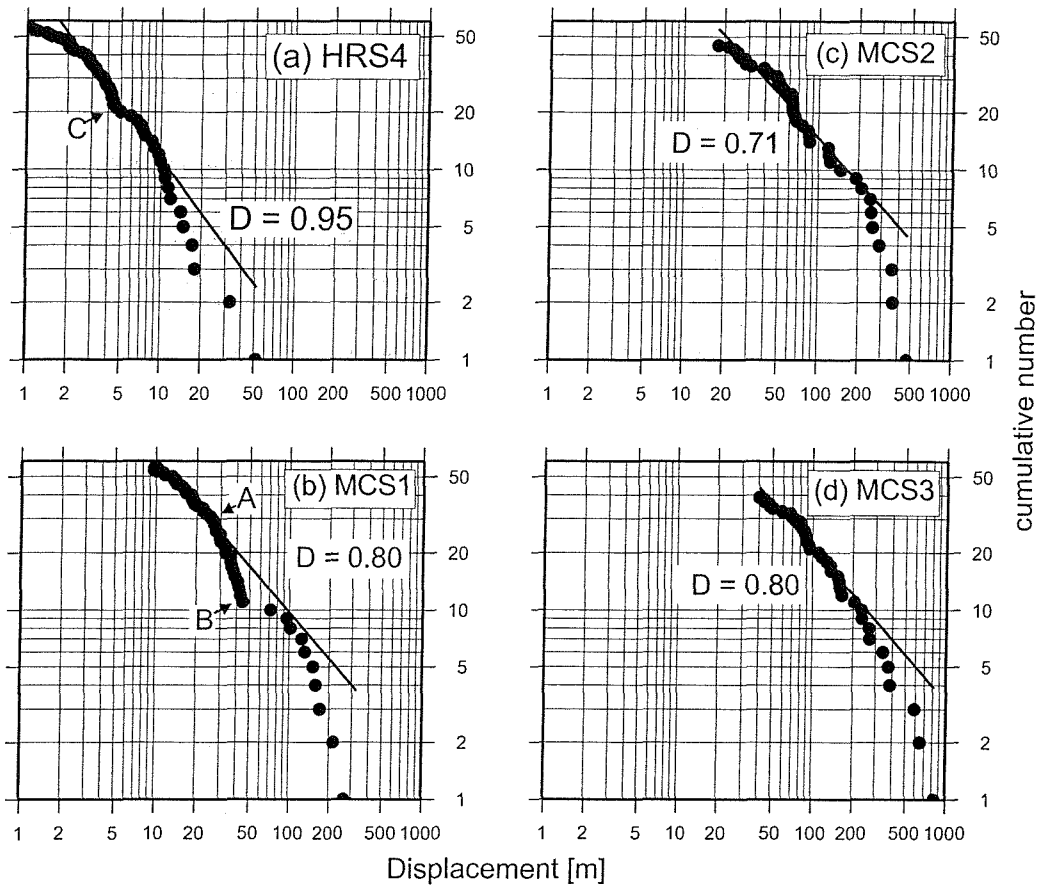

Figure 4.16: Displacement cumulative frequency distribution for horizons HRS4 (a) to MCS3 (d). 'Best fit' straight lines and corresponding D values are shown on each graph.

distribution. The large faults (lying to the right of point B on Figure 4.16b), once linked, do not propagate laterally. If the break in slope is a result of fault linkage and the largest faults have their lengths fixed at the time of linkage then the length distribution ought to show fewer than expected long faults. This effect may be visible in the fault length distribution on HRS4 where there is a convex section of the distribution between points A and B (Figure 4.15a).

Discrete Frequency Method

The data are binned into intervals of equal size and the number in each interval is plotted against the interval midpoint using log scales. The bin intervals may either be of equal size on a linear scale or on a logarithmic scale. The log-interval method means that there

are larger bins for the larger faults which are fewer in number, so the data are spread more evenly through the intervals. This method is unaffected by the finite range effect, but intervals covering the truncations may be only partially filled and should be excluded.

The results presented here are displayed using the log-interval method (Pickering et al., 1995), described by $log\ \mathbf{n}_{lg} = c\ -D\ log\ \mathbf{S}$ where n_{lg} is the frequency of values in an interval $log\ \mathbf{u} \pm \delta\ (log\ \mathbf{u})$. The results are shown for the length and displacement distributions in Figures 4.17 and 4.18, and the resulting D values are summarised in Table 4.3. The sample size is too small to be able to have a useful number of data bins and ensure that none of them are empty or partially filled; this is particularly noticeable in the displacement distribution where there are only five points on the graphs for the MCS horizons. The length distribution gave D values ranging from -0.70 to -1.19. The most well defined straight-line segment was found on horizon MCS1, containing five points and giving the lowest D value of -0.70. Variations in the value of D are considered to be a result of the small sample size, and little weight is given to these results.

	displacement	distribution	length	distribution
	Cumulative Frequency	Discrete Frequency	Cumulative Frequency	Discrete Frequency
HRS4	-0.95	-0.53	-1.12	-0.81
MCS1	-0.80	-0.93	-1.00	-0.70
MCS2	-0.71	-0.87	-0.97	-1.19
MCS3	-0.80	-0.70	-1.01	-0.83

Table 4.3: Power Law exponents for fault displacement and length distributions using cumulative and discrete frequency methods

4.7.3 Displacement/Length Distribution

Figures 4.19a shows the displacement of faults at horizon MCS1 plotted against their length including information from the regional survey lines that allows the full length and maximum observed displacements of faults R1, R5 and HW5 to be shown. The locations of these faults are shown in Figure 4.19b. This figure shows most of the faults lying below c. 2000 m length and below 50 m displacement, with ten faults having displacement between c 50 and 250 m and lengths of c. 1000 to 10000 m. The largest displacement is observed on the relatively short transfer fault R2 (indicated with a blue symbol on figure 4.19a), which lies at the centre of the linked Rangitaiki Fault system and is linked at both tips to faults R1 and R3. This fault was formed as a result of the breakdown of a relay between faults R1 and R3 (Chapter 6). The length distribution of the large (higher than 50 m displacement) faults overlaps the length range of the small (< 50 m displacement) faults and shows a weak

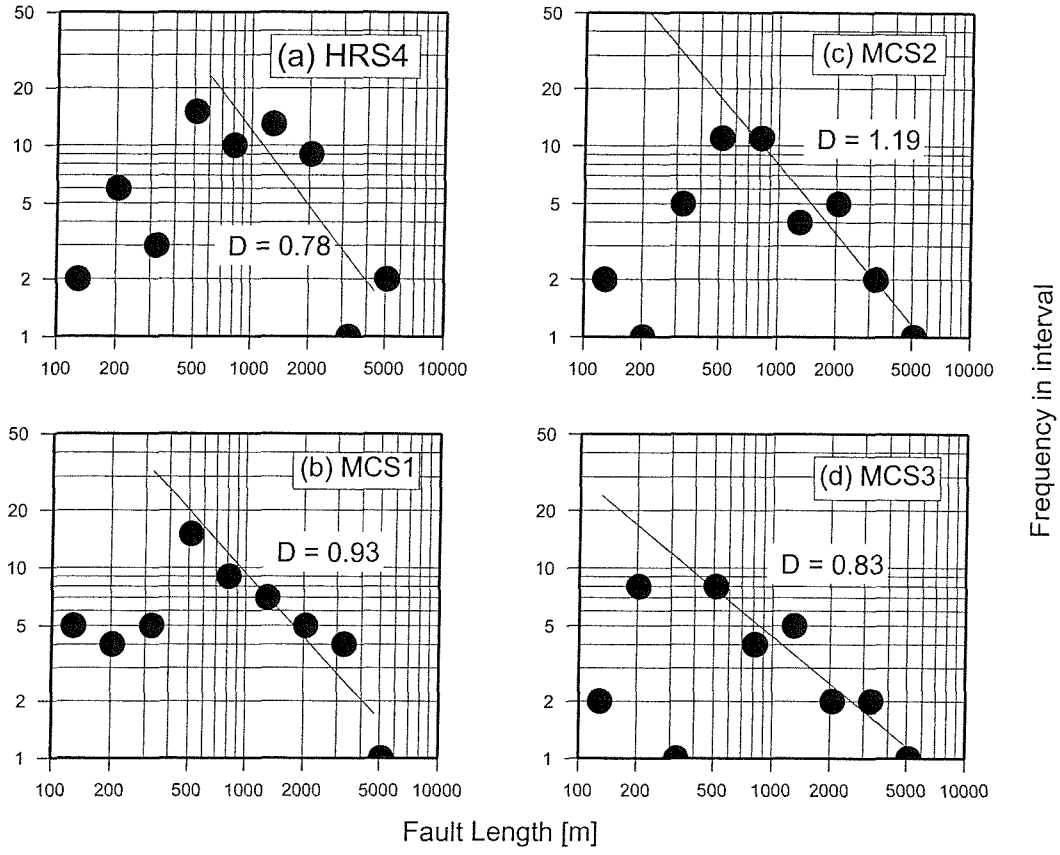

Figure 4.17: Length discrete frequency distribution for horizons HRS4 (a) to MCS3 (d). 'Best fit' straight lines and corresponding D values are shown on each graph.

positive correlation between fault displacement and length.

4.8 Dips of Faults

Measurements of fault dip are made on every pair of upthrown and downthrown depth converted fault picks in the MCS data. The mean dip of each fault is then calculated, and these values are shown in Figure 4.20. These results show an average 8° flattening of the fault plane between horizon MCS1 (mean dip 67°) and MCS3 (mean dip 59°). On average, the Rangitaiki Fault is shallower dipping than the smaller faults in its hanging-wall and footwall. The Rangitaiki Fault dips at 61° between MCS1 and MCS3, whereas the hanging-wall and footwall faults dip at 65° and 68° respectively.

The heave (horizontal component of displacement) of the faults in the high-resolution seismic profiles was below the resolution of the data, and the faults were assumed to be

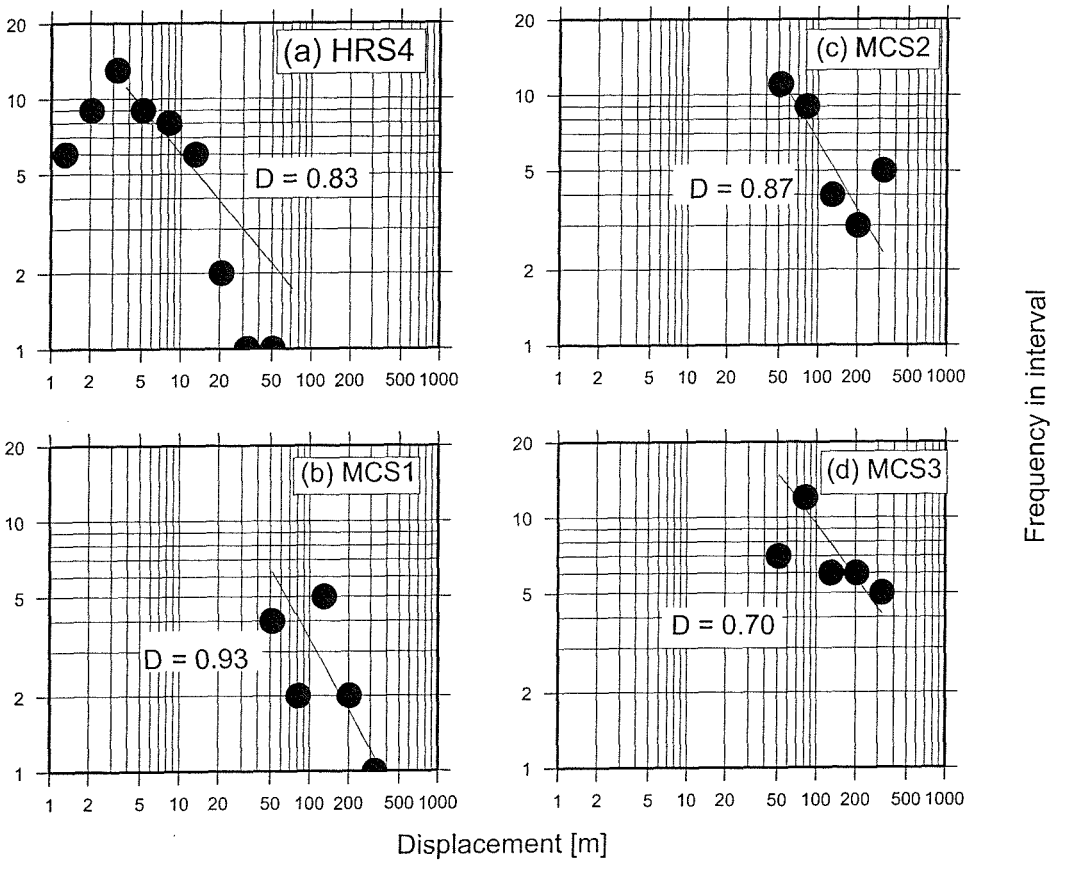

Figure 4.18: Displacement discrete frequency distribution for horizons HRS4 (a) to MCS3 (d). 'Best fit' straight lines and corresponding D values are shown on each graph.

vertical, although dips down to c. 70° may be possible. Geological mapping of faults within the onshore Whakatane Graben support the interpretation of these faults as vertical or near-vertical features (Nairn and Beanland, 1989).

4.9 Orientations of Faults

	HRS4	MCS1	MCS2	MCS3
All	62	57	55	54
HW	66	63	58	55
RF	58	57	60	66
FW	58	51	50	49

Table 4.4: Mean strike orientations for the fault groups

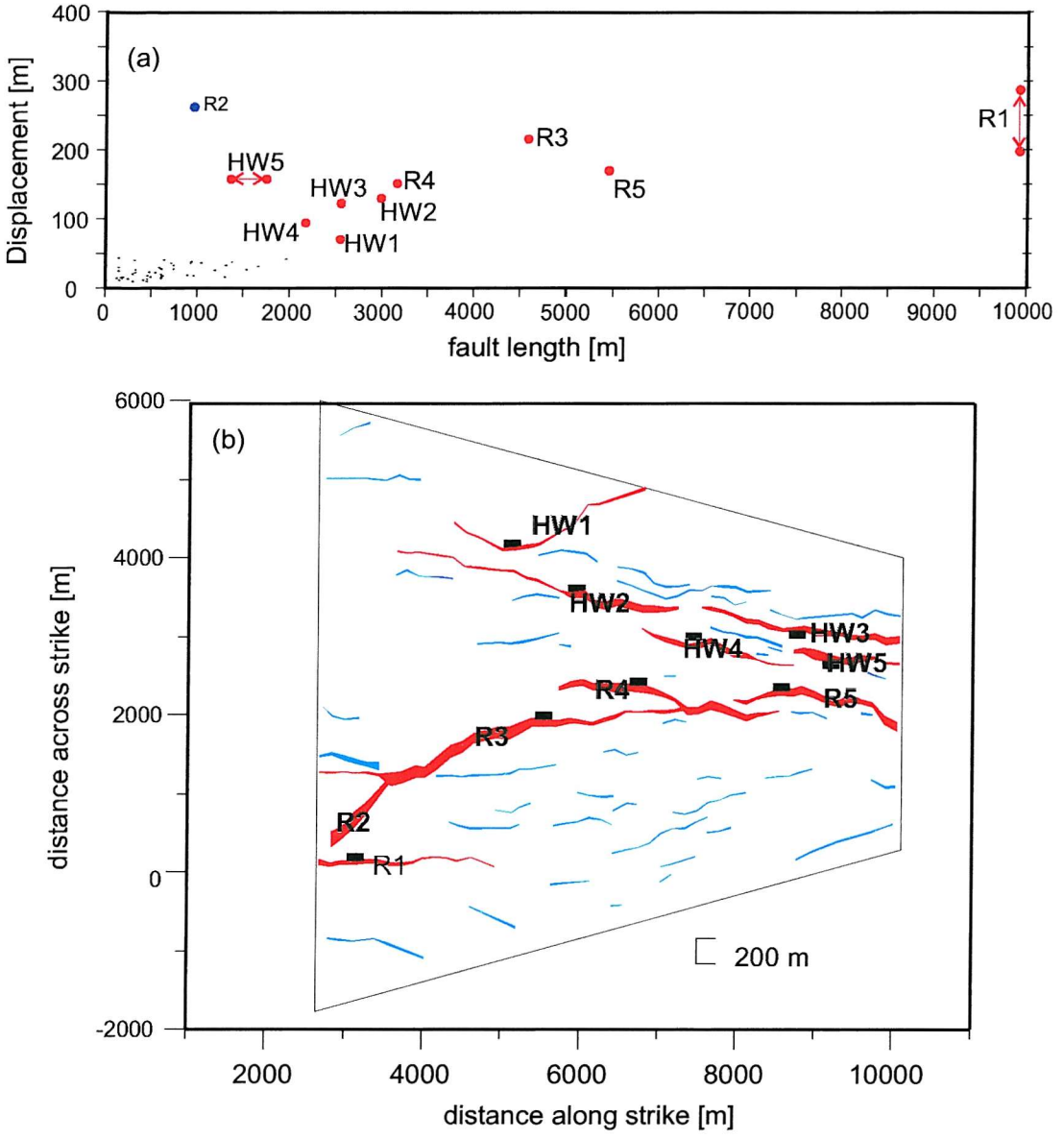

Figure 4.19: (a) Fault displacement plotted against length for horizon MCS1. Points for large faults are in red and labelled. Where results are uncertain a range of values is indicated. (b) Fault displacement map for horizon MCS1. Large faults from (a) are plotted in red and labelled.

Fault strike is calculated using a least squares best fit straight line through the fault contact points for each fault on each horizon. Rose plots showing the spread of strike measurements are shown in Figure 4.21 and a summary of mean strike values for the fault groups (Dips of Rangitaiki Fault segments (RF), fault in the hanging-wall (HW) and faults in the footwall (FW) as well as the mean dip angle for all the faults) is shown in Table 4.4.

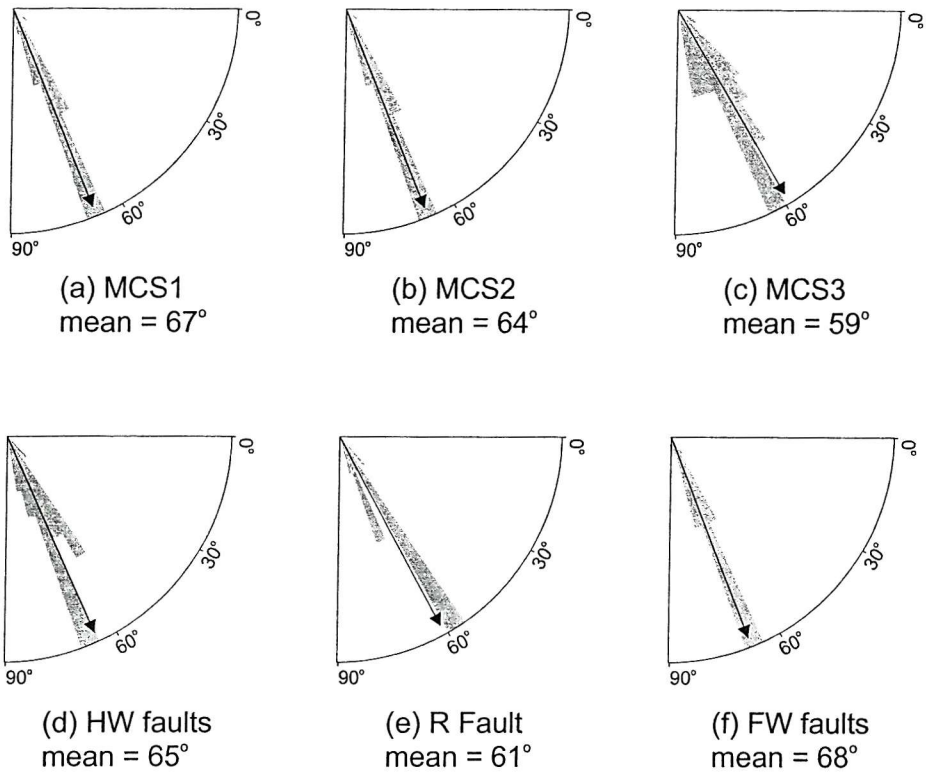

Figure 4.20: Fault dips calculated for multichannel seismic data. a - c: all faults crossing horizons MCS1 - MCS3. d - f: average dip of faults in hanging-wall (HW), Rangitaiki fault system (RF) and footwall (FW).

The measured strike of the Rangitaiki Fault in horizon MCS3 is an unexpected orientation, caused in part by the variable displacement of the fault. Near the centre of the Rangitaiki Fault there has been more displacement, and consequently the horizons are deeper and the points of measurement have moved further along the dipping fault plane than in the north of the survey area, causing an apparent clockwise rotation of the data (increasing the value of strike). The strike values found for MCS1 and HRS4 of 57° and 58° are more representative of the true strike of the faults.

The strike of the hanging-wall faults rotates from an average of 55° - 58° at MCS3 and MCS2 respectively, to 66° at HRS4. In the deeper horizons, the fault deformation is dominated by the large basement faults HW1 and HW2 that have similar strike to the Rangitaiki Fault. In contrast, the faulting in higher horizons is dominated by the hanging-wall graben. Many of these faults are limited to the upper c. 500 ms two-way time and are not as influenced by the basement trends of the TVZ, and as a result perpendicular to the

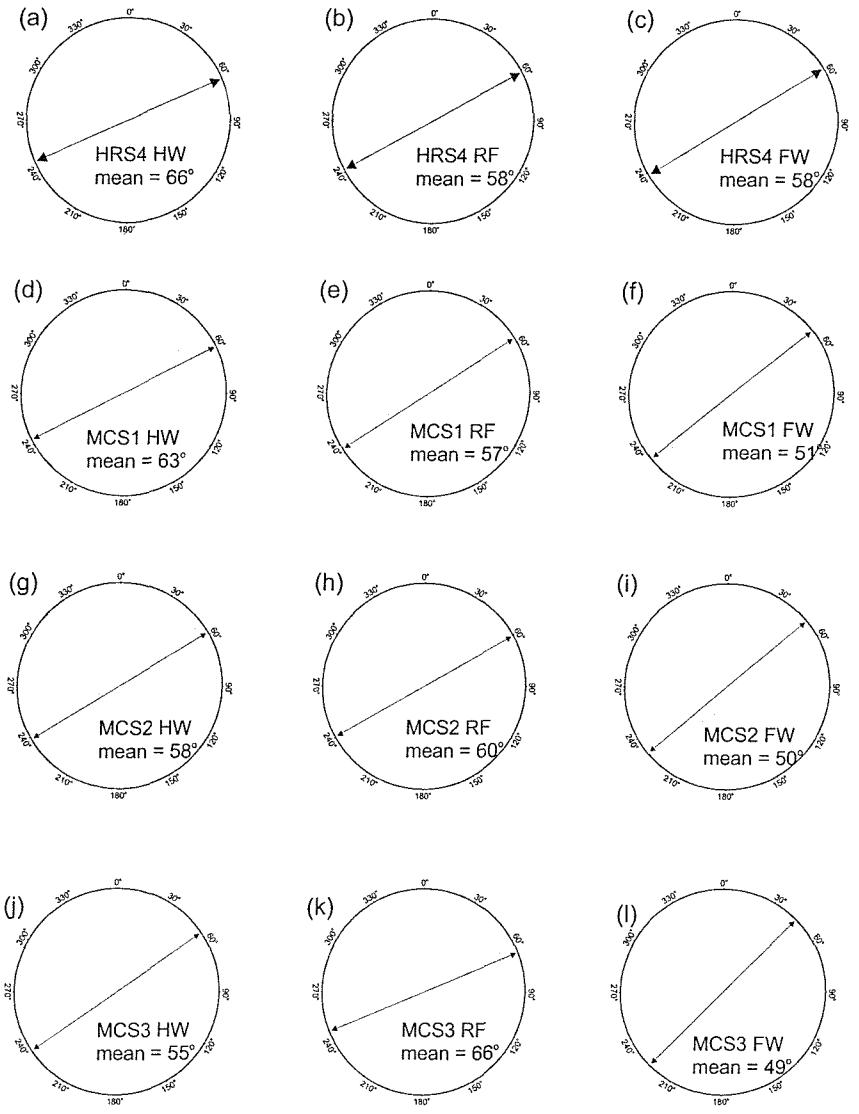

Figure 4.21: Rose plots of strike angles for faults crossing horizons HRS4 (a - c), MCS1 (d - f), MCS2 (g - i) and MCS3 (j - k). Separate rose plots are shown for Rangitaiki Faults (RF), hanging-wall faults (HW) and footwall faults (FW).

opening direction of the TVZ.

The footwall faults are all relatively short and so their strike is calculated on a smaller number of observations. These values are likely to be poorly defined in the deeper horizons. In the higher horizons, the average strike is similar to that of the Rangitaiki Fault.

4.10 Discussion

4.10.1 Fault Population Analysis

With the exception of the displacement distribution on MCS2, the discrete frequency method gave lower values of D than the cumulative frequency method. This may be a result of the finite range effect, which does not affect the discrete frequency method but could lead to an over estimate of D in the cumulative frequency method. Best-fit power-law exponents commonly lie between -1.1 and -2.0 for length distributions (Okubo and Aki 1987, Heffer and Bevan 1990, Gauthier and Lake 1993, Scholz et al. 1993, Barton 1995, Villemin et al. 1995, Cladouhos and Marrett 1996, Watterson et al. 1996), and -1.0 to -1.5 for displacement distributions (Scholz and Cowie 1990, Marrett and Allmendinger 1992, Villemin et al. 1995); the largest values coming from areas that have experienced at least two episodes of extension. The power law exponents for faults measured in the pseudo-3D survey area come from the lower end of this distribution, even when the assumed over-estimation caused by the finite range effect is taken into account, implying a smaller number of short faults for every long fault. This may be a result of the lateral sampling resolution of the data or, as Yielding et al. (1996) suggest, higher power-law exponents are related to more complex or reactivated structures; the low power-law exponent observed in the pseudo-3D data may be as a result of the youth of the Whakatane Graben.

Cladouhos and Marrett (1996) show a systematic decrease in the value of D through time in a numerical model that allows faults to grow through linkage. The decrease in D implies a decreasing importance of the smaller faults within the population. Walsh et al. (2003) present data from a fault population studied in the North Sea, and show it evolves due to progressive strain localisation onto larger faults and the death of small faults with increasing maturity of the system and go on to suggest that the development of a through-going fault leads to the breakdown of the power-law size distribution at the scale of the through-going linked fault. Once a through-going fault is developed at a given scale, the system is scale-bound at that scale because fault propagation processes are not able to increase the length of the large faults rapidly enough to maintain the power-law relationship.

There is no systematic change observed in the value of D from the deepest horizon (MCS3) to the shallowest (HRS4). These results are for the current fault geometry of the different horizons. Different results may be expected from fault size distributions if the displacement on each horizon were back-stripped to show the development of the fault system. Back-stripping of fault displacements has been done for the larger faults (see chapter 6) but smaller faults are often not laterally and vertically continuous enough to

permit correlation across horizons necessary for back-stripping.

The largest number of faults in the distributions is 56, a number too small to allow correction for the finite range effect (see section 7.1 above). The small size of the sample may also be responsible for the poorly defined power-law relationships observed and the cusps in the disiplacement distributions on horizons MCS1 and HRS4. In addition, it is questionable whether or not the area chosen is representative of the regional faulting style as the area was selected to observe the developing linkage of the Rangitaiki Fault and was not designed for fault population analysis.

The shape of the displacement distributions may not be a sampling artefact and may represent a true gap in the range of displacements. The faults that lie to the right of point B on Figure 4.16b are the same faults that lie in the > 50 m displacement distribution in Figure 4.19. These faults form the Rangitaiki Fault (R1 -R5), the major faults of the hanging-wall graben that are physically linked to the Rangitaiki Fault (HW3 - HW5) and two additional faults that define rotational fault blocks in the basement (HW 1 and HW2). All of these faults have large displacements at horizon MCS3 (summing the displacement of HW3 -HW5 onto the displacement of R5), and are inferred to continue to some depth below the penetration of the seismic data. The faults in the survey area might then be separated into groups containing relatively high-displacement basement faults that lie to the right of points B and C (figure 4.16) and low-displacement sediment cover faults lying to the left.

4.10.2 Evolution of Fault Population

The map view of faults suggests that faulting in the northeast of the psuedo-3D survey area is an evolved damage zone. Fault R1 is the dominant structure, shown to be c. 10 km long and having a high displacement rate. The remaining segments of the Rangitaiki Fault are significantly smaller and there are many more faults. Several of the faults in the damage zone are antithetic.

4.10.3 Extension in the Whakatane Graben

Estimates of displacement rate and fault dip are used to calculate extension across the pseudo-3D survey area. Extension rates are calculated for the Rangitaiki Fault system alone, and for all the faults in the pseudo-3D survey area, including an estimate for the White Island Fault. Estimates are made of the extension and strain rate over the period covered by the post-glacial sedimentation above HRS4 (17 $\pm$ 1 ka to present) and the sedimentation between MCS1 and HRS4 (300 $\pm$ 100 ka - 17 $\pm$ 1 ka).

Horizon HRS4 is tentatively correlated across the White Island Fault, but since the

requirement of infilling of accommodation space created by faults is not fulfilled, no displacement measurements are made (see chapter 5 for a discussion). Wright (1990) estimated displacement on the White Island Fault to be 1 $mmyr^{-1}$ from a tentative correlation of a still-stand terrace across the fault. Comparisons of post-glacial sediment thickness in the hangingwall depocentre of the White Island Fault in the pseudo-3D survey area with background 1 $mmyr^{-1}$ sedimentation rate give similar values (1.5 – 0.6 $mmyr^{-1}$).

The maximum post-glacial displacement rate observed on the Rangitaiki Fault is 3.4 ± 0.2 $mmyr^{-1}$ (see section on displacement rates above). Summing all the displacement measurements in the survey area (for all the faults, on all the line crossings) and dividing by the number of measurements, gives a mean post-glacial displacement rate of 3.1 $mmyr^{-1}$ and a mean displacement rate of 1.2 $mmyr^{-1}$ between 300 ka and 18 ka. To see the effect the exclusion of the White Island Fault has on estimates of strain and extension in the pseudo-3D box, the following calculation is also done with the 1 $mmyr^{-1}$ estimated displacement rate of the White Island Fault added to the mean post-glacial displacement rate of the pseudo-3D survey area.

To calculate the extension at seismogenic depth (6 – 8 km), the measured displacement rate is assumed to be the dip slip displacement rate and a fault dip for the seismogenic zone assigned. Beanland et al. (1990) and Wright (1990) use the 45 ± 10° dip value assigned to the Edgecumbe earthquake to convert dip slip to extension. This value is lower than the values seen in the multichannel data presented here, but since the fault dip decreases with depth and the seismogenic zone is up to 6 km depth (Bryan et al., 1999), this range of fault dip values are reasonable. The calculated extension and strain rates for a range of fault dips are shown in table 5. This table includes post-glacial strain rates calculated from the maximum displacement rate observed on the Rangitaiki Fault, the mean displacement rate for the whole survey area, and the mean for the survey area plus the estimated 1 $mmyr^{-1}$ contribution from the White Island Fault. The final row of the table shows the estimated strain and extension rates for the time period between 300 and 18 ka.

An assumed fault dip of between 35 ° and 55 ° at the seismogenic zone gives a mean post-glacial extension rate of 1.8 – 2.5 $mmyr^{-1}$ within the pseudo-3D survey area. These values do not include the contribution from the White Island Fault. Including this value increases the post-glacial extension rate estimate to between 2.4 and 3.4 $mmyr^{-1}$.

The extension rates calculated here cover approximately 6 km of distance across strike. Strain rates are calculated by dividing the extension rates by this distance. Post-glacial strain rates in the pseudo-3D survey area of between $0.3x10^{-6}yr^{-1}$ and $0.4x10^{-6}yr^{-1}$ are found, increasing to $0.4x10^{-6}yr^{-1}$ - $0.6x10^{-6}yr^{-1}$ if the displacement estimate across the

	Vertical displacement rate [mmyr^{-1}]	Extension rate [mmyr^{-1}]				Strain Rate [x10^{-6}yr^{-1}]	
		35 °	45°	55°	60°	35°	55°
Maximum Post-glacial rate on Rangitaiki Fault	3.4	3.1	2.6	2.1	1.9	0.5	0.4
Mean Post-glacial rate in Pseudo-3D area	3.1	2.5	2.2	1.8	1.6	0.4	0.3
Mean post-glacial rate in Pseudo-3D area plus White Island Fault	4.1	3.4	2.9	2.4	2.1	0.6	0.4
mean rate for period 300 - 18 ka	1.2	0.9	0.8	0.7	0.6	0.2	0.1

Table 4.5: Strain rate and extension rate estimates for the pseudo-3D survey area assuming fault dip of 45° at seismogenic depths

White Island Fault is included. Strain rates estimated for the period 300 ka to 18 ka are lower, between 0.1 x 10^{-6}yr^{-1} and 0.2 x 10^{-6}yr^{-1} suggesting an increase in strain rate within the detailed survey area over the last 300 ka.

Localisation of strain onto large fault structures is a commonly observed feature of developing fault networks (e.g. Gupta et al. 1998, McLeod et al. 2000, Meyer et al. 2002, Walsh et al. 2003), usually accompanied by the death of small faults in the fault population allowing the total strain rate of the region to remain constant. The faults in the hanging-wall and footwall of the Rangitaiki Fault increase in displacement rate along with the main Rangitaiki Fault itself. This observation requires that either the regional strain rate has increased with time, or that the localisation of strain has occurred over a length scale of more than 6 km (the width of the survey area).

Strain rates for the onshore Taupo Fault Belt determined from geodetic surveys range between 0.07 ± 0.08 x 10^{-6}yr^{-1} to 0.19 ± 0.10 x 10^{-6}yr^{-1} (Adams, 1983, Walcott, 1984; cited in Crook and Hannah 1989), with relative extension axes oriented between 143 ± 34° and 158 ± 12°. These geodetically determined strain rates are for the whole width of the TVZ on land, whereas the strain rate calculated from the pseudo-3D survey area covers only 6 km of the Whakatane Graben, recognised as the most active part of the TVZ. The geodetically determined regional strain rates are significantly lower than the post-glacial strain rates determined for the pesudo-3D survey area, suggesting that the psuedo-3D survey area on its own is not representative of the Taupo Volcanic Zone as a whole. The strain rate calculated in the pseudo-3D box for the period 300 - 18 ka is between 0.1 x 10^{-6}yr^{-1} and 0.2 x 10^{-6}yr^{-1}, similar to the estimates for the present day covering the whole TVZ. This suggests that the large increase of displacement and strain rates in the

pseudo-3D survey area over the last 300 ka is not related to an increase in regional strain rate, but instead a local increase in fault activity in the vicinity of the Rangitaiki Fault. The pseudo-3D survey area was chosen precisely because of its high fault displacements, not as representative of the regional fault activity – so an unrepresentative present day strain rate for the Whakatane Graben as a whole is not an unexpected result.

An explanation for this localised increase in activity may be that the locus of fault activity progresses from west to east (Davey et al., 1995). This is observed in coast-parallel seismic profiles (see figures in chapter 1) showing that the western side of the Taupo Volcanic Zone, the Motiti Graben is heavily faulted, although many of the faults terminate before reaching the surface. In contrast, the east of the Taupo Volcanic Zone (including the Whakatane Graben) is relatively undeformed, but the faults that are present are clearly active at the present day and break the surface.

4.10.4 Orientation of Fault Structures

The geodetically determined 158° extension direction of the Taupo Volcanic Zone (Walcott, 1987) is approximately 50° oblique to the 030° orientation of the Taupo Volcanic Zone (Figure 4.22b and c). At this angle of obliquity, analogue models do not predict the presence of any oblique- or strike-slip faults. Normal faults with moderate dips (c. 60°) are expected to form 20°-30° oblique to the rift trend (Withjack, 1986). Analogue models show that faults at the rift margin tend to be slightly oblique to the rift trend, while faults in the centre of the rift tend to be slightly oblique to the extension-normal direction (Clifton et al, 2000).

In the oblique setting of the TVZ, analogue models predict faults striking between 50°-60°. Faults closer to the rift margins should trend closer to the rift orientation, while faults in the centre of the graben should trend closer to the extension normal direction (Clifton et al, 2000). This implies faults close to the margin of the Whakatane Graben would have strikes tending towards 30°, while faults in the centre of the graben would strike closer to 60 – 70.

Both the Rangitaiki and White Island Faults strike in the expected range for faults in this oblique setting (Figure 4.22d). The average strike of the post-linkage Rangitaiki Fault is 57.5°, and a similar value is found for the White Island Fault when it is considered as three segments linked by north-south trending relay breaching faults (Chapter 5). In contrast, the hanging-wall faults in the near surface show an average strike closer to the extension normal direction. The hanging-wall faults show a rotation from an average strike of 55° for the deep faults to an average strike of 66° in the near surface. The hanging-wall faults in the

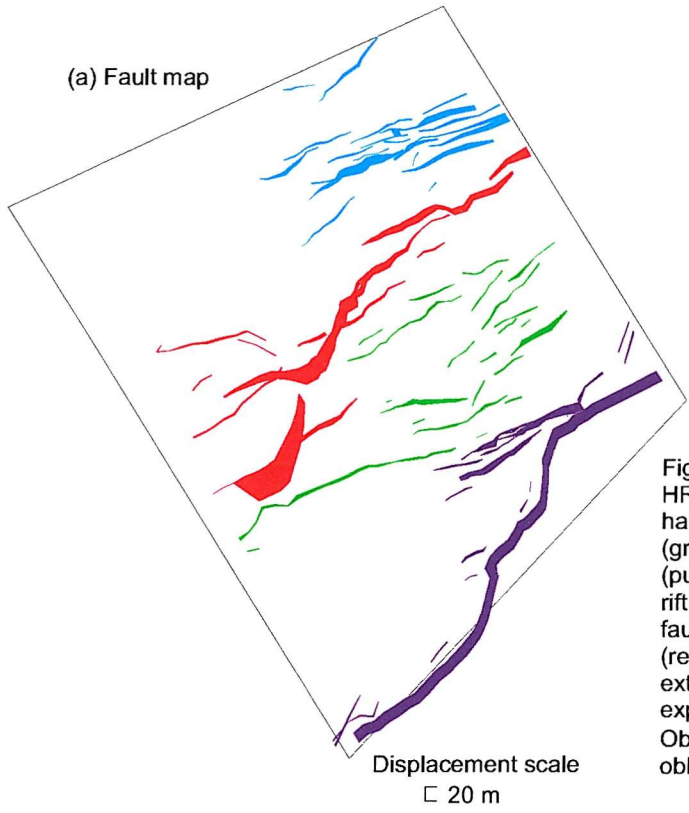

Figure 4.22: (a) Fault map for horizon HRS4, showing Rangitaiki Faults (red), hangingwall faults (blue), footwall faults (green) and the White Island Fault (purple). (b) Taupo Volcanic Zone (TVZ) rift trend at 30° (blue line) and expected fault orientations for orthogonal rifting (red line). (c) Geodetically determined extension direction (purple arrows), and expected fault orientations (red line). (d) Oblique extension α is the angle of obliquity.

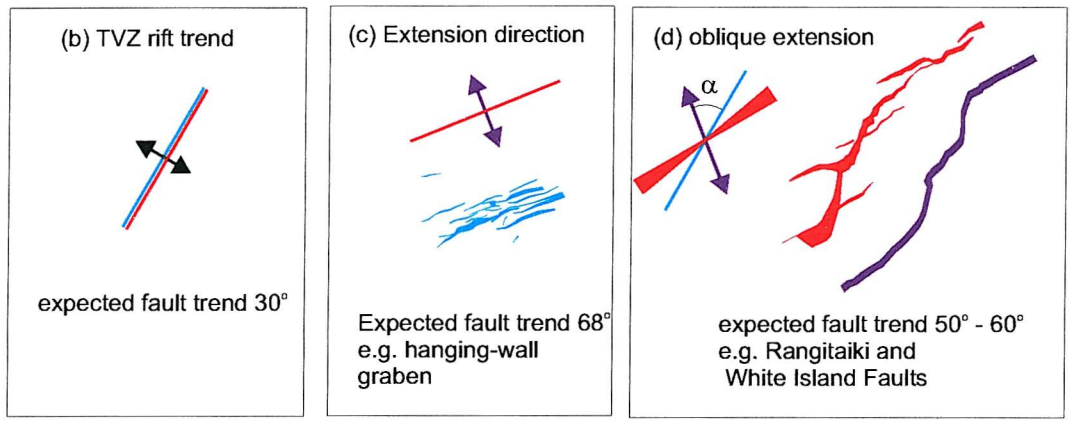

deeper horizons (MCS2 and MCS3) are dominated by the rotational block bounding faults HW1 and HW2; these faults have the strike expected for faults in the oblique extensional regime. The faults near the surface, however, have a mean strike value that would be expected if the extension direction were the only control on the development of faults. This rotation suggests a decrease in the influence of the 30° trend of the Taupo Volcanic Zone as the sedimentary sequence thickens. The interplay between the rift trend and extension direction also affects the way in which the Rangitaiki Fault segments behave after linkage. Once R3, R4a and R4b became connected at 300ka (see chapter 6), two possible fault

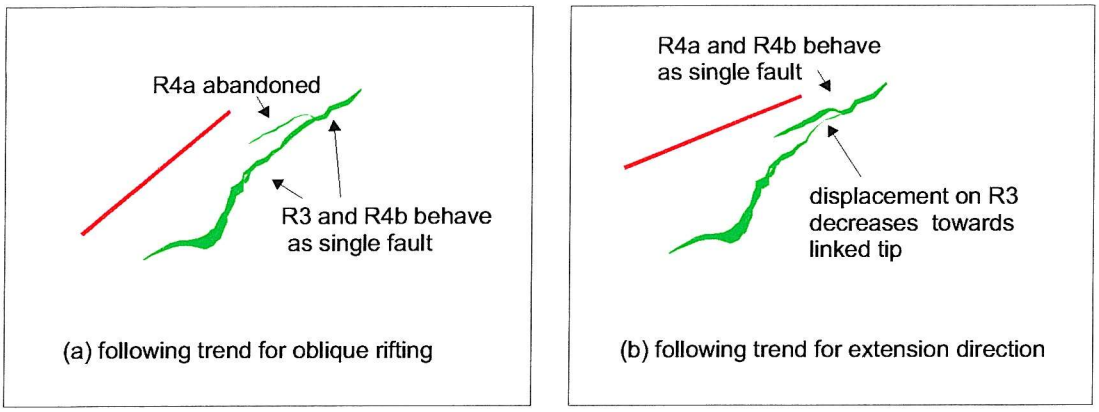

Figure 4.23: Cartoon showing expected fault orientations (red line) and associated appearance of faults R3 and R4 (green polygons) for (a) oblique rifting fault trend and (b) orthogonal extension fault trend. The surface data follow fault trend b, showing that the faults are affected by the extension direction only near the surface.

arrangements could have grown out of the three-way junction formed. Displacement could be transferred from R3 to R4b along strike, forming a single fault with orientation 54° (Figure 4.23a). Alternatively, R4a and R4b could begin to behave as a single fault with orientation 64° (Figure 4.23b). In the linked fault array, R4 does indeed behave as a single fault, selecting the orientation closer to extension normal and developing a displacement profile resembling that of an isolated fault. This change in fault orientation is interpreted to be because higher up the sedimentary package basement orientation has less influence over fault orientation.

4.10.5 Seismicity in the Whakatane Graben

Seismicity in the Taupo Volcanic Zone is characterised by shallow (< 10 km) earthquakes along much of the length of the zone and its offshore extension, with most of the earthquakes concentrated in a narrow band through the central and eastern parts of the TVZ. The seismic activity occurs in localised swarms followed by periods of relative quiescence (Bryan et al., 1999). The seismogenic zone lies between 3 and 6 km depth and corresponds to the zone of hydrothermal circulation.

Earthquake Repeat Times

The Edgecumbe earthquake ruptured a total length of 21.7 km and had a total slip area of $18.4 \times 10^3 m^2$, giving an average slip of 0.85 m (Beanland et al., 1989). The average

displacement rate calculated for the Rangitaiki Fault is 1.41 mmyr^{-1} (table 2, above). Dividing the average slip by the average slip rate gives an earthquake repeat time of 600 years for an Edgecumbe size event on the Rangitaiki Fault.

Another estimate of earthquake repeat time may be found using the empirically determined regression from Wells and Coppersmith (1994):

$$Mw = 6.78 \pm 0.12 + 0.65 \pm 0.25 log(averagedisplacement) \quad (4.2)$$

where Mw is the moment magnitude. Substituting the displacement rate of the Rangitaiki Fault for the average displacement in this equation gives the expected annual moment magnitude release. This empirical relationship is shown graphically in Figure 4.24, where repeat times for different sized earthquakes are shown for a range of displacement rates. Wells and Coppersmith (1994) found no systematic difference between Ms and Mw for the events in their database over the range of magnitude 5.7 to 8.0, but Ms is systematically smaller than Mw for magnitudes less than 5.7. The 6.6Ms magnitude of the Edgecumbe earthquake is shown in bold (assuming Mw≈Ms) and the vertical lines show displacement rates calculated for the Rangitaiki Fault and the pseudo-3D survey area. This shows that the empirical regression found by Wells and Coppersmith (1994) gives a repeat time of 320 years for an Edgecumbe size earthquake on the Rangitaiki Fault. The difference between these

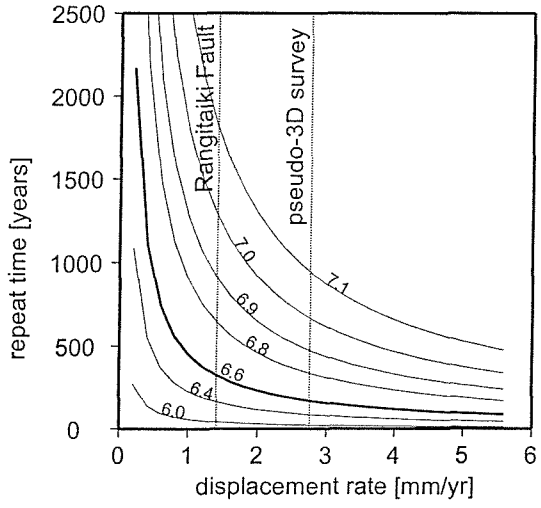

Figure 4.24: Earthquake repeat times against fault displacement rate for earthquakes ranging from moment magnitude (Mw) 6.0 to 7.1. Approximate moment magnitude of the Edgecumbe earthquake (Ms6.6) shown in bold. Dotted vertical lines show average displacement rates for the Rangitaiki Fault and whole pseudo-3D survey area.

two values is caused by the difference in methods of calculation. The empirical regression does not make use of the surface rupture information. Calculating the moment magnitude of the Edgecumbe earthquake from the average slip of the surface rupture gives a value of Mw = 6.7, this higher value of Mw leads to a longer earthquake repeat time.

Bibby et al. (1995) suggest that Edgecumbe size events would be required every 5 to 30 years within the TVZ to relieve all the strain accumulated through extension and state

that there have been too few large earthquakes in the last 100 years to account for this. The maximum extension rate cited by Bibby et al, (1995) has since been found to be too high (Darby et al, 2000). Using the revised extension values, a repeat time of 12 - 30 years would be required in the TVZ. This could be achieved with between 10 - 50 faults of the size and activity rate of the Rangitaiki Fault.

4.11 Conclusions

1. Fault displacement rates in the pseudo-3D survey area increase from 0.9 ± 0.3 $mmyr^{-1}$ to 2.6 ± 0.2 $mmyr^{-1}$ for the time periods 1340 – 300 ka and 17 ka – present respectively. The increase in displacement rate is observed in all fault groups. These results show that the rate increase observed on the Rangitaiki Fault is not caused by localisation of fault activity decreasing the displacement rate on other faults within the survey area.

2. Fault population analysis yields power-law exponents in the range 0.71 – 0.95 for the displacement distribution and 1.00 – 1.12 for the length distribution. These values are poorly constrained because of the small sample size and are relatively low compared with data from other field areas. Low power-law exponents imply fewer small faults for every large fault, which may be related to the youth of the Whakatane Graben, and suggest the faults in the Whakatane Graben are not reactivated older structures.

3. Faults in the survey area shallow with depth from vertical in the near surface to an average dip of 59° at the deepest horizon. The average dip of the Rangitaiki Fault is 61°, the faults in the footwall and hanging-wall are more steeply dipping.

4. Faults in the survey area that are rooted in the basement (e.g. Rangitaiki and White Island faults) have an average strike of c. 58°, the expected fault trend for the oblique setting of the 30° oriented TVZ with extension at 158°. Shallow faults (e.g. the hanging-wall graben) strike perpendicular to the extension direction (c. 68°).

5. The extension rate across the pseudo-3D survey area for the last 17 ± 1 ka is 2.4 – 3.4 $mmyr^{-1}$ assuming the faults dip 45 ± 10° at seismogenic depths. For the time interval between 300 – 17 ka, the extension rate is 0.7 – 0.9 $mmyr^{-1}$.

6. Strain rates across the pseudo-3D survey area are 0.4 -0.6 x $10^{-6}yr^{-1}$ for the last 17 ± 1 ka, and 0.1 -0.2 x $10^{-6}yr^{-1}$ for between 300 ka and 17 ka. The strain rate calculated for 300 - 17 ka is more representative of the geodetically determined strain rate for the whole Taupo Volcanic Zone.

7. The average displacement rate of the Rangitaiki Fault implies a repeat time of 320 – 600 years for Edgecumbe size events. For all the strain accumulated across the Taupo Volcanic Zone to be relieved seismically, between 10 and 50 faults of the size and displacement rate of the Rangitaiki Fault would be required.

Chapter 5

Post-Glacial Fault Activity in the pseudo-3D Survey Area

The sediments of the Whakatane Graben recorded in the high-resolution chirp, boomer and 3.5 kHz profiles show the post-glacial transgressive sequence overlying a transgressive marine ravinement surface. Within the post-glacial sequence there are several strong and laterally continuous reflectors, whose origin is uncertain but is likely to be either volcanic ash deposits or sea level still-stand terraces. These reflectors are displaced by active extensional growth faults. In this chapter, displacements on four post-glacial subsurface horizons found in the high-resolution pseudo-3D survey area are used to calculate displacement rates along an actively extending fault system over 17 $\pm$ 1 ka, separated into intervals of between 2 and 9 ka.

In chapters 4 and 6 only the base of the post-glacial sequence (HRS4) is used, and these data are integrated with the multichannel data to construct a fault activity history spanning c. 1340 ka. The four horizons interpreted within the post-glacial sequence span 17 $\pm$ 1 ka, a timescale of fault activity nearly two orders of magnitude smaller than that presented in chapters 4 and 6. This change of scale allows short term variations in displacement rate to be measured, giving a different view of fault growth to that seen on timescales of 10^6 years (e.g. Nicol et al. 1997).

The White Island Fault, poorly imaged in multichannel seismic profiles, is well defined in the chirp and boomer profiles imaging the postglacial sedimentation. In section 4 of this chapter the images of the White Island Fault sedimentation are described, and an interpretation of the origin of the observed structures is given in section 5.6.3.

5.1 Fault Geometry and Seismic Stratigraphy

Profiles in the pseudo-3D survey were collected perpendicular to the 57° strike of the Rangitaiki Fault. Ten of the 3.5 kHz profiles that were collected aboard *R/V Tangaroa* in 1999

are shown in Figure 5.1. The area covered by these profiles overlaps the boomer data collected aboard *R/V Kaharoa* in 2000 used in this chapter, and extends further northward. An example profile of the boomer data is shown in Figure 5.2 together with an interpretation, and the locations of profiles in Figures 5.1 and 5.2 are shown in Figure 5.3. The

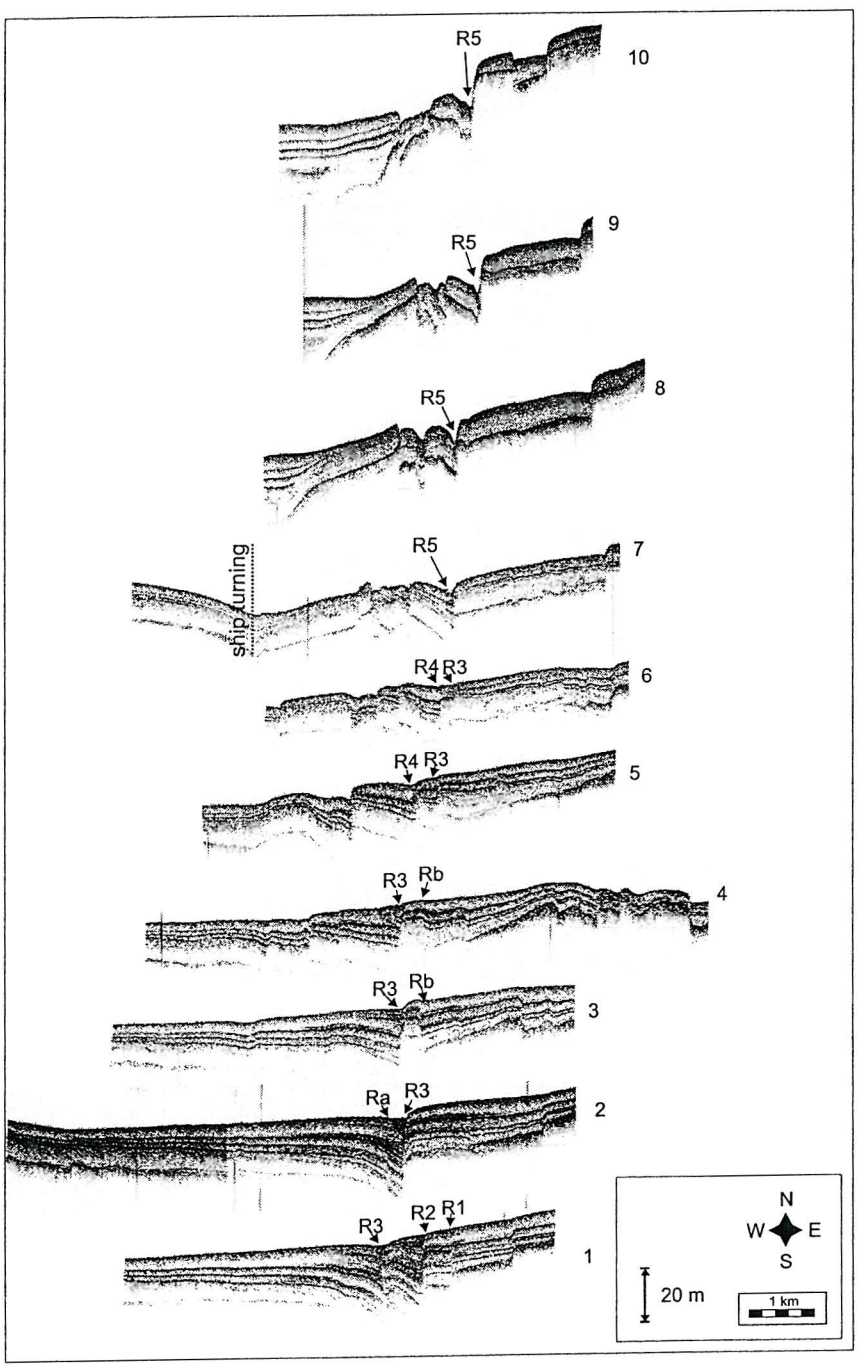

Figure 5.1: Example 3.5kHz profiles from the pseudo-3D survey area. Locations of profiles shown in figure 5.3.

profiles in Figure 5.1 show the change in faulting and sedimentation from the southwest

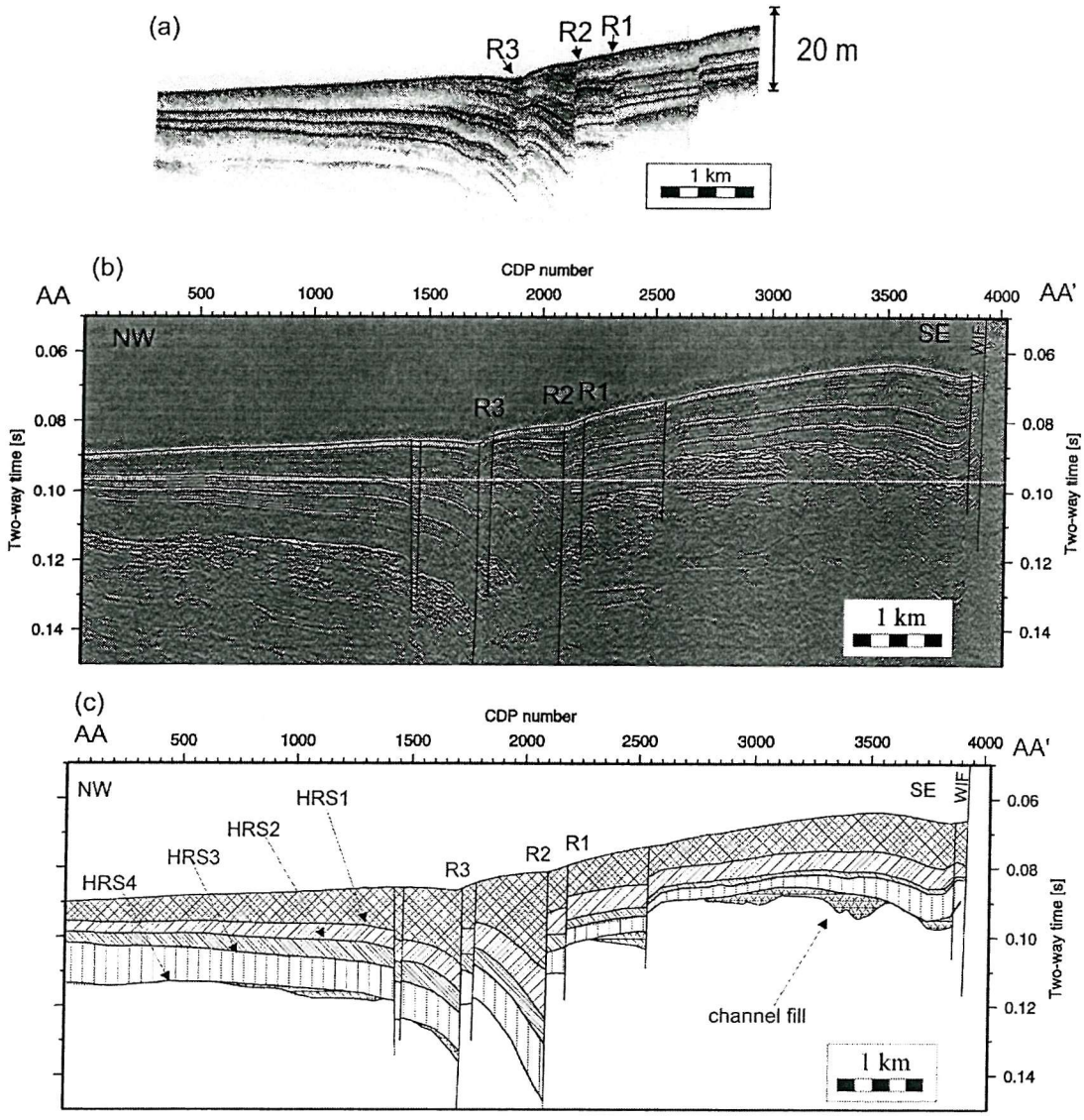

Figure 5.2: Example 3.5kHz and boomer profiles (a) 3.5kHz profile (profile 1 on figures 5.1 and 5.3), (b) boomer profile AA-AA' (figure 3), (c) interpretation of boomer profile AA-AA'.

of the pseudo-3D box (bottom of the page) to the northeast (top). In the SW, the post-glacial sedimentary package thickens into the hanging-wall of active faults and shows only very slight surface expression of the most active faults. The four horizons, HRS1 – HRS4, interpreted across the survey area are readily identified, and additional horizons are visible close to the Rangitaiki Fault hanging-wall where the sediments are thickest. Farther north, the sedimentary package thins and the horizons become less distinct, for example on Figure 5.1, profile 10, the sediment in the hanging-wall of fault R5 is 10 m thick above HRS4, but in profile 1 the sediment above HRS4 is over 40 m thick, and is too thick to be observed

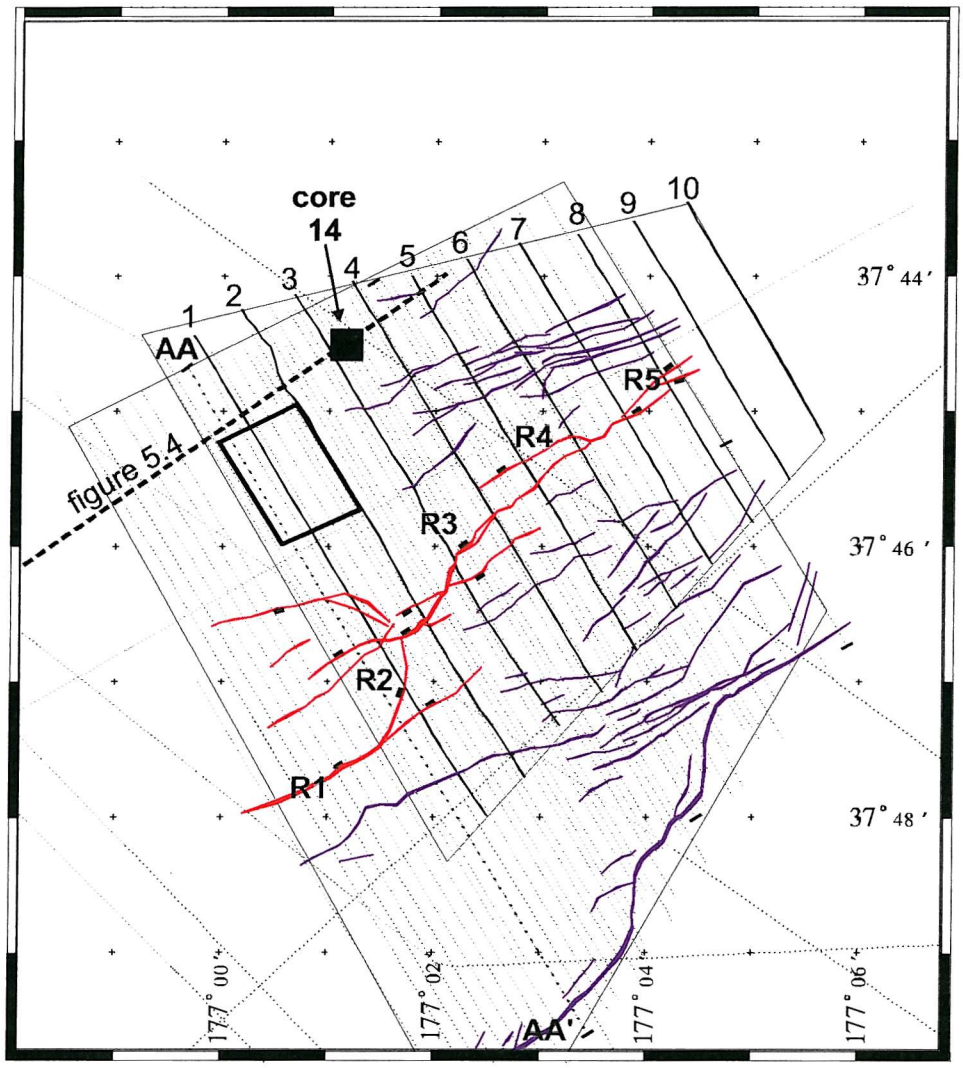

Figure 5.3: Location map of profiles and Faults. Faults are shown in red (Rangitaiki Fault) and purple. 3.5kHz profiles of figure 5.1 are labelled 1 - 10, the boomer profile from figure 5.2 is labelled AA-AA'. The location of boomer profiles used in this chapter shown as dotted lines. Black square: location of core 14. Bold dashed line: schematic location for the 3.5kHz profile shown in figure 5.4.

with the 3.5 kHz profiler. The decrease in sediment supply is manifest as progressively more surface expression of the faults to the northeast. This is most evident in profiles 9 and 10 of Figure 5.1, where there is a large surface expression of the Rangitaiki Fault. Because of the limited supply of sediment in the north of the pseudo-3D survey area used for the multichannel data, the high-resolution data used in this chapter do not extend as far north as these sections. The change in sedimentation rate is clearly demonstrated in Figure 5.4, a 3.5kHz profiler approximately perpendicular to the coast through core sites 14 and 15. The post-glacial sediment sequence is approximately the same thickness along the profile,

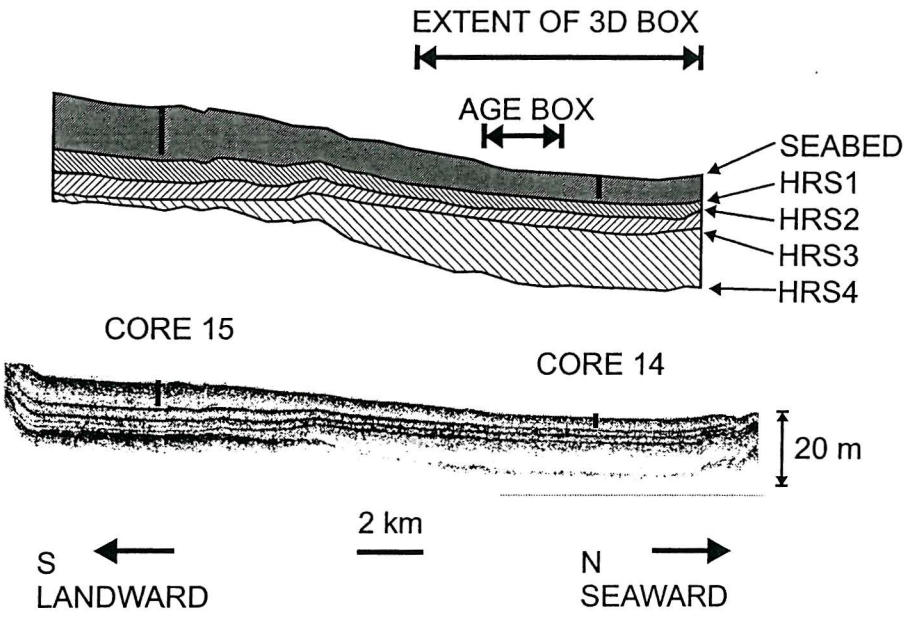

Figure 5.4: (a) 3.5kHz profiler strike line through core sites 14 and 15. (b) interpretation of the same profile (vertical scale x2). This line was collected whilst coring so ship speed and direction was not constant, a representative location for this profile is shown on figure 5.3.

but the sediments between HRS3 and HRS4 thin markedly landward, while the sediments between HRS1 and the seabed thicken. This landward shift in the locus of sedimentation is caused by the rising sea-level since the last glacial maximum. The extents of the pseudo-3D survey area and the age box are shown on Figure 5.4, in both of these ranges the horizons are well resolved and sediment thickness varies little, showing that the sedimentation rate in the survey area is not affected by the landward shift.

5.1.1 Stratigraphy and Age Control of Horizons

From at least 18 ka until 6.5 ± 0.1 ka, the New Zealand coastline saw episodic sea-level rise, with a notable still-stand at 9.2 – 8.4 ka, and a less significant still-stand from 7.5 – 7.3 ka (Herzer, 1981; Gibb, 1986), and since 6.5 ka the sea-level has been relatively stable (Gibb, 1986). Within the onshore Whakatane Graben, the coastline of the Rangitaiki Plain was deeply embayed at 6.5 ka with cliffs at Awakeri, and since then the Rangitaiki Plain has prograded at least 10 km, with volcaniclastic sediment transported to the coast down major rivers. Increased sedimentation rates have been noted following the Whakatane, Taupo and Kaharoa pyroclastic eruptions (Nairn and Beanland, 1989; Beanland and Berryman, 1992). The Rangitaiki fault trace north of Whale Island lies at water depths of 60 – 100 m, and

given that sediment has filled in any fault created accommodation space at the sea-bed, it is expected that the whole area would have been exposed at the last sea-level lowstand, and that a fluvial system would have drained the hinterland to the south.

Within the graben there are four strong laterally continuous horizons seen in the chirp, boomer and 3.5kHz data (HRS1 – HRS4, Figure 5.2). Swell-filtering of the boomer profiles (Chapter 2) has revealed the oldest of these laterally continuous horizons immediately overlies a system of incising channels (Figure 5.2). Horizon HRS4 is interpreted as the post-glacial onset of marine conditions – the flooding surface. The youngest (HRS1) is interpreted as related to the 9 ka still-stand described above.

Wright (1990) summarised in detail the seismic sequence imaged in the 3.5kHz profiles in the Bay of Plenty, and gives a comprehensive justification for interpreting the near-surface 5 – 60 m thick stratigraphic sequence as representing the post 18 ka transgression. Evidence to support this interpretation include: a series of landward thinning, conformable and onlapping seismic reflectors that form the uppermost sedimentary succession, which unconfomably overlies an acoustically reflective seismic basement which has been incised by near shore fluvial channels.

Wright (1990) identified an extensive still-stand terrace at -109 m immediately east of the Whakatane Graben, correlated with the 18 ka still-stand (Carter et al., 1986). This still-stand lies directly beneath a stratigraphic sequence, condensed with respect to the sequence found in the graben, but identical in all other ways.

Direct age control consistent with the transgressive sequence described above, is provided by 25 piston cores described by Kohn and Glasby (1978), and 18 shallow piston and gravity cores collected during cruise TAN99-14 (Lamarche, 1999). Physical property measurements for cores 14 and 15 are shown in chapter 2, and the chronology of the cores are detailed in Cooil (2000). A C14 calibrated age of 6856-6609 years BP was found at a depth of 2.67 m. This is used with the tephrachronology to constrain the sedimentation rate within the core. The sedimentation rate is less than 0.4 $mmyr^{-1}$ for the last 6.6 – 6.8 ka, but was substantially higher (1 $mmyr^{-1}$) prior to that. The shallowest reflector used to measure fault displacement offsets, inferred to be the still-stand terrace at c. 9 ka (Gibbs, 1986), is just beneath the base of the core (c. 4.2 m), and is consistent with the presence of the primary Mamaku Tephra (7.35 ka) at a depth of 3.40 – 3.43 m down the core. The lower sedimentation rate for the post- 6.5 ka sediments can be ascribed to the sea-level maximum, and the landward movement of the locus of sedimentation.

HRS4 is the horizon interpreted as the low-stand erosion surface formed in shallow water, with incised channel fill beneath. This horizon formed diachronously between the

current 120m water depth contour and the coast from 18 – 6.5 ka. The pseudo-3D survey area covers only a short range of water depths, and the age of horizon HRS4 is inferred to lie between 18 and 16 ka within the survey area (17 ± 1 ka). The youngest interpreted horizon (HRS1) is inferred to be the still-stand terrace at c. 9 ka (Gibbs, 1986).

The ages and provenance of horizons HRS2 and HRS3 are not linked to a recognised geological event. They may have been formed by other sea level still-stands (Carter et al., 1986) or volcanic events (Carter, pers comm., 2002). The ages of horizons HRS2 and HRS3 must lie between 17 ± 1 ka (HRS4) and 9 ± 1 ka (HRS1), but since no direct age control is available from cores or stratigraphic evidence, the ages of these horizons are interpolated from sediment thickness values within a subset of the survey area. The 2 km^2 area used in the age calculation (shown in figure 5.3) was chosen as it is unfaulted and lies on the line of the profile shown in figure 5.4 close to core site 14 where the sedimentation rate has been calculated (see Chapter 2). The sedimentation rate between the dated horizons HRS4 and HRS1 is assumed constant and representative of the non-faulting related sedimentation rate throughout the survey area. The 8 ka between the horizons is divided linearly to give the ages of HRS2 and HRS3. In the area used for the age calculation, the average two way time between horizons HRS1 and HRS4 is 17.5 ms, equivalent to 14.5 ± 0.8 m of sediment. This gives a sedimentation rate over the 8 ± 1.4 ka of 1.8 ± 0.3 $mmyr^{-1}$.

The sediment thickness between the horizons in the age box and the duration this represents are shown in Table 5.1. These results give the ages of HRS2 and HRS3 as 11.1 ± 1 ka and 13.3 ± 1 ka respectively.

Interval	Two way time [ms]	Thickness [m]	Duration [ka]
HRS1-HRS2	4.63	3.8	2.1±0.6
HRS2-HRS3	4.88	4.0	2.2±0.6
HRS3-HRS4	8.02	6.6	3.7±0.8

Table 5.1: Sediment Thickness between Horizons in the Post-Glacial Sequence

5.1.2 Fault Geometry

The faults have been divided into three groups – the Rangitaiki Fault system, faults in its hanging-wall (hanging-wall faults) and faults in its footwall (footwall faults). These divisions are made based on lateral coherence of fault displacement and physical connectivity of segments of the Rangitaiki Fault (see Chapter 6).

In the south of the survey area the profiles are dominated by the Rangitaiki Fault system (Figure 5.1, profiles 1 – 3). The Rangitaiki Fault segments have high displacement with

relatively undeformed sediments on either side. The amount of faulting within the hanging-wall area of the Rangitaiki Fault increases northwards, and by profile 5 (Figure 5.1), the Rangitaiki Fault is no longer the highest displacement fault in the section. The deformation in the Rangitaiki Fault hanging-wall develops northwards from these few large faults into the closely spaced and relatively low-displacement faulting of a collapse graben (profiles 7 – 9, Figure 5.1). This collapse graben contains closely spaced and overlapping synthetic and antithetic faults that intersect at depth, and converge onto the Rangitaiki Fault at c. 500 m depth. In the post-glacial sediments, however, the faults are vertical and do not intersect in section.

5.2 The Subsurface Horizons in Map View

Throughout the post-glacial sedimentary sequence (between HRS4 and the seabed), there is no observed lateral fault propagation. The distance between adjacent profiles means that only lateral propagation rates of more than 5 mm yr^{-1} may be observed; with 200 m line separation and time periods as short as 2 ka between horizons, lateral propagation rates of up to 100 mm yr^{-1} may be below the lateral resolution of the survey. Horizon structure maps are shown for the four interpreted subsurface horizons and the seabed (Figures 5.3 and 5.4). The fault maps do not change between horizons because there is no lateral propagation and the faults are close to vertical (70° - 90°) in the near surface. Local topographic lows are found against the hanging-wall of the Rangitaiki Fault in all of the horizons marking the locations of high displacement and increased sediment accommodation space (Figure 5.5). Although the Rangitaiki Fault system is a fully linked structure (Chapter 6), its segmented nature is still clear from the structure map of HRS4, where the structure contours show several separate topographic lows against the fault in the centres of the fault segments. The collapse graben in the Rangitaiki Fault hanging-wall is also a topographic low and location of increased sedimentation, although in the higher horizons (HRS1 and HRS2) the sediments are eroded from the graben around the northern margin of the survey area as the locus of sediment deposition moves landward (e.g. profiles 8-10 of Figure 5.1).

The White Island Fault in the survey area comprises three NE/SW striking sections separated by two north-south trending sections. NE/SW trending fault splays continue in the hanging-wall of the main White Island Fault strand. Between the fault splays and the White Island Fault, topographic highs are found in all of the horizons. The structure of the White Island Fault as revealed by the pseudo-3D survey data is discussed in detail in section 5.3 below. The seabed topography (Figure 5.6) has some similarities with the subsurface horizons; the deepest part of the survey area is again in the north, with the

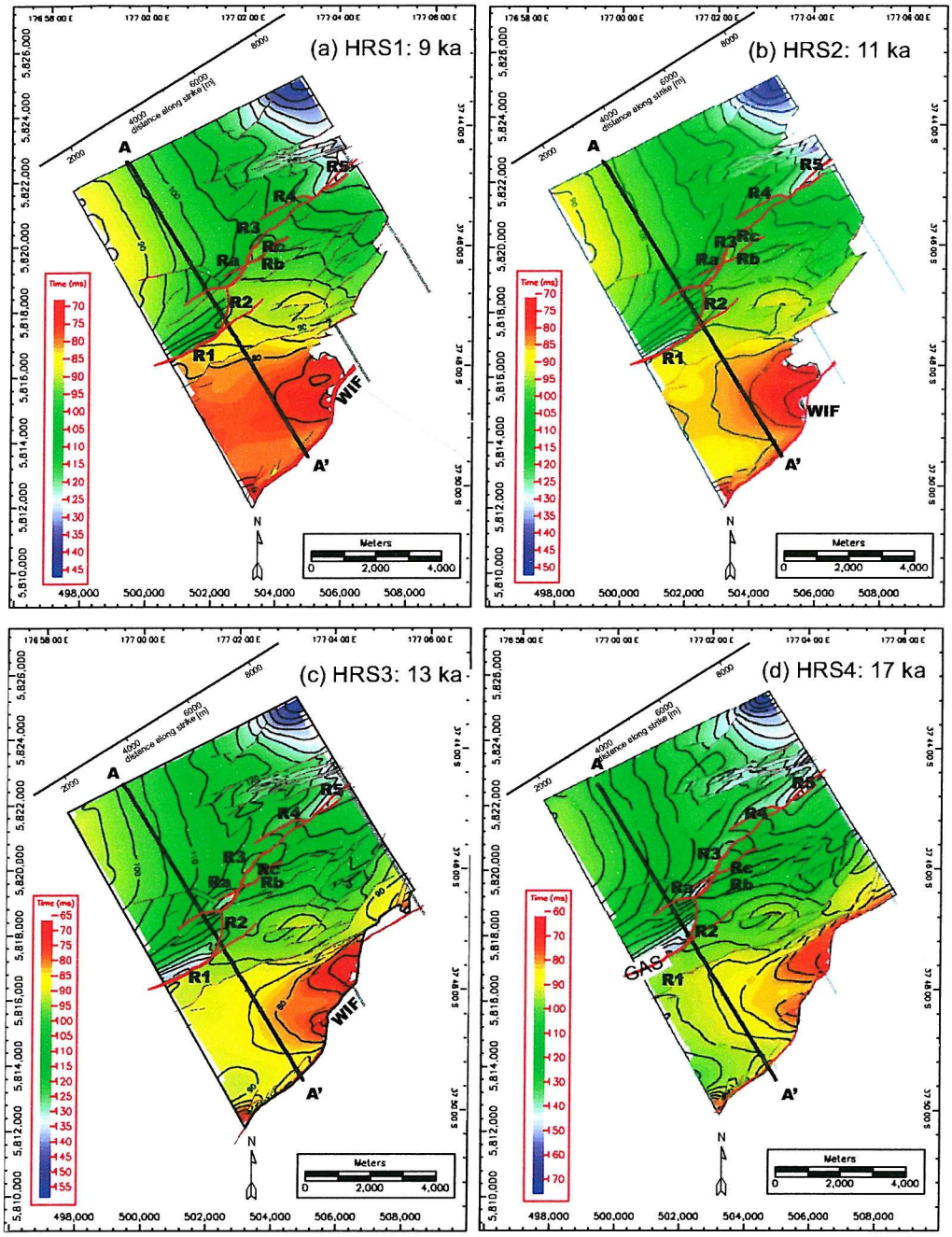

Figure 5.5: Structure maps of subsurface horizons HRS 1 - 4. Scale is in milliseconds two-way time, colours are from red (high) to purple (low). Faults are shown in red, segments of the Rangitaiki fault are numbered R1 - R5 and Ra to Rc. Strike projected distance along strike is shown above each map. These maps are shown reduced size on a single page for ease of comparison, full size versions of these figures are shown in appendix C.

seabed at 160 ms two-way-time at both the syncline and the eroded northern margin of the hanging-wall collapse graben. The shallowest points found in the survey lie landward of the closely spaced pseudo-3D area in the hanging-wall of the Rangitaiki Fault and in the footwall of the White Island Fault where the seabed is recorded at 20 ms two-way time

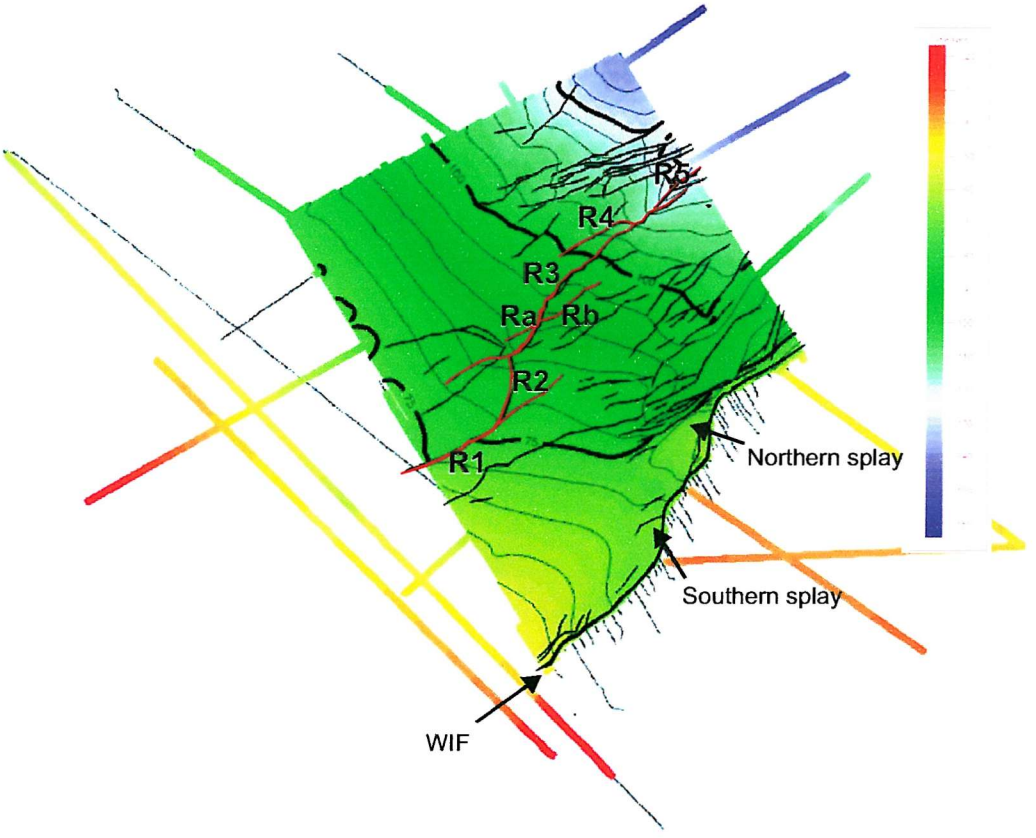

Figure 5.6: Structure map of the Seabed. The contoured region is the area covered by the pseudo-3D survey area, seabed interpretations on surrounding profiles are also included. Segments of the Rangitaiki Fault are shown in red and labelled R1 - R5, Ra and Rb. The White Island Fault (WIF) is shown and its major splays within the survey area are labelled northern and southern splays.

(Figure 5.6). This seaward slope of the seabed corresponds to a regional dip of less than 1°, this value is in agreement with the interpretation of this area lying on the continental shelf.

The structural highs in the White Island Fault hanging-wall are observed in the seabed and there is some surface expression of the northern fault splay (see Figure 5.6). In general, there is very little surface expression of the Rangitaiki Fault as the area is well supplied with sediment, with the exception of the erosion present at the northern margin of the survey area.

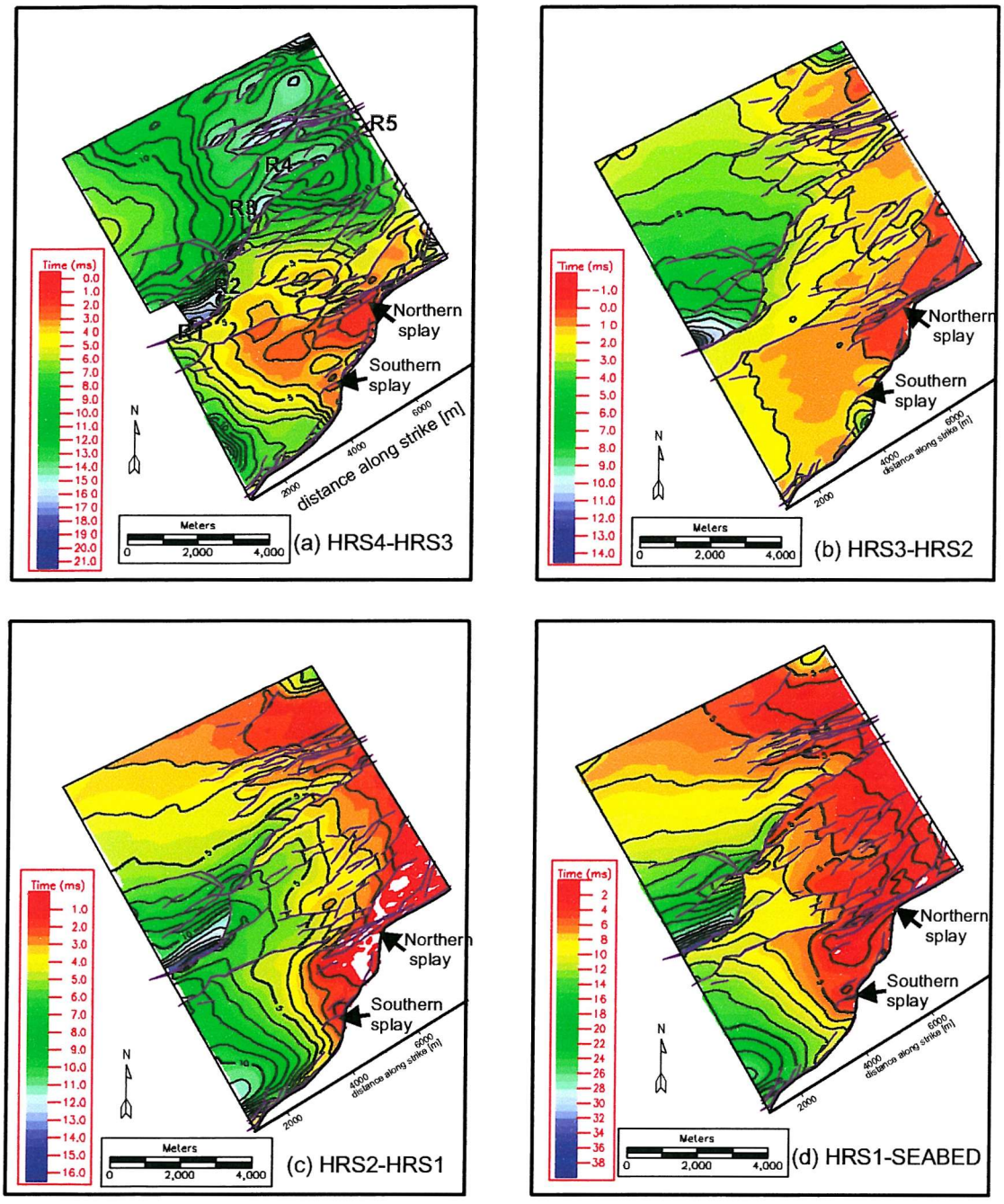

Figure 5.7: Isopach maps of sediment thickness. Contour values are in milliseconds two-way time, colours are from red (thin sediments) to purple (thick sediments). Rangitaiki Fault segments are labelled R1 - R5, northern and southern White Island Fault splays are shown. Strike projected distance along strike is shown for each map. See appendix C for full page isopach maps.

5.3 Isopach Maps

Isopach maps are shown for the sediment thickness between horizons in the high-resolution seismic survey (Figure 5.7). These maps show the locations of sediment deposition, which can be used to make qualitative observations about changing sediment supply, fault activity and structure of the seabed.

Between horizons HRS4 and HRS3 (17 – 13.3 ka, Figure 5.7a) the sediment package thickens in the hanging-wall of the Rangitaiki Fault, and is thickest against fault R1 south of the intersection with R2 (c. 3000 m along strike). Here the data are obscured by gas seeping up the fault plane, the thickest observed sediments are 21 ms TWT. As in the horizon structure maps, the segmented nature of the Rangitaiki Fault can be seen by the locally thickened sediments in the hanging-wall. Thickened sediments are seen also in the hanging-wall collapse graben, with up to 16.5 ms TWT of sediment seen in the centre. The thinnest sediments are found at structural highs on horizons HRS3 and HRS4 - between the White Island Fault and the fault splays in its hanging-wall, here the horizons are too close to be resolved separately. These splays contain dominantly northwest-dipping faults that are underfilled with sediment at the seabed and have a surface expression (Figure 5.6). The sediments thicken across-strike from the splay faults towards the White Island Fault itself, suggesting rotation of the blocks between the faults. The thinnest sediments on the crest of the rotated fault block suggest the block is tilting with a strike of c. 60°.

The isopach of sediments between horizons HRS3 and HRS2 (13.3 – 11.1 ka, Figure 5.7b) shows thickening of sediments against the Rangitaiki Fault is greatest at the southern limit of the survey area (against R1) with a maximum thickness of 14.5 ms TWT. The Rangitaiki Fault forms a single depocentre spanning the full length of the survey area, without showing any of the effects of segmentation seen in HRS4-3. The effect of fault block rotation in the hanging-wall of the White Island Fault is less pronounced than HRS4-3, but this may be because HRS3-2 represents a shorter period of time. There is a small (c. 1 km) area of thickened sediments (an increase to 4.5 ms TWT from the surrounding 1 – 2 ms TWT) against the White Island fault. This feature is observed on four profiles, and lies at the tip of a splay fault within the southern splay (see Figure 5.7) that has not propagated beyond HRS4.

The isopach maps for both HRS2-1 (Figure 5.7c) and HRS1-SEABED (Figure 5.7d) have very similar form, although HRS1-SEABED represents a longer time interval (c. 9ka rather than c. 2 ka) and has correspondingly thicker sediments (maximum thickness 39 ms TWT rather than 16.5 ms TWT). Differences are seen in the relatively sediment-starved White

Island Fault Splay, which in some places has no deposition between HRS2 and HRS1, but there is a sediment drape between HRS1 and the seabed. The sediment thickening against the Rangitaiki Fault again appears as a single depocentre, but with the thickest sediments lying farther north along R1 than before, and sediment thickness contours closing against R2. There is further development of the sedimentary depocentre against the White Island Fault in the south of the survey area (absent between HRS3 and HRS2). The thinnest sediments in these time intervals are not limited to the White Island Fault Hanging-wall splay, but continue west across the Rangitaiki Fault.

The time intervals HRS3 – HRS2 (13.3 ka – 11.1 ka) and HRS2 – HRS1 (11.1 ka – 9 ka) are of similar duration, but the isopach maps have different features. A major change between the isopach maps is the sediment volume deposited against faults R1 and R2. The maximum sediment thickness observed is similar in both (14.5 and 16.5 ms TWT), but the lateral extent of the thickened sediments is larger in the later time period, the faults appear to have provided more sediment accommodation space then. The sedimentation of the White Island Fault hanging-wall is different also. Both thin to below the vertical resolution north of 7000 m along strike, but at the southern limit of the survey area the sediment thickness varies between 2 ms TWT for HRS3 – HRS2 and 11 ms TWT for HRS2 – HRS1. This may indicate a change in the faulting style between the Rangitaiki and White Island faults, or may be a result of the landward shift in the locus of sedimentation.

In general, the sediments lying directly against the White Island Fault are uneven and have been severely deformed by fault drag, resulting in the creation of several small seismic-scale faults. The fault drag affects sedimentation up to 1 km away from the White Island Fault itself - the thickest sediments in the hanging-wall are found at this distance from the fault plane (e.g. Figure 5.7c and d). This large distance between fault plane and sedimentary depocentre is in contrast to the Rangitaiki Fault, where the thickest sediments lie directly against the fault. The difference in fault drag on these two faults is related to the difference in sediment age across the fault; the sediments of the footwall of the White Island fault are much older and more consolidated than those in the hanging-wall, and have been exposed at the surface forming a relatively hard and uneven fault surface. In the case of the Rangitaiki Fault large amounts of post-glacial sediment have been deposited on both sides of the fault preventing exposure of the fault surface and allowing the fault to move with only very localised drag.

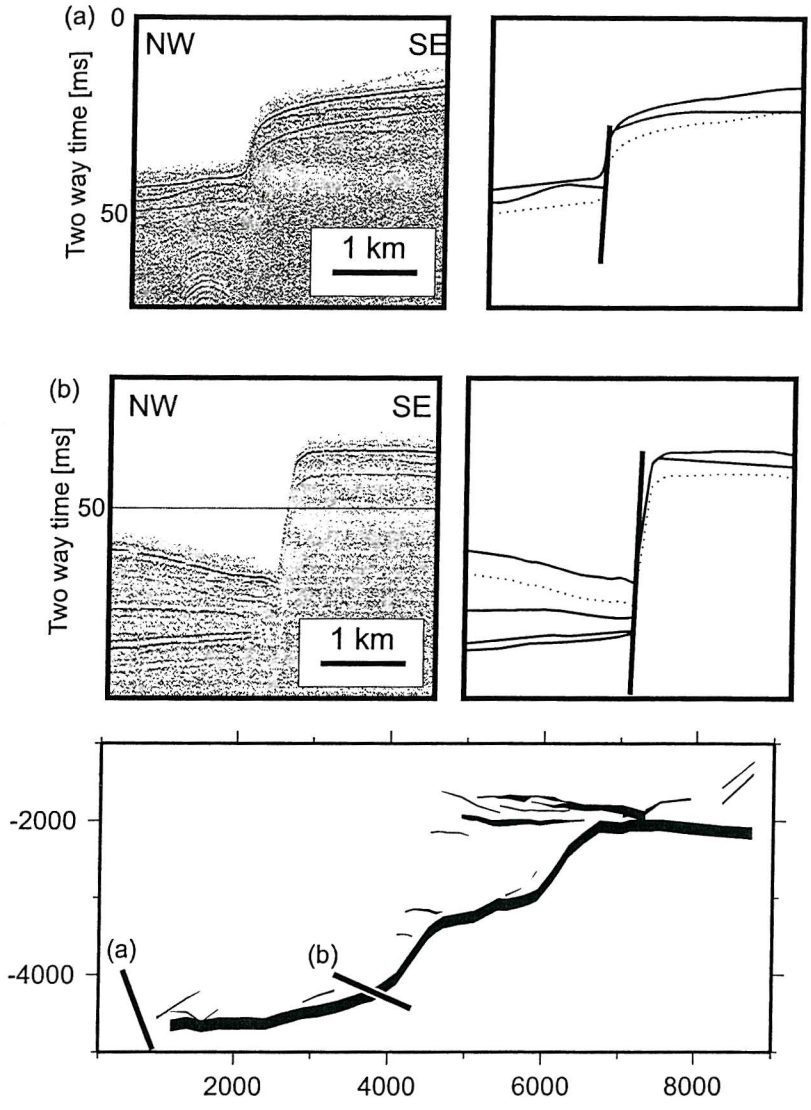

Figure 5.8: Chirp Profiles illustrating White Island Fault Footwall sedimentation (left hand figures) and interpretations of the profiles (right hand figures). Solid lines: horizons and the White Island Fault (bold). Dotted lines: seabed ghost. Fault map shows the location of profiles (a) and (b).

5.4 The White Island Fault Network

The White Island Fault marks the eastern boundary of the Whakatane Graben. There is up to 80 m surface expression (Wright, 1990) and the hanging-wall sedimentation is of variable thickness up to 40 m in the post-glacial sequence. The footwall remains a structural high, and as a result, the sedimentary package in the footwall is considerably condensed and difficult to correlate with sediments within the graben. The morphology of the fault

varies from a single scarp to a zone of normal faults (Wright, 1990). The fault trace is irregular (Figures 1.2 and 6.1) and has a pronounced zigzag arrangement in the outer shelf and further seaward (Wright, 1990).

Multichannel seismic data collected across the White Island Fault is of very low quality because of the strong velocity contrast across the fault and out-of-plane reflections from the uneven fault surface. The feature identified as the White Island Fault by Davey et al. (1995) has been reinterpreted as a fault within the North Island Shear Belt (J. Bull, pers. Comm. 2003). The White Island Fault lies c. 5 km to the west of this and has little expression at the basement level on the deep seismic (Figure 1.3 Chapter 1). The size of the fault at depth, and the model of eastward progression of fault activity (see Chapter 1) suggest that the White Island Fault is a very young feature. Poor seismic imaging of the White Island Fault at depth means that its origin remains enigmatic (see Chapter 1, Figure 1.3)

In contrast to the deep seismic data, the White Island Fault and the sediments in its immediate footwall and hanging-wall are well imaged by the chirp and boomer profiles. The post-glacial sedimentation on the footwall of the White Island Fault is condensed, and only one horizon is observed. This horizon is interpreted as an eroded ravinement surface HRS4 marking the base of the transgressive sequence. The high-resolution seismic profiles include the hanging-wall of the White Island Fault, but the limited recording interval meant that the top of the footwall is not recorded on those profiles. Some profiles, however, were recorded to illustrate footwall sedimentation, and these profiles show a highly condensed section.

Two examples of the White Island Fault scarp and footwall sediments are shown in the Chirp profiles of Figure 5.8. Profile (a) was recorded immediately south of the survey area, where a large amount of sediment has been deposited in the last 9 ka (since deposition of HRS1). A thin drape of sediment is seen in the footwall of the fault, tapering to nothing at the fault scarp. This thin sediment drape includes the entire post-glacial sedimentary sequence. In the hanging-wall, the interpreted horizons are too deep to be recorded on the Chirp profile, although some horizons can be seen close to the fault. Profile b was recorded through the survey area, but oblique to the strike projection. Here the fault scarp is large and the fault surface itself is steep and exposed. The footwall post-glacial sedimentation is again very thin, and reduces to zero some distance from the crest of the fault exposing the crest of the footwall. The hanging-wall sediments are thinner here than in profile a, and horizons HRS1, 2 and 3 are visible in the hanging-wall of the White Island Fault.

The large surface expression and lack of correlated horizons across the fault mean that

displacements are not readily determined for the White Island Fault system. Wright (1990) estimated the displacement rate of the fault at between 0.4 and 1 $mmyr^{-1}$ during the postglacial period. Comparisons of post-glacial sediment thickness in the hanging-wall depocentre of the White Island Fault in the pseudo-3D survey area with background 1 mm/yr sedimentation rate give similar values (1.5 - 0.6 $mmyr^{-1}$, see Chapter 4).

5.4.1 Sedimentation in the Hanging-wall of the White Island Fault

Although no reliable measurements of fault displacement were made across the White Island Fault, some qualitative observations of fault movement may be made from the sedimentary package deposited in the hanging-wall. Figure 5.9 shows the development of the hanging-wall sediment package through time. For Figures 5.9a to 5.9d the Palaeo-seabed is drawn horizontal, although Figure 5.9e shows that the seabed is not flat and is unlikely to have been so in the last 18 ka. Although the assumption of a reasonably flat seabed does not hold, the horizon-flattening operation assists in identifying locations of increased sedimentation and probable increased fault activity.

This figure shows a progression from an initially even coverage of sediments in the hanging-wall (Figure 5.9a) to the sediment being dominantly deposited in the south of the survey area (up to 4000 m along strike in Figure 5.9d). Changes in sediment deposition are located where there are bends in the fault, for example at c. 7000 m along strike, where hanging-wall sedimentation ceases after the deposition of horizon HRS3 (Figure 5.9b). At each bend in the White Island Fault the hanging-wall steps down towards the south; these steps in the graben floor have acted as barriers to sedimentation, and became the location of the lateral limit of sediments as the supply decreased over time. In map view (Figure 5.9f), the White Island Fault in the Pseudo-3D survey area comprises three sections striking in a similar orientation to the Rangitaiki Fault (57°, across the page in the strike projected map). The central section is the shortest at only 1.5 km long. Each of these sections step to the left by c. 1 km and they are linked by approximately north-south trending sections of the fault. These offsets in map view are accompanied by the vertical offsets in the hanging-wall (Figure 5.9e and f). In addition to the main strand of the White Island Fault there are a series of faults splaying from the main White Island Fault. These fault splays lie in the hanging-wall at the lateral continuation of the 57° striking sections of the fault. These fault splays are shown in profile in Figure 5.10. In this figure, profiles (a) to (c) pass through the southern splay and profiles (d) and (e) pass through the northern splay (locations of the profiles are shown on the map). Profile (a) lies south of the faults, although the effects are still seen in fault related folding (shown in dashed lines). This profile passes through

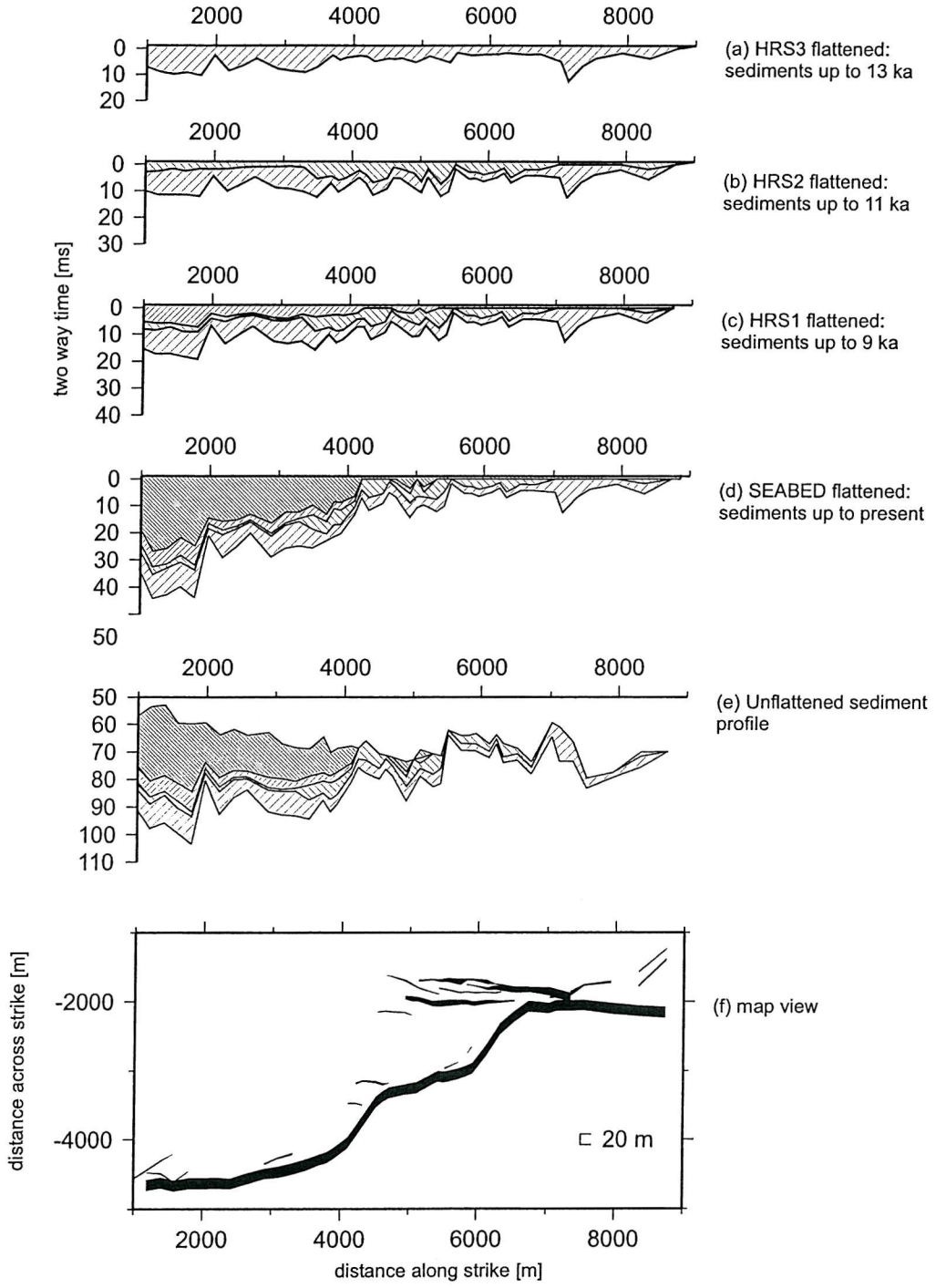

Figure 5.9: Hanging-wall sedimentation of the White Island Fault. Figures (a) to (e) are profiles with successive horizons flattened. (f) is a displacement map of the White Island Fault from horizon HRS4.

the area of thickened sediments between horizons HRS3-2 (Figure 5.7c). The sediment thickening lies above a fault (i) that has not propagated above HRS4. On this profile the whole sediment package thickens towards the White Island Fault. In contrast, the sediments

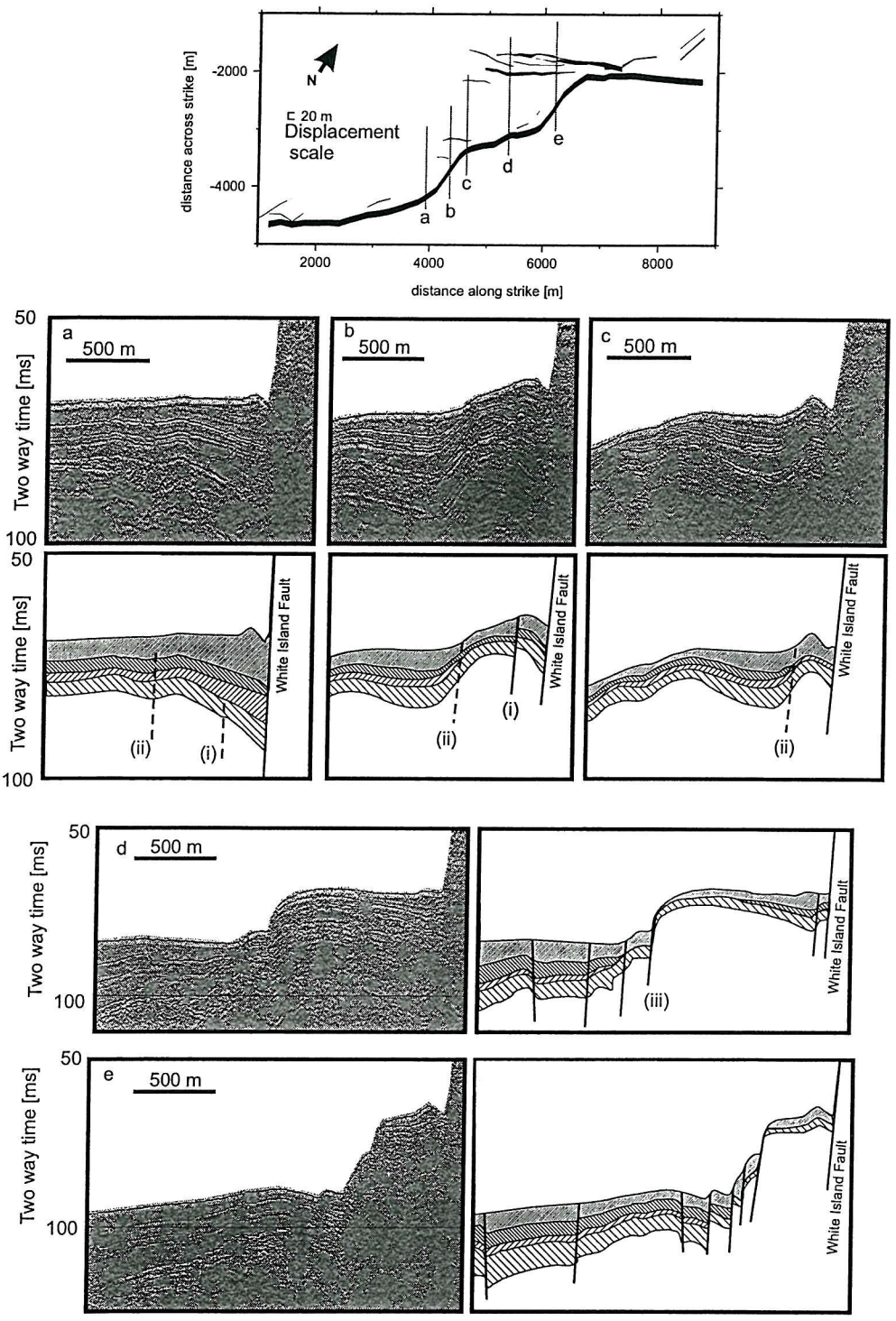

Figure 5.10: Example boomer profiles through White Island Fault splays. The map at the top of the figure shows the locations of profiles a to e. Profiles a to c pass through the smaller southern splay, showing monoclinic folds above blind faults. Profiles d and e pass through the larger northern splay of surface breaking faults, and show large topographic expression of the faults (up to c. 25 ms twt). All profiles run northwest to southeast.

in profiles b and c are thinned by the relative uplift caused by the splay faults. Profiles b and c show sediments thinning or pinching out across an upward propagating fault (ii).

Fault (i) breaks the surface in profile b, where it is close to its intersection with the White Island Fault. The northern fault splay is much larger (its component faults are up to 3 km long) and has a large surface expression. In profile d, one fault (iii) breaches the surface, with several others deforming the sediments without breaking the surface. In profile e there are four surface breaking faults in the splay.

This information can give some indication of the age of the WIF, and suggests that the linkage of the fault occurred less than 9kyr ago.

5.5 Fault Displacements

A displacement map for horizon HRS4 (17 $\pm$ 1 ka) is shown in Figure 5.11. This shows the faults separated into the three groups defined above and in Chapter 4 (the Rangitaiki Fault, hanging-wall faults and footwall faults). The fault maps are the same for all horizons in the high-resolution survey (see section 2) so only this one is shown. In Figure 5.12, the displacement profiles for faults within each fault group are shown along with the aggregate profile for the group (in bold). Profiles are shown for the four interpreted horizons (HRS1 at the top of the page, to HRS4 at the bottom), and in all cases show an upward (HRS4 – HRS1) decrease in total fault displacement as is expected in a growth-faulting environment.

5.5.1 Hanging-wall Faults

In the postglacial sequence, 22 SE and NW faults are identified in the Rangitaiki Fault hanging-wall. Some of the hanging-wall faults seen in the MCS interpretation (Figures 4.6 – 4.8, Chapter 4) can be distinguished in the displacement map of HRS 4 (Figure 5.11). The development of the hanging-wall graben is covered in more detail in Chapter 4.

Observed in the post-glacial sediments, the hanging-wall faults combine to create a total displacement profile similar to that of a single isolated fault (e.g. Muraoka and Kamata, 1983) with a tip at c. 4500 m along strike, and maximum displacement of c. 40 m at c. 8000 m along strike on HRS4. The graben continues northward beyond the survey area, but erosion from the centre of the graben means that the sediments may not be reliably recording fault motions here (see Figure 5.1, profiles 8 - 10).

If the displacement distribution of the hanging-wall faults were symmetrical about the point of maximum displacement (as for a single isolated fault) then the northern tip would be expected at 10500 m along strike. This is some 500 m beyond the most northern profile of figure 5.1, although here the hanging-wall faulting is already limited to two faults of c. 6 m displacement at HRS4, with minor flexure of the horizon between. A total of c. 12 m displacement at 10000 m (location of profile 10) fits with the supposition of a symmetrical

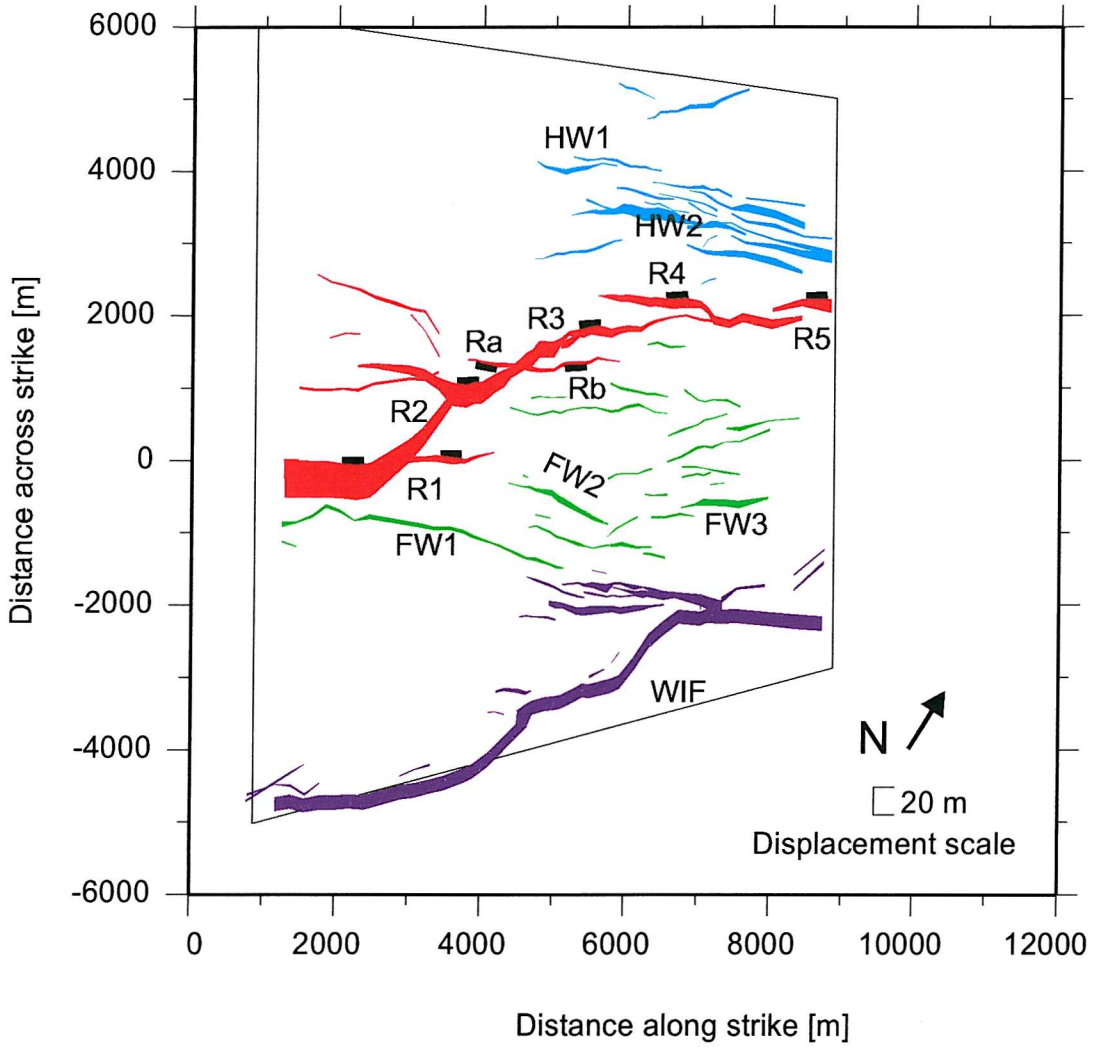

Figure 5.11: Fault displacement map for horizon HRS4 showing faults divided into: Rangitaiki Fault (red), hangingwall faults (blue), footwall faults (green) and White Island Fault (purple). Down thrown sides of major faults shown by black tickmarks.

displacement profile for the hanging-wall faults.

5.5.2 Footwall Faults

Three faults (FW1 – FW3) stand out amongst the 15 SE and NW faults identified in the Rangitaiki Fault footwall (Figure 5.11). These three faults have maximum displacements of around 10 m at HRS4, a value that would be considered low-displacement in the more active Rangitaiki Fault and hanging-wall fault groups. The total displacement profile does not resemble a single isolated fault as in the hanging-wall faults, but instead show two local maxima where the maximum displacements of FW2 and FW3 contribute to the total. These displacement maxima flank the extremities of the White Island Fault hanging-wall

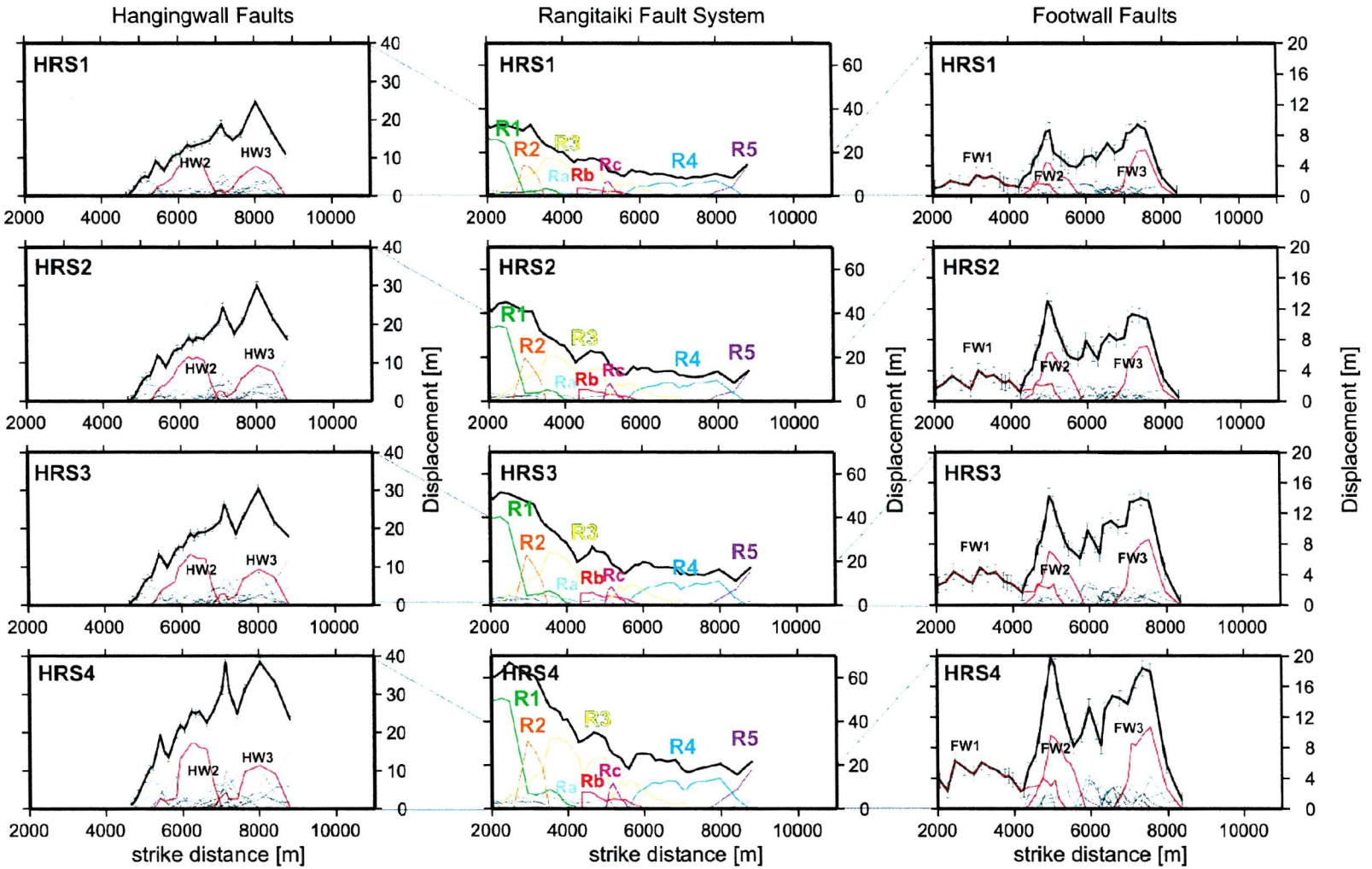

Figure 5.12: Pseudo-3D survey area fault displacement profiles for the high-resolution data. Profiles are shown for horizons HRS1 - HRS4, faults are separated into Rangitaiki Fault segments (centre column), hanging-wall faults (left column) and footwall faults (right column). Bold black lines show the aggregate displacement profile for each fault group. Fault segments discussed in the text are highlighted and labelled.

splays. With the exception of FW1-3, displacements on individual footwall-faults do not exceed 5 m at HRS4. These faults are evenly spread through the Rangitaiki Fault Footwall (e.g. Figure 5.3) north of FW2. South of this, the displacement is entirely taken up on FW1, and the remainder of the Footwall is undeformed until the effects of the White Island Fault drag and splays are reached.

5.5.3 Rangitaiki Fault System

These profiles show the displacement on the Rangitaiki Fault network decreasing from the centre of the linked fault network (2500 m along strike, fault R1) to the northern limit of the survey area. The major segments of the fault (R1 –R5) overlap and their displacements sum to produce a coherent fault profile. At HRS4, the displacement is above 20 m across the whole survey, accounted for in places by a single fault (e.g. R4 at c. 7500 m along strike).

The long-timescale development of segments R1 –R5 is discussed in Chapter 6, some smaller details are resolved in the high-resolution data that are not observed in the multi-channel data.

In addition to segments R1 – R5, the Rangitaiki Fault includes some smaller fault segments. Faults Ra and Rb are downfaulted to the southeast (antithetic to the main segments of the Rangitaiki Fault) and cross segment R3 at 4200 m along strike (Figure 5.11). Rb is observed in the multichannel seismic profiles, and does not intersect R3 below horizon MCS1. Ra is not observed in the multichannel seismic data and has lower displacement than Rb on all horizons at the intersection point (Figure 5.12). There is a notch in the displacement profile of R3 at its intersection with Ra and Rb. The sum of displacements on Ra and Rb at the intersection point is the same as the difference between the observed notched profile and a projected smoothed profile for R3.

Fault Rc is a small splay fault in R3, with maximum displacement of 12 m at 5200 m along strike on horizon HRS4. The displacement of Rc is almost exactly complimentary to the displacement of R3.

5.5.4 Fault Growth and Displacement Rates

The important issues for determining fault displacement rates are the age of the horizons, how accurately the ages are known and how much time the horizons themselves represent. The origin of the horizons is discussed above (section 1.1). The horizons were either formed by sea-level still-stands (lasting c. 1000 years) or volcanic deposits (instantaneous events). Thus the time taken to form the horizons is short, meaning that they may be considered

instantaneous across the pseudo-3D survey area over the timescales considered here. As a result, relative changes in displacement rate observed along strike for a given interval are well constrained. In contrast, the time at which the horizons formed is less well known, and consequently absolute displacement rate differences over time are less well constrained. Displacement differences for the fault groups in the pseudo-3D survey are shown in Figure 5.13, and these values are converted to displacement rates in Figure 5.14 and smoothed with a five-point running mean to highlight the broader scale features of the displacement distribution. Displacement differences calculated for the faults forming splays from the White Island Fault are unreliable because of the limited sediment supply at the border of the graben, but are included to give an impression of the fault motions on the fault splays. These values are shown above the results for the faults that lie well within the Whakatane Graben. No values are shown here for the main White Island Fault structure itself. The aggregate displacement profiles show total displacement or displacement rate at each point along strike summed across strike. Taking the mean value of the aggregate profiles then gives a mean value for the displacement for the whole area. Mean values of displacement are useful in comparing activity rates between time intervals and between fault groups.

Mean displacement rates calculated from the aggregate profiles for the fault groups in the survey area are shown in Table 5.2. The mean displacement rate is calculated by summing the displacement rate values calculated for all of the profiles and then dividing by the number of measurements. In Table 5.3, the maximum displacement rate for each fault group is given (note that this value has been calculated from the data in Figure 5.13, not the smoothed profiles of Figure 5.14). The errors quoted against each value include uncertainty estimates for the age of the horizons as well as for displacement measurements. If the age of the horizons is assumed to be known exactly, the errors in displacement rates become constant for each interval and are listed in Table 4. These values are useful for comparing displacement rates along strike for a single interval.

	Whole Survey	Footwall Faults	Rangitaiki Fault	Hanging-wall Faults
HRS4-HRS3	3.5 ± 1.4	0.6 ± 0.3	2.0 ± 0.8	0.9 ± 0.4
HRS3-HRS2	2.8 ± 1.8	0.5 ± 0.5	1.6 ± 1.1	0.7 ± 0.6
HRS2-HRS1	3.7 ± 2.5	0.7 ± 0.6	2.2 ± 1.5	0.8 ± 0.6
HRS1-SEABED	2.9 ± 0.3	0.4 ± 0.1	1.8 ± 0.2	0.7 ± 0.1

Table 5.2: Average post-glacial displacement rates on the Faults in the pseudo-3D survey area [$mmyr^{-1}$]

The total fault displacement in the pseudo-3D survey area between horizons HRS4 and HRS3 (Figure 5.13a, 5.14a) is roughly uniform across the whole survey area, so the total

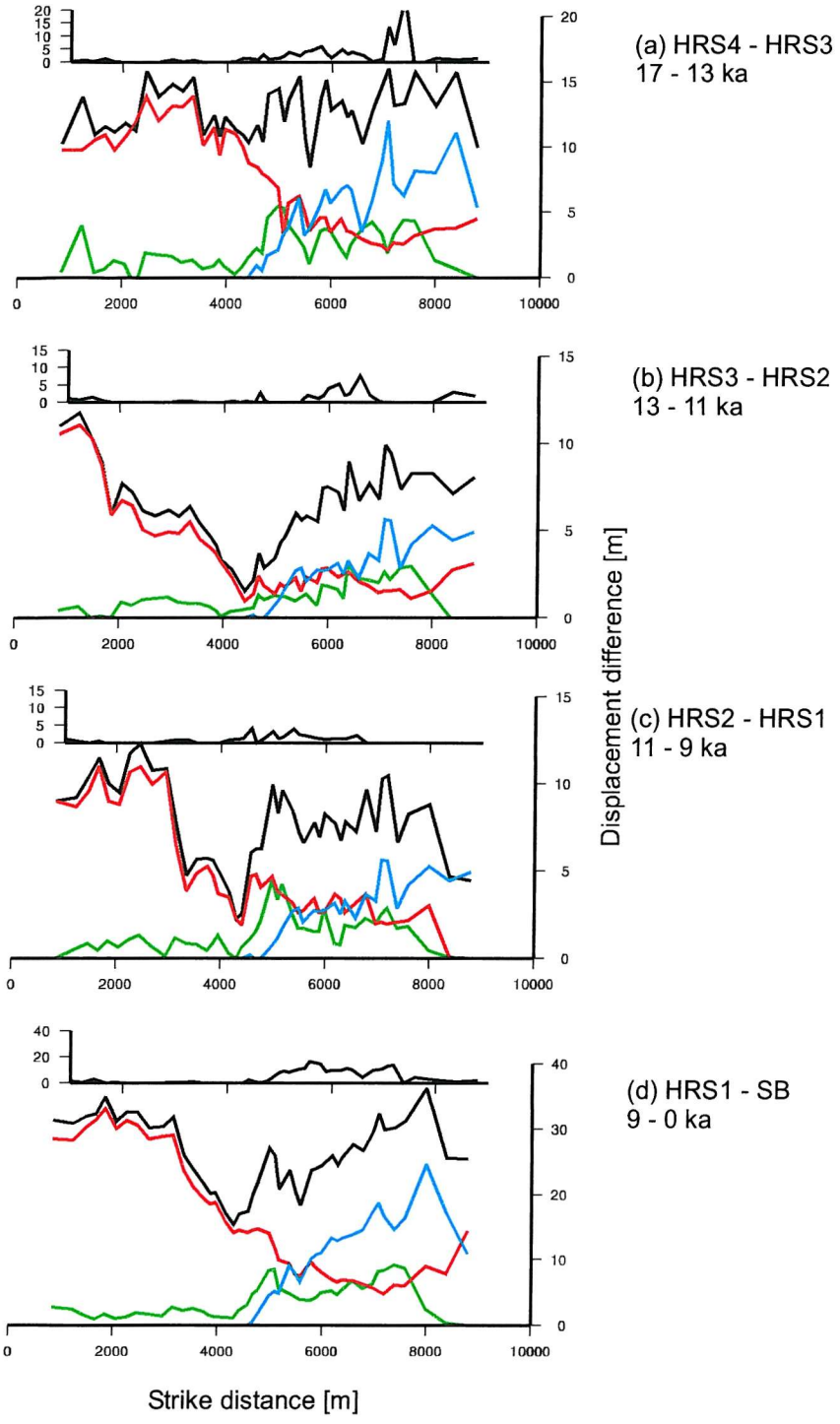

Figure 5.13: Displacement differences between horizons from (a) oldest (17 - 13 ka) to (d) youngest (9 - 0 ka). Totals are shown for each fault group, Rangitaiki fault (red), hanging-wall faults (blue), footwall faults (green) and the total for all faults in the survey (black). Above each is the measured contribution from the White Island Fault splay group, not including the White Island Fault itself. These faults are not reliably infilled with sediment and are included for qualitative discussion.

displacement during this period has been evenly distributed along strike. The average displacement rate for this time is 3.5 mmyr^{-1}, to which the Rangitaiki Fault contributes

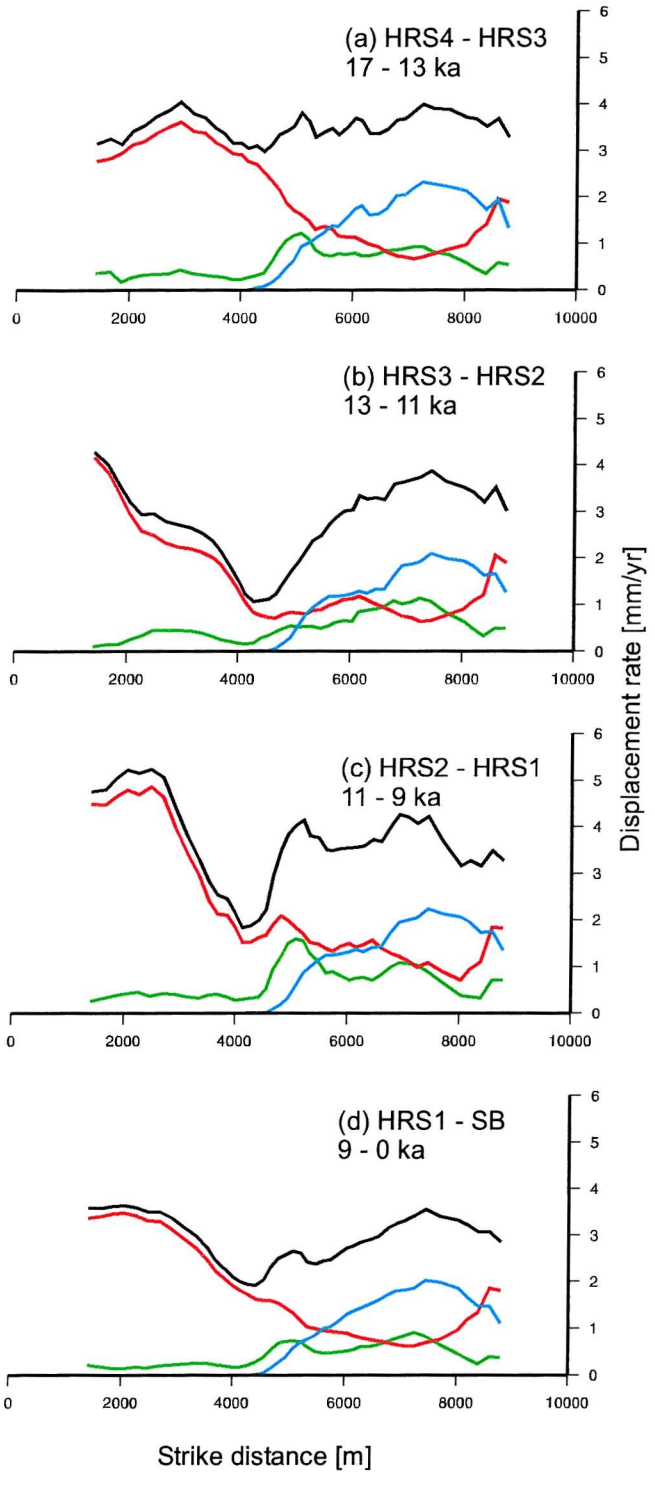

Figure 5.14: Displacement rates for time intervals (a) oldest (17 - 13 ka) to (d) youngest (9 - 0 ka). Totals are shown for each fault group, Rangitaiki fault (red), hangingwall faults (blue), footwall faults (green) and the total for all faults in the survey (black). These data have been smoothed with a five point running mean.

2.0 mmyr^{-1}. The Rangitaiki Fault crosses the full length of the survey, and is the dominant structure in the southwest of the survey area. Its maximum displacement rate of 3.8 mmyr^{-1} is found at 2500 m along strike, while its minimum displacement rate of 0.6 mmyr^{-1} is found at 7000 m along strike. The displacement of the hanging-wall faults is zero until 4000 m along strike. Over the full length of the survey area the average displacement rate of these

	Footwall Faults	Rangitaiki Fault	Hanging-wall Faults
HRS4-HRS3	1.4 ± 0.6	3.5 ± 1.2	3.0 ± 1.1
HRS3-HRS2	1.2 ± 0.8	4.4 ± 2.1	2.3 ± 1.2
HRS2-HRS1	1.9 ± 1.1	4.6 ± 2.3	2.4 ± 1.3
HRS1-Seabed	1.0 ± 0.3	3.7 ± 0.7	2.7 ± 0.6

Table 5.3: Maximum postglacial fault displacement rates [mmyr^{-1}]

	Uncertainty in Rate [mmyr^{-1}]
HRS4-HRS3	±0.2
HRS3-HRS2	±0.4
HRS2-HRS1	±0.4
HRS1-SEABED	±0.1

Table 5.4: Uncertainty in displacement rate values assuming horizon ages are known exactly

faults is 0.9 mmyr^{-1}, with a maximum value of 3.0 ± 1.1 mmyr^{-1} at the same position as the minimum on the Rangitaiki Fault, at 7000 m along strike. The footwall faults cross the whole survey, with a mean displacement rate of 0.6 ± 0.3 mmyr^{-1} and maximum 1.4 ± 0.6 mmyr^{-1} at 5000 m along strike at the centre of fault FW2. This is where the maximum displacement transfers from the Rangitaiki Fault to the hanging-wall faults. In the White Island Fault splay group, there is an apparent peak at c. 7000 m along strike, at this point along strike there is a structural high in the WIF hanging-wall (Figure 5.9), and this result is likely to have been caused by the topography of the fault scarp, and is not representative of fault displacement.

Between HRS3 and HRS2 (Figures 5.13b, 5.14b), the average total displacement rate is 2.8 mmyr^{-1}, ranging from 5.3 mm yr^{-1} at 1200 m along strike down to 0.7 mmyr^{-1} at 4400 m along strike. At two points along strike the displacement rate on the Rangitaiki Fault system drops to its minimum value of 0.5 mmyr^{-1}; one is at 7500 m along strike close to the 2.3 ± 1.2 mmyr^{-1} maximum in the hanging-wall faults, and the other at 4400 m along strike, where there are no other faults to compensate for the drop in displacement rate. The displacement rate minimum at 4400 m is not compensated for by any other faults, leaving an anomalous displacement rate low at that point and affecting displacement up to a kilometre away on either side. In addition to this anomalous displacement rate low in the Rangitaiki Fault, some of the larger faults in the hanging-wall and footwall fault groups (e.g. FW2 at 5000 m and HW2 at 6000 m along strike) have been less active compared with the previous interval.

The displacement low at c. 4400 m along strike is retained between HRS2 and HRS1, and again between HRS1 and the Seabed, although it is less broad and becomes less pronounced

in the younger sediments. Between HRS2 and HRS1, the average displacement rate is 3.8 $mmyr^{-1}$, with a maximum value of 5.9 $mmyr^{-1}$ at 2500 m along strike and a minimum of 1.1 $mmyr^{-1}$ at 4300 m along strike. Between HRS1 and the seabed, the average displacement rate is 2.9 $mmyr^{-1}$, with maximum and minimum values of 4.0 $mmyr^{-1}$ and 1.7 $mmyr^{-1}$ at 7900 m and 4300 m along strike respectively. The displacement rates on the Rangitaiki Fault are a minimum at 7000 – 8000 m along strike in both of these intervals. The displacement low in the Rangitaiki Fault at 4300 m seen between HRS3 and HRS2 is less prominent between HRS2 and HRS1, and is limited to a flexure of the profile between HRS1 and the seabed.

5.5.5 Displacement Rate Variations along the Rangitaiki Fault

The displacement rate variations along the Rangitaiki Fault are shown for the last 1340 ka in Chapter 6, and demonstrate the development of the fault system from initially isolated faults to a fully linked fault system. In this chapter only the postglacial and therefore post-linkage data are considered. Here the faults are not observed propagating laterally, nor is there an observed change in fault geometry. These data instead show the short timescale changes in fault activity associated with former segment boundaries.

Displacement difference and displacement rate plots for the individual Rangitaiki Fault segments are shown in Figure 5.15. The black line shows the aggregate displacement for the Rangitaiki Fault system (the red line in Figure 5.13). The same fault segments are present throughout the post-glacial sequence, and show no lateral propagation. Large differences in displacement rate are observed where the segments intersect and interact. The variations in displacement rate between interacting segments of the Rangitaiki Fault are described with reference to four strike locations (Figure 5.15):

1. 3100 m (R2 maximum, overlapping tips of R1 and R3),
2. 4400 m (R3 crossed by antithetic faults Ra and Rb),
3. 5200 m (Rc splay from R3) and
4. 7100 m (Tip of R3 intersecting the centre of R4).

Location (1) runs through the centre of the overlap zone of faults R1 and R3, where R2 has its maximum displacement rate throughout the post-glacial sequence. R1 overlaps (1) by 1 km, its displacement rate profile has a minimum at (1) and it has a local maximum at 3500 m along strike, at the northern tip of R2. The tip of R3 in the overlap zone has a variable displacement rate profile through time. At interval (a), the profile shows a steep

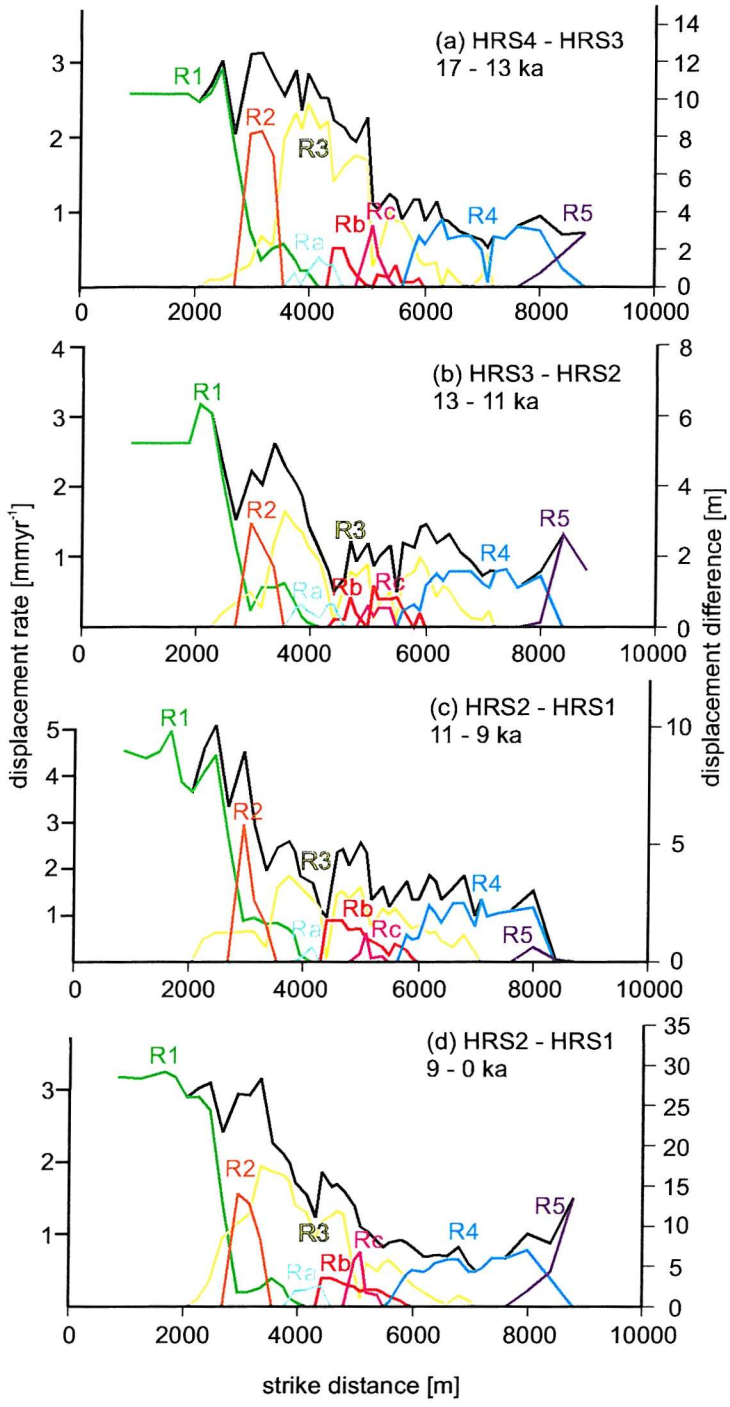

Figure 5.15: Displacement differences and rates for the Rangitaiki Fault in the post-glacial sediments, from (a) oldest (17 - 13 ka) to (d) youngest (9 - 0 ka). Segments numbered R1 - R5 and Ra to Rc are referred to in the text. Aggregate profiles shown in black.

displacement gradient up to location (1) and a 1 km long tail to the south. In intervals (b) and (c) the displacement gradient is relatively steep at the tip followed by a low displacement rate (< 1 mmyr^{-1}) section, 1 km long in interval (c), before the displacement rate increases again north of R2. In intervals (a) to (c) the displacement rate of R3 is less than 1 mmyr^{-1} at (1), but in interval (d) the displacement rate is 1.28 mmyr^{-1}, almost as much as the 1.44 mmyr^{-1} maximum on R2. In this interval, the displacement profile is approximately linear

from the maximum displacement rate on R3 at 3500 m to the tip at 2000 m.

The interaction with antithetic faults Ra and Rb has an enormous effect on the displacement rate profile of R3 at location (2). At interval (a), the displacement profile of R3 is disrupted from the ideal profile by a notch at the intersection point. The drop in displacement seen at this notch is equal to the sum of displacements on Ra and Rb at the intersection point. In intervals (b) and (c), R3 is effectively pinned at the intersection point, with a negligible displacement rate. At interval (b), Ra has the largest displacement rate of 0.33 $mmyr^{-1}$ at the intersection point. Both Ra and Rb have irregular displacement profiles. At interval (c), the displacement profiles of Ra and Rb are more regular, the displacement of Rb increases steadily from its tip at 6000 m along strike to the intersection point at 4400 m along strike. The displacement of Ra is zero at the intersection point, and has its maximum displacement close to its centre. At interval (d), R3 is reactivated at the intersection point and both Ra and Rb have even displacement profiles increasing from their tips towards the intersection.

At location (3), the displacement is divided between R3, Rb and Rc. The displacement profile of Rc almost exactly matches a notch in the displacement profile of R3, this relationship is most clearly seen in the longer time intervals (a) and (d). The intersection of R3 and R4 (location 4) shows a variety of configurations. At interval (a), the displacement on R4 drops to almost zero at the intersection, whilst the displacement on R3 increases at the tip to 0.46 $mmyr^{-1}$, leaving only a small drop in the aggregate displacement profiles at this point. At interval (b) the displacement of the tip of R3 is 0.23 $mmyr^{-1}$, a similar drop is seen in the profile of R4. In both interval (c) and (d) there is a small increase in displacement rate on R3 close to the tip, but the tip itself has a negligible displacement rate.

These results show that it is the largest fault segment (R3) that is most variable over short time periods, and accumulation of displacement is severely disrupted by the intersection of R3 with the conjugate faults Ra and Rb.

5.6 Discussion

The sediment supply to the Whakatane Graben decreases over the post-glacial period and the locus of sedimentation shifts landward with the effect that the northern limit of the survey area is the northern limit of current sedimentation. Both the White Island and Rangitaiki Faults are observed in the postglacial sediments as linked, segmented structures. Although they are physically linked structures, their segmented nature continues to affect how they move. This segmented nature can be seen in the isopach map of sediments

deposited between HRS4 and HRS3 (Figure 5.7a), where the hanging-wall sediments of the Rangitaiki Fault are separated into small isolated depocentres located at the centres of the fault segments.

5.6.1 Post-glacial displacement rates in the Whakatane Graben

No temporal trends such as those seen over 1340 ka (Chapter 4) are visible in the displacement rates recorded by the post-glacial sediments. However, differences are seen in the distribution of the displacements accumulated on the faults over 9 ka, and those accumulated over 2 ka. In Figure 5.14 the displacement rates of the faults in the pseudo-3D survey area are shown summed across strike for the four time intervals represented in the post-glacial data. This figure shows that the aggregate displacement rate of the hanging-wall fault group (shown in blue) changes very little between intervals, regardless of duration. This group is represented mainly by relatively small faults (compared with Rangitaiki Fault segments), so the seismic cycle may be represented fully by small and frequent fault slips and is fully represented at the 2 ka timescale. In contrast, the Rangitaiki Fault comprises a smaller number of large fault segments. The larger faults are able to release stress through larger and less frequent movements, so the aggregate profile appears different at 2 ka and 9 ka timescales. The features of the overall fault displacement profiles for the pseudo-3D survey area are dominantly controlled by the movements of the major Rangitaiki Fault segments. Locations where the fault geometry becomes a barrier to fault slip creates displacement lows which are not compensated for by development of, or increased activity on, surrounding faults. These features are likely to be short lived, compensated for in later fault movements.

5.6.2 Short timescale behaviour of the Rangitaiki Fault

The long-timescale (c. 1 – 2 Ma) behaviour and development of the Rangitaiki Fault is described and discussed in Chapter 6. In this chapter, the last 17 $\pm$ 1 ka of fault activity is observed in detail. The Rangitaiki Fault is a fully linked structure throughout this time-period (see Chapter 6), and the major control on measured fault activity rates is the length of time between horizons. The two longest time intervals within the postglacial sediments are HRS3 - HRS4 and HRS1 – seabed. In both of these intervals the total displacement profile for the fault is complimentary to the hanging-wall fault displacement profile, and more closely resembles the long-term displacement profiles (figure 5.16). The shorter time periods (HRS3 – HRS2 and HRS2 – HRS1), both c. 2 ka in duration, show much more irregular displacement profiles, with zero displacement rates recorded at some points on

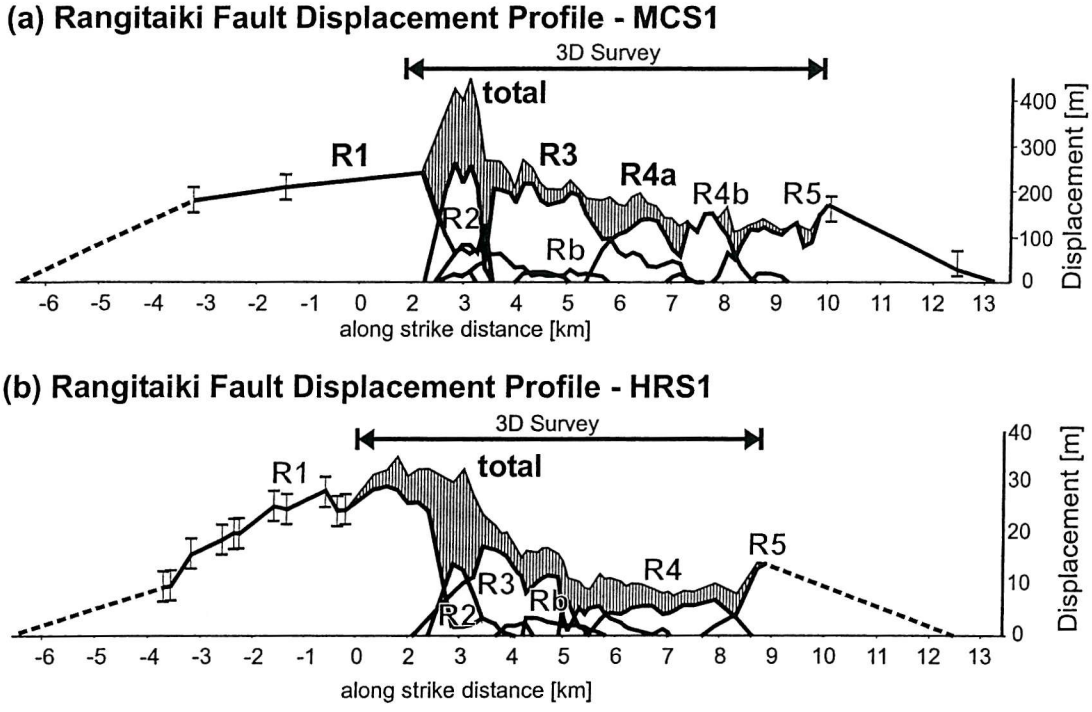

Figure 5.16: Displacement profiles for the Rangitaiki Fault at horizons MCS1 (a) and HRS1 (b). Segments of the Rangitaiki Fault are labelled R1 - R5 and Ra - Rc. Limits of the pseudo-3D survey area are shown by double-headed arrow, measurements of displacement outside the 3D area are made on regional MCS profiles and 3.5 kHz profiles.

the profiles (e.g. location 2, figure 5.15). These points with zero displacement rates clearly demonstrate that the displacement on the faults has accumulated through a series of slip events that do not necessarily rupture the entire fault plane. These results suggest that displacement rates (and associated extension and strain rates) measured over timescales of less than 2 ka may not include representative contributions from large faults. Geodetic measurements made over timescales of 20 – 50 years (e.g. Sissons, 1979; Darby et al. 2000) may not give a representative view of activity on large faults. One of the implications of this observation is a constraint on the frequency of large earthquakes rupturing the whole fault plane. Earthquake recurrence times can be calculated for a given earthquake size on a fault, but further information regarding the earthquake size population (such as a limiting frequency of the largest possible earthquake on a fault) is required to fully define the seismic

cycle. A recurrence interval for Edgecumbe-like earthquake events on the Rangitaiki Fault is derived in Chapter 4, and in Chapter 7 the limiting frequency of whole fault rupturing earthquakes proposed here is applied as a constraint to the seismic cycle.

5.6.3 Development of the White Island Fault

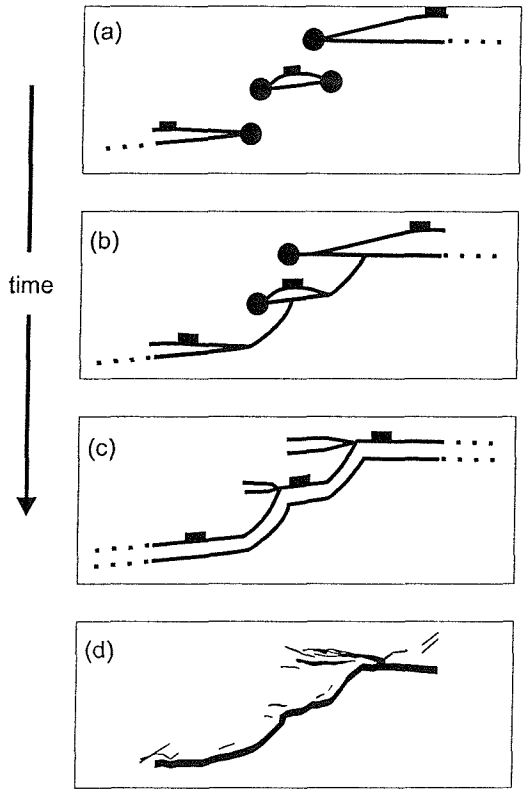

Figure 5.17: Schematic maps of possible growth history for the White Island Fault. (a) three unlinked en echelon segments of the White Island Fault. (b) faults link by breaching the hanging-wall. (c) displacement accumulates on linked fault trace leaving abandoned splays at segment overlaps. (d) data: White Island Fault map at base of post-glacial sequence (HRS4).

The structure of the White Island Fault in the pseudo-3D survey area is interpreted as three 57° trending, offset and overlapping faults that have linked forming the north-south trending sections of the fault, and leaving the fault splays in the hanging-wall. The proposed evolution of this fault is summarised in Figure 5.17. Figure 5.17a shows the three en echelon faults, overlapping but not linked. In Figure 5.17b the fault segments have linked by breaching the footwall. As time progresses, displacement is accumulated on the linked fault trace (Figure 5.17c) leaving abandoned fault splays at the segment overlaps. Figure 5.17d is a displacement map of the White Island Fault (thickness of the fault trace is proportional to displacement, where no displacement measurement was made on the main fault a value of 20 m displacement is used) at the base of the post-glacial sequence (HRS4), showing the three 57° trending segments linked by approximately North-South trending sections of the fault, with splays of small faults at the abandoned fault tips.

Beyond the limit of the pseudo-3D survey area, the trace of the White Island Fault has a

pronounced zigzag arrangement, observed only at a larger scale where the data are sparser e.g. the 4 – 5 km long east-west trending section north of the RF (e.g. Figure 6.1). The north-south trending transfer faults seen within the pseudo-3D survey area occur between left-stepping fault segments, whereas the east-west trending transfer fault seen north of the Rangitaiki Fault (Figure 6.1) lies between right-stepping en echelon fault segments. The zigzag nature of the White Island Fault trace suggests that the linked-segmented model of the White Island Fault proposed for the pseudo-3D survey area is more broadly applicable to the White Island Fault in its entirety. Surveying of the White Island Fault trace with higher spatial resolution may resolve further bends in the fault trace associated with former segment boundaries.

The difference in sediment thickness observed in the footwall and hanging-wall of the White Island Fault suggest that it has been a basin bounding fault for at least the last 20 kyr, although the development of the fault splays in the hanging-wall suggests that the linkage of the segments observed in the psuedo-3D survey area has been relatively recent.

5.6.4 Crossing synthetic and antithetic Faults

Studies of conjugate faults are concentrated on faults where the line of intersection is perpendicular to the displacement direction (e.g. Nicol et al., 1995; Watterson et al., 1998; Ferril et al., 2000) (Figure 5.18a). In these cases, inter-fault volumes generally undergo ductile (sub-seismic) strains close to the intersection; the effects will be reflected in the observed distributions of displacements on the constituent faults (Barnett et al., 1987). The decrease in resolved displacement towards the intersection of seismically mapped conjugates is only an apparent decrease as the missing displacement is accommodated on many sub-seismic scale faults in the intersection zone (Nicol et al., 1995; Watterson et al, 1998). It is unlikely that both tip-lines will reach a potential intersection point at the same time and instead the intersection will occur between a tip line and some point on the fault surface of the opposed dipping fault. T or Y junctions are likely to occur where the tip line of the intersecting fault is stopped (Nicol et al., 1995).

In contrast, where the intersection line of opposed dipping faults is in the same orientation as the slip vector of the fault (Figure 5.18b), both faults may remain active (Jackson and McKenzie, 1983).

In the MCS data the segments of the Rangitaiki Fault dip at ~60°, increasing to near vertical in the postglacial sediments (Chapter 4). The curvature of the faults means that the line of intersection between R3 (dipping towards north-west) and Rb (dipping towards south-east) is curved also (Figure 5.18c). The curvature means that the intersection changes

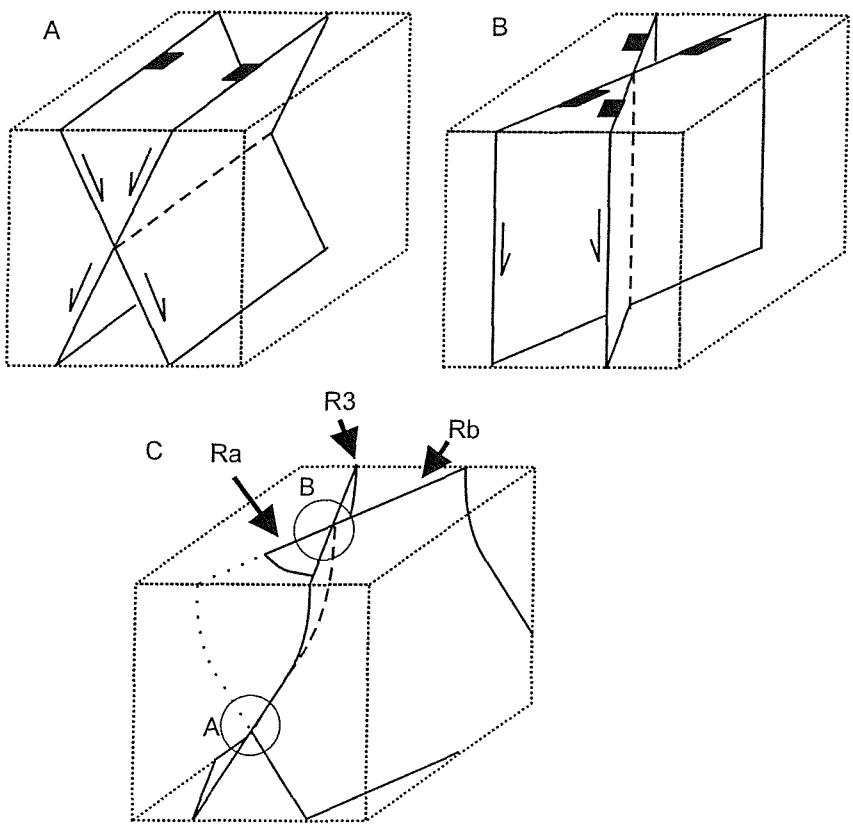

Figure 5.18: Conjugate fault relationships.(A) dipping conjugate faults with horizontal intersection line perpendicular to fault motion. (B) vertical conjugate faults with vertical intersection line parallel to fault motion. (C)Schematic block diagram of intersection of faults R3, Rb and Ra: curved faults with curved intersection line changing from situation (a) to situation (b).

from being at a high angle to the displacement direction where the faults dip at ~60°, to being parallel to displacement direction near the surface.

The displacement rate low in the total for the survey is seen at the point where the antithetic faults Ra and Rb cross R3. Between deposition of HRS3 and HRS1 there was no movement on fault R3 at the conjugate intersection point. In the time both before and after this the displacement rate is reduced at the intersection relative to the survey mean, but the reduction is compensated for in the total by displacements of faults Ra and Rb. Horizon maps shown in chapter 4 (Figures 4.5 – 4.8) show the development of the conjugate faults R3-Ra-Rb. The conjugate relationship changes from where the faults are dipping at ~60° and the line of intersection is approximately horizontal (and perpendicular to the displacement direction) to where the faults are nearly vertical and the line of intersection is also vertical (the displacement direction) (Figure 5.18c). Where the faults intersect horizontally (Figure

5.18a), synchronous displacement on both faults is inhibited, and displacement is expected to be accommodated on several small (sub-seismic) faults. This is observed in the low in the displacement profile of R3 where it intersects the tip of Rb at horizon MCS1 (Figure 4.10, Chapter 4). Rb is not observed crossing R3 at this level, and the intersection forms a T-junction. In the post-glacial sediments where the faults are vertical and the line of intersection is in the displacement direction, displacement is transferred across R3, creating the small fault Ra and an X-junction. In the total displacement profiles (Figure 5.12) and the displacement rate plots (Figure 5.15) the displacement accumulation on Ra is less than on Rb. This result follows from the observation that Rb exists at depth, whereas Ra exists only at the surface. The displacement on Ra is the amount of displacement that has been transferred across R3 and shows that the intersection with R3 changes from a T-junction to an X-junction (Figure 5.18c).

5.6.5 Fault Rc – Asperity Bifurcation

Fault Rc is observed only in the high-resolution profiles as its proximity to fault R3 means it is below the lateral resolution of the MCS profiles. The displacement profile of fault Rc is complimentary to a drop in displacement in R3 between 5000 and 5500 m along strike (Figure 5.10). Although it is not observed directly in the MCS data, its effects are possibly seen in the displacement profiles of horizon MCS1 (Figure 5.10e) as a displacement low in R3 at 4500 – 5000 m along strike. This small feature is interpreted as being where an irregularity in the slip surface of the fault is bypassed by a straighter slip surface in later fault movements, known as an asperity bifurcation (Childs et al., 1996).

5.7 Conclusions

1. Laterally continuous subsurface horizons are identified in the high-resolution data and dated at 17 ± 1 ka, 13.3 ± 1 ka, 11.1 ± 1 ka and 9 ± 1 ka. Continuing sea level rise has led to the locus of sedimentation shifting southwards, reducing the sediment supply in the north of the survey area above the youngest horizon and resulting in erosion and the development of surface expression of the faults here.

2. Throughout the post-glacial sequence, the Rangitaiki Fault has been a fully linked segmented structure, showing no lateral propagation of the individual segments. Despite the level of linkage, the accumulation of displacement is still dominated by the relict segment boundaries.

3. The White Island Fault is interpreted to have formed by linkage of overlapping seg-

ments leading to the zigzag arrangement of the fault trace. Abandoned fault splays are observed at the segment overlaps within the pseudo-3D survey area.

4. The maximum displacement rate observed at any time on the Rangitaiki Fault is 3.8 $\pm$ 2.5 mmyr^{-1}, between 17 and 13.3 ka. The minimum displacement rate observed is zero for periods of approximately 2 ka, at the conjugate intersection of faults R3, Ra and Rb.

5. Aggregate fault displacement profiles spanning c. 2 ka are coherent and smooth for groups of small faults (such as the hanging-wall faults) but irregular for large faults (the Rangitaiki Fault segments).

6. The intersection of conjugate faults R3 and Rb changes from a T-junction, where Rb abuts R3, to an X-junction where displacement on Rb is transferred across R3, forming fault Ra. The reason for this change in fault geometry is the increase in dip of the faults causing the line of intersection of the two faults to rotate from horizontal (perpendicular to displacement and inhibiting synchronous motion on both faults) to vertical (parallel to displacement).

Chapter 6

Normal Fault Growth and Linkage during the last 1.3 Million Years: An Example from the Whakatane Graben, New Zealand[1]

Determination of fault growth rates and fault network evolution at time-scales from 10^4 – 10^6 years has been hampered by a lack of a well-constrained stratigraphic succession that provides a high-fidelity record of fault development over these time periods. Here we show how seismic reflection data of different spatial resolutions can be used to constrain the linkage history and displacement rate variations of a single major fault. We present data collected in the offshore Whakatane Graben, Bay of Plenty, New Zealand, where intense normal faulting occurs as a result of active back extension. The focus of our study is the Rangitaiki Fault, a linked segmented normal fault which is the dominant active structure in the graben. The total linked fault length is c. 20 km long and has a displacement of up to 826 m in the top 1.5 km of sediments. The fault has been actively growing for the last c. 1.3 Ma and has developed from isolated fault segments to a fully linked fault system. Initially, the dominant process of fault growth was tip propagation, with an average displacement rate of 0.52 ± 0.18 mm yr^{-1}. Interaction and linkage became more significant as the fault segments grew towards each other, resulting in the fault network becoming fully linked between 300 and 18 ka. Following fault segment linkages, the average displacement rate of the fault network increased by almost three-fold to 1.41 ± 0.31 mm yr^{-1}. This is the first time that the growth rate of unlinked fault segments has been resolved, and has been shown to be slower than in the subsequent linked fault system.

[1]This chapter is a modified version of an article submitted to the Journal of Geophysical Research. The authors of this article are: S. K. Taylor, J.M. Bull, G. Lamarche and P. M. Barnes. The order of these names represents the level of contribution to the submitted manuscript.

6.1 Introduction

Geological faults develop over long time periods, c. 10^6 y, but variations in the mechanics and kinematics of faulting are poorly constrained over their history. Seismology and geodetic studies provide detailed information on co-seismic displacements and aspects of the seismic cycle; c. 10^2 y. Palaeoseismology and longer term geodetic information may constrain fault movements over several thousand years, but this is very short compared to the time scale of geological processes. The key problem is to integrate these different types of data to understand how fault systems develop through time. Because structural features formed in evolving fault systems e.g. relays, breached relays, transfer faults and overlaps (e.g. Childs et al, 1995, Peacock et al., 2000) are essentially temporary, the study of these features is best addressed in recently active or neotectonic fault systems where temporal constraints are available over periods ranging from 10^2 to 10^6 years. Understanding the detailed planform of fault systems through time will aid the development of rupture segmentation models and help constrain earthquake hazard.

There are two main mechanisms for fault growth: tip growth and segment linkage. The first model considers that fault grow by a process of tip propagation in which the rupture dimensions for each slip event depends on the size of the earthquake and the length of the fault (Walsh and Watterson, 1988; Cowie and Scholz 1992a, b). The second mechanism comprises propagation, interaction and linkage of segments (Peacock and Sanderson, 1991, 1994; Trudgill and Cartwright, 1994; Cartwright et al., 1995, 1996). Linkage provides a mechanism for developing large faults (by coalescing the small faults that nucleate) and localising the deformation after only a few percent strain. The dominant process of fault growth, plus the rate of growth will affect basin geometry and drainage patterns, and thus sedimentary facies and sediment accumulation rates (e.g. Cowie et al., 2000). The fieldwork of Wu and Bruhn (1994) and Cartwright et al. (1995) in Utah has shown that fault linkage may be a dominant mechanism, at least in simple, low-strain settings. Poor temporal constraints on these data mean that the timescales over which these processes occur, and the variations in fault displacement rates that result are poorly defined.

The elucidation of fault behaviour on time-scales of 10^4 to 10^6 years requires an area with good stratigraphic resolution, which most commonly occurs where the fault system is youthful and active, and sediments record the displacement history. In particular, to faithfully record normal fault development three factors are critical: (1) the sedimentation rate must be of the same order of magnitude as the dip-slip rate on the faults; (2) the sedimentary history must contain identifiable horizons or surfaces whose date of formation

is well constrained; and (3) it must be possible to correlate horizons across the fault from hanging-wall to footwall.

The Whakatane Graben, the offshore continuation of the Taupo Volcanic Zone, New Zealand (Figure 6.1), has an exceptionally well developed array of normal faults widely distributed over the graben that meets these criteria and is amenable to study using high-resolution seismic reflection surveying and sediment coring. Pseudo-3 Dimensional seismic reflection experiments were conducted in 1998 (multichannel seismic) and 2000 (single channel chirp and boomer) over an active fault in the graben, providing a set of closely spaced seismic profiles of differing vertical resolutions. The aim of this chapter is to use a long-timescale history of fault array development to place temporal constraints on models of fault growth. We integrate the two sets of pseudo 3D seismic data to document the full spatial and temporal development of a central part of the Whakatane Graben, where we identified several fault strand terminations and relays within a thick late Pleistocene sequence.

The focus of this chapter is the development, linkage and rate of growth of the Rangitaiki fault system (Figure 6.1). This fault is the main structural element of the central part of the graben, as shown by the largest measured displacement within the graben and a vertical slip-rate of 2.3 $\pm$ 0.5 mm yr^{-1} over the last 18 ka (Wright, 1990). Furthermore, the Rangitaiki Fault has a hanging wall and footwall stratigraphy that is well imaged on seismic reflection data.

6.2 Regional Tectonic Setting

The Whakatane Graben is situated in shallow water depths in the Bay of Plenty (Figure 6.2). The graben is part of the currently active Taupo Fault Belt, which is the youngest rift system within the Taupo Volcanic Zone (TVZ). The TVZ marks the zone of Quaternary back-arc rifting and calc-alkaline volcanism associated with the oblique westward subduction of the Pacific plate beneath the Australian plate at the Hikurangi plate-boundary margin (Cole, 1981; Wright, 1992). The TVZ has been active for the last 2 Ma, while large caldera forming ignimbrite eruptions have occurred for the last 1.6 Ma (Houghton et al., 1995). The Whakatane Graben began to subside between 0.6 and 1 Ma (see Nairn and Beanland; 1989; Walcott, 1984; Wright, 1990; 1992; Davey et al., 1995). Near the Bay of Plenty coast, the extension rate has been estimated to be 12 mm yr^{-1} in a NNW-SSE direction across the full 120 km of the bay (Walcott, 1987), although Nairn and Beanland (1989) note that the strain is concentrated within the Whakatane Graben. The most recent analysis of geodetic data within the TVZ shows that strain is not homogeneous, and suggests an extension rate of 8 $\pm$ 2 mm yr^{-1} for the period 1949-1997 (Darby et al., 2000).

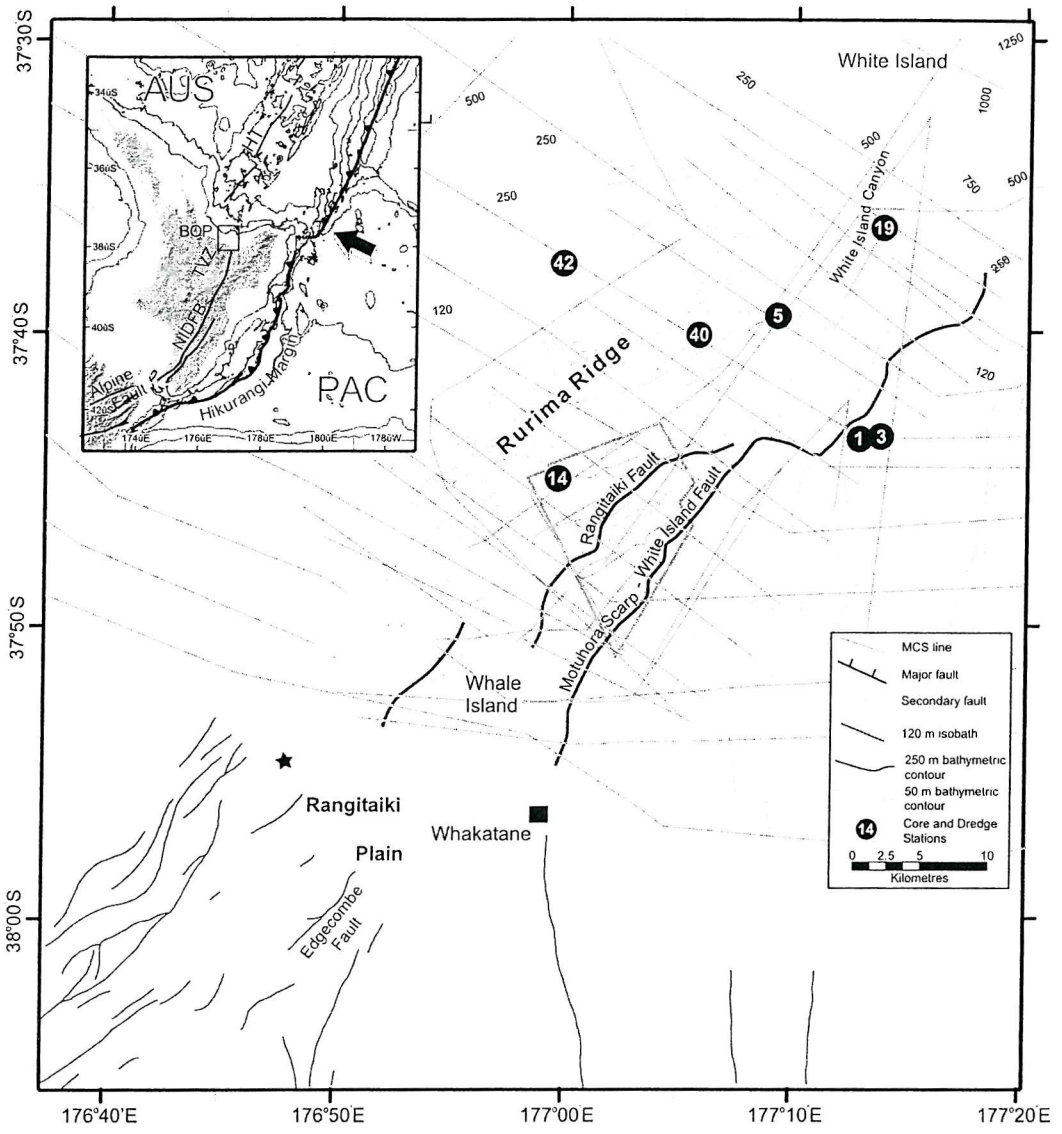

Figure 6.1: Offshore bathymetric map and onshore digital terrain model of the central Bay of Plenty, with simplified structural features modified from Wright (1990), Lamarche (2000) and onshore fault database from the Institute of Geological and Nuclear Sciences, New Zealand. Shaded area indicates pseudo 3D-experiment. Star marks the main-shock epicentre of the M_L6.3 Edgecumbe earthquake from Nairn and Beanland (1989). Insert: Geodynamic environment of North Island, New Zealand. Arrow indicates NUVEL 1A PAC-AUS relative plate motion (De Mets et al., 1994). Bathymetric contour 500 m. bold lines indicate major fault systems, NIDBF: North Island Dextral Fault belt, HT. Havre Trough, TVZ: Taupo Volcanic Zone; Teethed line indicates Hikurangi subduction front.

The largest part of the Whakatane Graben extends some 50 km offshore beneath the continental shelf of the Bay of Plenty from the coastline to White Island volcano (Wright, 1990). The graben lies in less than 200 m water depth except for deeply incised canyons in the north. Morphologically, the graben is characterised by a 15 km-wide subdued bathymetric trough bounded by the Motuhora scarp to the east and Rurima Ridge to the west.

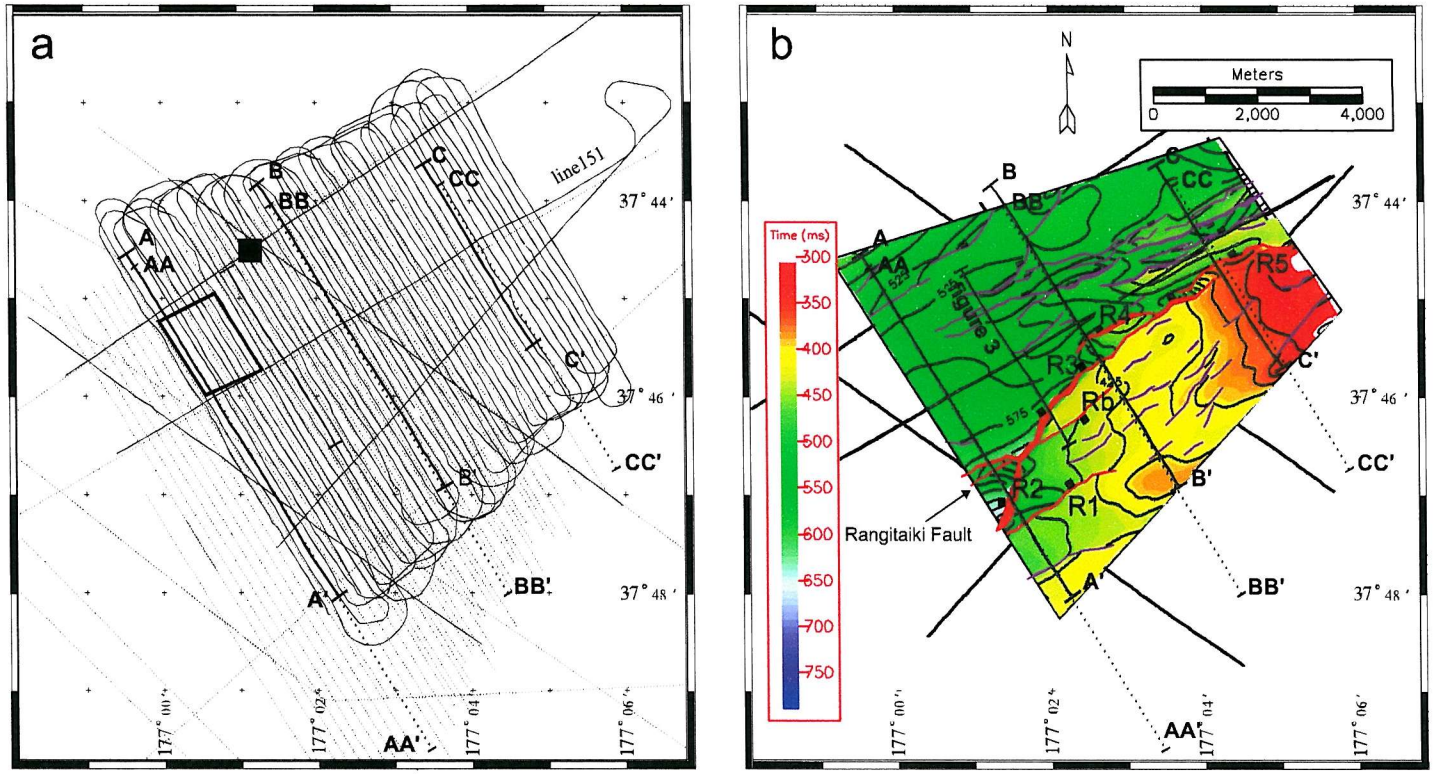

Figure 6.2. (a) Seismic profiles in the pseudo-3D survey area. The survey data comprises multichannel seismic profiles and 3.5 kHz profiles(solid lines) and high-resolution chirp and boomer profiles (dotted lines). The survey location is indicated in figure 6.1. The refraction sonobuoy was recorded along line 151. The position of multichannel seismic profiles A-A', B-B' and C-C' and high resolution profiles AA-AA', BB-BB' and CC- CC' illustrated in Figures 6.6 and 6.7 are shown. The location of core TAN99-14/14 is shown by the black square. Sediment thickness values from the small boxed area were used in calculating the horizon ages; note that there are no faults in this area. (b) Horizon and structure map of the shallowest horizon interpreted in the multichannel seismic reflection data (MCS1). The position of the profile shown in figures 4 is highlighted, as are the positions of multichannel seismic profiles A-A', B-B' and C-C', shown in figures 7. The segmented Rangitaiki fault is the major fault system running through the area imaged in the multichannel seismic reflection data. Note that the White Island Fault (see Figure 1) is just outside the area, but is imaged in the high resolution seismic data.

Seismic reflection data show that the Whakatane Graben is characterised by a 15-20 km wide zone of active normal faulting with shallow sub-surface displacements on many faults (Lamarche et al., 2000; Wright, 1990). The graben is filled by approximately 3 km of sediments overlying an irregular basement interpreted as Mesozoic greywackes with volcanic intrusions (Davey et al, 1995). Structurally the graben is limited to the east by the west dipping White Island Fault and to the west by a diffuse zone of intense faulting on the crest of Rurima Ridge. The White Island Fault has a conspicuous seabed expression along the Motuhora scarp, which reaches 80 m in height, and along the White Island canyon. Extensional tectonic structures of the Whakatane Graben extend northward to the base of the continental slope at 36°45'S (Wright, 1990). Davey et al. (1995), on the basis of a single multichannel seismic (MCS) reflection profile postulate that the locus of active deformation has moved eastwards with time, and that the most recently formed faults occur in the eastern margin of the Whakatane Graben (Figure 6.1).

Wright (1990) estimated minimum subsidence and extension rates since 18 ka, from 3.5 kHz seismic reflection data acquired across the offshore graben. Subsidence rates range from 0.4 to 3.5 mmyr^{-1}, with an average of ca. 2 mm yr^{-1} (Wright, 1990). Summation of fault heaves derived from measurements of vertical deformation and assuming a constant fault dip of 45° to 10 km depth indicate an extension rate of 3.5 $\pm$ 1.7 mm yr^{-1}. Subsidence within the onshore graben is estimated by Nairn and Beanland (1989) and Beanland et al. (1990) to be 1 – 2 mm yr^{-1} since 0.6 Ma, while the western edge has been uplifted at c. 1 mm yr^{-1}, and the eastern edge by c. 0.5 mm yr^{-1}.

The Rangitaiki fault lies in the centre of the graben and extends for about 20 km with a mean orientation of 57° N. The fault runs from 2 km north of Whale Island and ends in a complex deformed zone 1.2 km from the White Island Fault (Figure 6.1). We identify five active linked segments in the Rangitaiki Fault, and position the fault correctly compared with previous work.

6.3 Data Sources

The data used in this study is part of a large dataset covering the central Bay of Plenty and the entire offshore Whakatane Graben and is described in detail in chapter 2, with a summary given here. The data consists largely of MCS air-gun and high-resolution single channel seismic reflection data, as well as a number of shallow core and dredge samples. This dataset includes regional seismic profiles and a pseudo-3D seismic reflection experiment over the central Whakatane Graben, which includes the Rangitaiki Fault. Seismic refraction data were collected to improve velocity control for depth conversion of the MCS data. The

variety of resolutions and penetration enabled us to constrain the evolution of the fault system on timescales of thousands (the top 1 – 60 m) to millions of years (the top 1.5 km) (Lamarche et al., 2000).

This chapter focuses on the Rangitaiki Fault and pseudo-3D survey (Figures 6.2 and 6.3), which covers an area of 7.5 x 5 km with seismic profiles 150 m apart. The area was chosen from preliminary shipboard analysis that indicated a well-developed stratigraphy with good potential for recording fault evolution. Excellent quality seismic data were recovered in this area, gas within the sediments was scarce and sufficient water depth limited water-bottom multiple interference.

6.3.1 Multichannel Seismic Reflection Data

The seismic reflection data was collected using a GI gun seismic source and a 48-channel streamer aboard *R/V Tangaroa* in November 1999. The GI gun was used in harmonic mode ($75/75in^3$), which optimised the peak to peak energy ratio (Pascouet, 1991), thus combining a high-frequency input signal with sufficient energy to provide high quality data to a minimum of 1.5 seconds two-way travel time (TWT).

Data processing included true amplitude recovery, band-pass filter (minimum phase, with corner frequencies 15, 20, 120 and 150 Hz), predictive deconvolution (operator length 80 ms, predictive distance 8 ms), long offset mute, normal move-out correction, stack and migration (Kirchoff-Stolt migration using 105 % of stacking velocities). The stacked seismic data are 12 fold with a CDP spacing of 6.25 m (see appendix A).

6.3.2 High Resolution Seismic Data

3.5 kHz seismic reflection profiles were collected in 1999, along with the MCS pseudo-3D box and regional profiles in the offshore Whakatane Graben. Subsequently in 2001, 160 km of Chirp sub-bottom profiler, 460 km of Boomer sub-bottom data and 30 km of sidescan data were acquired aboard *R/V Kaharoa*. Forty-six strike-perpendicular boomer profiles were collected across the Rangitaiki Fault, overlapping the pseudo-3D box of the *R/V Tangaroa* cruise, although extending further to the south and east to include the hanging wall sediments of the White Island Fault (Figure 6.2). These profiles provided information on the top 60 m of sediments. The post 20 ka maps and fault displacement data presented in this paper were derived from the digital boomer dataset. The 3.5kHz and chirp profiles were utilised in improving line-to-line correlation of faults and regional interpretation of stratigraphy.

Tidal and swell effects are below the resolution of the MCS data, but both the Chirp

sonar and Boomer profiles required tide and swell filtering. These filters considerably improve the interpretability of the profiles, and do not affect measurement of fault displacement. The boomer data illustrated in this paper were bandpass filtered (zero phase, corner frequencies 300, 1000, 2500, 3000 Hz) following the tidal and swell filtering (see chapter 2 and appendix B).

6.3.3 Sonobuoy data

One seismic refraction line was recorded using a sonobuoy within the central Whakatane Graben, along line 151 (Figure 6.2). Three major refracted arrivals could be identified enabling us to construct a 2D ray-tracing forward model and invert the direct, reflected and refracted arrivals. The model was constructed iteratively downward from the well-constrained velocity profiles of the water column (via an XBT), and near-surface sediments. The interval and layer boundary velocities obtained from the sonobuoy analysis are summarised in Table 6.1. These values agree well with those from velocity analyses of the MCS reflection data.

Refractor	Layer depth in model [m]	Interval Velocity [m s-1]	Layer Boundary Velocity [m s-1]		Calculated Two way time to Horizon [ms]
			upper	lower	
Sea Surface	0	1500±10	0	1490	
Seabed	100±10	1715±20	1510	1610	133±10
A	300±30	1925±50	1820	1850	366±40
B	630±60	2160±50	2000	2050	709±82
C	1180±100	2700±100	2270	2400	1218±137

Table 6.1: Velocity model from Sonobuoy Analysis. Note that horizons A and C map to MCS1 and MCS 3, but horizon B cannot be reliably associated with MCS2.

6.3.4 Cores and Dredge Samples

Direct age control consistent with the transgressive sedimentary sequence in the graben is provided by 25 piston cores described by Kohn and Glasby (1978) and 18 shallow piston cores collected as part of this project (Lamarche, 1999). Particular reference is made here to Core 14 (figure 6.2), which sits within the detailed survey area, and for which age control has been established. The eighteen cores collected within the study area were used to derive velocity for the near-surface sediment, and to constrain the time-to-depth conversion. The cores, up to 4.5 m long, were split and logged using a whole core geophysical logger (Best and Gunn, 1999). An average interval velocity of 1550 ms^{-1} was found for the relatively uncompacted near-surface sediment within the pseudo-3D box.

6.4 Stratigraphic Framework

Sediments within the Whakatane Graben provide a high-fidelity record of fault behaviour. In order to constrain the rates at which faults have grown and interacted, we need to understand the stratigraphic framework and age constraints on horizons within the sediment package, which have been used for displacement analysis. The stratigraphy, prominent reflectors imaged and age control of the each of the seismic reflection datasets will be considered in turn.

6.4.1 Deeper Stratigraphy (18 ka – 1.5 Ma)

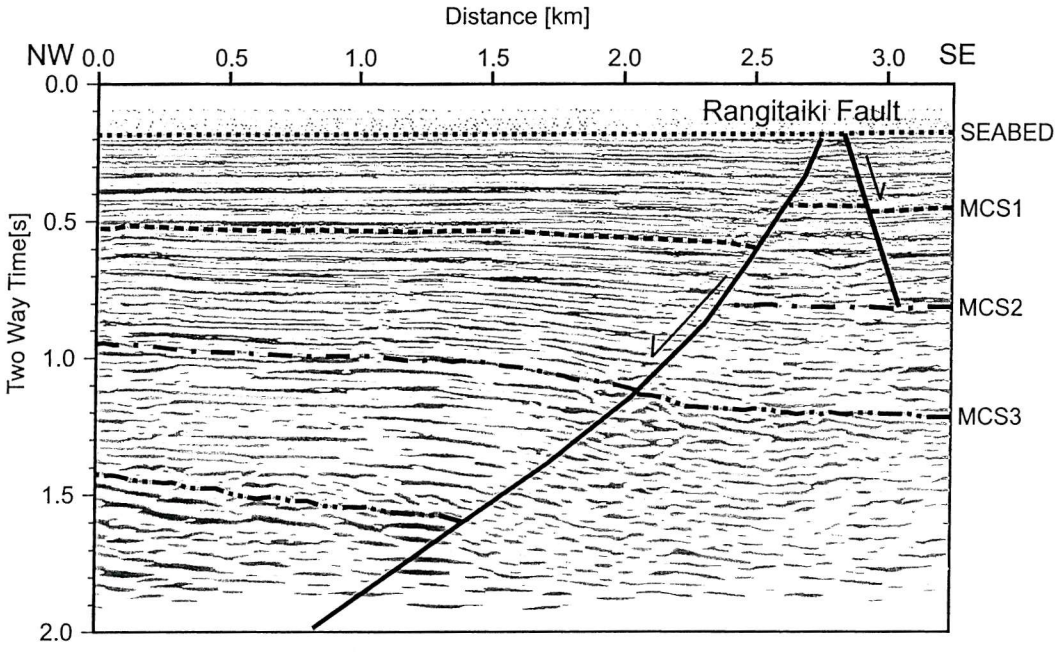

Figure 6.3. An example of the layered sedimentary sequence imaged by the multichannel seismic data, location shown in figure 6.2. The Rangitaiki Fault is an extensional growth fault, with no measurable displacement on the MCS data at the seabed. The maximum displacement is generally at horizon MCS3, the highest displacement measured is 826m (this profile). The average dip of the fault is 61° although this is variable both vertically and along strike. Horizons MCS1 and MCS2 are characterised by onlap above high amplitude, continuous reflections. Horizon MCS3 is identified by a strong but discontinuous low frequency reflection associated with a large velocity contrast. The time section is shown at a scale chosen to minimise vertical exaggeration (~1:1 @ 2000 ms^{-1}).

Three reflectors (MCS1-3) within the MCS profiles collected by the *R/V Tangaroa* could be unambiguously tied around the 3D box. The overall geometry to 2 seconds TWT is consistent with a crustal seismic reflection profile across the Bay of Plenty which imaged

a variable sedimentary thickness of up to 2.5 seconds TWT, with basement being clearly recognised in places (Davey et al., 1995; Davey and Lodolo,1995). The sediments are displaced by extensional faults, and show thickening into the hanging wall of the fault. The seabed multiple is very low amplitude because of the soft sediment covering the seabed in the graben. Although the total age range of the sedimentary sequence imaged is constrained to 0 – 2 Ma (Nairn and Beanland; 1989; Walcott, 1984; Wright, 1990; 1992; Davey et al., 1995) age control on the reflectors imaged is constrained by extrapolation of near-surface sedimentation rates, and this is now discussed.

Horizon MCS1 is identified as a strong positive and laterally continuous reflector overlying a unit of variable thickness characterised by up to three strong negative peaks. Above horizon MCS1 the overlying sediments onlap (Figure 6.3, in the hanging wall of the Rangitaiki Fault), although this angular relationship is not well developed on dip sections owing to the regional dip of the seabed. Similarly, horizon MCS2 is defined by a strong reflection with onlapping sediments above (Figure 6.3).

Horizon MCS3 is defined mainly as a change in seismic character with the seismic attribute becoming noticeably lower frequency (Figure 6.3), and this coincides with a sharp increase in velocity (Table 6.1) giving rise to a strong reflector. Figure 6.3 illustrates a rotated fault blocks, with layered sediment above and more chaotic low-frequency reflections below. There are often diffractions from the tops of the fault blocks on horizon MCS3, although these have been reduced considerably by migration. Horizon MCS3 is interpreted as a change in compacted sedimentary rocks. Dredge and core stations 1, 3, 5, 19, 40, and 42 (Figure 6.1) from positions where reflections in older sequences are exposed at the seafloor, recovered a range of lithologies including weakly to strongly compacted mudstone and sandstone, carbonate-cemented siliceous lapilli tuff, and indurated and cemented volcanoclastic sediments. In addition, on Whale Island tuffaceous marine sediments separated by lavas, volcanic breccias and slope-wash deposits are exposed (Burt et al., 1996), and indicate an inhomogeneous sequence of mudstone and volcaniclastic sediments.

We obtained and dated rock dredge samples from seafloor exposures in order to constrain the age of the multichannel seismic sequence. Dredge samples 5, 19, and 40, from sediments correlated in seismic lines to lie stratigraphically above MCS1, or within 200 ms TWT of this horizon, have been dated biostratigraphically using nannoflora, foraminifera, and palynology, to be of New Zealand Haweran (Wq) stage (<0.34 Ma). Considering the stratigraphic positions of these samples, we infer a conservative age range of 300 ± 100 ka for MCS1 (Table 2). Considering the depth of MCS1, this age implies an accumulation rate of compacted sediment of 1.05 ± 0.30 $mmyr^{-1}$. This rate is in broad agreement with the

post-18 ka sedimentation rate derived in the following section.

No such biostratigraphic ages are available for the seismic sequence below MCS1. Ages for MCS2 and MCS3, of 770 ± 240 ka and 1340 ± 420 ka, with a 30% error, similar to that of MCS1 age, have been inferred by extrapolating the sediment accumulation rate above MCS1 to the depth converted positions of these horizons (Table 6.2). These ages seem reasonable considering the relative stratigraphic positions of the reflectors in the extension graben sequence and the likelyhood that much of this sequence developed since inception of backarc extension about 2 Myr ago.

Layer	Thickness [ms TWT]	Interval Velocity [ms^{-1}]	Thickness [m]	Age [ka] of base of layer
SEABED-MCS1	367±21	1715±20	315±18	300±100
MCS1-MCS2	513±25	1925±50	493±27	770±240
MCS2-MCS3	556±32	2160±50	601±37	1340±420

Table 6.2: Age estimates for the horizons interpreted in the MCS data. Age of MCS1 is constrained by biostratigraphy, while ages for horizons MCS2 and MCS3are calculated using a 1.05 mm yr^{-1} sedimentation (see text). Errors are discussed below.

6.4.2 Near-surface Stratigraphy (0 – 18 ka)

Within the graben there are four strong laterally continuous and easily correlated reflectors in the chirp, boomer and 3.5 kHz data (HRS1 – 4), which can be used to constrain fault evolution (Figure 6.4a). Their geometry is summarised in Figure 6.4b, illustrating the sediment wedge on a strike-line up the axis of the Whakatane Graben from the Whale Island platform through the 3D box. HRS4 overlies an eroded stratigraphy with the wedge of sediments on a strike line north of Whale Island revealing that horizons HRS1-3 progressively onlap HRS4 towards the coast (Figure 6.4b). The unit between HRS4 and HRS3 thins shoreward, whereas the most recent sediments above HRS1 thicken shoreward. The sequence immediately beneath HRS4 (Figure 6.4b) dips and progrades to the west.

It is widely recognised (e.g. Lambeck and Chappell, 2001) that, during the Quaternary, ice ages were times of sea level low stands and interglacials were times of relatively high stands. The New Zealand coastline saw sea-level rising from at least 18 ka until 6.5 ± 0.1 ka with a notable stillstand from 9.2 – 8.4 ka, and a less significant stillstand from 7.5 – 7.3 ka (Herzer, 1981; Gibb, 1986; Carter et al., 1986). Gibb (1986) found that during the last 6.5 ka, that sea-level has been relatively stable. The coastline of the Rangitaiki Plain was deeply embayed at 6.5 ka and has since prograded at least 10 km with volcaniclastic sediment supply from major rivers. Notable sedimentation episodes followed the Whakatane, Taupo

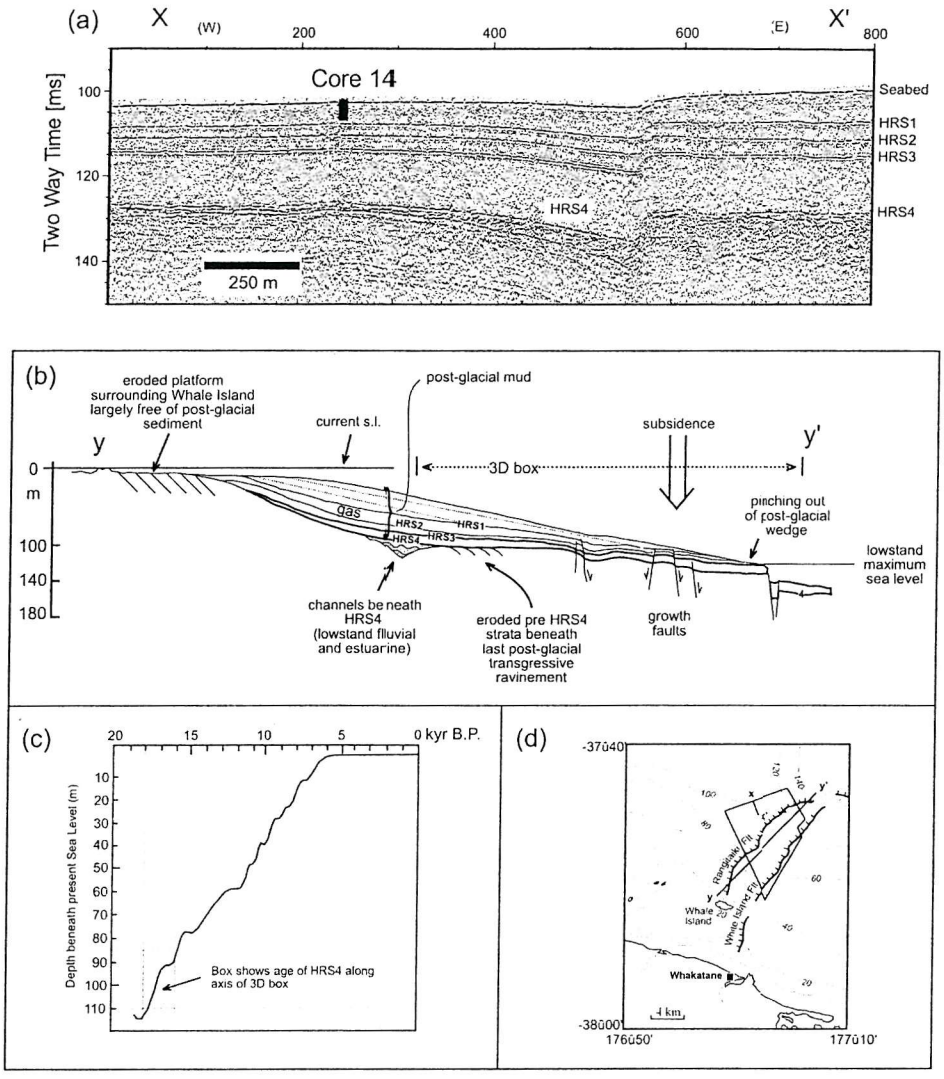

Figure 6.4. (a) The position of core 14 and the four horizons interpreted in the high-resolution seismic data used for measuring fault displacements, location shown in d. Note that HRS4 is picked as the reflector immediately underlying the transparent layer, and is interpreted as a transgressive marine ravinement associated with the lowstand maximum (see b). The small fault at CDP 560 has a maximum displacement of 9m at horizon HRS4, and thickening of the syn-deformational sediments can be seen in the hangingwall of the fault. Vertical Exaggeration is c. 14:1. (b) Schematic of the post-glacial wedge on a strike-line up the axis of the Whakatane Graben from Whale Island through to the 3D box (position shown in d). The channel system shown would have incised during the last lowstand when the mean elevation of the 3D box would have been at least 70 m above the lowstand maximum. The channels are preserved due to subsequent rapid episodic transgression over the area. (c) The sea-level curve of Carter et al. (1986), and the likely age range of HRS4 in the 3D box is 16-18ka. Note that sea-

and Kaharoa pyroclastic eruptions (Nairn and Beanland, 1989; Beanland and Berryman, 1992).

The Rangitaiki fault trace north of Whale Island lies at water depths of 60 – 100 m (Figure 6.1). It is to be expected that, at the last sea-level lowstand (with sea-levels 120 – 140 m below present), an incising fluvial system would have drained the hinterland to the south within the axis of the subsiding Whakatane Graben. HRS4 is the youngest regionally extensive erosion surface, and likely formed in very shallow water (< 20 m) at the low-stand maximum (120-140 m), and diachronously between 120 m and the coast from 18 – 6.5 ka as the zone of marine abrasion moved up. Using the sea-level curve of Carter et al. (1986), and inferred water depths in the study area near the Rangitaiki fault at the time of formation of HRS4, we can state that the age of HRS4 in the area relevant to this study is 16 – 18 ka (Figure 6.4b). Underlying HRS4 there are clear examples of 'nested' channels, which are most likely fluvial systems that fed the Canyon system to the north during the last lowstand. The fact that these fluvial channels are preserved supports sea-level rising rapidly over the area of the 3D box during the formation of HRS4. We cannot rule out a tidal-estuarine origin for these systems, however this is not important in terms of assigning an age to HRS4. HRS4 is the transgressive (diachronous) marine ravinement surface, whereas the base of the nested channel-fill sequence, whatever its origin, is the true sequence boundary for the last sea-level cycle.

Several lines of seismic stratigraphic evidence indicate that the near-surface 5 – 60 m thick stratigraphic sequence represents the post c. 18 ka transgression. Firstly, a series of landward thinning, conformable and onlapping seismic reflectors form the uppermost sedimentary succession that unconformably overlies a strongly reflective horizon, which truncates older stratigraphy. Secondly, fluvial channels occur near-shore beneath the sequence. Thirdly, a still-stand terrace at -109 m immediately east of the graben, which is correlated with the 18 ka stillstand (Carter et al., 1986), conformably underlies an identical, but condensed stratigraphic sequence to that found in the graben. Our estimate of 9 (± 1) ka for HRS1 agrees with the previous estimate of 8.5 – 9.4 ka made by Wright (1990). Underlying the transgressive sequence is HRS4, which as discussed earlier, is interpreted as a transgressive ravinement surface.

Core 14 sediment is a green coarse to fine silty-clay punctuated by distinct coarse-grained ash rich events down the depth (4m) of the core. Shells at a depth of 2.67 m have a C14 calibrated age of 6856-6609 years B.P. (2002) at the 95 percent confidence interval. This together with the presence of the Mamaku tephra could be used to constrain the sedimentation rate within the core. At this site the sedimentation rate was less than

0.4 mm yr−1 for the last 6.6 – 6.8 ka, but substantially higher (1.0 mm yr−1) prior to that. The shallowest reflector used to measure fault displacement offsets (HRS1), is just beneath the base of the core (c. 4.2 m), and is consistent with the presence of the primary Mamaku Tephra (7.35 ka; Froggatt and Lowe, 1990) at a depth of 3.40 – 3.43 m. The lower sedimentation rate for sediments less than 6.5 ka can be ascribed to a landward shift in the position of maximum sediment accumulation.

Horizons HRS2 and HRS3 are inferred to be 11.1 (± 1) and 13.3 (± 1) ka. These ages were derived by taking sediment thicknesses over a 2 km^2 area, indicated in Figure 6.2a, close to core 14, and interpolating between the inferred ages of the HRS1 (9 ka) and HRS4 (16-18 ka). The area used in the age calculation was chosen because it is close to the site of core 14; relatively unfaulted and is away from the influence of the Rangitaiki Fault.; and is representative of the overall stratigraphic framework shown in Figure 6.4b. The uncertainties in age stated reflect that the HRS4 unconformity is diachronous, but that the water depths within the 3D box area are relatively uniform (a range of 20 m).

6.5 Measurements of Fault Displacement

All fault displacement diagrams in this paper are strike-projected along a N57°E x-axis, which corresponds to the average strike of the Rangitaiki Fault. In this projection the x-axis is referred to as 'along strike' and the perpendicular y-axis as 'across strike'. This projection displays fault displacements advantageously, and is valuable for comparing faults across strike (e.g. Childs et al., 1993). Most fault segments within the central Whakatane Graben are only slightly oblique to the x-axis.

The fault planes exhibit variable dip laterally and vertically, so both the heave and throw components of fault movement are measured, and combined to give the displacement. The difference in displacement on a fault between successive horizons represents the displacement increment in the period between deposition of the two horizons [Childs et al., 1993]. Fault displacement rates for each time period were calculated using the displacement difference between horizons and age estimates of those horizons.

6.5.1 Aggregate Displacement Profiles and Average Displacement Rate Values

Strike projected displacement measurements are summed across strike to produce aggregate displacement profiles for the Rangitaiki Fault on each horizon. Average displacement rates for the Rangitaiki Fault system are calculated using aggregate displacement rates across the length of the survey area and taking the mean value. Mean displacement rates are used

to describe relative changes in activity on the Rangitaiki Fault as they include more of the data and are more reliable than single observations of maximum displacement (Dawers et al., 1993).

6.5.2 Sources of Error

Errors in the measurement of fault displacements and sediment thickness come from uncertainties in horizon picks, the interval velocities used in depth conversion and corrections for sediment compaction. Other sources of uncertainty – for example acquisition and time migration – are considered negligible (see Thore, 2002 for a review on error in MCS interpretation).

Uncertainties in horizon picks are estimated to be one wavelength. The nominal frequency of the data at horizon MCS1 is 70 Hz, reducing to 40 Hz at MCS3. This equates to ± 15 ms at MCS1 and ± 25 ms at MCS3. For the high-resolution boomer profiles, an estimated uncertainty of ± 0.5 ms is included in each horizon pick. Seismic profiles where the interpretation of the horizons was ambiguous were not included in calculating the fault displacements. The velocity used for depth migration of high-resolution profiles was determined from in situ physical property measurements made on cores collected within the Whakatane Graben, a value of 1550 ± 25 ms^{-1}. Velocities used for depth migration of the MCS horizons were determined from the sonobuoy model using wide angle reflected and refracted arrivals. The errors derived from inverting the model are shown in table 6.1.

Decompaction is performed using the assumption that the change in porosity with depth follows an exponential curve with parameters defined by sediment type [Sclater and Christie, 1980]. In the case of growth faulting, displacement is accumulated on a fault whilst it is being buried, so a proportion of the displacement is accumulated on sediments that have already been compacted. Decompaction of displacements must take into account the displacement that occurred whilst the horizon was near the surface – which should be decompacted to the surface value of porosity – and displacement that occurred whilst the horizon is at the depth the measurements were taken at, where no decompaction is required. The effect of varying the parameters of decompaction through a reasonable range for the sediments studied gives a variation in displacement of around 2%. The effect of sedimentary compaction is greatest where the sediments are thickest – the difference between decompacted and compacted fault displacement measurements remains within the estimated uncertainty range for the displacement.

In many cases there is some fault drag adjacent to the fault planes observed in both the footwall and the hanging-wall. This local perturbation to the displacement fields was

corrected for using the technique employed by Chapman and Menielly [1991] and Mansfield and Cartwright [1996] whereby the horizons are projected towards the fault plane.

6.6 Results

In this chapter we first describe in general terms the structure of the central offshore Whakatane Graben, as interpreted from the 3D-seismic experiment, in order to demonstrate that the Rangitaiki Fault is the main structural feature in the area. We subsequently provide detailed information on the structures of the Rangitaiki Fault from five individual segments to a single linked fault, and finally discuss the processes involved in the evolution of the Rangitaiki Fault, chiefly fault tip propagation and linkage.

6.6.1 Structural Style in the Whakatane Graben

In all, over eighty fault segments were identified displacing the seven horizons interpreted in the pseudo-3D seismic survey (figure 6.5), the most active are those making up the Rangitaiki Fault and White Island Fault networks. Displacements on horizon HRS4 range from the resolution of the boomer data (50 cm) up to 50 m. The spatial activity of faults within the detailed study area can be illustrated with an isopach map of sedimentation through the last 16-18 ka (Figure 6.5). Two main fault systems dominate the area: the Rangitaiki Fault, which is the subject of this paper, and the White Island Fault. The White Island Fault is the dominant fault at the eastern boundary of the Whakatane Graben, and in contrast to the Rangitaiki Fault is not well infilled with sediment and retains a large surface expression throughout the survey area. In addition to the major Rangitaiki and White Island Fault systems, smaller faults displace the sediments in the blocks between. In the hanging wall of the Rangitaiki Fault there is a series of smaller faults related to a graben (profile CC-CC on Figure 6.6). Between the Rangitaiki Fault and White Island Fault there are several relatively low displacement faults, some of these faults form a hanging wall splay at a bend in the White Island Fault (Figure 6.5). The thickest accumulation of sediments is found along the Rangitaiki Fault wall. This is in contrast with sediment thickest accumulation found between 300 and 1000 m west of the White Island Fault wall (AA' on Figure 6.6a). The positions of three example seismic profiles shown in Figure 6.6 (high resolution seismic) and Figure 6.7 (multi-channel seismic) are shown on Figure 6.5, and on Figure 6.2b respectively. These seismic profiles show major faults displacing the full thickness of the section, with some smaller faults that are limited in vertical extent. With few exceptions, the faults have been active whilst the sediments were deposited, shown by thickening of the sediments in the hanging wall and displacement on the faults decreasing

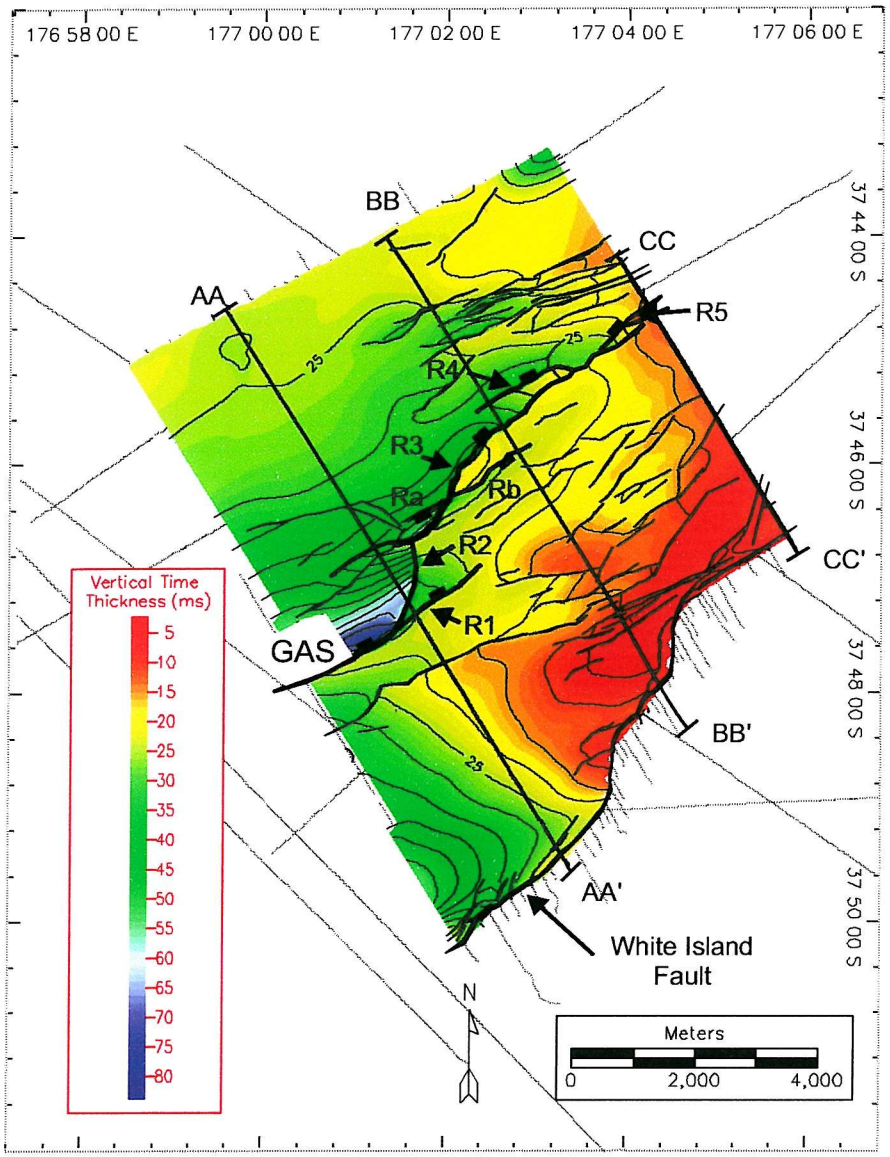

Figure 6.5. Fault and Isopach map of sediments deposited during the last 16 - 18 ka derived from high resolution data shown in Figure 6.2. The five segments of the Rangitaiki fault (R1 - R5) are shown with clear sediment depo-centres in their hanging-walls. The White Island fault, which has a scarp at the seabed, is also shown with the centre of the sediment depo-centre occurring c. 1 km away from the fault. See text for more discussion. The position of the three profiles shown in Figures 6.6 and 6.7 is also shown.

upwards. The faults have an average dip of 61° between horizons MCS1 and MCS3 and gradually increase in dip to 70° to near vertical in the top c. 100 m.

In profile A-A (Figure 6.6 and 6.7), deformation is concentrated on the two major fault systems (Rangitaiki and White Island), with relatively flat lying sediments and very few faults between. In contrast, in the centre of the survey area (profile B-B), the faulting is

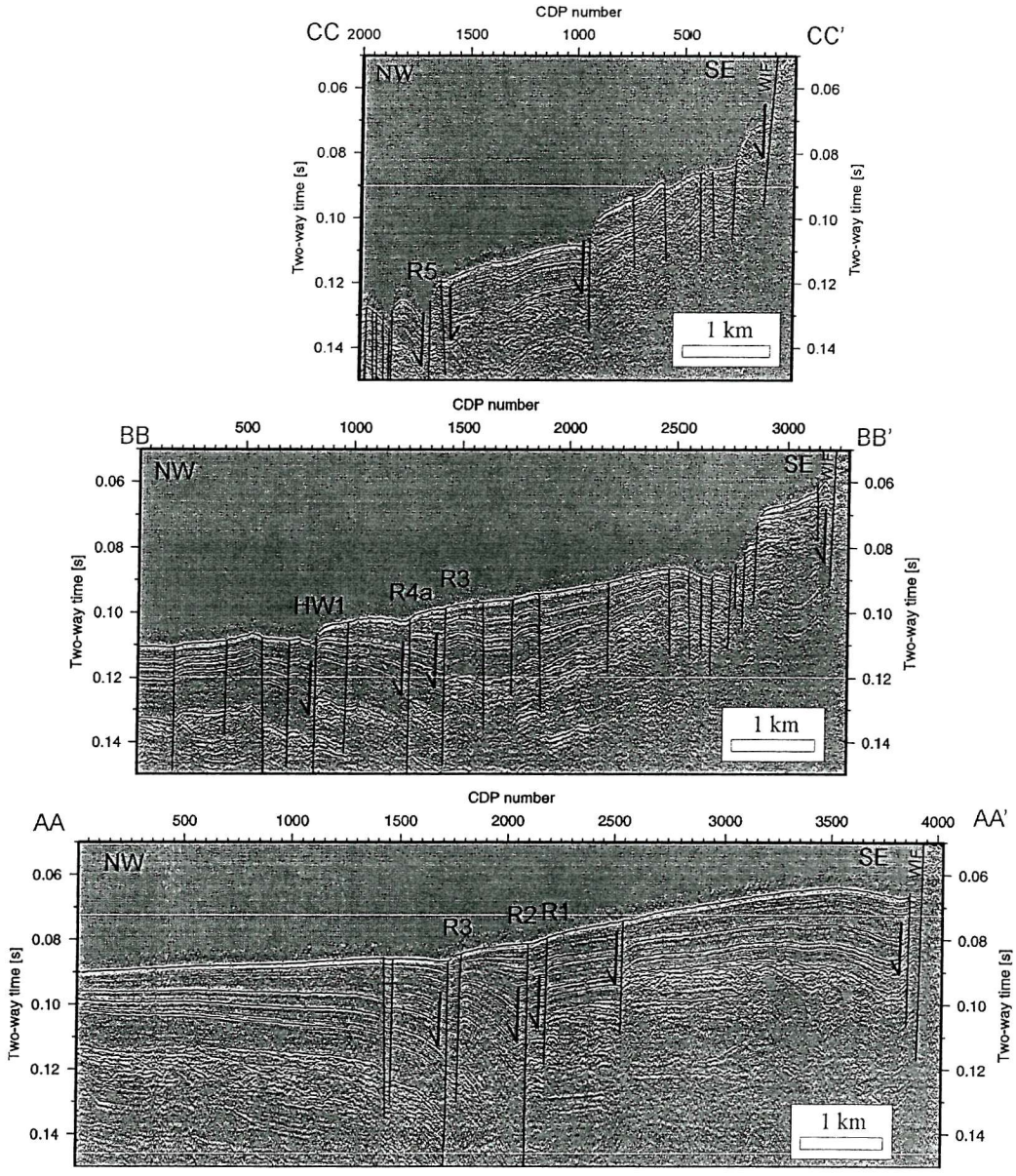

Figure 6.6. Three example boomer profiles illustrating the Rangitaiki and White Island faults, showing data (figure 6.6a) and interpretation (figure 6.6b). The locations of profiles A, B and C are shown in figure 6.2. These profiles image the post-glacial sedimentation in the Whakatane Graben (horizons HRS1-4 and a probable fluvial system beneath). Vertical Exaggeration is c. 45:1.

more evenly distributed through the section and the sediments are tilted into rotated fault blocks in the hanging wall of the Rangitaiki Fault. The block-bounding faults are laterally discontinuous, and are not seen in profile C-C where the hanging wall of the Rangitaiki Fault is dominated by a collapsed graben.

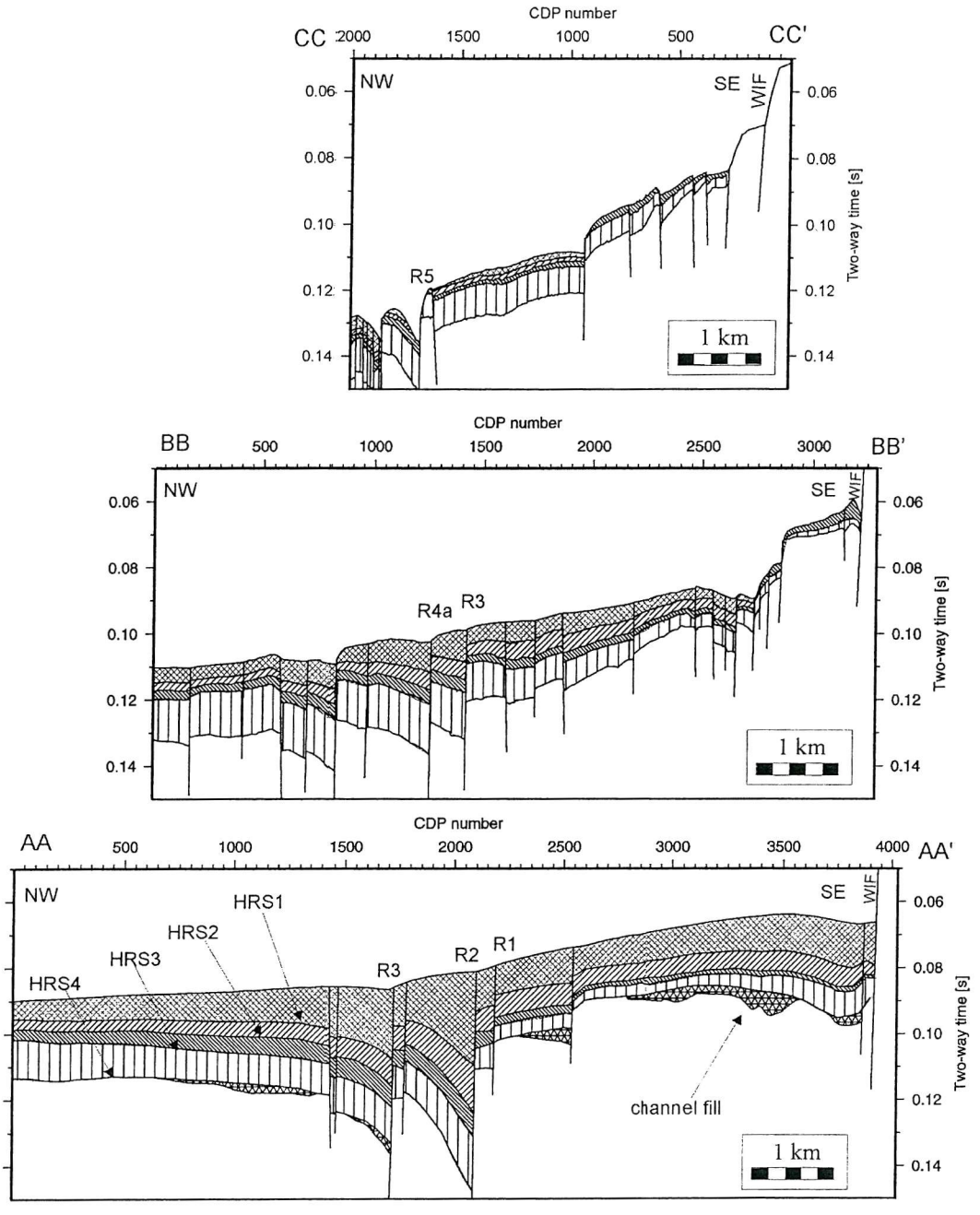

Figure 6.6b: Interpreted boomer profiles, see previous page for caption

6.6.2 Structure of the Rangitaiki Fault

Within the pseudo-3D survey area the Rangitaiki Fault comprises five major overlapping and interacting segments (R1, R2, R3, R4 and R5, Figure 6.8). Interpretation of regional profiles allows us to constrain the displacement profile of the Rangitaiki Fault beyond the survey area, albeit in less detail. The regional profiles show the displacement of segments R1

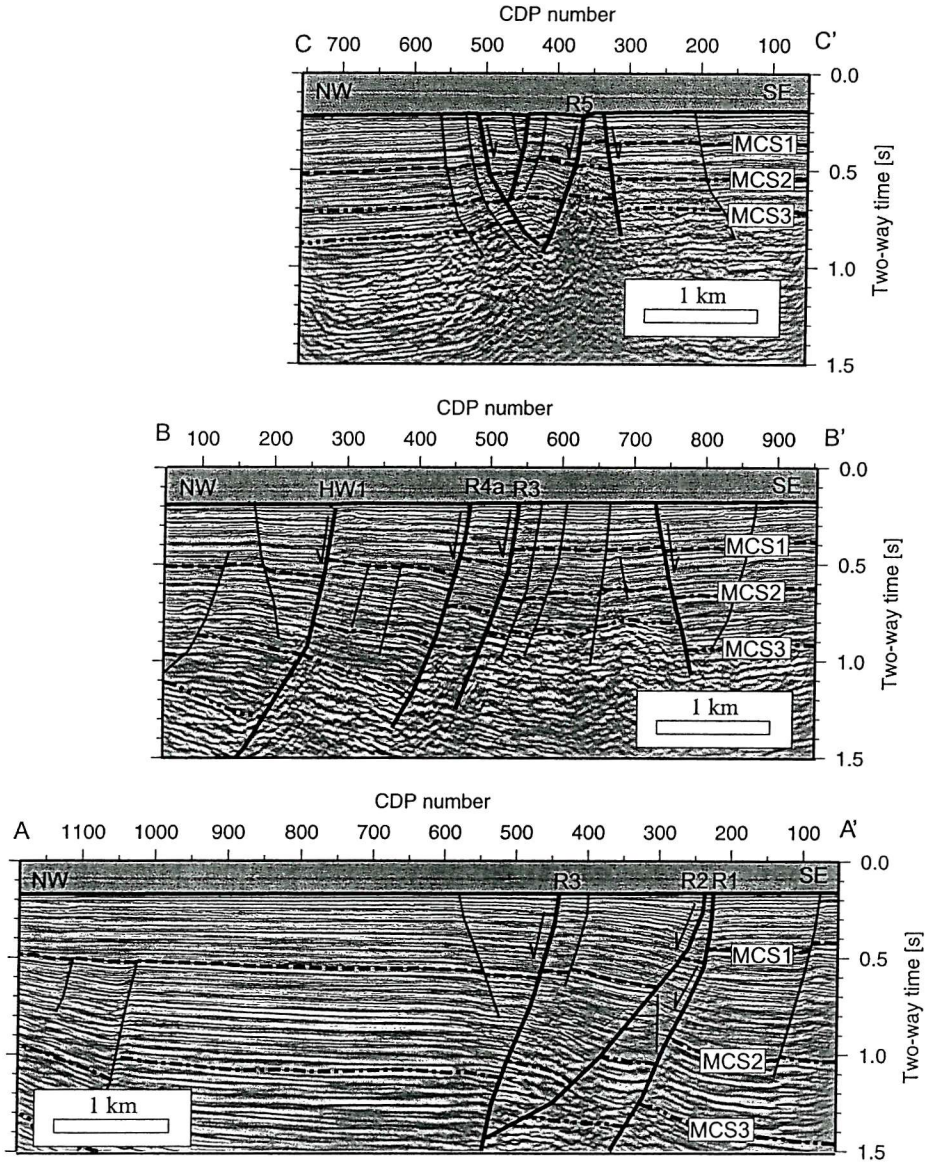

Figure 6.7. Three example multichannel seismic profiles from the pseudo-3D survey area illustrating the Rangitaiki Fault displacing horizons MCS1-3. The location of profiles A, B and C are shown in figure 6.2. The five main segments of the Rangitaiki Fault are indicated with numbers. Profiles show the displacement on the Rangitaiki Fault decreasing and the sedimentary layer thinning by c. 50% to the north, towards the tip of the Rangitaiki Fault. Vertical Exaggeration is c. 2:1 @ 2000 ms^{-1}

and R5 decreasing away from the detailed survey area towards the fault tips. The maximum displacement observed on the Rangitaiki Fault, within the 3D box (i.e. not over the whole length of the Rangitaiki Fault) is 826 m on the oldest horizon (MCS3) in the centre of segment R3 (Figure6.9g). Other Rangitaiki Fault segments have maximum displacements of c.300 m. On the younger horizons the maximum displacement is observed on R2 or R1.

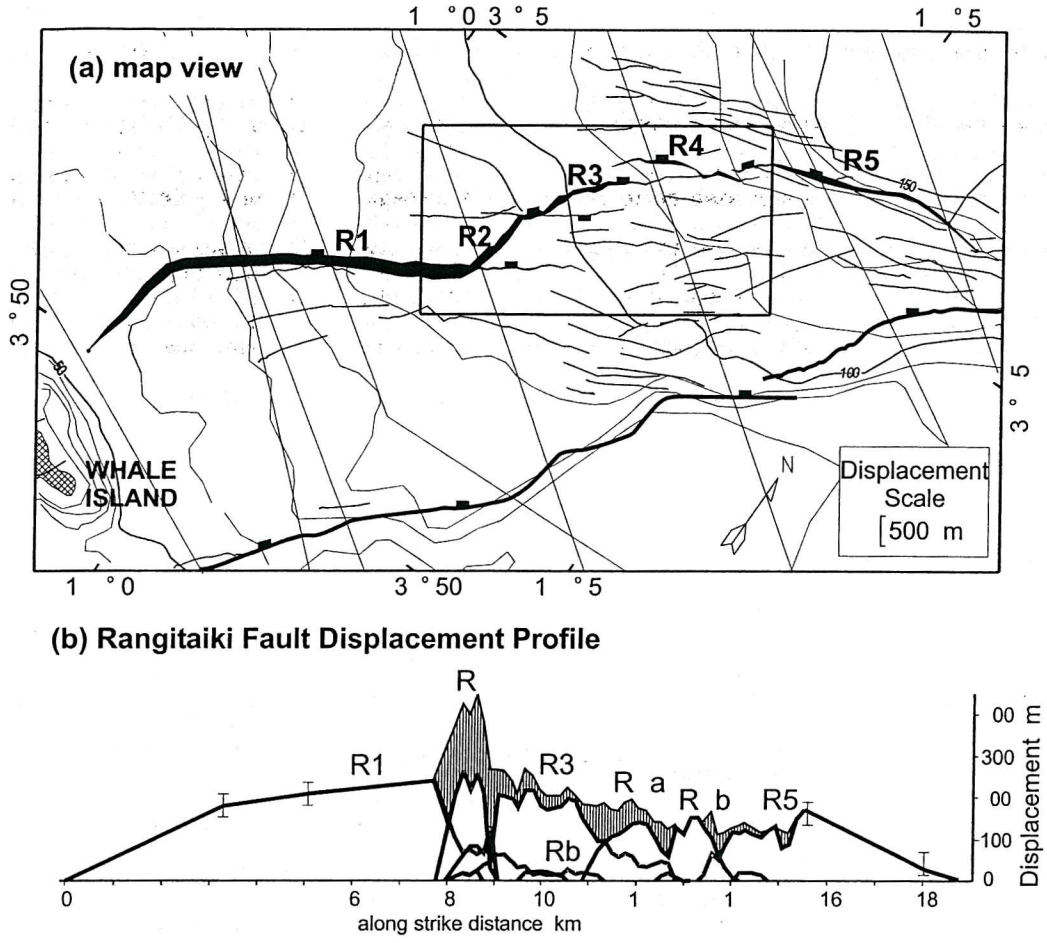

Figure 6.8. (a) Map of the Rangitaiki Fault at horizon MCS1 (300 ±100 ka). The main segments of the Rangitaiki Fault are numbered, the thickness of the fault represents the displacement as it varies along strike, dots show fault tips. Other faults are in thinner solid lines. Bathymetry contours shown in blue; there is a large surface expression of the White Island Fault. The black rectangle shows the extent of the pseudo-3D survey area, other fault displacement measurements are made from regional seismic lines (thin black lines) for MCS1, and from numerous 3.5 kHz, Chirp and boomer profiles (not shown) for HRS1. (b) The aggregate displacement profile for MCS1 (above hatched area in pseudo-3D area) for the linked Rangitaiki Fault has the form of a single isolated fault, with displacement lows at segment overlaps. (c) The aggregate displacement profile for HRS1 (above hatched area in pseudo-3D area) for the linked Rangitaiki Fault. While the positions of the tips of the fault are well constrained, there is less control on displacement close to the tips (indicated by the dashed line).

South of the 3D box, horizons MCS2 and MCS3 are poorly imaged on the MCS data and horizons HRS2 – 4 are not imaged in the high resolution data due to the shallower water depths introducing multiples, and the presence of gas. For this reason the reconstruction of fault evolution for the Rangitaiki system over 1.3 Ma is only precisely constrained within the 3D box, and this is the focus of the arguments developed in Figures 6.9 – 6.11. This affects the southernmost segment, R1, whose evolution is well constrained for the last 300

ka. Later (Figure 6.12) we consider the evolution of the entire Rangitaiki system in general terms.

The displacement profiles for the Rangitaiki Fault at the seven interpreted horizons (Figure 6.9) show these five segments as well as three smaller faults (Ra – Rc) in the pseudo-3D survey area. In general, the displacement of these faults decreases up section indicating syn-sedimentary growth faulting, and on each horizon the total displacement decreases from southwest to northeast. Individual fault segments are identified based on changes of fault displacement between adjacent segments and abrupt changes of strike.

The southern most segment of the Rangitaiki Fault (R1) is 10 km long, accounting for half of the entire length of the Rangitaiki Fault (Figure 6.8). The southern tip of the R1 appears controlled by the position of Whale Island (Motuhora Island), an island that was formed before 450 ka BP (see Burt et al., 1996 for a review). The displacement profile of R1 is strongly asymmetric, with the maximum displacement only 2 km southwest of its northern tip. Peacock and Sanderson (1994) interpreted similar asymmetric profiles as resulting from overstepping fault segments linked by a relay ramp. Hence, we infer that the asymmetric R1-R3 displacement profile is the result of the R2 relay between the two overlapping R1 and R3 segments. The transfer zone is imaged in both the high-resolution seismic reflection data and MCS reflection data, an example is shown in Profile A-A (Figures 6.6 and 6.7). Most of the displacement in this profile is taken up on the transfer fault (R2), although R2 and R3 intersect at 1.4 s two-way-time, so in deeper sediments the displacement must be accommodated solely by R1 and R3.

North of the transfer zone, the intersecting antithetic faults Ra and Rb control the displacement profile of R3, from horizon MCS1 onwards. At the line of intersection there is a decrease in displacement in R3 that matches the displacement at the intersecting tips of Ra (observed only in high-resolution data) and Rb. In the high-resolution data, Rc and R3 have complimentary displacement profiles; the drop in displacement in R3 is matched by the displacement of Rc.

Northwards, R3 connects with R4, and the rotation of the sediments in the ramp between the two interacting faults is most pronounced at horizon MCS1 (Figure 6.7, Profile B-B). R4 has distinct displacement profiles that divide the fault into segments R4a and R4b. From MCS1 onwards, faults R4a and R4b appear linked, with only a small drop in displacement where they connect with fault R3 (Figure 6.9e to g).

R5 overlaps R4b, and continues to the northern tip of the Rangitaiki Fault. This segment is 5 km long and has a collapse graben in its hanging wall (Figures 6.5 and 6.7 Profile C-C). R5 continues northwards beyond the pseudo-3D survey area and terminates in a highly

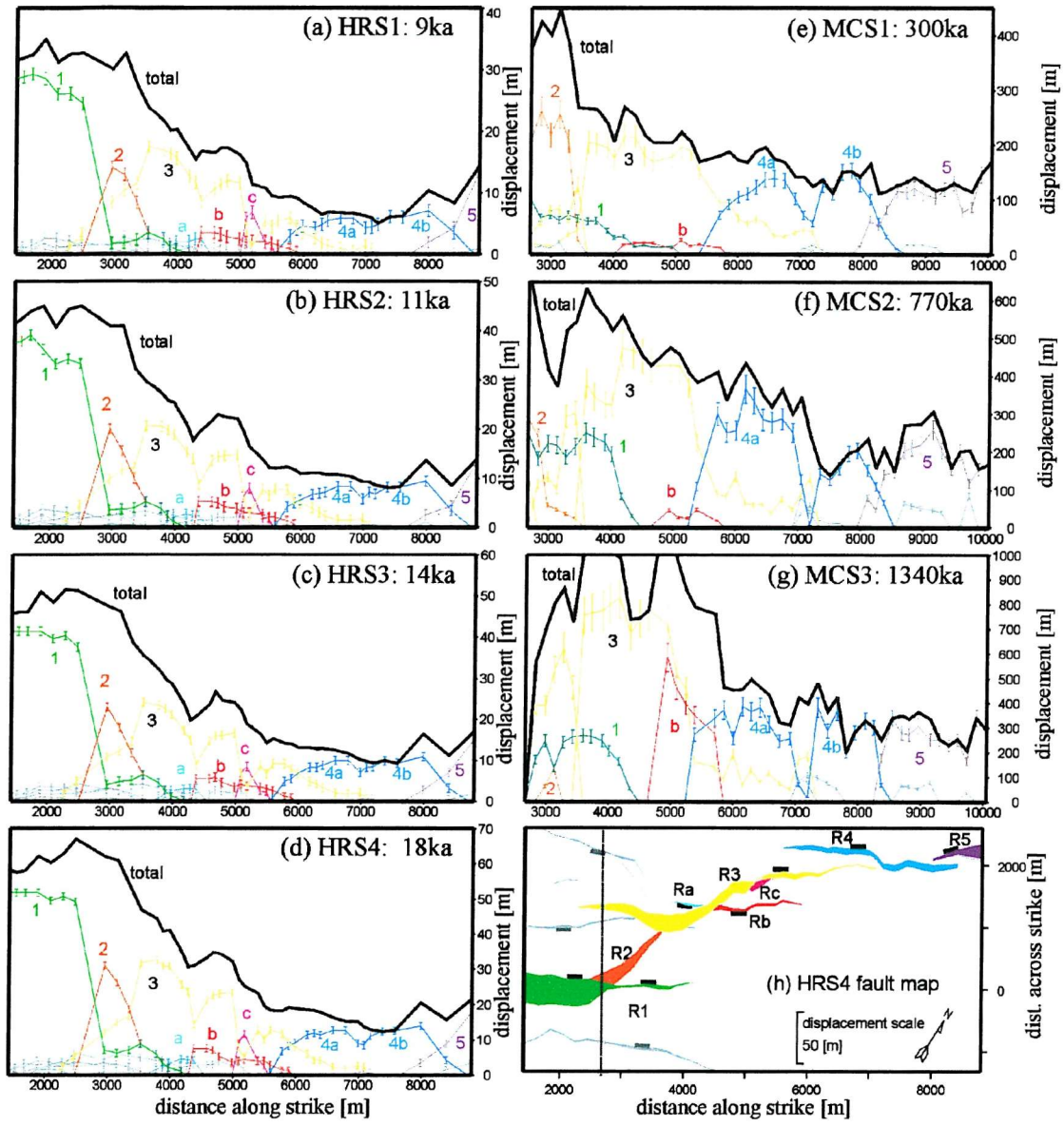

Figure 6.9. Profiles of total displacement measured on the four high-resolution (a-d) and three multichannel (e-g) horizons *within the 3D box*. Displacement maps are shown for horizon HRS4 (h). The main segments of the Rangitaiki Fault are named and in colour, the aggregate displacement profile for each horizon is shown in black. See main text for a detailed discussion of the figure. Segment R1 continues south of the 3D box (see Figure 6.8), but is not well imaged at HRS2-HRS4 levels on the high resolution data, or at MCS2 and MCS 3 levels in the multichannel seismic data.

faulted area close to the White Island Fault.

6.6.3 Displacement Rates and Linkage History of the Rangitaiki Fault

Displacement maps of the Rangitaiki Fault system at horizons MCS3 and HRS4 are shown in figure 6.10. The development of displacement on the faults at MCS3 is shown at five locations (grey vertical areas in Figure 6.10) along strike, from the deposition of MCS3

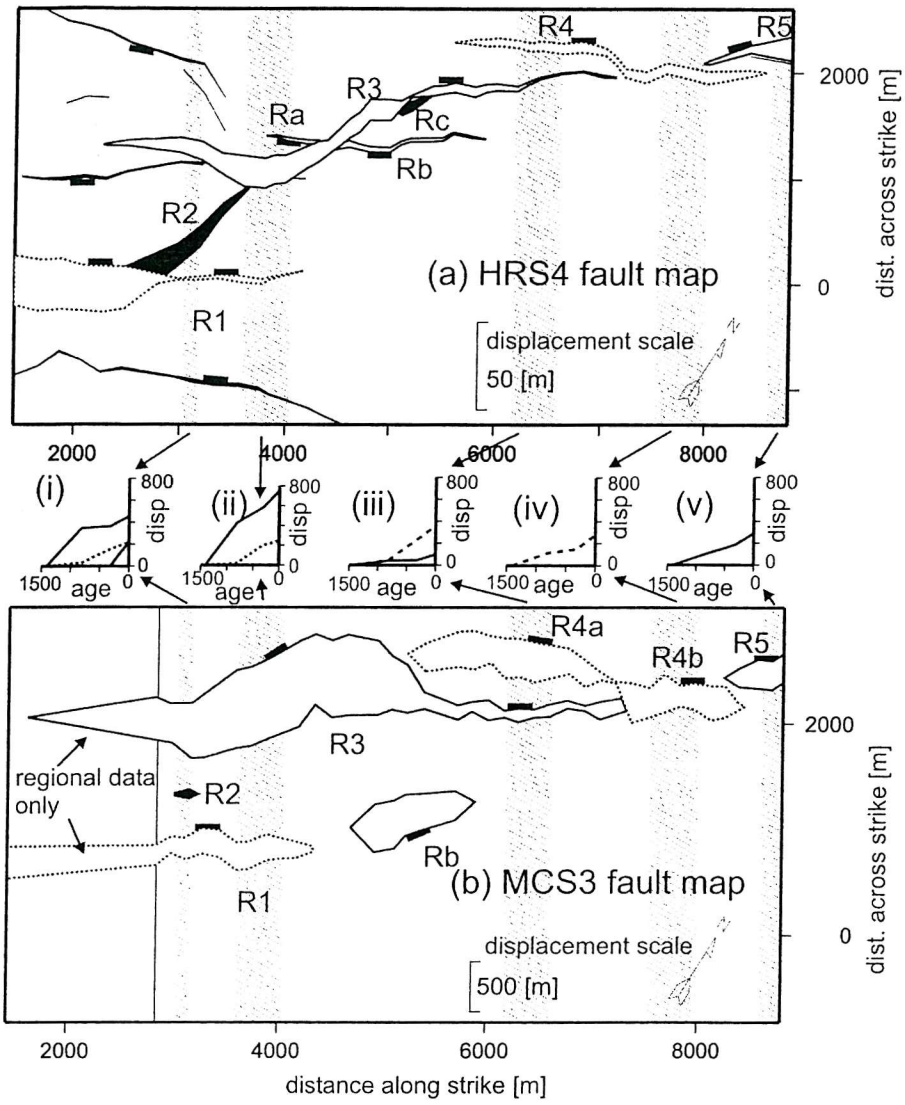

Figure 6.10. Maps showing the changing fault geometry of the Rangitaiki fault system at horizons HRS4 (16-18 ka) and MCS 3 (1340 ± 420ka). The displacement of the faults is shown by the thickness of the fault trace on the map (note that the figures have different displacement scales). Grey bars show the five locations where displacement rates are measured (Table 6.3). The graphs at these locations show the development of displacement through time on MCS3, and the segment line type is as for the plan views (R1, dashed line; R2, solid line; R3, dotted line; R4 dot-dashed line, R5 solid line)

at 1340 ka to present. R3 shows the largest displacement recorded on MCS3 (Figure 6.9g) while the largest displacement on horizon HRS4 is recorded on R1 (Figure 6.9d). Location 1 (Figure 6.10b-i) shows the development of the faults through the relay zone and in particular the late onset and subsequent rapid growth of fault R2. North of the transfer zone, at location 2, the displacement rate on fault R1 decreases and the displacement rate of R3

increases at 770 ka, i.e. after effective linkage of R2 and R3, to the south.

Fault R3 changes in dip from its shallow dipping, high displacement centre (4000 – 5000 m along strike) to a steeply dipping, low displacement northern section where it is overlaps fault R4a (5500 – 7000 m along strike). An important consequence of the variation in fault dip is the vertical changes in the structural relationships between the faults; for example, at horizon HRS4 the downthrown side of R3 is no longer co-linear with the downthrown side of R4a as it is at MCS3. Fault propagation and linkage of interacting faults can be inhibited or enhanced depending on their relative positions, so a change in fault geometry will alter the way the faults behave.

The average displacement rate for the Rangitaiki Fault in the pseudo-3D survey area for each of the four time intervals is shown in table 6.3 along with individual displacement rate observations for the faults at the five locations shown in figure 6.10. The calculation of average displacement rates for the entire fault system was determined by summing the aggregate strike projected displacement rates and dividing by the number of observations (line crossings). The average displacement rate increases with development of the fault system from 0.52± 0.18 mm yr^{-1} (1340 – 770 ka) to 1.41 ± 0.31 mm yr^{-1} (18ka to present).

Fault displacement rates for the Rangitaiki Fault segments are shown for four time periods in the development of the fault network in figure 6.11 (1340 – 770 ka, 6.11a; 770 – 300 ka, 6.11b; 300 – 18 ka, 6.11c; and 18 ka to present, 6.11d). In this figure the thickness of the fault trace represents the displacement rate, so the most active faults can be easily recognised by the thickest traces. The location of the fault trace is determined from the position of the fault down section, so displacement rates for the oldest time (1340 – 770 ka) are shown on the fault map for the oldest horizon (MCS3). Where measured displacement rates are below the estimated uncertainty range the displacement is assumed negligible, and fault tips are placed where the displacement first reaches a measurable value. Presenting the data in this way assists in reconstructing the fault geometry and shows the development of the surface rupture through time. In addition, spatial and temporal variations in fault displacement rates can be clearly seen. In the following we analyse in detail the information provided by figure 6.11.

Faults R1, R2 and R3 – Linkage event at 300 ka.

R2 shows a displacement maximum at horizon MCS1 (Figure 6.9e), with displacement decreasing both upwards and downwards away from this horizon. At this horizon and above, R2 links R1 and R3 (Figure 6.11c), but this is not the case in deeper horizons

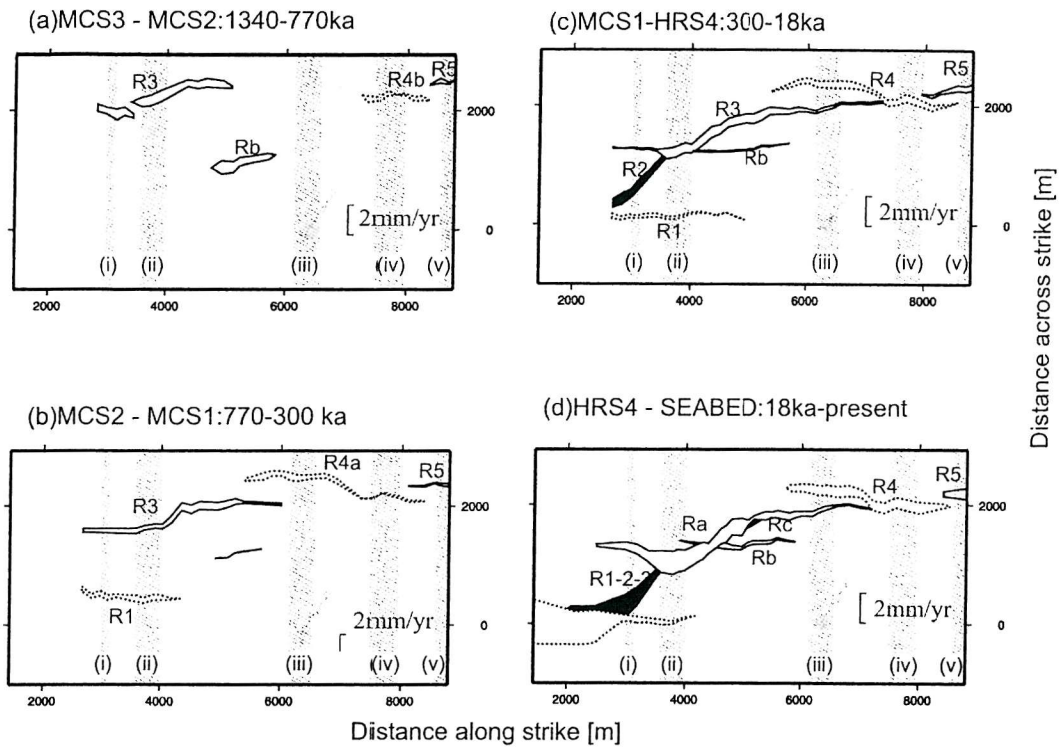

Figure 6.11. Spatial and displacement rate evolution for the Rangitaiki Fault system, within the 3D box, in map view, for four time periods. The position of the fault is the mid point between the upthrown and downthrown sides of the older horizon. The thickness of the fault is given by its displacement rate during the time between deposition of the two horizons. The vertical hatched bars show the five locations of displacement measurements in table 6.3, chosen to highlight segment interaction. Note that segment R1 continues south of the 3D area (see Figure 6.8 and 6.12). These maps show the progression from isolated faults (a) to a fully linked fault system (d), and illustrate the changing fault growth mechanisms from

(Figure 6.11b). Assuming that this fault initiated at or near the surface implies that R2 initiated at c. 300 ka as a transfer fault between R1 and R3, and has been transferring displacement between R1 and R3 ever since.

During the first observed time interval (1340 – 770 ka), displacement at location 1 is entirely taken up on R3. Between MCS2 (Figure 6.9f) and MCS1 (Figure 6.9e) the tip line of R1 propagates from 4300 to 4900m along strike, indicating that R1 grew in length by nearly 600 m. While R1 is propagating laterally (770 – 300 ka), the displacement rate on R3 is minimal with a value of 0.08 ± 0.08 mmyr^{-1} (Table 6.3), reduced from 0.60 mmyr^{-1} for the previous time period. Similarly, at location 2 the displacement rate of R3 decreases from 0.72 mmyr^{-1} to 0.31 mmyr^{-1} as R1 propagates and overlaps R3. After the transfer fault R2 has linked R1 and R3, R1 ceases to propagate laterally, and all three faults are active at the same time, with R2 being the most active.

	Average	Location 1			Location 2	
		R1	R2	R3	R1	R3
1340-770ka	0.52±0.18	negligible	X	0.60±0.20	negligible	0.72±0.23
770-300ka	0.47±0.15	0.32±0.12	X	0.08±0.08	0.38±0.13	0.31±0.12
300-18ka	0.75±0.23	0.23±0.10	0.79±0.24	0.34±0.13	0.17±0.09	0.65±0.20
18-0ka	1.41±0.31	0.37±0.08	1.60±0.36	0.75±0.17	0.28±0.06	1.76±0.4

	Location 3		Location 4	Location 5
	R3	R4a	R4b	R5
1340-770ka	negligible	negligible	0.20±0.11	0.19±0.11
770-300ka	negligible	0.40±0.14	negligible	0.18±0.09
300-18ka	0.18±0.10	0.43±0.15	0.45±0.15	0.39±0.14
18-0ka	0.24±0.05	0.66±0.15	0.74±0.17	1.01±0.23

Table 6.3: Fault displacement rates in mm yr^{-1} determined within the 3D box. Where rates are quoted as negligible they are below 0.10 $mmyr^{-1}$ and have errors larger than the calculated rate.

Higher up the section – and so later in the fault history – at horizon HRS4 (Figure 11d), the tip of R1 is at 4200 m along strike, showing that the active tip of R1 has retreated since its maximum length at the time horizon MCS1 was deposited and the faults linked (300 ka).

These observations show that the increased active length and displacement rate of R1 is limited to around the time that the relay system breached and R2 was formed. After R1 and R3 are linked their overlapping tips become relatively inactive and accommodate a smaller proportion of the overall fault displacement (Figure 6.9d).

Faults R3, R4a and R4b – Fault Tip Propagation and Linkage

Figures 6.11a-6.11d show fault R3 propagating northwards and intersecting R4a and R4b between 300 and 18 ka. Prior to linkage, segments R4a and R4b are alternately active, with negligible displacement rate on R4a and a maximum of 0.20 ± 11 mmyr−1 (Table 3) on R4b between 1340 and 770 ka (Figure 6.11b), and maximum 0.40 ± 0.14 $mmyr^{-1}$ on R4a and negligible displacement rate on R4b between 770 and 300 ka (Figure 11c). After linkage at 300 ka, the displacement rates on R4a and R4b are similar (0.43 ± 0.15 and 0.45 ± 0.15 mm yr^{-1}, table 6.3). The current displacement profiles (Figure 6.9) show that the intersection point between R4a and R4b has its maximum displacement at horizon MCS1 (Figure 6.9e). Assuming that the linkage initiated at or near the surface, these observations suggest that R4a and R4b linked at c. 300 ka, forming a kinematically coherent fault segment, R4. This linkage occurred at approximately the same time as, and may have been driven by, the

linkage of R3 with these faults.

Figure 6.10b shows the hanging wall cut-off of R3 is approximately co-linear with the hanging wall cut-off of fault 4a at horizon MCS3, which is no longer the case at younger horizons (Figure 6.10a). The displacement rate map for the earliest observable time on the seismic sections (Figure 6.11a) shows R4a has virtually no displacement except at the south-eastern tip. This active tip of R4a may be the continuation of R3 along strike at this horizon. This co-linear relationship is not preserved up-section because the faults are slightly curved and have variable dip along strike. We infer that the damage caused by the propagation of R3 and its eventual linkage with R4 was what initiated the linkage between R4a and R4b.

R4 and R5 – Kinematically linked faults

The total displacement across R4 to R5 has a flat-topped profile, i.e. the aggregate displacement profile shows no significant decrease across the overlap, (Figure 6.9). Childs et al. (1993) interpreted similar flat-topped profiles, as observed in sandbox analogue models, to be a result of upward propagation of a single large fault. These faults step-over only 200m, a small distance compared with their lengths of between 3 and 5 km (cf. ¿ 1 km offset between R2 and R3). The fault displacement rates are in phase throughout their history (Table 3). This fault interaction history is interpreted as the result of tip line bifurcation (Huggins et al 1995; Childs et al, 1996), where the vertical propagation of the tip line is locally retarded by heterogeneity in the rock.

Faults Ra, Rb and R3 – Intersecting Conjugate Faults

The five main segments of the Rangitaiki Fault network all dip towards the northwest; fault Rb, however, dips towards the southeast. The opposing dips of faults R3 and Rb cause their relative positions to change on each successive horizon (Childs et al, 1995) until they eventually connect at horizon MCS1. The effect of the intersection is seen in the displacement profiles of horizon MCS1 (figure 6.9e), where the southern tip of Rb (4000m along strike) coincides with a drop in displacement in R3. The relationship between these faults is further changed up section as both the faults become steeper towards the seabed until they are both close to vertical. Where both faults are vertical, the slip vectors of the faults are in the same orientation, and both faults may remain active (Jackson and McKenzie, 1983). A consequence of this is that displacement may be transferred across fault R3. This transfer of displacement results in the continuation of fault Rb across R3, forming fault Ra (Figures 6.9a – 6.9d). Nicol et al. (1995) found a reduction in displacement on

discrete faults and a corresponding increase in ductile strain at the seismic scale. The data presented here agree with this result, as total displacement for the Rangitaiki Fault system shows a drop in displacement around the intersection point. In all the horizons where Ra is observed, its displacement is less than the displacement of Rb at the intersection (figures 6.9a – 6.9d). This is interpreted to be because only Rb is driving the displacement on Ra from seismogenic depths (Ra is not observed any deeper than HRS4) and the transfer of displacement across R3 also involves transfer of displacement onto sub-seismic scale faults.

6.7 Discussion

The observations above enable us to make the following interpretation of the evolution of the Rangitaiki Fault.

6.7.1 Fault Evolution

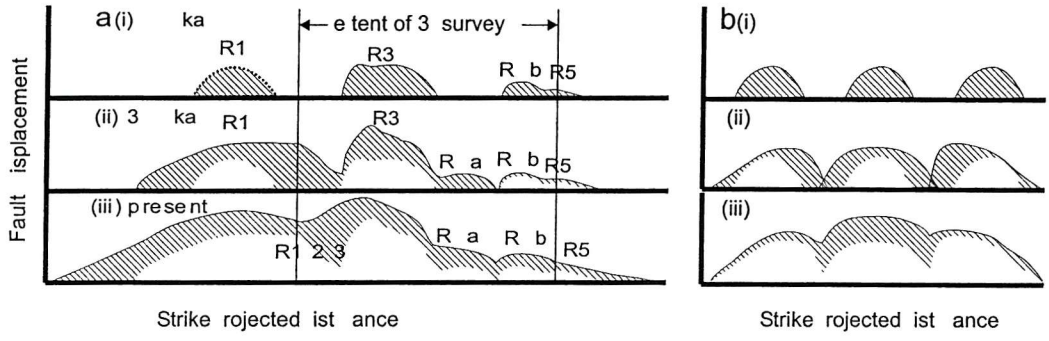

Figure 6.12. Schematic showing the temporal development of displacement on the Rangitaiki fault system (a) as a strike projection of the oldest horizon (MCS3) within the detailed study area, and comparison with a model (b) of tip propagation and linkage for normal faults proposed by Cartwright et al. (1995). Hatched areas indicate where new displacement is accumulated in comparison to the previous time periods. This figure shows the evolution from isolated faults to a fully linked system over 1.3 Ma. The position of the southernmost segment of the Rangitaiki Fault, R1, is less well constrained for the earliest time period, and this is indicated by the dashed displacement profile. The Rangitaiki Fault is the most active fault in the offshore Whakatane Graben and this figure summarises its complete history.

These data (Figure 6.11 and 6.12) show the development of a fault network from isolated faults to a fully linked structure, initially by tip propagation followed by the development of relay zones and their subsequent breaching. The imaging of horizon MCS3, which formed early (1.3 Ma) in the development of the rift, ensures that the entire history of fault growth can be determined. The total displacement accumulated over the last c. 20 ka (i.e. displace-

ment profile on HRS4, figure 6.9d) resembles an isolated fault with maximum displacement near the centre tapering to zero at the tips, suggesting that over long timescales (tens of thousands of years) the entire Rangitaiki Fault is now behaving as a single fault structure, from seismogenic depths (c.6 km; Bryan et al., 1999) to the surface. The displacement profiles of MCS2 and MCS3 reflect displacements accumulated both when the Rangitaiki Fault behaved as a single fault and when the Rangitaiki Fault comprised isolated and laterally propagating faults. The combination of fault growth regimes results in distorted displacement profiles at MCS2 and MCS3 and large displacement gradients at segment boundaries (figure 6.9f and 6.9g).

The evolution of the fault system from isolated faults to a fully linked network is summarised below.

1340-770ka – Isolated Fault Segments

Within the pseudo-3D survey area, the Rangitaiki Fault comprised five short, isolated faults dipping both to the northwest and the southeast (figure 6.11a). The active segments were two separate en echelon segments of R3, R4b, R5 and Rb. R1 was not active within the survey area at this time, although regional seismic profiles show it to be active within 1-2 km to the south (Figure 6.12). We cannot identify the active length of R1 at this time because we have not been able to identify MCS3 and MCS2 along the southern part of R1. The deformation is limited to a 1.5 km-wide deformation band, with an average displacement rate of 0.52 ± 0.18 mm yr^{-1}. The Rangitaiki Fault is dominantly growing at this time through the processes of fault nucleation and tip propagation, comparable with the early rift initiation stage described by Cowie et al. [2000].

770-300ka – Early Fault Interaction

At this stage the faults were beginning to overlap and interact but with no increase in overall displacement rate (Figure 6.11b). The average displacement rate on the Rangitaiki fault at this time was 0.47 ± 0.15 mm yr^{-1}. All the displacement was taken up on northwest dipping faults, as the antithetic fault Rb is not active at this time (Figure 6.9f and 6.11b). Activity on faults Rb and R4b is negligible, and the two segments of R3 that were identified in the older sediments must have linked, as they are indistinguishable at this level. The northern tip of R3 has propagated laterally and overlaps R4a by 600 m. R1 propagated into the survey area and overlapped R3 by nearly 2 km. R4a ceased to be co-linear with R3, and was offset by c. 500 m.

300-18ka – Fault Interaction and Linkage

During this time fault linkage became an important process in the development of the fault network, and the Rangitaiki Fault became a fully linked system (Figure 6.11c). The

average displacement rate on the whole system almost doubled to 0.72 ± 0.23 mm yr^{-1}. The five linked segments produce a continuous fault of total length c. 20 km (Figure 6.12).

The relay ramp between overlapping faults R1 and R3 was breached by the development of the oblique transfer fault R2. The development of the newly linked fault network was accompanied by increased displacement rates on, and lateral propagation of R1. R1 now has a length of c. 10 km; approximately half the length of the linked fault system (Figure 6.8). Faults R3, R4a and R4b also linked at this time, and R4 began to behave as a single fault with a displacement low remaining at the intersection with the tip of R3.

18ka-present - Fully Linked Fault Network

Throughout the last 18 ka the Rangitaiki Fault has been a fully linked fault system (Figure 6.11d; Figure 6.12). The overlapping tips of R1 and R3 are now relatively inactive. R4 is well developed as a single structure, with evidence for the previous segmentation remaining only as a minor displacement low in the centre of the displacement profile. The average displacement rate of the Rangitaiki Fault network has increased through time from its initial rate of 0.52 ± 0.18 $mmyr^{-1}$ initially, when the faults were isolated, to 1.41 ± 0.31 mm yr^{-1} in the fully linked network.

6.7.2 Implications for fault growth models

The base of the seismogenic zone beneath the Taupo Volcanic Zone can be defined as the depth above which 80

The youthfulness of the Rangitaiki fault system, together with our stratigraphic resolution, means that we are able to document the full history of fault evolution. Unlike previous studies (e.g. Nicol et al., 1997) we are able to resolve the earliest stages of fault evolution. We show that displacement rates are relatively slow during the earliest history of fault growth (the first c. 1 Ma), and that there is a three-fold increase in the displacement rate of the linked fault system in comparison with the unlinked system. In common with the analogue models of Mansfield and Cartwright (2001), there is considerable spatial variability in displacement rate between segments in both the linked and unlinked fault systems as relict boundaries still remain significant barriers to displacement accumulation. In addition, the reliance on discrete stratigraphic markers will undoubtedly hide complexity in the temporal changes in slip rates (for discussion of the intrinsic variability of slip rates see McCalpin, 1995).

Comparison of the three-fold increase in displacement rate observed during the development of a fully linked system for the Rangitaiki Fault with other fault systems is hampered by insufficient temporal and spatial resolution in previously published work. One of the few

documented examples of displacement rate increase caused by fault linkage is found in the Northern North Sea. McLeod et al (2000) found a fault displacement rate increase from 0.055mm yr^{-1} to 0.092mm yr^{-1} in the Strathspey-Brent-Statfjord fault associated with a major phase of fault linkage. This linkage event occurred between 10 – 14 Ma after rift initiation (McLeod et al, 2000).

On the Rangitaiki Fault, where displacement rates are approximately eight times faster than in the North Sea, interaction and linkage become the dominant processes only after c. 1 Ma of fault activity – again approximately eight times faster than in the North Sea setting seen by McLeod et al. [2000]. Although these displacement rate changes and linkage events are happening on different time- and length- scales, the simple scaling of rates of displacement and rates of linkage are suggestive that the same process is responsible for each, and is happening at different scales.

Localisation of strain onto major through-going fault structures is often accompanied by a corresponding decrease in activity on surrounding faults (McLeod et al., 2000; Meyer et al., 2002) such that the overall strain rate for the region may remain constant (Gupta et al., 1998). The pseudo-3D survey area was selected to document the development of the Rangitaiki Fault system, and does not include a representative sample of regional faulting. Because of this it cannot show conclusively whether the recorded increase in displacement rate on the linked fault system is at the expense of displacement accumulation on adjacent faults. However, the seismic profile interpreted by Davey et al. (1995) does show a concentration of recent TVZ fault activity in the eastern Whakatane Graben, including the Rangitaiki Fault. Considering the deformation of the whole TVZ permits the constraint of constant regional strain rate to be satisfied without demanding the faults immediately adjacent to the Rangitaiki Fault decrease in activity.

Figure 6.12 shows a schematic of the evolution of the entire Rangitaiki fault system, and a comparison with a model of tip growth and linkage proposed by Cartwright et al. (1995). The position of R1 at the earliest time period is less well constrained, but it is clear that the segments R1, R3, and R4b-R5 were isolated faults. The segments propagated towards each other, initially with high displacement gradients at their segment tips. Between 300 ka and 18 ka the system linked and displacement accumulated on segments with a reduction in displacement gradient within the linked system. The displacement rates on segments of the Rangitaiki Fault are such that the linked array displacement profile approximates to an idealised isolated fault. Displacement rates on individual fault segments are highly variable along strike, and are influenced more by interactions with neighbouring faults and their location within the linked system than by their initial length. In this paper we have

demonstrated that the broad conceptual idea of fault growth by tip growth and segment linkage is correct, but also show how displacement rates and displacement gradients evolve over the entire history of fault growth.

6.8 Conclusions

In this paper we have investigated the complete evolution of the most active fault system within the Whakatane Graben – the Rangitaiki Fault. The fault initiated as 5 isolated segments, which grew together over 1 Ma. Fault tip propagation was the dominant faulting process initially (from 1340 ka to 770 ka), followed by the development of relay zones and their subsequent breaching. The system became fully linked between 300 ka and 18 ka. Due to the stratigraphic range and resolution of our seismic reflection data sets, and the youthfulness of the fault, we are able to show that the average displacement rate (0.52 $\pm$ 0.18 mm yr^{-1}) was relatively low during the earlier (unlinked) stages of fault growth. Following linkage, the average displacement rate increased three-fold in comparison to the unlinked array, to 1.41 $\pm$ 0.31 mm yr^{-1}.

The displacement profile of the fully linked Rangitaiki Fault resembles that of a single fault, whereas displacement profiles of horizons deposited before the faults linked are irregular and have strong displacement gradients on the fault segments. More generally, we show that displacement profiles derived from offsets on horizons formed early in a fault systems evolution will exhibit complex displacement profiles due to the superposition of processes operating when the system operated as a single fault, and when its constituent segments were isolated and laterally propagating.

[0] **Acknowledgements** – This work was funded by the Natural Environment Research Council (GR3/11862), United Kingdom and the New Zealand Foundation for Research Science and Technology (FRST-CO1X0038). We are grateful to the officers and crew or R/V Tangaroa and R/V Kaharoa for their dedication during TAN-99-14 and KAH01-02, and to Justin Dix and the technical team at NIWA for their expertise in geophysical data acquisition. We thank the following for their biostratigraphic input: Tony Edwards (Stratigraphic Solutions) and Graeme Wilson, Dallas Mildenhall, and Percy Strong (Institute of Geological and Nuclear Sciences). Dave Sanderson, Patience Cowie, and Ian Wright are thanked for their support and helpful comments.

Chapter 7

Discussion

7.1 The Rangitaiki Fault

Following analysis of high resolution (chirp, boomer and 3.5 kHz sediment profiles) and multichannel seismic data collected during cruises TAN99-14 and KAH01-02, the Rangitaiki Fault is now recognised as a highly active, 20 km long, linked, segmented normal fault. The Rangitaiki Fault has an average strike of 57°, and has an irregular trace at the seabed. Abrupt changes in fault strike are found at former segment boundaries; these segment boundaries remain barriers to fault slip over short time periods (c. 2 ka, e.g. figure 5.15), but at longer time intervals the aggregate displacement profile for the Rangitaiki Fault is less influenced by the segmentation and resembles that of a single fault (e.g. figure 6.8b and c).

The southernmost segment of the Rangitaiki Fault (R1) is the largest, and at 10 km long accounts for approximately half the length of the linked fault structure. Northwards, the segments become shorter and progressively more faults are found surrounding the Rangitaiki Fault (the hanging-wall faults, e.g. figure 4.9). The broad zone of faulting around the northern half of the Rangitaiki Fault (dominated by the hanging-wall fault group) is interpreted as an evolved damage zone that lies ahead of the propagating Rangitaiki Fault. Displacement on the Rangitaiki Fault dies out to the north in a complex zone of faulting as the Rangitaiki and White Island Faults converge (figure 6.1). The northern tip of the Rangitaiki Fault is identified in the centre of this damage zone, lying 2 km to the west of the White Island Fault. Further fault slip on the Rangitaiki Fault will result in continued evolution of the damage zone, with more faults becoming recognisably part of the Rangitaiki Fault system, and ultimately linking the Rangitaiki and White Island Faults.

To the south, the Rangitaiki Fault trace curves so it strikes nearly north-south, its southern tip lying approximately 2 km north of Whale Island (figure 6.1). The presence of the volcanic Whale Island, which is older than 450 ka BP, appears to limit the southward prop-

agation of the Rangitaiki Fault, with displacement potentially transferred to the favourably located Thornton Fault (figure 7.1a). The Thornton fault was identified from displacement

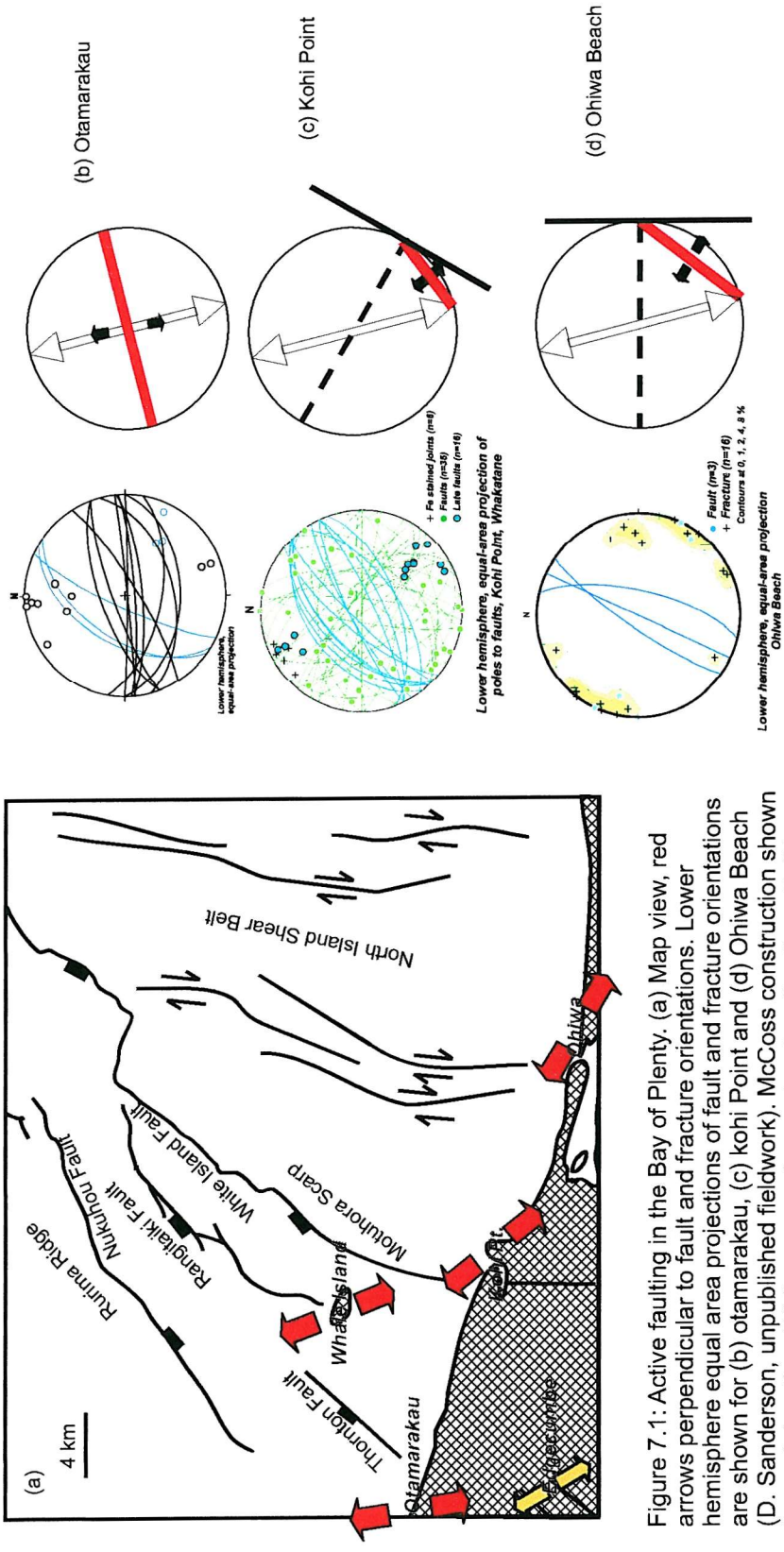

Figure 7.1: Active faulting in the Bay of Plenty. (a) Map view, red arrows perpendicular to fault and fracture orientations. Lower hemisphere equal area projections of fault and fracture orientations are shown for (b) otamarakau, (c) kohi Point and (d) Ohiwa Beach (D. Sanderson, unpublished fieldwork). McCoss construction shown for each location. White arrows show extension direction . Solid black lines show orientation of basement structures, dashed black lines show normal to this orientation. Red lines show surface fault orientations predicted by the McCoss construction, black arrows show orientation of structures shown in equal area projection and on map.

measurements on 3.5kHz and MCS profiles and is the largest fault at the landward limit of the offshore data. Continuation of this fault trend landward intersects the area affected by surface ruptures associated with the Edgecumbe earthquake. The inference that the Rangitaiki Fault is associated with the Edgecumbe Fault means that estimates of long-term fault activity rates and earthquake recurrence times calculated offshore may be applicable onshore, and can be used in hazard assessment for the Bay of Plenty region.

The data presented in Chapter 6 show the Rangitaiki Fault developing through a combination of tip propagation and segment linkage, following the model of Cartwright et al., (1996) (figure 6.12), although the under-displaced stage immediately after linkage predicted by this model is not observed. The lack of an under displaced stage following fault linkage is attributed to the stress fields of the faults interacting, prior to the faults becoming physically linked (soft linked stage, e.g. Walsh and Watterson, 1991; Roberts and Yielding, 1994). The interacting stress fields mean that the displacement profiles of the faults distort to make the aggregate displacement profile of the soft-linked fault resemble a single fault (Willemse, 1997).

The irregularity in displacement profiles observed over short timescales compared with longer timescales observed in the Rangitaiki Fault is predicted by analogue models (e.g. Mansfield and Cartwright, 2001). The persistence of segmented behaviour in linked fault networks leads to preservation of displacement minima at fault boundaries (e.g. McLeod et al., 2000). Peacock and Sanderson (1994) attribute the minimum at fault oversteps and linkage points to rotation of bedding and folding in the hanging-wall and footwall.

The displacements observed on the Rangitaiki Fault are too large to have formed from a single slip event, and must therefore be a superposition of many slip events (e.g. Walsh and Watterson, 1987; Peacock and Sanderson 1996). The irregular displacement profiles observed on the Rangitaiki fault over short time intervals (figure 5.15) include zero displacement sections, demonstrating that earthquake slip events do not always rupture the entire fault plane. In the fault growth model presented by Cowie and Shipton (1998), only patches of the fault slips in any single rupture event, and linear displacement gradients are predicted towards the fault tip when the size of the slipping patch is much smaller than the dimensions of the fault plane and fault healing is instantaneous. Displacement profiles of the segments of the Rangitaiki Fault are distorted by interactions with other faults so the identification of linear fault displacement gradients associated with this model is impossible.

7.2 The Development of the Fault Population in the Whakatane Graben

A positive correlation is observed between fault length and maximum displacement (figure 4.19); however the data are too few to distinguish between a linear or power-law correlation (Schliche et al., 1996; Cowie and Scholz, 1992; Gillespie et al., 1992; Marrett and Allmendinger, 1991; Watterson, 1986; Walsh and Watterson, 1987, 1988). The fault population is divided into two distinct populations; there are forty short and low displacement faults, with displacement lower than 50 m at horizon MCS1, and ten larger faults, with displacements between 70 and 300 m. These larger faults are the segments of the Rangitaiki Fault, and five faults within the Rangitaiki Fault hanging-wall that have large displacements at horizon MCS3 and are inferred to continue to the base of the faulted layer. The smaller faults are found to be limited vertically and either do not span the range of the seismic data, or have low displacements at the deepest horizon (MCS3).

In Chapter 6, the displacement rate of the Rangitaiki Fault was found to increase from 0.52 ± 0.18 mm yr^{-1} in the unlinked array (1340 – 770 ka) to 1.41 ± 0.31 mm yr^{-1} in the fully linked array above the 17 ± 1 ka surface; these rates have large error bars indicating the considerable uncertainty in horizon age. An increase in displacement rate on a linked fault is commonly associated with decrease in displacement rate and high mortality of adjacent smaller faults, an effect related to the localisation of strain in the fault population (McLeod et al., 2000; Meyer et al., 2002; Walsh et al., 2003). The decrease in displacement on faults surrounding the linked structure acts to maintain a constant strain rate in the region. Within the pseudo-3D survey area, the faults surrounding the Rangitaiki Fault do not show a decrease in displacement accumulation rate, and instead increase in rate such that their displacement remains complimentary to the displacement of the Rangitaiki Fault (Figure 14, Chapter 4). This result shows that the total displacement rates – and so strain and extension rates – have increased in the Whakatane Graben.

The total increase in displacement rate within the pseudo-3D survey may be explained by considering the broader structure of the Taupo Volcanic Zone. Strain rates of 0.1 – 0.2 x $10^{-6}yr^{-1}$ estimated for the pseudo-3D survey area prior to the linkage of the Rangitaiki Fault (chapter 4) are similar to current geodetically determined estimates for the whole TVZ of 0.07 ± 0.08 x $10^{-6}yr^{-1}$ to 0.19 ± 0.10 x $10^{-6}yr^{-1}$ (Adams, 1983; Walcott, 1984). Figure 5, Chapter 1 shows a seismic section across the Taupo Volcanic Zone and shows the change in faulting style from the west (Motiti Graben) to the east (Whakatane Graben). In the west, there are several large, inactive and buried faults displacing a thick sedimentary

sequence. In the Whakatane Graben to the east, the large faults all reach the surface and displace a thinner and younger sedimentary sequence than in the west. It is not clear whether the transfer of fault activity from the Motiti Graben to the Whakatane Graben was a gradual eastward migration or a rapid switching of faulting regimes.

Another important question is whether the strain rate within the pseudo-3D survey area increased because the Rangitaiki Fault linked, rather than the Rangitaiki Fault linking because of an increase in strain rate. There are three possible explanations:

1. Faults within the Taupo Volcanic Zone, including the Rangitaiki Fault, linked through spontaneous localisation of strain in the fault population. Decreases in adjacent faults are not properly recorded because the pseudo-3D survey area is tightly confined to the immediate surroundings of the Rangitaiki Fault and is not representative of faulting at the regional scale.

2. The Rangitaiki Fault linked and became a dominant seismogenic-zone-spanning fault in the Whakatane Graben. The increase in size of the linked Rangitaiki Fault allows higher displacement rates, and a greater proportion of the regional strain rate is accommodated by faulting within the Whakatane Graben.

3. The rates of faulting within the pseudo-3D survey area increased because of localisation of strain in the Whakatane Graben. To accommodate the increased strain rate, the Rangitaiki Fault linked allowing larger earthquakes and faster displacement rates.

Linkage of fault structures and localisation of strain occur spontaneously in fault populations because of the fractal nature of mechanisms of fault growth (e.g. Gupta et al. 1998; Cowie et al., 1995; Cowie, 1998), so an additional mechanism for strain localisation need not be imposed. Populations of small faults have been observed clustering around large faults as a damage zone (Knipe et al., 1996, Fossen and Hesthammer, 2000), so the increase in displacement rate of small faults in the immediate vicinity of the Rangitaiki Fault is again consistent with other fault development observations. However, model 1 implies localisation happening throughout the TVZ penecontemporaneously. The seismic section of Figure 1.5, Chapter 1 shows an eastward shift in fault activity, leading to the rejection of this model.

Both models 2 and 3 are consistent with the currently available data, showing an eastward migration of tectonic activity. The difference between the models lies in whether the strain rate in the Whakatane Graben increases because the Rangitaiki Fault links (model 2), or the Rangitaiki Fault links because of increased strain rate in the Whakatane Graben (model 3).

Davey et al. (1995) show a seismic section across the Bay of Plenty including the offshore TVZ. They identify predominantly normal and listric faulting downfaulted to the west and displacing basement over most of the TVZ. The faults are observed to dip at around 60°, decreasing to around 10° with depth and sole out at around 3 seconds TWT. Davey et al. (1995) interpret a change with time from east-dipping normal faults including the Tauranga Fault, to west dipping faults such as the Rangitaiki and White Island Faults and an associated increase in magnitude of faulting. They propose the faulting in the TVZ has proceeded in a similar way to the asymmetric imbricate rifting model of Wernieke and Burchfiel (1982) in which the leading edge of the decollement propagates eastwards into the east coast greywackes with time. This interpretation is in agreement with model 3 presented above, where the displacement rate of faults within the Whakatane Graben increases leading to the linkage of the Rangitaiki Fault.

7.3 Seismic Risk in the Bay of Plenty

The observed rate of earthquakes (n) with seismic moment $\geq M_0$ follows a power-law distribution: $n(M_0) = aM_0^{-B}$ or in log form $log[n(M_0)] = A - bM_0$ (Gutenberg and Richter, 1954). Gutenberg and Richter (1954) defined this relation only up to earthquake magnitudes Ms ~7.5, above which the relationship degenerated, later found to be a result of saturation in the magnitude scale at this point. For small earthquakes the gradient of this straight-line distribution, -b, is found to lie between 0.8 and 1.2 (Pacheo et al, 1992). If this relationship is scale invariant, then the distribution should be described by the same straight line and b value over the entire range of magnitudes. However, geometrical constraints are different for earthquakes that are limited to the brittle crust (small earthquakes) compared to those that span the brittle layer (large) earthquakes (Scholz, 1982): small earthquakes can grow both laterally and vertically as their rupture dimensions have no bounds, large earthquakes have no lateral restriction to their rupture length, but are restricted vertically by the thickness of the seismogenic layer (beneath which no earthquakes can be generated). Because of this, small earthquakes are confined by fault structures in two dimensions, where large earthquakes are confined in only one. This difference in dimensions affects the scaling properties of earthquakes from small to large events. Seismic moment is found to scale as the cube of the rupture length for small events (e.g. Hanks, 1977) and as the square of the rupture length for large events, and is proportional to the down dip width of the seismogenic thickness (Scholz, 1982; Shimazaki, 1986; Pegler and Das, 1996). Because these two sets of faults scale differently they belong to two distinct size distributions.

Rundle (1989) derived frequency magnitude relations for small and large earthquakes

and found the b value changed from 1.0 to 1.5 from small to large earthquakes, while Paceco et al. (1992) found a change in b value from 0.94 to 1.39 between large (Mw≥6) and small (6 ≥ Mw ≥ 3) earthquakes. For an individual fault the increase in b value in larger earthquakes means that large earthquakes occur more frequently than predicted by extrapolation of small earthquakes.

This change in earthquake scaling could affect the predicted recurrence time of large earthquakes on the Rangitaiki Fault (Chapter 4) and the associated seismic risk in the Bay of Plenty. As the Rangitaiki Fault spans the seismogenic layer, earthquakes that rupture the entire fault plane also span the seismogenic layer and scale as large earthquakes.

Population analysis (Chapter 4) of the faults within the pseudo-3D survey area suggests a distinction between the large, through-going Rangitaiki Fault and the smaller faults in its hanging-wall and footwall (Chapter 4, Figures 4.16 and 4.19). This distinction is interpreted as the difference between large faults that span the seismogenic zone (the Rangitaiki Fault and hanging-wall faults HW1-HW5) and the small faults that are limited in vertical extent. The faults spanning the seismogenic zone all have larger displacement than the vertically limited faults and most are longer (Chapter 4, Figure 4.19). These faults consistently show greater displacement rates than the vertically limited faults, although this result may be biased by poor resolution of small faults at depth.

If the data used to determine displacement rate did not include a full seismic cycle i.e. does not include at least one earthquake that ruptured the full fault plane of every fault, then the recurrence rate is only defined for small earthquakes and the seismic risk will be under-estimated. The displacement profiles of the Rangitaiki Fault observed in the high-resolution data (Chapter 5) show that patches of the fault remain inactive for periods of at least 2 ka. During these periods, there can have been no earthquakes that have ruptured the entire fault plane. Displacement rates derived from longer time periods include large earthquakes (rupturing the entire fault plane). From this it can be inferred that the fault displacement rate determined from the entire 18 kyr post-glacial sequence does include contributions from large earthquakes and the recurrence rate is properly defined.

Wells and Coppersmith (1994) empirically determined the relationship between the moment magnitude of an earthquake and the rupture area as $M = 3.93 \pm 0.23 + 1.02 \pm 0.10 * \log$ (rupture area in km^2). Using this relationship, the moment magnitude of an earthquake rupturing the entire Rangitaiki Fault can be estimated. The Rangitaiki Fault is approximately 20 km in length (chapter 6), and its width (vertical extent) is defined by the base of the seismogenic zone, here at 6 km depth (Bryan et al. 1999), giving a total faulted area of 120 km^2. Using the empirical relation shown above, an earthquake rupturing this

surface area is expected to have a moment magnitude of between 5.6 and 6.5. This places the Edgecumbe earthquake (Ms6.6) at the upper limit of earthquake size possible on the Rangitaiki Fault.

The repeat time of 320 – 600 years calculated for Edgecumbe-like events in Chapter 4 assumes that only whole-fault rupturing earthquakes occur on the Rangitaiki Fault, however, this is not likely to be the case. The post-glacial sediments in the Whakatane Graben record fault movements over timescales of c. 2 ka that show sections of the Rangitaiki Fault remained pinned, whereas sediments accumulated over time intervals greater than 4 ka show similar structures to those accumulated over 300 ka and include no points with zero displacement (Chapter 5). Assuming that a large earthquake ruptures the entire Rangitaiki Fault every 2000 years, the 320 - 600 year recurrence rate assuming only large earthquakes can be used to determine the strain release due to small earthquakes. The recurrence rate assuming only large earthquakes is ~4 times smaller than the observed minimum rate. From this, it can be deduced that small earthquakes that do not rupture the entire fault surface accommodate three quarters of the strain release due to seismic-scale faulting.

7.4 Link to Onshore Structures

Structural observations in the onshore TVZ are limited by poor exposure. Fault traces, largely interpreted from aerial photographs trend NE-SW, with faulting younging towards the axis of the extensional system (Berryman and Villamoor, 1999). Extensional strain is accommodated by movement on steep, predominantly normal faults (Grindley, 1965), with little distributed permanent strain throughout the rock mass (Villamoor and Berryman, 2000).

An extension axis oriented at 045° is inferred for the Bay of Plenty Region from the Okataina Volcanic Centre to the Bay of Plenty coast and beyond, including the Whakatane Graben, defined by a polarity switch in fault dip direction (Rowland and Sibson, 2000). Fault orientations range over 40° and are bimodally distributed with SE dipping faults trending predominantly NNE-SSW and NW dipping faults trending more easterly. Fault strike observations in the offshore Whakatane Graben range between 50° – 60° (Lamarche et al., 2000). The bimodal strike distribution observed in the onshore faults population may be present in the offshore faults, arising from the difference in faulting styles between the Rangitaiki Fault and the hanging-wall faults. The segments of the Rangitaiki Fault strike on average at 57° and dip dominantly to the northwest, whereas the hanging-wall faults, which have a more easterly mean orientation (66°, Chapter 4) contain a significant proportion of southeast dipping faults.

The back-arc extension of the TVZ is oblique to the TVZ orientation, and the strike angles of faults in the offshore Whakatane Graben reflect this (see Chapter 4). The McCoss construction (McCoss, 1986) makes use of basic geometry to define the relationship between expected fault orientations, opening direction and rift orientation at obliquely converging or diverging tectonic zones. In the construction the rift opening direction and the normal to the rift boundary are drawn as diameters of a circle. The line joining these directions at the circles circumference bisects the angle between them, and so has the orientation of the instantaneous strain and fault structures.

In the TVZ, the extension direction has been estimated using earthquake focal mechanisms (Beanland et al., 1989) and geodetic surveys (e.g Darby et al., 2000) and trends approximately NNW-SSE. Observations of fault and fissure orientations forming a coastal transect show a progressive clockwise rotation from east (outside the Whakatane Graben) to west (central Whakatane Graben) (Figure 7.1; Sanderson, unpublished fieldwork). Assuming these faults have formed under the same extension conditions (NNW-SSE extension), the orientation of these faults reveals the dominant basement orientation underlying the surface structures.

Faults observed in a cliff section at Otamarakau (figure 7.1b) are oriented approximately perpendicular to the geodetically determined opening direction and have similar orientations to the hanging-wall faults of the pseudo-3D survey area (see chapter 4 discussion). These faults are in the centre of the graben, some 15 km from the eastern boundary of the TVZ, and formed with little or no influence from the rift zone orientation.

Late faults at Kohi Point (Figure 7.1c) are oriented at approximately 60°; which combined with the NNW-SSE extension direction implies a 30° basement control. These faults lie close to the eastern margin of the TVZ and their orientation has been influenced by the 030° orientation of the TVZ margin. Similar results are found for faults on Whale Island and the slip direction of the Edgecumbe Earthquake (Beanland et al., 1989).

Fractures observed at Ohiwa Beach (figure 7.1d) trend 030°. These faults overlie one of the north-south trending faults of the North Island Shear Belt. The McCoss construction again shows the fault orientation consistent with oblique extension, however faults here are influenced by the north-south faulting trend of the North Island Shear Belt.

These observations are consistent with fault orientations within the pseudo-3D survey area, and show the effect a variation in basement orientation may have on surface faulting (see Chapter 4, Section 4.10.4). The 57° strike of the Rangitiaiki Fault and White Island Fault incicates a 30° basement control, as seen at Kohi Point. The younger, and shallower faults in the pseudo-3D survey area (dominantly the hanging-wall faults) strike almost

perpendicular to the extension direction, indicating - as at Otamarakau - that there has been little influence on fault orientation from the orientation of the Taupo Volcanic Zone.

7.5 The White Island Fault, Onset of Subsidence in the Whakatane Graben, and Style of Faulting at Depth.

This thesis is part of a larger ongoing study of the Whakatane Graben. Detailed observations of faulting in the pseudo-3D survey area may also be used to address some questions concerning the development of tectonism in the Bay of Plenty. These include the origin of the White Island Fault, the onset of subsidence in the Whakatane Graben, and the nature of faulting at depth.

Previous surveys of the Bay of Plenty have shown the complex structure of the White Island Fault, but its origins remain enigmatic. The White Island Fault has a pronounced 'zigzag' arrangement at the surface (Figure 7.1a), the largest example of this is the approximately 4 km east-west trending section of the fault north of the Rangitaiki Fault. The zigzag arrangement of the White Island Fault has been interpreted by Lewis and Pantin (1984) and Wright (1990) as the result of the intersection of extension in the TVZ and dextral displacement along the North Island Shear Belt. Wright (1992) interprets similar zigzag features of the Tauranga Fault Zone at the western boundary of the TVZ to have the same origin as the margins of the TVZ were coincident prior to the onset of extension. The increased spatial resolution provided by cruise TAN99-14 suggests that the complex structure of the White Island Fault is a direct result of the structural evolution of the Taupo Volcanic Zone, and the abrupt changes in fault strike are breached relay systems.

The eastward migration model of Davey et al. (1995), in which faulting in the TVZ has propagated eastward from a crustal detachment initially formed by a caldera eruption at the western margin of the TVZ, suggests that the eastern margin of the TVZ steps progressively eastward. The eastward step has been demonstrated in the seismic section in Figure 1.4, where the faulting in the Motiti Graben is buried whereas faulting in the more recent Whakatane Graben is currently active as the majority of faults have surface breaks. At c. 300ka, displacement rates in the pseudo-3D survey area increase markedly and the Rangitaiki Fault becomes a fully linked structure. New results from the broader regional survey suggest that the White Island Fault linked at this time; and it is proposed that this marks a stepwise eastward propagation, where the eastern boundary of the Taupo Volcanic Zone stepped from the western side of the Rurima Ridge bounding the Motiti Graben, to the White Island Fault bounding the Whakatane Graben. The evidence for this lies in the 4 km east-west trending section of the White Island Fault lying to the north of the

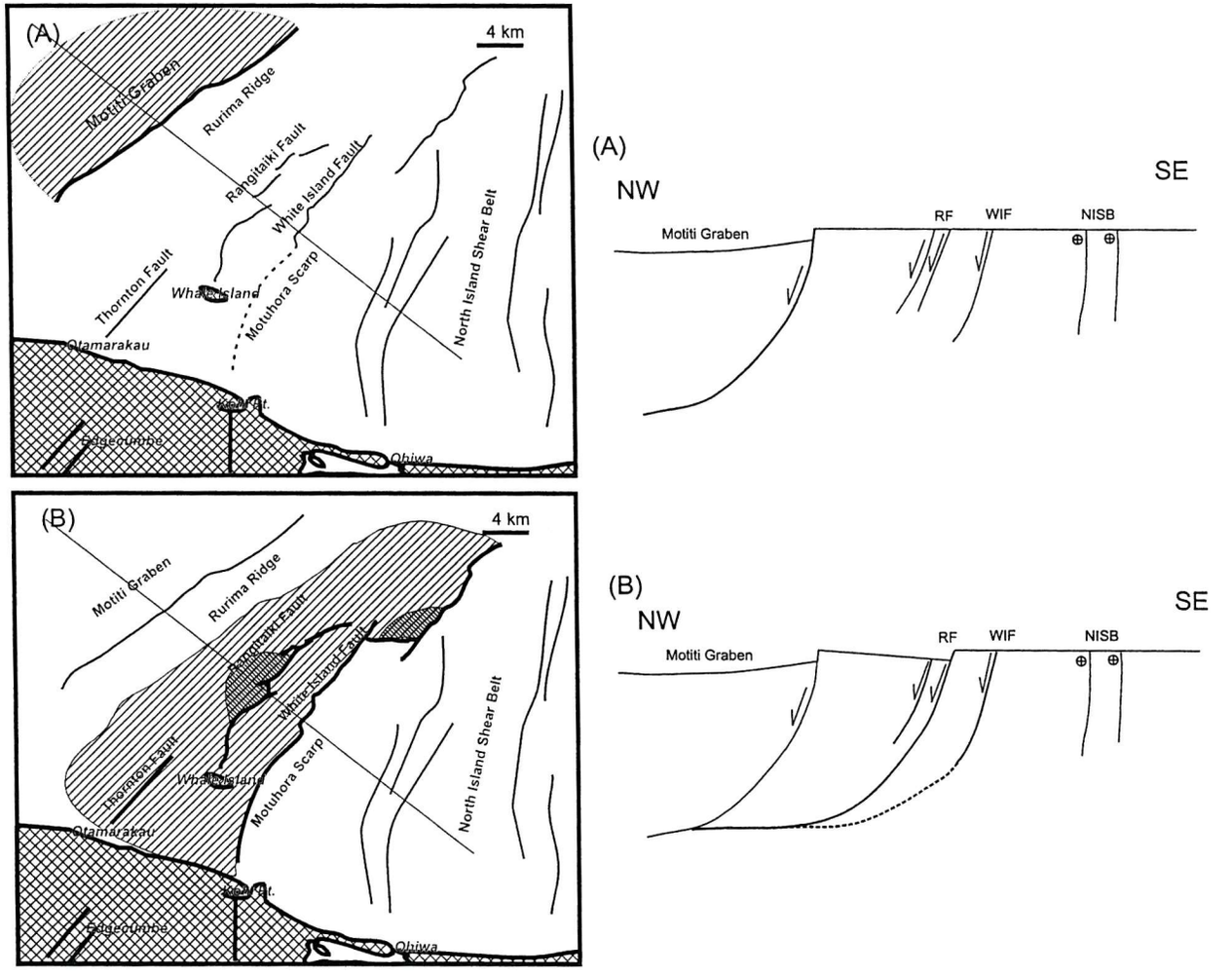

Figure 7.2: Schematic maps and cross sections showing development of faulting in the Whakatane Graben. The figures represent faulting up to 300 ka (a) and 300 ka to present (b). Major active faults are shown in bold, hatching shows areas of high tectonic activity and sedimentation. In figure 7.2a, tectonic activity is concentrated in the Motiti Graben, with minor faulting present in the Whakatane Graben. Figure 7.2b shows the major tectonic activity located further east in the Whakatane Graben - the Rangitaiki Fault (RF), and possibly the White Island Fault (WIF), are inferred to be connected to a detachment fault in the west.

Rangitaiki Fault. This feature is a breached relay system, lying between the overlapping tips of the two original faults. The breaching of the relay system is constrained in time by the development of a sedimentary depocentre above the 300 ka seismic horizon (MCS1) located in the hanging-wall of the relay-breaching fault.

The evolution of the Taupo Volcanic Zone is summarised in figure 7.2. Figure 7.2a shows the dominant faulting in the Motiti Graben with minor faulting throughout the remaining TVZ - including the unlinked Rangitaiki Fault and White Island Fault, that has been shown to have a similar strain rate as the TVZ as a whole. Figure 7.2b shows the increased displacement rate on the Rangitaiki Fault and Sedimentary deposition in the hanging-wall of the breached White Island Fault. The schematic cross section shows the proposed basal detachment underlying the Whakatane Graben.

7.6 Comparison with Other Extensional Settings

Migration of extension toward the subduction hinge is observed in the back-arc basins associated with the Appenines-Calabrian subduction system (the Tyrrhenian Sea and the Liguro-Provençal basin) and in the Aegean Sea. In the Appennines-Calabrian subduction system the migration of activity has been recorded in the ages of synrift deposits, radiometric ages of exhumed metamorphic rocks and of magmatic events (Jolivet et al., 1999). The Liguro-Provençal basin was the first back-arc basin formed at this margin between 30 and 35 Ma ago and continued extension until 15 Ma (Faccenna, 1997). During this time the slab dip increased and the subduction hinge migrated rapidly eastward. Following this there was a pause in subduction for about 5 Ma as the subducting slab again increases in dip. When subduction resumed the rollback of the subduction hinge increased and the Tyrrhenian Sea was formed in the thickened crust (Faccenna et al, 2001).

The migration of extension toward the subduction hinge in the TVZ (Davey et al., 1995) is suggestive of slab rollback, and implies that the Whakatane Graben is comparable with the Liguro-Provençal basin, an early-formed and rapidly extended back-arc basin. If this is the case then continuation of subduction and slab rollback at the Hikurangi Margin will result in continued eastward migration of faulting, taking in the north-south trending North Island Shear Belt and eventually extension in the thickened sediments of the Hikurangi Margin.

Continental rifts are often strongly asymmetrical in cross section (e.g. Figure 7.3). This asymmetry is necessary if the extension is largely accommodated on low angle normal faults that span the brittle seismogenic zone of the crust, as a symmetrical arrangement of opposing low-angle detachments would lead to the locking of one of the detachments

(Bosworth, 1985). Figure 7.3 shows cross sections through three extensional systems: the Taupo Volcanic Zone (Figure 7.3a), the Northern North Sea (Figure 7.3b) and the Gulf of Suez (Figure 7.3c). Rifts commonly show half-grabens normal to the rift axis, with most of the basin relief generated by a single rift-bounding fault. The asymmetry of the Whakatane Graben is demonstrated by the dominance of northwest dipping faults such as the Rangitiaki and White Island Faults. The WIF being an example of the rift-bounding fault, thin footwall sedimentation and large surface expression guiding sedimentation into the Whakatane Graben. The geometry of faults within a rift or back-arc graben is controlled

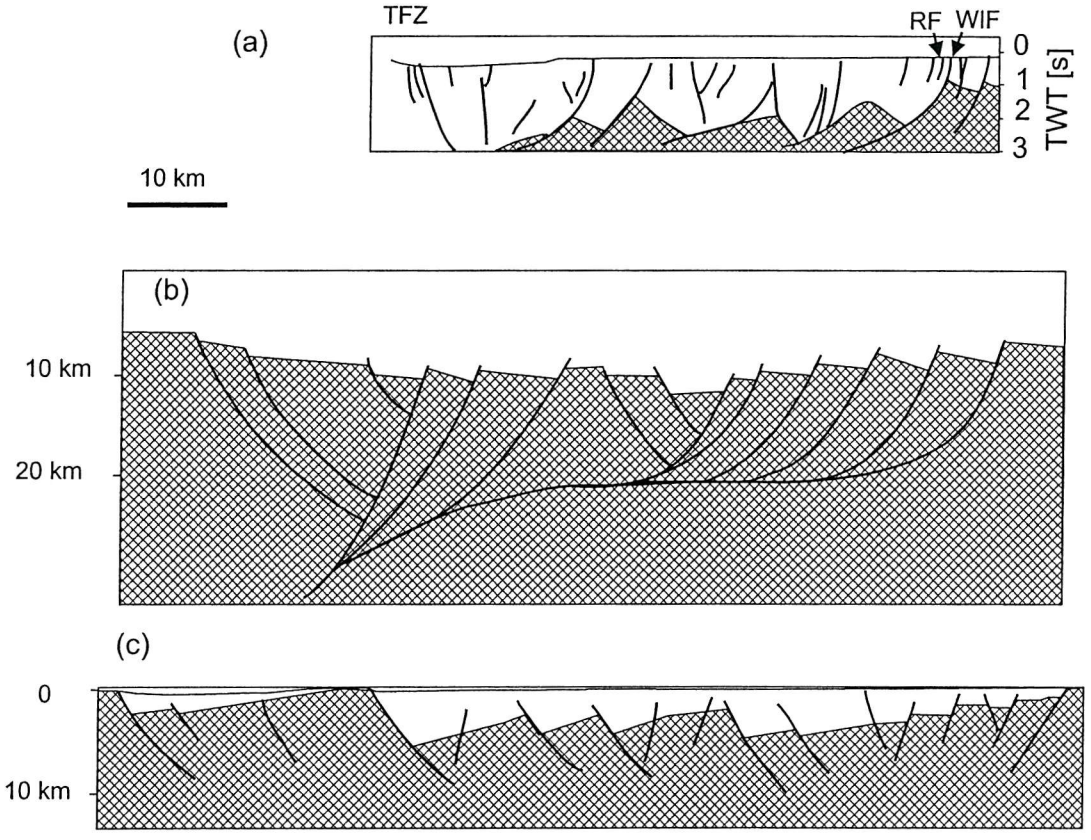

Figure 7.3: Cross sections through asymmetric rifts (a) Taupo Volcanic Zone; TFZ,Tauranga Fault Zone; RF, Rangitaiki Fault; WIF, White Island Fault. (b) Central North Sea and (c) Gulf of Suez ((a) after Davey et al., 1995; (b) and (c) after Bosworth, 1985). Hatched areas represent pre-rift basement.

by the angle between the extension direction and the rift orientation. Analogue models of rift systems show that where the extension direction is orthogonal to the rift margins, faulting is characterised by long, relatively straight rift border faults and shorter intra-rift faults. In contrast, oblique rifts have segmented border faults parallel to the zone of rifting but intra-rift faults form at high angles to the direction of extension (McClay and White,

1995; Clifton et al., 2000). The Ethiopian Rift is a roughly NE-oriented segment of the East African Rift System, which extends from the Afar to Southern Ethiopia. The border faults trend 30° –40°, while the intra-rift faults (Wonji Fault Belt) trend from N-S to 20° in response to a Quaternary extension direction trending E-W (Boccaletti et al., 1998). Similar to faults in the pseudo-3D survey area, the en echelon faults of the Wonji Fault belt include faults trending perpendicular to the extension direction (N-S trending faults), and faults oblique to both the extension and the rift orientations (20° trending faults). Boccaletti et al. (1992) observed a high sinistral shear gradient near the eastern border of the Main Ethiopian Rift and cite this as the cause of transtensional structures such as rhomb-shaped features and pull-apart basins. Such features have been observed on land within the Taupo Volcanic Zone.

These examples show that features such as rift asymmetry, propagation of faulting towards the subduction hinge and faults striking obliquely to both the extension direction and the rift axis observed in the Whakatane Graben have been observed elsewhere in other rifts of similar settings.

7.7 Future Work

The pseudo-3D survey area was found to include too few faults for fault population analysis. The sample size of at most 56 faults meant that the correction for the finite range effect could not be calculated. For fault population analysis a survey size at least twice the area of the pseudo-3D survey would be required (sampling over 100 faults). To correctly sample the largest faults the sample area would need to be larger in the along strike direction (57°). The sample was found to be distorted by the presence of the Rangitaiki Fault, and to correct for this, the sample area would need to be increased in the across strike direction (147°).

The strain rates calculated within the pseudo-3D survey area were found to be three times higher than the geodetically determined rates for the Taupo Volcanic Zone as a whole. The increase in across-strike survey length would improve the confidence of fault population analysis, and potentially provide a more representative area for estimating extension and strain rates.

In the high-resolution survey, the seismic profiles were too far apart to resolve lateral propagation of the faults in the post-glacial sediments. At the current resolution, lateral propagation of more than 5 $mmyr^{-1}$ can be resolved. More closely spaced 2D profiles or high-resolution 3D seismic could be used to define lateral propagation rates. True 3D chirp data, with CDP spacing of 0.9 m (inline CDP spacing of the 2D chirp used in the pseudo-3D survey, see chapter 2) in both inline and cross-line directions would theoretically be able to

resolve down to 0.5 $mmyr^{-1}$ lateral propagation rates.

The seismic signal used to collect the MCS data presented here was strongly attenuated below 2 seconds TWT, and no primary reflections could be confidently identified below this level. The pre-rift greywacke basement is inferred to lie approximately 0.5 – 1 second of TWT beneath horizon MCS3. A lower frequency seismic source could be used to identify the pre-rift basement of Davey and Lodolo (1995) within the pseudo-3D survey area. Seismic profiles imaging the pre-rift basement and deeper would be used to constrain the timing of the onset of rift related faulting, and also demonstrate conclusively whether or not the faulting observed in the Whakatane Graben is part of a reactivated fault system or (as has been inferred in chapter 6) an entirely new fault population.

Dating of sediments within the cores collected during cruise Tan99-14 was instrumental in deriving the ages of all the seismic horizons that have been interpreted. However, none of these horizons were physically sampled by the cores leading to large uncertainty ranges on the assigned ages of the horizons. Core samples from within the Whakatane Graben that sample the horizons MCS1 – MCS3 could be used to depth convert the seismic data, date the horizons and measure porosity at depth. This would enable more control on the timing of linkage, more accurate determination of fault slip rates, and allow better assessment of seismic risk to be completed.

Chapter 8

Conclusions

The data presented in this thesis reveal both long-term and short-term normal fault behaviour in a fault population surrounding and including the Rangitaiki Fault. The Rangitaiki Fault is now recognised as a 20 km long, linked, segmented normal fault lying in the centre of the Whakatane Graben. The displacement profile of the fully linked Rangitaiki Fault resembles that of a single fault, with a maximum close to the centre and displacements decreasing towards the tips. In chapter 6 the complete evolution of the Rangitaiki Fault was investigated. The fault was found to have initiated as 5 isolated segments, which grew together over 1 Ma. Fault tip propagation was the dominant faulting process initially, followed by the development of relay zones and their subsequent breaching. The system became fully linked between 300 ka and 17 ka. During the time interval spanned by the seismic data the Rangitaiki Fault increased in displacement rate from 0.52 ± 0.18 mm yr^{-1} (from 1340 ka to 770 ka) to 1.41 ± 0.31 mm yr^{-1} (17 ka to present).

Faulting in the pseudo-3D survey area is dominated by segment R1 of the Rangitaiki Fault in the southwest, passing into more broadly distributed faulting with more variable dip directions in the north. This is interpreted as a damage zone propagating ahead of a major fault (R1). The fault system present today may then be interpreted as a highly evolved damage zone, where optimally oriented and located faults have linked to form the major Rangitaiki Fault structure and have increased in displacement rate. To the north, the Rangitaiki Fault dies out in a complex zone of less-evolved damage-zone faulting where the Rangitaiki and White Island Faults converge.

Segment R1 of the Rangitaiki Fault continues southward from the psuedo-3D survey area for some 10 km, its southern tip (and that of the Rangitaiki Fault system) lying approximately 2 km north of Whale Island. Displacement is transferred southward from the Rangitaiki Fault onto the newly identified Thornton Fault. Displacement interaction between the Thornton Fault and the surface ruptures of the Edgecumbe earthquake are inferred based on their position at the landward continuation of the Thornton-Rangitaiki

Fault trend. Assuming that the average displacement rate of the Rangitaiki Fault applies to the Edgecumbe fault as a continuation of the same fault system, a repeat time of 320 – 600 years is inferred for Edgecumbe size events, which are close to the maximum magnitude for that size of fault. For all the strain accumulated across the Taupo Volcanic Zone to be relieved seismically, between 10 and 50 faults of the size and displacement rate of the Rangitaiki Fault would be required and distributed throughout the TVZ, with values at the lower end of this range more likely based on estimates of displacement rates on currently mapped faults.

Despite the level of linkage in the Rangitaiki Fault, the accumulation of displacement is still dominated by the relict segment boundaries acting as barriers to displacement accumulation. While displacement rates were found to be highly variable at short timescales, and between individual faults, the long-term evolution of the population as a whole is more ordered, and shows an average increase from 0.9 ± 0.3 $mmyr^{-1}$ to 2.6 ± 0.2 $mmyr^{-1}$ in the 1340 kyr since the deposition of horizon MCS3 (cf. displacement rate increase of the Rangitaiki Fault alone, see above paragraph).

The Whakatane Graben is a back-arc basin where the locus of activity has propagated to the southeast over time (Davey et al., 1995), the Rangitaiki and White Island Faults being two of the most recent structures. The White Island Fault is interpreted to have formed by linkage of overlapping segments leading to the zigzag arrangement of the fault trace. Abandoned fault splays are observed at the segment overlaps within the pseudo-3D survey area.

Currently, the Whakatane Graben is the most active section of this back-arc zone, extension accounts for approximately half of the extension across the whole Taupo Volcanic Zone (Wright, 1990). The displacement history shown in chapter 4 suggests that this was not always the case. The extension rate across the pseudo-3D survey area for the last 17 ± 1 ka is 2.4 – 3.4 $mmyr^{-1}$ assuming the faults dip 45 ± 10° at seismogenic depths. For the time interval between 300 – 17 ka, the extension rate is 0.7 – 0.9 $mmyr^{-1}$.

Strain rates across the pseudo-3D survey area derived from displacement measurements are 0.4 – 0.6 x $10^{-6}yr^{-1}$ for the last 17 ± 1 ka, and 0.1 – 0.2 x $10^{-6}yr^{-1}$ for between 300 ka and 17 ka. The extension and strain rates of the Taupo Volcanic Zone are known from recent geodetic surveys to be strongly heterogeneous (e.g. Crook and Hannah, 1989), and seismic sections across the TVZ (Davey et al., 1995; Lamarche et al, 2000) show that extension has migrated eastward (towards the subduction hinge) through time. The increase in strain rate observed in the Whakatane Graben is therefore interpreted as resulting from the eastward migration of the locus of deformation in the Taupo Volcanic Zone towards the subduction

hinge of the Hikurangi Margin.

The observed increase in displacement rate is consistent across all of the faults within the pseudo-3D survey area, showing that the increase in displacement rate on the Rangitaiki Fault is *not* matched by decreasing displacement rates on surrounding faults. This result is in keeping with the interpretation of eastward migration of tectonic activity, but contrasts with the observation of localisation of faulting observed in other rift systems (e.g. Gupta et al., 1998; McLeod et al., 2000; Meyer et al., 2001) where increased displacement rates in the largest faults post-linkage are balanced by decreasing displacement rates in surrounding small faults.

Appendix A

Multi Channel Seismic Processing

This appendix details the processing steps and parameters used in processing of the Multichannel seismic data from the pseudo-3D survey collected during cruise TAN99-14. See section 1 of chapter 3 for information about data acquisition and figure 2.4 for an overview of the processing workflow.

A.1 Navigation Data Processing

The DGPS positions on the field tapes are recorded in latitude and longitude, given in degrees and decimal minutes. The position recorded is that of the GPS antenna at the time the shot was fired; the navigation data processing is required to obtain the source and receiver locations. Some additional processing is required as several shots have erroneous GPS locations recorded.

The field tapes (SEG-D format on Digital Linear Tape (DLT)) are read using ProMAX, and the position information exported in ASCII format. At the end of the processing flow each trace has a source position, receiver position and CDP bin number and position associated with it. These values are imported back into ProMAX to be merged with the seismic data.

A.2 Removal of Navigation Outliers and Repeats

Throughout the recording of the pseudo-3D box, the GPS records contain outliers and consecutive shots with identical locations. Generally, these GPS errors are limited to a single shot within the profile, in which case the incorrect position is replaced by a value interpolated from the two adjacent records. In cases where large numbers of consecutive shots have no GPS values the data are disregarded.

A.3 Calculation of Shot and Receiver Locations

All the GPS locations are projected into UTM metres using the GMT command mapproject. UTM metres are used to make the geometry calculations more straightforward. For each trace the source-GPS and receiver-GPS offset distances are measured back along the ships track to give the source and receiver locations.

The assumption that the streamer and airgun closely follow the ships track is reasonable as the streamer was lying directly behind the vessel at the start of each line, and recording was stopped before turning at the end of each line. In addition, the feathering angle of the streamer was estimated at the mid-point of each line and was found to be negligibly small throughout the survey.

A.4 CDP Location and Trace Binning

The CDP location for each source-receiver pair is assumed to be the mid point between the two in the xy-plane. The CDPs are divided into 6.25 m long bins, giving an average 12 fold coverage. For each seismic line, the best-fit straight line through all the CDPs is calculated, and the 6.25 m ling CDP bins are measured out along it. The mean x and y co-ordinates of the CDPs in each bin are calculated and used as the bin location.

A.5 Seismic Data Processing

The traces were viewed in receiver gathers so misfired shots and noisy receiver channels could be easily identified. Any noisy channels or shots are removed (amplitude set to zero) at this stage. Channel 11 recorded no data throughout the pseudo-3D survey, and channels 10 and 46 were often noisy enough to degrade the stacked signal. Parameters for the processing steps were chosen on test panels.

A.5.1 Band-Pass Filter

A Minimum phase Ormsby band-pass filter was used with corner frequencies 10-15-120-150Hz.

A.5.2 True Amplitude Recovery

A time-power constant of 1.5 gave the best results.

A.5.3 Deconvolution

The data window for deconvolution was picked on each receiver gather. The data window begins just below the strong seabed reflection and continues down to 1 second two-way-time.

Minimum-phase predictive deconvolution with an operator length of 80ms and a predictive distance of 8ms was found to give the clearest results.

A.5.4 Time-Varying Band-Pass Filter

The high frequency component of the data was found to be strongly attenuated with depth, and the data signal was only present in the lower frequencies. A time varying band-pass filter was applied to improve the interpretability of the lower part of each seismic section. Three filters were used: 10-15-120-150Hz in the upper part of each seismic section, 10-15-70-80Hz in the middle and 10-15-40-60Hz in the lower part of each seismic section. The two-way times at which each filter was applied was determined by inspecting the data.

A.5.5 Velocity Analysis

Velocity analysis produced good results for the first 0.8 – 1.0 second of two-way time, with a maximum velocity of 2300m/s. Velocity analyses were generated at least every 100 CDPs giving about 10 analyses on each line.

A.5.6 Long Offset Mute

A long offset mute was designed at each analysis location. The shallow arrivals at long offsets are severely distorted by the normal move-out correction (NMO), and in some instances contain shallow-refracted arrivals. Both effects reduce the high frequency content of the signal and can hide the detail of the shallow arrivals. The long offset mute is tapered out before the seabed multiple arrivals to ensure maximum attenuation of the multiple by NMO.

A.5.7 Normal Move-Out (NMO) Correction and Stack

The effect of varying source-receiver offsets is removed by NMO. Long offset shallow arrivals are removed by the long offset mute (see above). The CDP gathers are stacked once the NMO correction is applied Within the area of the pseudo-3D survey area, the water bottom multiple is relatively low energy and can be satisfactorily attenuated by normal move-out correction alone.

A.5.8 Migration

Kirchoff-Stolt migration was applied using 105% of the stacking velocities. Migration considerably improves the lateral resolution and interpretability of the data.

Appendix B

High Resolution Seismic Processing

This appendix details the processing steps and parameters used in processing of the high-resolution seismic data (chirp and boomer) from the pseudo-3D survey collected during cruise KAH01-02. See section 2 of chapter 2 for information about data acquisition and figure 2.6 for an overview of the processing workflow.

B.1 Navigation Processing

The recorded navigation data, containing the time and position of each location fix, is compared with the seismic data profiles which have a record of the time for each recorded trace.

All times are recorded in New Zealand Daylight Saving Time (GMT+13), and are converted to decimal seconds, beginning at midnight on 18^{th} of January using the following equation.

$$Decsecs = (day - 18)x86100 + hourx3600 + minutex60 + second \tag{B.1}$$

The x- and y- co-ordinates of each trace are calculated by comparing the navigation files and seismic header records, and applying a shift along the ship track to compensate for the layback (the distance between the DGPS antenna and the source/receiver location).

There was no offset in navigation between the Boomer and Chirp data or between lines collected right-to-left and those collected left-to-right. For the first boomer line (BOOM3) the navigation and SES clocks were not synchronised, which resulted in an apparent shift of 80 metres. Later in the survey the printer was found to be causing some interference with the firing rate, affecting the recording of line BOOM145. Timing problems were limited to these two profiles and were corrected easily by applying a modified layback value to the data.

B.2 Chirp Sonar

B.2.1 Band-Pass and Notch Filtering

Filter test panels show that the signal content is dominantly beneath 4 kHz, the best results were found using a zero-phase band-pass filtered with corner frequencies 150, 1000, 4000 and 4500 Hz. Energy spikes are seen at several frequencies, only one (at 3140Hz) is within the data bandwidth, and is notch filtered.

B.2.2 F-X Deconvolution

F-X deconvolution uses the assumption that the frequency content of neighbouring traces will be similar and that any discrepancies are caused by random noise. The data are Fourier Transformed and a prediction filter is applied in distance for each frequency in a specified range (see ProMAX user manual p973-975).

Parameters

Horizontal window length	10 traces
% White noise	0
No. of filter samples	5
Time window length	10 ms
Time window overlap	5 ms
F-X frequency range	0 – 4000 Hz

B.2.3 Dynamic Signal/Noise Filtering

Dynamic S/N filtering enhances the lateral coherency of data by weighting each frequency by a function derived from the local signal-to-noise ratio. The signal component at each frequency is assumed to change only in phase from trace to trace, and the noise contribution is assumed to be random (ProMAX user manual p937-959).

Parameters

Horizontal Window length	20 traces
Time window length	10 ms
Time window overlap	5 ms
F-X frequency range	0 – 4000 Hz

B.2.4 Automatic Gain Control

Automatic gain control was used on the data to balance the energy along the traces as true amplitude recovery and geometric spreading corrections did not work well. A window of 20ms was found to produce the best results.

B.3 Boomer Profiles

A zero phase band-pass filter with corner frequencies 300, 1000, 2500 and 3000 Hz was applied to the boomer data. Other processing steps produced no appreciable improvement in interpretability and were deemed unnecessary.

B.4 Static Corrections

Static shifts introduced into the data by swell noise, tides, towfish depth and electronic delays in triggering, correlation and recording are corrected using the header statics function in ProMAX. The details of quantifying and correcting for these static shifts are given in the main text, chapter 2 section 2.2.1.

Appendix C

Structure maps of horizons interpreted in high-resolution siesmic data

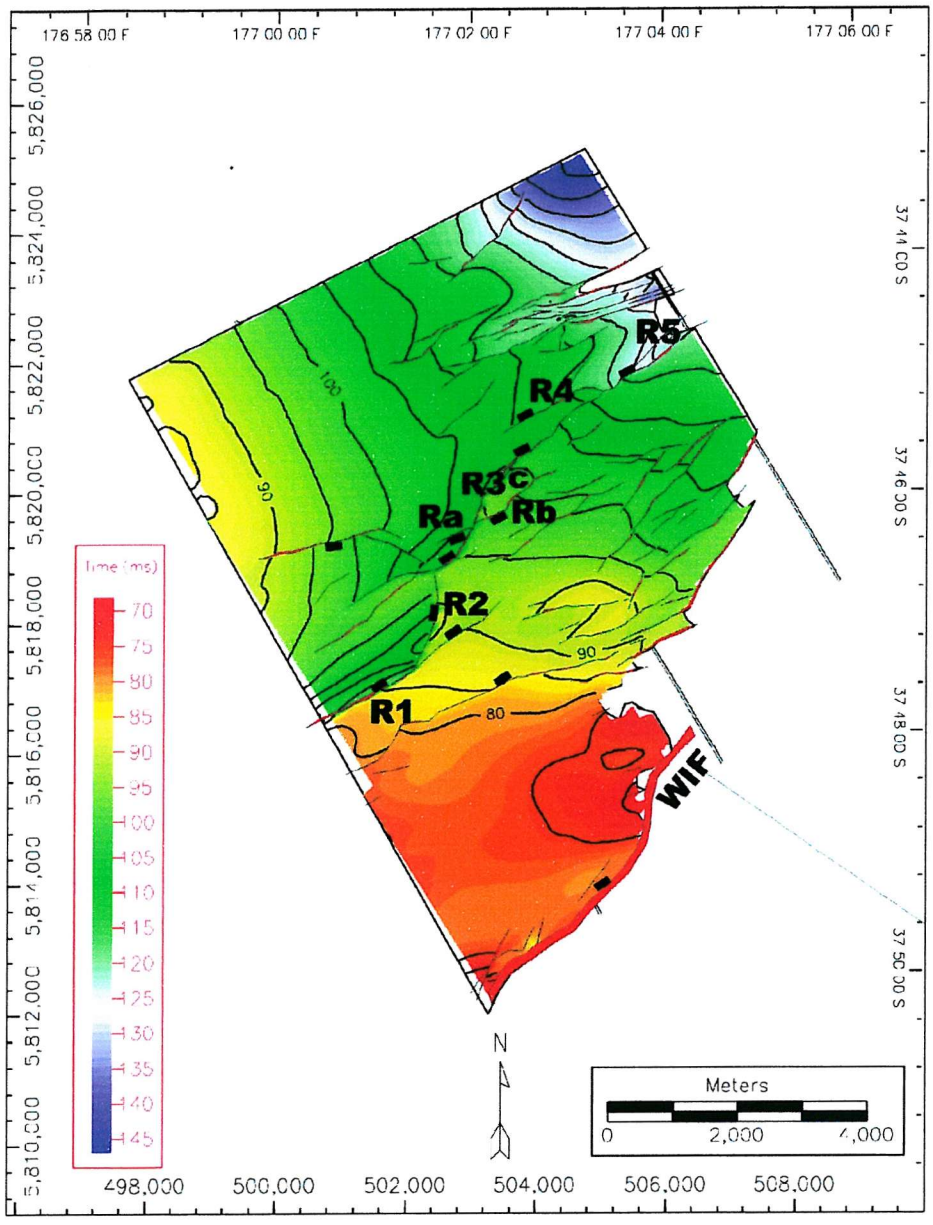

Figure C.1: Structure map of horizon HRS1. Structure contours are in milliseconds two-way-time, red areas are structural highs, purple areas show structural lows. Segments of the Rangitaiki Fault are labelled R1 to R5. WIF indicates the White Island Fault. Black rectangles indicate downthrown side of faults.

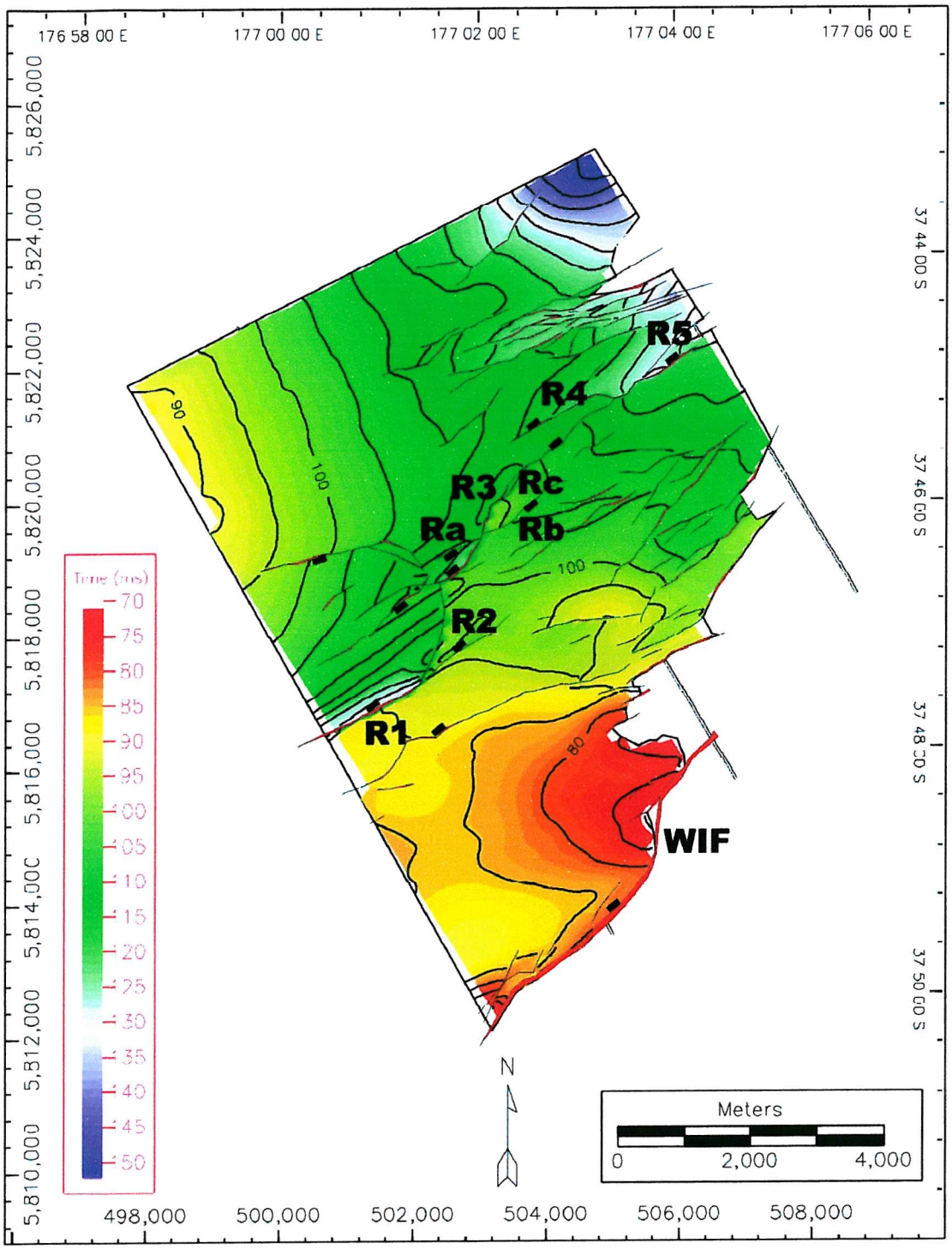

Figure C.2: Structure map of horizon HRS2. Structure contours are in milliseconds two-way-time, red areas are structural highs, purple areas show structural lows. Segments of the Rangitaiki Fault are labelled R1 to R5. WIF indicates the White Island Fault. Black rectangles indicate downthrown side of faults.

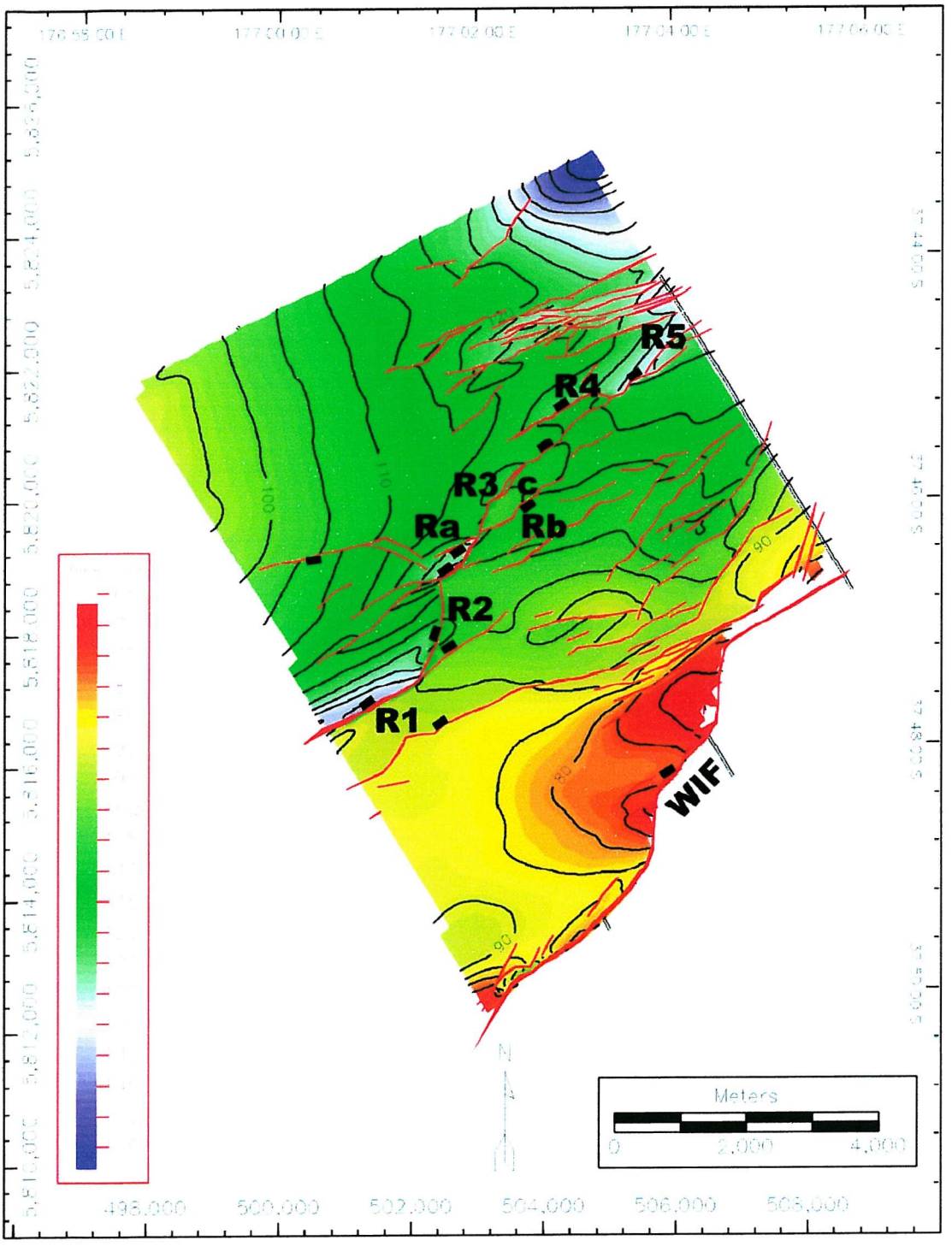

Figure C.3: Structure map of horizon HRS3. Structure contours are in milliseconds two-way-time, red areas are structural highs, purple areas show structural lows. Segments of the Rangitaiki Fault are labelled R1 to R5. WIF indicates the White Island Fault. Black rectangles indicate downthrown side of faults.

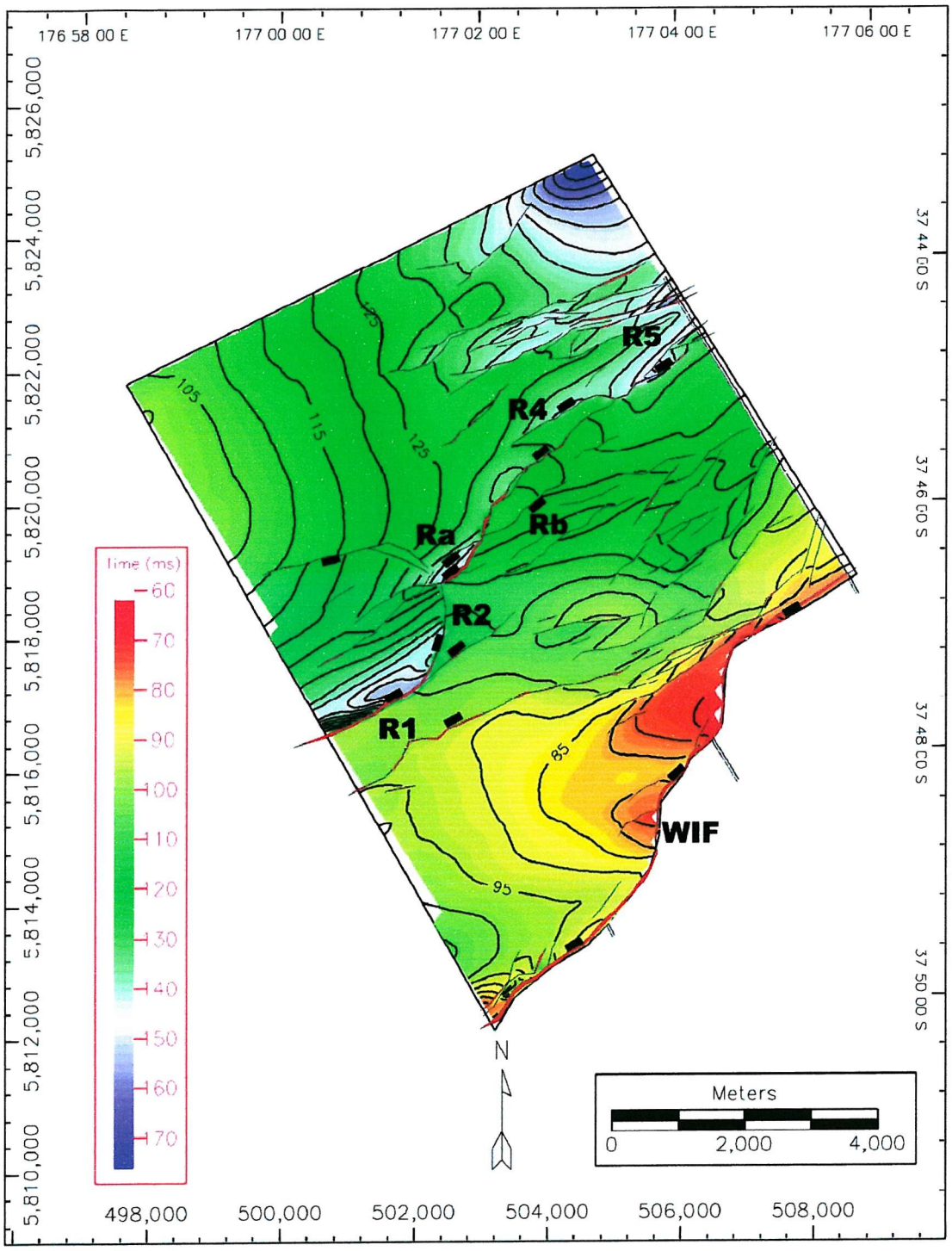

Figure C.4: Structure map of horizon HRS4. Structure contours are in milliseconds two-way-time, red areas are structural highs, purple areas show structural lows. Segments of the Rangitaiki Fault are labelled R1 to R5. WIF indicates the White Island Fault. Black rectangles indicate downthrown side of faults.

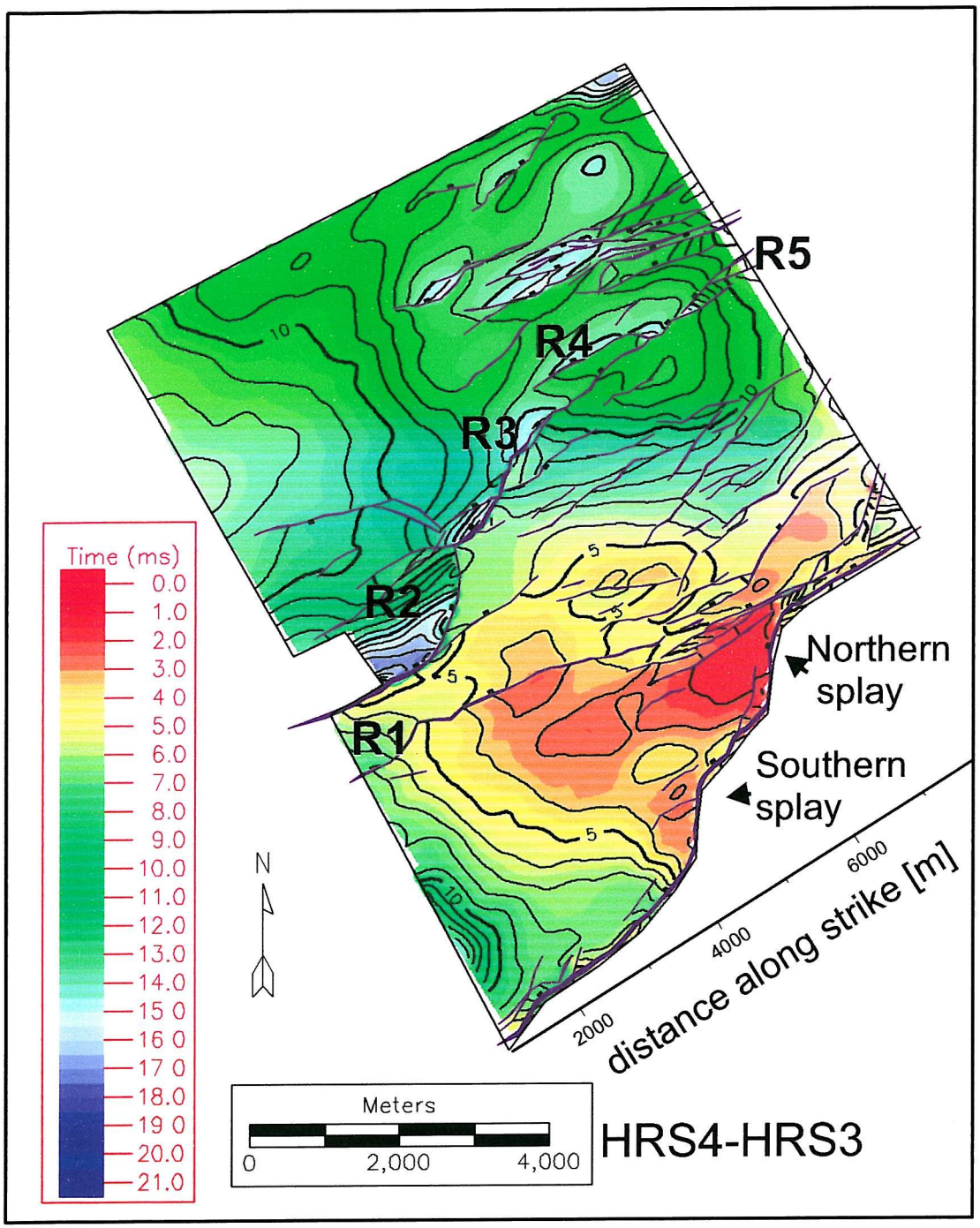

Figure C.5: Isopach maps of sediment thickness between horizons HRS4 and HRS3 (17 - 13 ka). Contour values are in milliseconds two-way time, colours are from red (thin sediments) to purple (thick sediments). Rangitaiki Fault segments are labelled R1 - R5, northern and southern White Island Fault splays are shown. Strike projected distance along strike is shown for each map.

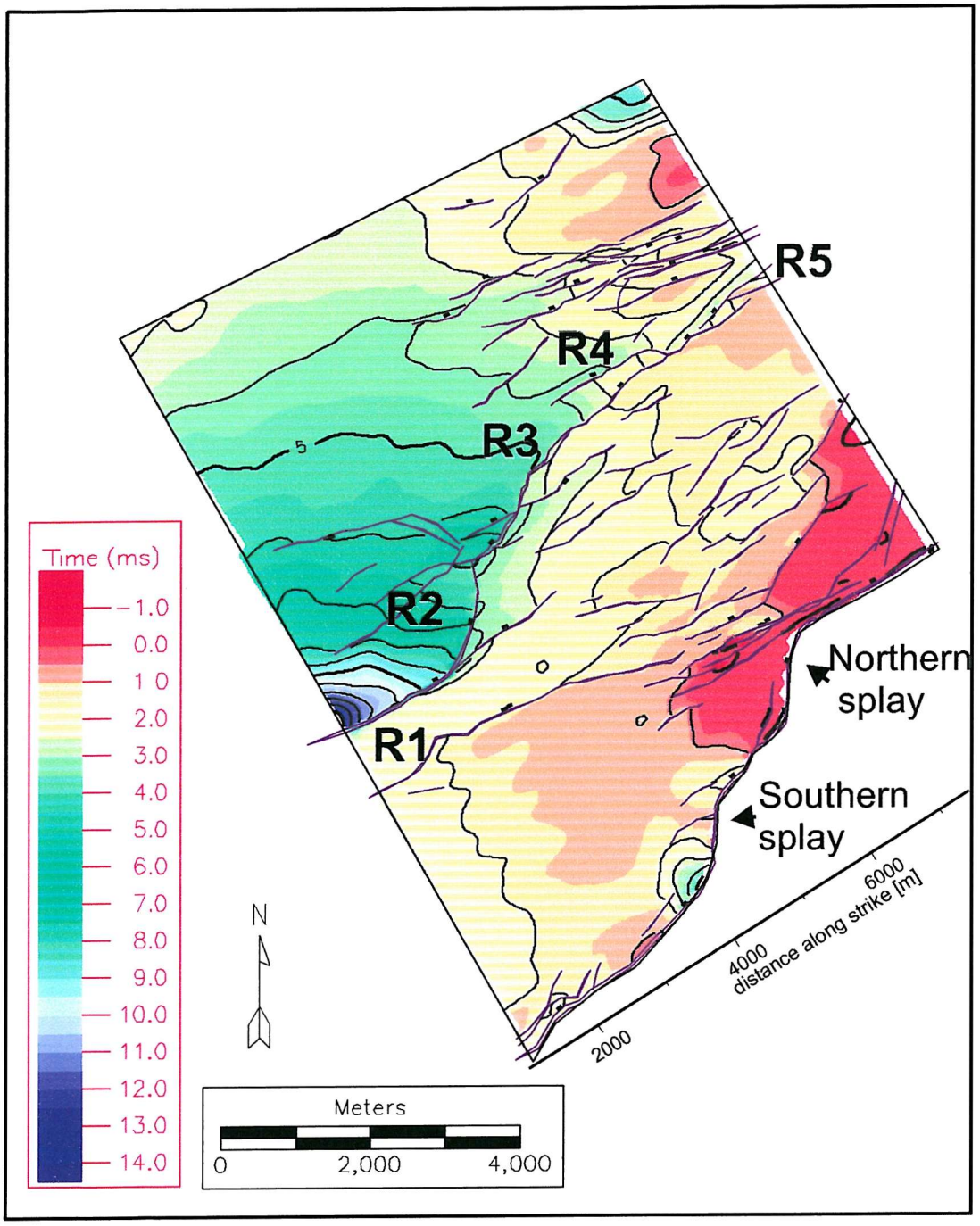

Figure C.6: Isopach maps of sediment thickness between horizons HRS3 and HRS2 (13 - 11 ka). Contour values are in milliseconds two-way time, colours are from red (thin sediments) to purple (thick sediments). Rangitaiki Fault segments are labelled R1 - R5, northern and southern White Island Fault splays are shown. Strike projected distance along strike is shown for each map.

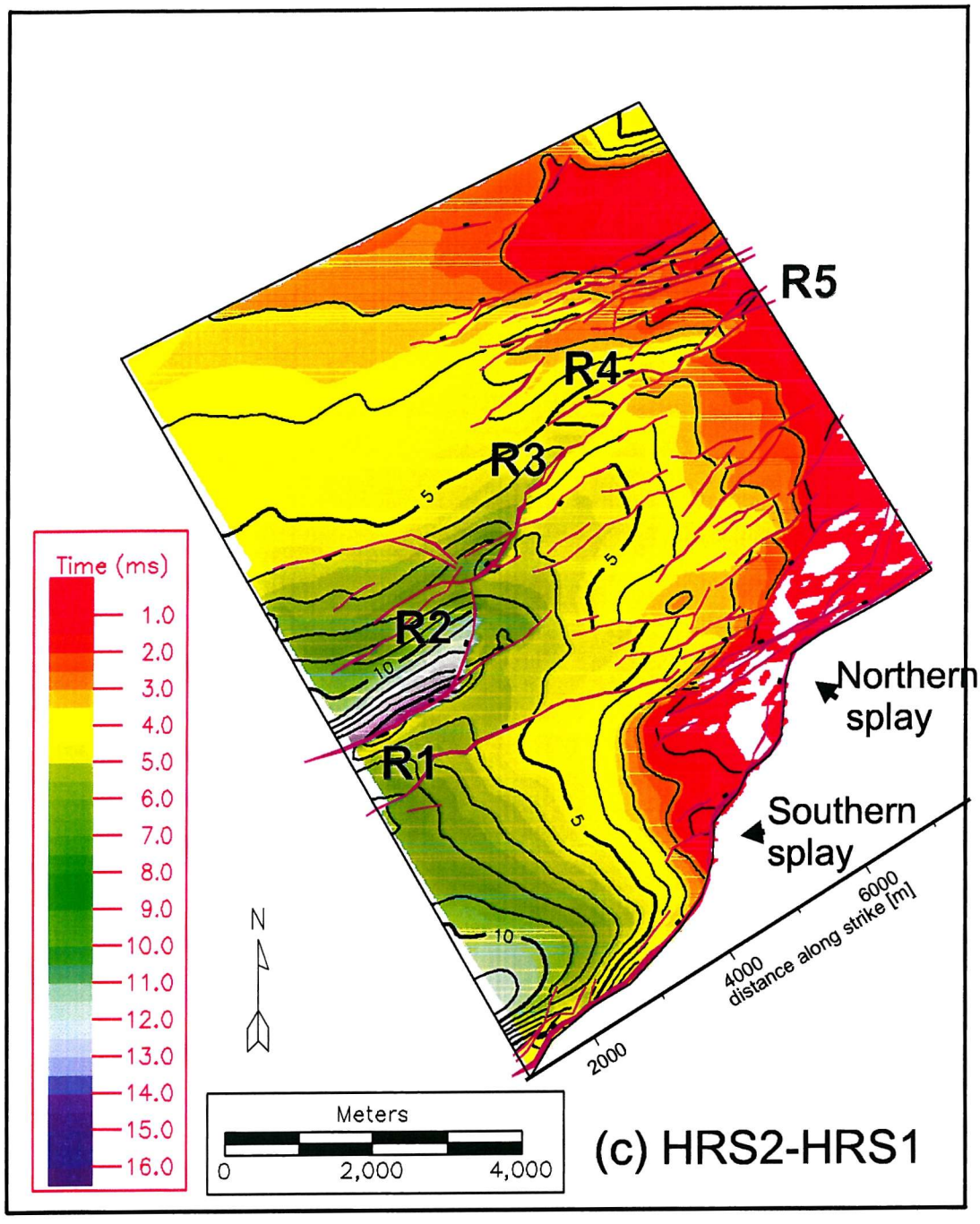

Figure C.7: Isopach maps of sediment thickness between horizons HRS2 and HRS1 (11 - 9 ka). Contour values are in milliseconds two-way time, colours are from red (thin sediments) to purple (thick sediments). Rangitaiki Fault segments are labelled R1 - R5, northern and southern White Island Fault splays are shown. Strike projected distance along strike is shown for each map.

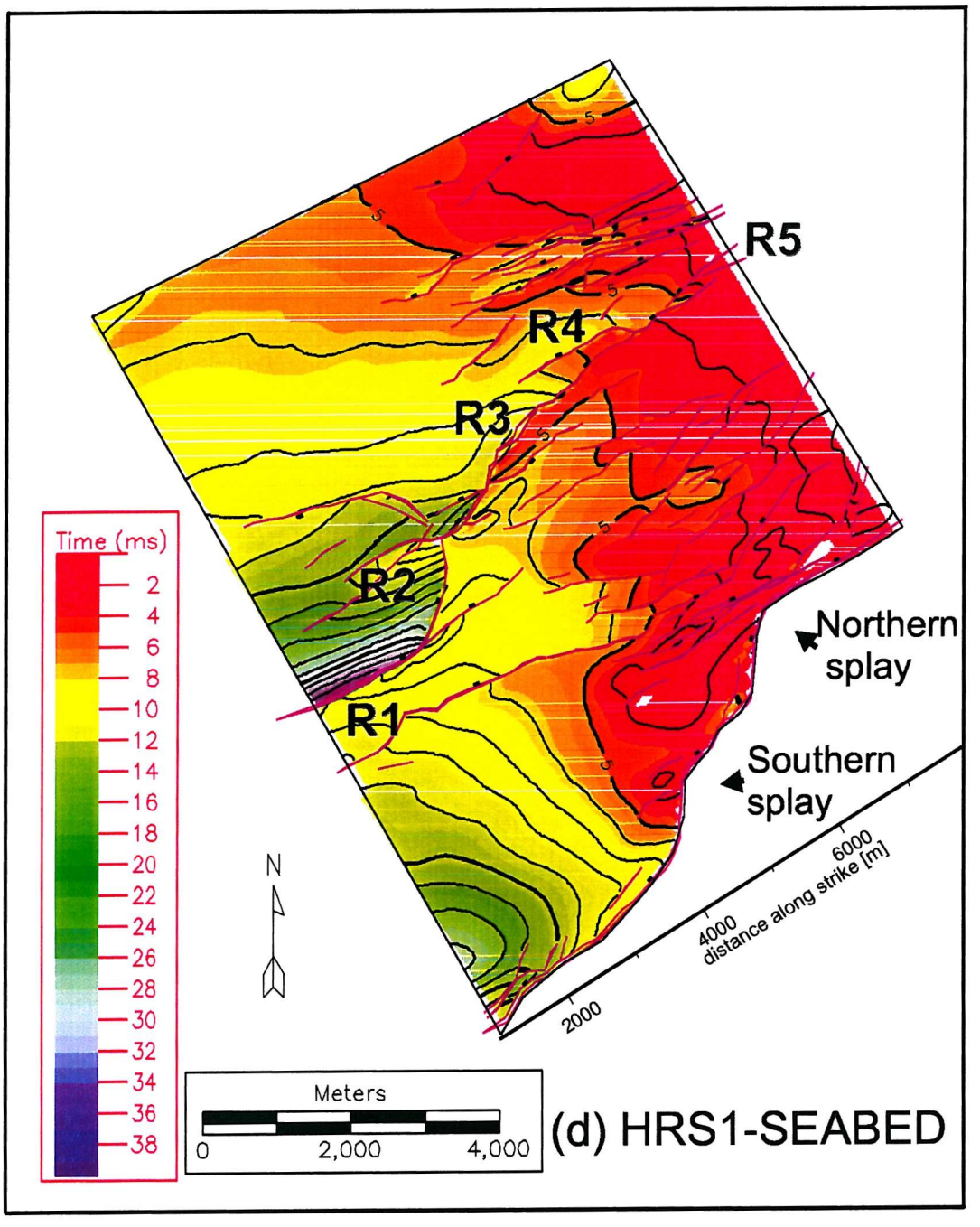

Figure C.8: Isopach maps of sediment thickness between horizons HRS1 and the seabed (9 ka - present). Contour values are in milliseconds two-way time, colours are from red (thin sediments) to purple (thick sediments). Rangitaiki Fault segments are labelled R1 - R5, northern and southern White Island Fault splays are shown. Strike projected distance along strike is shown for each map.

Bibliography

[1] D.A. Adams. The theory and application of geodetic net adjustments and strain analysis. Unpublished final report for a research contract between the Department of Lands and Survey and Victoria University of Wellington., 1983.

[2] D.A. Adams. Some methods of analysis of geodetic data and their applications to the measurement of crustal deformation. Master's thesis, Victoria University, Wellington, New Zealand., 1984.

[3] R.D. Adams and T. Hatherton. Seismological and geothermal research in new zealand. *Nature*, 246:262–264, 1973.

[4] H. Anderson and T. Webb. The rupture process of the 1987 edgecumbe earthquake, new zealand. *New Zealand Journal of Geology and Geophysics*, 32(1):43–52, 1989.

[5] R.T. Bachman. Acoustic and physical property relationships in marine sediment. *Journal of the Acoustic Society America*, 78(2):616–621, 1985.

[6] P.F. Ballance. Simplification of the southwest pacific neogene arcs: inherited complexity and control by a retreating pole of rotation. In MacMiocaill C. and Ryan P.D., editors, *Continental Tectonics*, volume 164 of *Geological Society of London Special Publication*, pages 7–19. 1999.

[7] J.A.M. Barnett, J Mortimer, J.H. Rippon andJ.J. Walsh, and J. Watterson. Displacement geometry in the volume containing a single normal-fault. *AAPG bulletin-American Association of Petroleum Geologists*, 71(8):925–937, 1987.

[8] S. Beanland and K.R. Berryman. Holocene coastal evolution in a continental rift setting; bay of plenty, new zealand. *Quataternary International*, 15/16:151–158, 1992.

[9] S. Beanland, K.R. Berryman, and G.H. Blick. Geological investigations of the 1987 edgecumbe earthquake, new zealand. *New Zealand Journal of Geology and Geophysics*, 32:73–91, 1989.

[10] S. Beanland, G.H. Blick, and D.J. Darby. Normal faulting in a back-arc basin: Geological and geodetic characteristics of the 1987 edgecumbe earthquake, new zealand. *Journal of Geophysical Research*, 95:4693–4707, 1990.

[11] K.R. Berryman and P. Villamoor. Spatial and temporal zoning of faulting in the taupo volcanic zone, new zealand. volume 107A of *Miscellaneous Publicatons*. Geology Society of New Zealand, 1999.

[12] A.I. Best and D.E. Gunn. Calibration of marine sediment core loggers for quantitative acoustic impedance studies. *Marine Geology*, 160:137–146, 1999.

[13] W.H. Beyer. *CRC Standard mathematical tables*. CRC Press, Inc., 28th edition, 1987.

[14] M. Boccaletti, M. Bonini, R. Mazzuoli, B. Abebe, L. Piccardi, and L. Tororici. Quaternary oblique extensional tectonics in the ethiopian rift (horn of africa). *Tectonophysics*, 287:97–116, 1998.

[15] W. Bosworth. Geometry of propagating continental rifts. *Nature*, 316:625–627, 1985.

[16] N. Bruguier and T. Minshull. Accurate modelling of sonobuoy refraction data to determine velocity variations in oceanic crust. *Marine Geophysical Researches*, 19:25–36, 1996.

[17] C.J. Bryan, S. Sherburn, H.M. Bibby, S.C. Bannister, and A.W. Hurst. Shallow seismicity of the central taupo volcano zone, new zealand: its distribution and nature. *New Zealand Journal of Geology and Geophysics*, 42:533–542, 1999.

[18] J. Bull, J. Dix, G. Lamarche, S. Taylor, and P. Wiles. Active faulting in the southern whakatane graben - application of high resolution reflection seismology. Unpublished cruise report, KAH0102, Southampton Oceanography Centre, 2001.

[19] R. Burgmann, D.D. Pollard, and S.J. Martel. Slip distributions on faults: effects of stress gradients, inelastic deformation, heterogeneous host rock stiffness, and fault interaction. *Journal of structural Geology*, 16:1675–1690, 1994.

[20] R.M. Burt, J.W. Cole, and P.Z. Vroon. Volcanic geology and geochemistry of motuhora (whale island), bay of plenty, new zealand. *New Zealand Journal of Geology and Geophysics*, 39:565–580, 1996.

[21] R.M. Carter, L. Carter, and D.P. Johnson. Submergent shorelines, sw pacific: episodic post-glacial transgression. *Sedimentology*, 33:629–649, 1986.

[22] J.A. Cartwright, C. Mansfield, and B. Trudgill. The growth of faults by segment linkage. In P.G. Buchanan and D.A. Nieuwland, editors, *Modern Developments in Structural Interpretation, Validation and Modelling*, volume 99 of *Geological Society Special Publications*, pages 163–177. 1996.

[23] J.A. Cartwright, B.D Trudgill, and C.S. Mansfield. Fault growth by segment linkage: and explanation for scatter in maximum displacement and trace length data from the canyonlands grabens of se utah. *Journal of Structural Geology*, 17(9):1319–1326, 1995.

[24] T.J. Chapman and A.W. Meneilly. The displacement patterns associated with a reverse-reactivated, normal growth fault. In A.M. Roberts, G. Yielding, and B. Freeman, editors, *The Geometry of Normal Faults*, volume 56 of *Geol. Soc. Special Publications*, pages 183–191. 1991.

[25] C.G. Chase. Plate kinematics: the americas, east africa and the rest of the world. *Earth Planet. Sci. Lett.*, 37:355–348, 1978.

[26] C. Childs, S.J. Easton, B.C. Vendeville, M.P.A. Jacksona, S.T. Lin, J.J. Walsh, and J. Watterson. Kinematic analysis of faults in a physical model of growth faulting above a viscous salt analogue. *Tectonophysics*, 228:313–329, 1993.

[27] C. Childs, J. Watterson, and J.J. Walsh. Fault overlap zones within developing normal fault systems. *J. Geol. Soc. Lond.*, 152:535–549, 1995.

[28] C. Childs, J. Watterson, and J.J. Walsh. A model for the structure and development of fault zones. *Journal of the Geological Society, London*, 153:337–340, 1996.

[29] T.T Cladouhos and R. Marrett. Are fault growth and linkage models consistent with power-law distributions of fault lengths? *Journal of Structural Geology*, 18(2/3):281–293, 1996.

[30] A.E. Clifton, R.W. Schlische, M.O. Withjack, and R.V. Ackermann. Influence of rift obliquity on fault-population systematics: results of experimental clay models. *Journal of structural geology*, 22:1491–1509, 2000.

[31] J.W. Cole, D.J. Darby, and T.A. Stern. Taupo volcanic zone and central volcanic region back-arc structures of north island, new zealand. In Brian Taylor, editor, *Back-arc Basins: Tectonics and Magmatism.* Plenum Press, 1995.

[32] J. Conteras, M.H. Anders, and C.H. Scholz. Growth of a normal fault system: observations from the lake malawi basin of the east african rift. *Journal of Structural Geology*, 22:159–168, 2000.

[33] C. Cooil. Constraining the near-surface stratigraphy in the bay of plenty, new zealand, from sedimentary cores collected during the research cruise tan99-14, november 1999. Master's thesis, Southampton Oceanography Centre, 2000.

[34] P.A. Cowie. A healing-reloading feedback control on the growth rate of seismogenic faults. *Journal of Structural Geology*, 20:1075–1087, 1998.

[35] P.A. Cowie, S. Gupta, and N.H. Dawers. Implications of fault array evolution for synrift depocentre development: insights from a numerical fault growth model. *Basin Research*, 12:241–261, 2000.

[36] P.A. Cowie and G.P. Roberts. Constraining slip rates and spacings for active normal faults. *Journal of Structural Geology*, 23:1901–1915, 2001.

[37] P.A. Cowie and C. H. Scholz. Growth of faults by accumulation of seismic slip. *J. Geophys. Res.*, 97:11085–11096, 1992b.

[38] P.A. Cowie and C.H. Scholz. Physical explanation for the displacement-length relationship of faults using a post-yield fracture mechanics model. *Journal of Structural Geology*, 14(10):1133–1148, 1992.

[39] P.A. Cowie and Z.K. Shipton. Fault tip displacement gradients and process zone dimensions. *Journal of Structural Geology*, 20:983–997, 1998.

[40] P.A. Cowie, D. Sornette, and C. Vanneste. Multifractal scaling properties of a growing fault population. *Geophysical Journal International*, 122:457–469, 1995.

[41] C.N. Crook and J. Hannah. Regional horizontal deformation associated with the march 2, 1987 edgecumbe earthquake, new zealand. *Geophysical Research Letters*, 15(4):361–364, 1988.

[42] C.N. Crook and J. Hannah. Regional horizontal deformation associated with the 1987 edgecumbe earthquake, bay of plenty, new zealand - an introduction. *New Zealand Journal of Geology and Geophysics*, 32:93–98, 1989.

[43] D.J. Darby, K.M. Hodgkinson, and G.H. Blick. Geodetic measurement of deformation in the taupo volcanic zone, new zealand: the north taupo network revisited. *New Zealand Journal of Geology and Geophysics*, 43:157–170, 2000.

[44] F.J. Davey, S.A. Henrys, and E. Lodolo. Asymmetric rifting in a continental back-arc environment, north island, new zealand. *Journal of Volcanology and Geothermal Research*, 68:209–238, 1995.

[45] F.J. Davey and E. Lodolo. Crustal seismic study of and ensialic back-arc basin (bay of plenty) new zealand. *Bollettino di Geofisica Teorica ed Applicata*, 37(145):25–37, 1995.

[46] N.H. Dawers and M.H. Anders. Displacement-length scaling and fault linkage. *Journal of Structural Geology*, 17(5):607–614, 1995.

[47] N.H. Dawers, M.H. Anders, and C.H. Scholz. Growth of normal faults: Displacement-length scaling. *Geology*, 21:1107–1110, 1993.

[48] E.J.M.Willemse. Segmented normal faults: Correspondence between three-dimensional mechanical models and field data. *Journal of Geophysical Research*, 102(B1):675–692, 1997.

[49] C. Faccenna, T. Becker, F. Pio Lucente, L. Jolivet, and F. Rossetti. History of subduction and back-arc extension in the central mediterranean. *Geophysical Journal International*, 14:809–820, 2001.

[50] C. Faccenna, M. Mattei, R R. Funiciello, and L. Jolivet. Styles of back-arc extension in the central mediterranean. *Terra Nova*, 9:126–130, 1997.

[51] H. Fossen and J. Hesthammer. Possible absence of small faults in gulfaks field, northern north sea: implications for downscaling of faults in some porous sandstones. *Journal of Structural Geology*, 22:851–863, 2000.

[52] P.C. Froggatt and D.J. Lowe. A review of late quaternary silicic and some other tephra formations from new zealand: their stratigraphy, nomenclature, distribution, volume and age. *New Zealand Journal of Geology and Geophysics*, 33:89–109, 1990.

[53] K. Gallagher. An examination of some uncertainties associated with estimates of sedimentation rates and tectonic subsidence. *Basin Research*, 2:97–114, 1989.

[54] J.G. Gibb. A new zealand regional holocene eustatic sea-level curve and its application to determination of vertical tectonic movements. a contribution to igcp- project 200. *Royal Society of New Zealand, Bulletin*, 24:377–395, 1986.

[55] P.A. Gillespie, J.J. Walsh, and J. Watterson. Limitations of dimension and displacement data from single faults and the consequences for data analysis and interpretation. *Journal of Structural Geology*, 14:1157–1172, 1992.

[56] Grindley. *Sheet 8 - Taupo. Geological map of New Zealand 1:250 000.* Department of Scientific and Industrial Research, Wellington, New Zealand, 1960.

[57] G.W. Grindley and A.G. Hull. Historical taupo earthquakes and earth deformation. In W.I. Reilly and B.E. Harford, editors, *Recent Crustal Movements of the Pacific Region*, volume 24, pages 173–186. 1986.

[58] D.E. Gunn and A.I. Best. A new automated non-destructive system for high resolution multi-sensor core logging of open sediment cores. *Geo-Marine letters*, 18:70–77, 1998.

[59] S. Gupta, P.A. Cowie, N.H. Dawers, and J.R. Underhill. A mechanism to explain rift-basin subsidence and stratigraphic patterns through fault array evolution. *Geology*, 26:595–598, 1998.

[60] B. Gutenberg and C.F. Richter. *Seismicity of the Earth and Associated Phenomena.* Princeton University Press, Princeton, New Jersey., 1954.

[61] C. H. Scaling laws for large earthquakes: consequenes of phusical models. *Bull seism. Soc. Am.*, 72:1–14, 1982.

[62] T. C. Hanks. Earthquake stress drops, ambient tectonic stresses and stresses that drive plate motions. *Pure and Applied Geophysics*, 115:441–458, 1977.

[63] J. Healy, J.C. Schofield, and B.N. Thompson. *Sheet 5, Rotorua (1st ed), Geological Map of New Zealand 1:250 000.* New Zealand Department of Scientific and Industrial Research, Wellington, 1965.

[64] R.H. Herzler. Late quaternary stratigraphy and sedimentation of the canterbury continental shelf, new zealand. *New Zealand Oceanographic Institution memoir*, 89, 1981.

[65] B.F. Houghton, C.J.N. Wilson, M.O. McWilliams, M.A. Lanphere, S.D. Weaver, R.M. Briggs, and M.S. Pringle. Chronology and dynamics of a large silicic magmatic system: Central taupo volcanic zone, new zealand. *Geology*, 23:13–16, 1995.

[66] P. Huggins, J. Watterson, J.J. Walsh, and C. Childs. Relay zone geometry and displacement transfer between normal faults recorded in coal-mine plans. *J. Struct. Geol.*, 17:1741–1755, 1995.

[67] J. Jackson and D. McKenzie. The geometrical evolution of normal fault systems. *Journal of Structural Geology*, 5:471–483, 1983.

[68] F.B. Jensen, W.A. Kuperman, M.B. Porter, and H. Schmidt. *Computational Ocean Acoustics*. American Institute of Physics, 1994.

[69] L. Jolivet, C. Faccenna, N. dAgostino, M. Fournier, and D. Worrall. The kinematics of back-arc basins, examples from the tyrrhenian, aegean and japan seas. In C. Mac Niocaill and P.D. Ryan, editors, *Continental Tectonics*, volume 164 of *Geological Society of London Special Publications*, pages 21–53. 1999.

[70] J.W.Cole and K.B. Lewis. Evolution of the taupo-hikurangi subduction system. *Tectonophysics*, 72:1–21, 1981.

[71] B.P. Kohn and G.P. Glasby. Tephra distribution and sedimentation rates in the bay of plenty, new zealand. *New Zealand Journal of Geology and Geophysics*, 21:49–70, 1978.

[72] G. Korvin. Shale compaction and statistical physics. *Geophys. J. R. astr. Soc.*, 28:35–50, 1984.

[73] G. Lamarche, P. Barnes, J. Bull, R. Garlick, A. Hill, H. Horgan, J. Mitchell, S. Taylor, and S. Wilcox. Bay of Plenty Neotectonics, Whakatane Graben extension. Unpublished cruise report, TAN9914, NIWA, Wellington, New Zealand, 1999.

[74] G. Lamarche, J. Bull, P. Barnes, S. Taylor, and H. Horgan. Constraining fault growth rates and fault evolution in the bay of plenty, new zealand. *Eos: Transactions American Geophysical Union*, 81(42):481–486, 2000.

[75] K. Lambeck and J. Chappell. Sea level change through the last glacial cycle. *Science*, 292:679–686, 2001.

[76] K. Lewis and H. Pantin. Intersection of a marginal basin with a continent: structure and sediments of the bay of plenty, new zealand. In B. Kokelaar and M. Howells, editors, *Marginal basin geology: volcanic and associated sedimentary and tectonic processes in modern and ancient marginal basins*, volume 16 of *Geological Society Special Publications*, pages 121–135. 1984.

[77] J. Loss, I.A Pecher, and U.S. ten Brink. Raygui: a graphical user interface fro interactive ray tracing (rayinvr). US Geological Survey open file report, 1998.

[78] K. Magara. Comparison of porosity/depth relationships of shale and sandstone. *J. Petrol. Geol.*, 3:175–185, 1980.

[79] I. Manighetti, G.C.P. King, Y. Gaudemer, C.Scholz, and C. Doubre. Slip accumulation and lateral propagation of active normal faults in afar. *Journal of Geophysical Research*, 106(B7):13667–13696, 2001.

[80] C. Mansfield and J. Cartwright. Fault growth by linkage: observations and implications from analogue models. *Journal of Structural Geology*, 23:745–763, 2001.

[81] C. S. Mansfield and J.A. Cartwright. High-resolution displacement mapping from three-dimensional seismic data: evidence for dip linkage during fault growth. *J. Struct. Geol.*, 18:249–263, 1996.

[82] D. Marchal, M. Guiraud, and T. Rives. Geometric and morphologic evolution of normal fault planes and traces from 2d to 4d data. *Journal of Structural Geology*, 25:135–158, 2003.

[83] D. Marchal, M. Guiraud, T. Rives, and J. Van Den Driessche. Space and time propagation processes of normal faults. In G. Jones, Q. J. Fisher, and R.J. R. J. Knipe, editors, *Faulting, Fault Sealing and Fluid Flow in Hydrocarbon Reservoirs*, volume 147 of *Geological Society Special Publication*, pages 51–70. 1998.

[84] R. Marrett and R. W. Allmendinger. Estimates of strain due to brittle faulting: sampling of fault populations. *Journal of Structural Geology*, 13:735–738, 1991.

[85] J. P. McCalpin. Frequency distribution of geologically determined slip rates for normal faults in the western united states. *Bull. Seismol. Soc. Am.*, 85:1867–1872, 1995.

[86] K. McClay and M. J. White. Analogue modelling of orthogonal and oblique rifting. *Marine and Petroleum Geology*, 12:147–151, 1995.

[87] A. M. McCoss. Simple construction for deformation in transpression/transtension zones. *Jounal of Structural Geology*, 8(6):715–718, 1986.

[88] A. McLeod, N.H. Dawers, and J. R. Underhill. The propagation and linkage of normal faults: insights from the strathspey-brent-statfjord fault array, northern north sea. *Basin Research*, 12:263–284, 2000.

[89] C. De Mets, R.G. Gordon, D.F. Argus, and S. Stein. Effect of recent revisions to the geomagnetic reversal time scale on estimates of current plate motions. *Geophysical Research Letters*, 21:2191–2194, 1994.

[90] V. Meyer, A. Nicol, C. Childs, J. J. Walsh, and J. Watterson. Progressive localisation of strain during the evolution of a normal fault population. *Journal of Structural Geology*, 24:1215–1231, 2002.

[91] H. Muraoka and H. Kamata. Displacement distribution along minor fault traces. *Journal of Structural Geology*, 5(5):483–495, 1983.

[92] I. A. Nairn and S. Beanland. Geological setting of the 1987 edgecumbe earthquake, new zealand. *NZ. J. Geol. Geophys.*, 32:1–13, 1989.

[93] I. A. Nairn and A. G. Hull. Post-1800 years b.p. displacements on the paeroa fault zone, taupo volcanic zone. *N. Z. Geol. Surv. Rec.*, 8:135–142, 1985.

[94] A. Nicol, J. J. Walsh, J. Watterson, and P.G. Bretan. 3-dimensional geometry and growth of conjugate normal faults. *Journal Of Structural Geology*, 17(6):847–852, 1995.

[95] A. Nicol, J.J. Walsh, J. Watterson, and J.R. Underhill. Displacement rates on normal faults. *Nature*, 390:157–159, 1997.

[96] P. M. Otway. Vertical deformation associated with the taupo earthquake swarm, june 1983. *R. Soc. N. Z. Bull.*, 24:187–200, 1986.

[97] J. F. Pacheo, C. Scholz, and L. R. Sykes. Changes in frequency-size relationship from small to large earthquakes. *Nature*, 355:71–73, 1992.

[98] A. Pascouet. Something new under the water: The bubbleless air gun. *The Leading Edge*, 10(11):79–81, 1991.

[99] D. Peacock and D. Sanderson. Displacement, segment linkage and relay ramps in normal fault zones. *Journal of Structural Geology*, 13(6):721–733, 1991.

[100] D. C. P. Peacock, R. J. Knipe, and D. J. Sanderson. Glossary of normal faults. *J. Struct. Geol.*, 22:291–305, 2000.

[101] D. C. P. Peacock and D. J. Sanderson. Geometry and development of relay ramps in normal fault systems. *AAPG Bulletin*, 78(2):147–165, 1994.

[102] D. C. P. Peacock and D. J. Sanderson. Effects of propagation rate on displacement variations along faults. *Journal of Structural Geology*, 18(2/3):311–320, 1996.

[103] D. C.P. Peacock. Propagation, interaction and linkage in normal fault systems. *Earth-Science Reviews*, 58:121–142, 2002.

[104] Pegler and Das. Analysis of the relationships between seismic moment and fault length for large crustal srike slip earthquakes between 1977 - 1992. *Geophysics Research Letters*, 23:905–908, 1996.

[105] R. Perrier and J. Quiblier. Thickness changes in sedimentary layers during compaction history: methods for quantitative evaluation. *AAPG Bulletin*, 58(3):507–520, 1974.

[106] D. D. Pollard and P. Segall. Theoretical displacements and stresses near fractures in rock: with applications to faults, joints, veins, dikes and solution surfaces. In B. Atkinson, editor, *Fracture Mechanics of Rock*. Academic Press, London., 1987.

[107] P.Villamoor and K. Berryman. A late quaternary extension rate in the taupo volcanic zone, new zealand derived from fault slip rates. *New Zealand Journal of Geology and Geophysics*, 44:243–289, 2001.

[108] W. I. Reilly. Horizontal crustal deformation on the hikurangi margin. *N. Z. J. Geol. Geophys.*, 33(2):393–400, 1990.

[109] W. P. Richardson. The matata earthquake of 1977 may 31: a recent event near edgecumbe, bay of plenty, new zealand. *N. Z. J. Geol. Geophys.*, 32(1):17–30, 1989.

[110] A. Roberts and G. Yielding. Continental extensional tectonics. In P. L. Hancock, editor, *Continental Deformation*, pages 223–250. Pergamon Press, 1994.

[111] J. V. Rowland and R. H. Sibson. Extensional fault kinematics within the taupo volcanic zone, new zealand: Soft linked segmentation of a continental rift system. *New Zealand Journal of Geology and Geophysics*, 44:27–283, 2000.

[112] J.G. Sclater and P.A.F. Christie. Continental stretching: an explanation of the post-mid-cretaceous subsidence of the central north sea basin. *Journal of Geophysical Research*, 85(B7):3711–3739, 1980.

[113] R.C. Shelley. Porosity gradients in the north sea oil-bearing sandstones. *J. Geol. Soc. Lond.*, 135:119–132, 1978.

[114] K. Shimazaki. Earthquake source mechanics. Number 37 in AGU Geophysical monographs, pages 209–216. 1986.

[115] B.A. Sissons. *The horizontal kinematics of the North Island of New Zealand*. PhD thesis, Victoria University, Wellington, New Zealand, 1979.

[116] E.G.C. Smith, B.J. Scott, and J.H. Latter. The waiotapu earthquake of 1983, december 14. *Bull. N. Z. Nat. Soc. Earthquake Eng.*, 17(4):272–279, 1984.

[117] R.B. Smith and R.L. Bruhn. Intraplate extensional tectonics of the eastern basin range: inferences on structural style from seismic reflection data, regional tectonics, and thermo-mechanical models of brittle-ductile deformation. *J. Geophys. Res.*, 89:5733–5762, 1984.

[118] W.H.F. Smith and D. T. Sandwell. Global seafloor topography from satellite altimetry and ship depth soundings. *Science*, 277:1957–1962, 1997.

[119] T.A. Stern. Asymmetric back-arc spreading, heat flux and structure associated with the central volcanic region of new zealand. *Earth Planet. Sci. Lett.*, 85:265–276, 1987.

[120] P. Thore, A. Shtuka, M. Lecour, T. Ait-Ettajer, and R. Cognot. Structural uncertainties: determination, management, and applications. *Geophysics*, 67:840–852, 2002.

[121] B.D. Trudgill and J.A. Cartwright. Relay ramp forms and normal fault linkages - canyonlands national park, utah. *Bull. Geol. Soc. Am.*, 106:1143–1157, 1994.

[122] R.I. Walcott. The kinematics of the plate boundary zone through new zealand: a comparison of short- and long-term deformations. *Geophysical Journal of the Royal Astronomical Society*, 79:613–633, 1984.

[123] R.I. Walcott. Geodetic strain and the deformational history of the north island of new zealand during the late cainozoic. *Phil. Trans. R. Soc. Lond.*, A 321:163–181, 1987.

[124] J.J. Walsh, C. Childs, J. Imber, T. Manzocchi, J. Watterson, and P.A.R. Nell. Strain localisation and population changes during fault system growth within the inner moray firth, northern north sea. *Journal of Structural Geology*, 25:307–315, 2003.

[125] J.J. Walsh and J. Watterson. Distributions of cumulative displacement and seismic slip on a single normal fault surface. *Journal of Structural Geology*, 9:1039–1046, 1987.

[126] J.J. Walsh and J. Watterson. Analysis of the relationship between displacements and dimensions of faults. *Journal of Structural Geology*, 10:239–247, 1988.

[127] J.J. Walsh and J. Watterson. Geometric and kinematic coherence and scale effects in normal fault systems. In A.M. Roberts, G. Yielding, and B. Freeman, editors, *The Geometry of Normal Faults*, volume 56 of *Geology Society Special Publication*, pages 193–203, 1991.

[128] J. Watterson. Fault dimensions, displacements and growth. *Pure and Applied Geophysics*, 124:365–373, 1986.

[129] J. Watterson, A. Nicol, J.J. Walsh, and D. Meier. Strains at the intersections of synchronous conjugate normal faults. *Journal of Structural Geology*, 20(4):363–370, 1998.

[130] T.H. Webb, B.G. Ferris, and J.S. Harris. The lake taupo, new zealand, earthquake swarms of 1983. *New Zealand Journal of Geology and Geophysics*, 29(4):377–389, 1989.

[131] D.L. Wells and K.J. Coppersmith. New empirical relationships among magnitude, rupture length, rupture width, rupture area and surface displacement. *Bulletin of the Seismological Society of America*, 84(4):974–1002, 1994.

[132] B. Wernike and B.C. Burchfiel. Modes of extensional tectonics. *Journal of Structural Geology*, 4:105–115, 1982.

[133] M.O. Withjack and W.R. Jamison. Deformation produced by oblique rifting. *Tectonophysics*, 126:99–124, 1986.

[134] I.C. Wright. Late quaternary faulting of the offshore whakatane graben, taupo volcanic zone, new zealand. *New Zealand Journal of Geology and Geophysics*, 33:245–256, 1990.

[135] I.C. Wright. Shallow structure and active tectonism of an offshore continental back-arc system: the taupo volcanic zone, new zealand. *Marine Geology*, 103:287–309, 1992.

[136] D. Wu and R.L. Bruhn. Geometry and kinematics of active normal faults, south oquirrh mountains, utah: implications for fault growth. *Journal of Structural Geology*, 16:1061–1075, 1994.